
Numerical Analysis of a Morphing Fairing for Folding Wingtip Joints

By

Nuhaadh Mohamed Mahid 



School of Civil, Aerospace and Design Engineering

University Of Bristol

A dissertation submitted to the University of Bristol in
accordance with the requirements for award of the degree of
Doctor of Philosophy in the Faculty of Engineering.

December 2024

Word Count: Approximately Forty-Seven Thousand

ABSTRACT

Airliners spend the majority of their flight time in the cruise phase. The induced drag is one of the largest contributors to drag in the cruise phase. The induced drag can be reduced by increasing the wing's aspect ratio with a longer wingspan, reducing fuel consumption. The airport gate codes specify a range for the wingspan of aircraft that may use each gate type, thereby restricting the types of aircraft that can fly between two airports. Moreover, a long wingspan increases the peak bending moment at the wing root, imposing a structural weight penalty. It further increases the aerodynamic roll damping of the aircraft, reducing its ability to meet the roll manoeuvre requirements for certification. Various solutions are proposed in the literature to circumvent these constraints and achieve the fuel efficiency benefits of high aspect ratio wings.

Aircraft with foldable wingtips (e.g., Boeing 777X) extend their wingtips to planar position before take-off to benefit from the long wingspan. The wingtip is folded after landing to reduce the wingspan, enabling the use of airport gate codes with a smaller wingspan range. The Semi-Aeroelastic Hinge (SAH) concept introduced a wingtip attached to the inboard wing with a free/flexible hinge oriented at an outward angle (referred to as flare angle) to the aircraft's longitudinal axis. The free/flexible hinge reduces the bending moment transferred from the wingtip to the inboard wing and alleviates the aerodynamic roll damping. The flare angle creates a coupling where the local angle of attack at the wingtip decreases with the upward rotation of the wingtip. Aeroelastic studies on the SAH concept show gust load alleviation, which is improved with a high flare angle, low torsional stiffness, and light wingtip. As the SAH wingtip will be in free response for a non-negligible portion of the flight time to alleviate gust load and roll damping, a fairing is required to improve airflow around the joint and seal its components from debris. A morphing fairing is preferred to provide a continuous and smooth surface enclosing joint with its actuator and clutch components.

The thesis presents a numerical analysis of a morphing fairing for folding wingtip joints. The fairing is made of Geometrically Anisotropic Thermoplastic Rubber (GATOR) skin with an accordion-type core sandwiched between two elastomeric facesheets. The GATOR skin is supported by a hinged rib, which is co-located with the SAH hinge but rotates independently of the folding angle. Additional ribs connected only to the fairing are added to maintain its cross-section shape at their locations. The fairing is flexible in direction across the hinge to enable rotation of the wingtip with minimal torsional stiffness. It has near zero Poisson's ratio to minimise the cross-section distortion due to the wingtip folding. It is also stiff in the out-of-plane direction to carry the pressure loads. The GATOR skin offers these properties and is manufactured via multi-material 3D printing.

The initial study identifies the level of fidelity required to model the GATOR panel fairing using a simplified geometry representing a fairing slice along the span at the thickest chordwise location of the aerofoil. It proposes a multi-scale modelling approach where the fairing is modelled as a shell surface with the equivalent shell properties of the GATOR panel. The study compares analytical and

FE-based methods of homogenising GATOR panel stiffness to equivalent shell stiffness. The study further considers the effects of core-facesheet interaction, transverse shear stiffness and geometric nonlinearity in the fairing deformation. It is proposed that FE-based homogenisation for the GATOR panel be used to capture the effects of core-facesheet interaction while ignoring the effects of transverse shear and geometric nonlinearity in the fairing deformation to keep the computation cost affordable. The proposed approach offers good agreement between the multi-scale and full-scale models of the fairing slice for the baseline design case up to a moderate folding angle.

Secondly, a parametric study of the GATOR fairing over the folding wingtip joint is presented using the multi-scale modelling approach. The study aims to reduce the torsional stiffness and the distortion of the fairing, measured as reaction torque and reduction in fairing thickness, respectively, as the wingtip folds. The study identified the feasibility of reducing the trade-off between the objectives by using pairs of variables that have a strong effect on different objectives. It showed thinner facesheets reduced torque with little effect on distortion, and thicker cores reduced distortion with little effect on torque. It also showed that floating ribs reduce distortion at the cost of torque, but the torque increase can be offset by increasing the fairing span. Pre-straining the fairing along the span further reduced distortion by delaying the buckling of the top skin as the wingtip folds.

Thirdly, the benefits of spatially varying the geometry of the fairing are studied using a beam-based model of the core (without the facesheet). The beam-based model explicitly represents the cells of the core with varying orientation, size and shape over the fairing geometry. The spatially varying geometry is derived by using the principal strain directions derived from a deformed shell-based fairing with isotropic properties. The principal strain lines are traced on the surface to create a lattice representing an accordion-type core with spatially varying geometry. This spatially varying core reduced the distortion of the fairing significantly relative to the baseline case with a uniform core. However, the effects of the spatially varying core on torque were dependent on its cell density relative to the baseline core.

Overall, the thesis presents a systematic study of the modelling techniques, the design space offered by the GATOR panel and the benefits of spatially varying geometry on a folding wingtip joint's fairing. The thesis made novel contributions in developing a framework for the analysis of flexible skins on wing geometry using a multi-scale modelling technique to reduce computation costs. It also made novel contributions in identifying the benefits of spatially varying core geometry to reduce the distortion of the morphing fairing. The thesis further identifies the limitations of the modelling approaches, their implications for the study, and recommendations for future work to address these limitations.

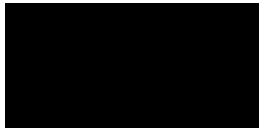
DEDICATION AND ACKNOWLEDGEMENTS

This thesis is dedicated to everyone who contributed to my academic journey. To my family for their unconditional support. To all my friends for their continual encouragement. To my primary supervisor, Dr. Benjamin Woods, for all the years of support and guidance that shaped my academic journey. To my secondary supervisors, Dr. Branislav Titurus and Dr. Mark Schenk, for their invaluable feedback and guidance. To my research placement supervisor, Dr. Stephen Daynes, for his technical guidance. To all my colleagues for innumerable discussions. To CoSEM CDT directors for their mentorship and the management for their support.

AUTHOR'S DECLARATION

I declare that the work in this dissertation was carried out in accordance with the requirements of the University's *Regulations and Code of Practice for Research Degree Programmes* and that it has not been submitted for any other academic award. Except where indicated by specific reference in the text, the work is my own work. Work done in collaboration with, or with the assistance of, others, is indicated as such. Any views expressed in the dissertation are those of the author.

SIGNED:



DATE: 24th December 2024

TABLE OF CONTENTS

1.	Problem Statement.....	1
1.1.	Motivation.....	1
1.2.	Potential of Morphing Aircraft	3
1.3.	Folding Wings.....	8
1.3.1.	Semi-Aeroelastic Hinge Concept.....	12
1.3.2.	Types of Folding Wing Fairing Structures.....	15
1.4.	Morphing Skins	21
1.4.1.	Elastomers.....	22
1.4.2.	Cellular Cores	23
1.4.3.	Corrugated Panels.....	28
1.5.	Proposed Folding Wingtip Fairing Concept.....	30
1.5.1.	Fairing Requirements	30
1.5.2.	Support Structure	31
1.5.3.	Skin Structure.....	33
1.6.	Research Gaps.....	35
1.6.1.	Stiffness Properties of Flexible Sandwich Panels	35
1.6.2.	Spatial Variation of Cellular Core Orientation.....	37
1.6.3.	Research Objectives and Thesis Outline	37
2.	Equivalent Elastic Properties of GATOR Morphing Sandwich Panels.....	41
2.1.	Modelling Considerations for Compliant Sandwich Panels	41
2.2.	Development of a Multi-scale Modelling Framework	47
2.2.1.	Analytical Homogenisation	49
2.2.2.	Finite Element Homogenisation.....	51
2.2.3.	Full-Scale Panel Analysis	54
2.2.4.	Simplified Fairing Analysis.....	56
2.3.	Results and Discussion	57
2.3.1.	Timoshenko Beam Assumption	58
2.3.2.	Laminated Plate Assumption	60

2.3.3.	Kirchhoff-Love Plate Assumption	64
2.3.4.	Linear Elasticity Assumption	65
2.4.	Conclusions	68
3.	Design Studies of GATOR Morphing Fairings for Folding Wingtip Joints	69
3.1.	Modelling of GATOR panel Fairing	69
3.1.1.	Definition of Wing Fairing Geometry	71
3.1.2.	Design Metrics for Quantifying Fairing Mechanical Performance	76
3.2.	Results and Discussion	80
3.2.1.	Sensitivity Study	80
3.2.2.	Panel Layer Thicknesses	81
3.2.3.	Chevron Geometry	83
3.2.4.	Fairing Geometry Variables	85
3.2.5.	Key Insights	89
3.2.6.	Proposed Solution	90
3.2.7.	Pressure load considerations	92
3.3.	Conclusions	95
4.	Preliminary Studies of Spatially Varying Core Geometry	97
4.1.	Motivation for the Method	97
4.2.	Approach and Methodology	100
4.2.1.	Derivation of the Material Orientation	102
4.3.	Trial of Material Orientation Methods Using a Shell-Based Model	108
4.3.1.	Elastomeric Matrix Composites	108
4.3.2.	Analysis of the Cantilevered Square Plate	109
4.4.	Fairing Core Analysis Using a Beam-Based Model	112
4.4.1.	Generation of Core Geometry for the Beam-Based Model	113
4.4.2.	Stiffness Properties of the Core	115
4.4.3.	Validation of the Beam-Based Fairing Model	118
4.4.4.	Analysis of Spatially Varying Core Geometry	118
4.4.5.	Limitations of the Beam-Based Modelling Approach	125
4.5.	Conclusions	126
5.	Conclusions	129
5.1.	Summary of the Results and Novel Contributions	130

5.2. Recommendations for Future Work	133
Reference	135

LIST OF TABLES

Table 1. Wingspan restrictions for airport gate compatibility [58, 59].....	10
Table 2. Dimensions of the unit cell geometry.	48
Table 3. Elastic properties of the materials used for the panel.	49
Table 4. Poisson's ratio terms of the GATOR panels from FE-based homogenisation.....	55
Table 5 Comparison of analytical and FE-based homogenisation for default configuration.....	58
Table 6. Variables of the fairing section.....	70
Table 7. Elastic properties of the materials used for the panel [133].....	70
Table 8. Variables of the sandwich panel.....	71
Table 9. Constraints applied to fairing ribs.	75
Table 10. Reduced design space that improves the fairing relative to the baseline.	90
Table 11. Proposed Design.....	91
Table 12. Elastic properties of the material [125, 136, 137].....	108
Table 13. Baseline configuration of the core.	116
Table 14. Equivalent stiffness properties of the core obtained from a solid, linear beam and quadratic beam model of the unit cell.	117

LIST OF FIGURES

Figure 1. Trends in CO ₂ emissions through aviation, along with estimates for reduced CO ₂ emissions through technology development so far and potential reductions in the future [6].....	2
Figure 2. Wing trailing edge devices for morphing. (a) shows a plain flap (Adapted from [22]), (b) shows a segmented flap from DLR “finger” concept (Reproduced from [23]), and (c) shows a deformable flap from DARPA Smart Wing Program - Phase 2 (Reproduced from [24]).....	3
Figure 3. Various wing morphing concepts (Adapted from [27]).	4
Figure 4. Examples of each morphing type. (a) shows Akaflieg Stuttgart fs29 glider with a variable span wing (Reproduced from [28]), (b) shows Bakshev LIG-7 aircraft with a variable chord wing (Reproduced from [28]), (c) shows F-111 aircraft with a variable sweep wing (Reproduced from [29]), (d) shows a variable thickness wing cross-section (Reproduced from [30]), (e) shows FlexSys flap on a variable camber wing (Adapted from [31]), (f) shows X-53 aircraft with a twisting wing (Reproduced from [32]), and (g) shows XB-70 aircraft with a folding wing (Reproduced from [33]).	5
Figure 5. Drag breakdown for a typical medium-range jet aircraft. (a) shows the components of drag (Reproduced from [53]). (b) shows the variation of zero-lift drag and lift-induced drag with flight speed (Adapted from [54]).....	8
Figure 6. Folding wing joints without fairing. (a) shows the Mikoyan MiG-29K (Reproduced from [61]). (b) shows the Boeing 777X aircraft (Reproduced from [62]).	11
Figure 7. Folding wingtip joint of XB-70 aircraft. (a) shows the outer magnesium thorium fairing (Reproduced from [63]), and (b) shows the internal power hinge system on the wing spar (Reproduced from [48]).	11
Figure 8. Semi-Aeroelastic Hinge (SAH) concept (Reproduced from [66]). (a) shows the top view, and (b) shows the front view of the aircraft’s starboard side.....	12
Figure 9. Folding wingtip concepts with rigid fairings. (a) shows the split wingtip concept (Adapted from [88]), (b) shows the Spanwise Adaptive Wing (SAW) concept (Adapted from [89]), and (c) shows the folding wing concept using the Brazier effect (Adapted from [90]).	16
Figure 10. Folding wingtip concepts with primary load-carrying adaptive structures. (a) shows a chiral structure joint with actuation rods (Adapted from [100]), (b) shows the asymmetric stiffness twin corrugated panel joint (Adapted from [101, 102]), and (c) shows a pressure-actuated cellular structure (PACS) joint (Adapted from [103]).....	18

Figure 11. Folding wingtip concepts with secondary load-carrying adaptive structures. (a) shows the “Z-wing” concept studied by Lockheed Martin (Adapted from [112, 113]), and (b) shows the corrugated panel wingtip fairing studied in the MORPHLET project (Adapted from [114]).	20
Figure 12. Stiff and flexible direction for (a) span morphing, (b) chord and camber morphing wing (Adapted from [122]).	22
Figure 13. Fibre-reinforced elastomer skins. (a) shows straight fibre-reinforced elastomer skin (Reproduced from [122]), and (b) shows curvilinear fibre-reinforced elastomer skin (Adapted from [126]).	23
Figure 14. Unit cell shapes generated using topology optimisation for the one-directional morphing application (Reproduced from [131]). The morphing direction is horizontal.	24
Figure 15. One-directional morphing sandwich panels. (a) shows the zero-Poisson’s ratio cores (Adapted from [123]), (b) the accordion core used for chord morphing (Reproduced from [128]), (c) shows the fibre-reinforced elastomer skin with an accordion-type core used for span morphing (Adapted from [127, 132]), and (d) shows the 3D-printed GATOR skin panel (Reproduced from [133]).	25
Figure 16. Non-uniform strain distribution on the facesheet of the GATOR panel (Reproduced from [139]). The parameter γ represents the ratio of deformed length to undeformed length of the panel in morphing direction.	27
Figure 17. Stiffness properties of various configurations of corrugated panels (Reproduced from [142]). (a) shows the 4 configurations of the corrugated panel skin. (b) shows their stiffness properties where (i) and (ii) show the longitudinal tensile modulus and flexural rigidity as a ratio of transverse tensile modulus, and (iii) and (iv) show the specific tensile and flexural modulus in the longitudinal direction.	28
Figure 18. Corrugated panel skin for camber and chord morphing application (Reproduced from [144]). (a) shows the design of the morphing skin panel, and (b) shows the panel deformation due to camber and chord change.	29
Figure 19. Types of fairings for Semi-Aeroelastic Hinge (SAH) wingtip concept. (a) shows a bullet-shaped rigid casing around the joint, and (b) shows a morphing fairing that encloses the joint section.	30
Figure 20. The morphing section has ribs that are free to pivot at their attachment to the spar, supporting flexible fairing (Adapted from [145]). (a) shows the morphing section geometry with the SAH hinge, which is shown in red, and pivoted rib hinges in blue. (b) shows the folding angle (θ) and rib pivoting angles (μ_1 and μ_2) for varying amounts of moment applied to the wingtip. (c) shows the deformed shape of the fairing with pivoted and fixed rib support structures.	32

Figure 21. Proposed support structure for the fairing. (a) shows the location of the morphing fairing section, (b) shows the pivoting and floating ribs used to support the fairing, and (c) shows the cross-section view of these ribs from the rear	33
Figure 22. Geometry and orientation of the proposed GATOR fairing for folding wingtip joints.....	34
Figure 23. An example of the sort of continuous spatial variation of the local core orientation that is proposed for this fairing concept, as explored in Chapter 4. (a) shows the three-dimensional wing section, and (b) shows a flattened representation of the core within the fairing.....	35
Figure 24. GATOR panel fairing on a folding wingtip joint.	42
Figure 25. The geometry of the GATOR panel unit cell. Blue annotations show the variables defining the geometry. Red annotations show effective lengths used in the modified analytical homogenisation of the core.	47
Figure 26. GATOR panel unit cell deformed to each shell deformation mode. Note that curvatures are stated in the form $\kappa\alpha\beta$ where $\alpha, \beta \in [1, 2]$. It represents a midplane curvature evaluated by the gradient $\delta\delta\beta\delta\delta\alpha$ (U) where U is the displacement vector. A positive curvature is a hogging deformation while a negative curvature is a sagging deformation. For instance, κ_{11} represent a hogging curvature (about 2-axis) resulting from the nodes in the face normal to 1-axis being displaced in the 13-plane.	53
Figure 27. Tip displacement of the GATOR panel to evaluate equivalent flexural modulus and study the effects of transverse shear. (a) shows the loading diagram, and (b) shows an example of the full-scale model with 10 cells along the length.	54
Figure 28. Representative fairing model for analysis of the effects of geometric nonlinearity in the GATOR panel deformation.	56
Figure 29. Effects of changing the chevron dimensions on the error between the equivalent moduli values from modified analytical formulation and FE-based homogenisation. Note that each carpet plot varies the length of the chevron wall and one of the cross-section dimensions, thereby, changing the slenderness ratio of the chevron wall.	59
Figure 30. The direct stress and strain distribution in the height-wise (3-axis) direction for various core heights for the load case of $\varepsilon_{xx} = 1$ in the FEM homogenisation. (a) shows the stress distribution, and (b) shows the strain distribution.	60
Figure 31. Comparison of various methods of homogenising the GATOR panel stiffness properties.....	61
Figure 32. The error in equivalent properties from the combined approach using FE-homogenised core properties relative to FE-based homogenisation of the GATOR panel. It shows the error due to facesheet-core interaction for various values of facesheet and chevron thickness.....	62

Figure 33. Direct strain distribution in the morphing direction (1-axis) on the facesheet from the top view for an applied strain of $\varepsilon_{11} = 1$ for various values of facesheet and chevron thickness.	63
Figure 34. Equivalent flexural modulus ($E1D$) along 1-axis evaluated by fitting full-scale FE analysis data to Euler and Timoshenko beam equations. The reference value is from the FE-based homogenisation of the GATOR panel unit cell. (a) shows the equivalent $E1D$ values, (b) shows their error relative to the reference value, and (c) shows the incremental change in the equivalent $E1D$ values as panel length increases.	64
Figure 35. Comparison of torque response between multi-scale and full-scale for the twin-plate models.....	66
Figure 36. Deformed shapes of the full-scale model of the fairing slice at 20-degree rotation (a) and (b) shows the 0% and 10% pre-strain case for the fairing slice without floating rib. (c) and (d) shows the 0% and 10% pre-strain case for the fairing slice with a floating rib.	67
Figure 37. The geometry of the GATOR panel unit cell.....	71
Figure 38. Fairing geometry. (a) shows the X and Y coordinates of the scaled grid and rotated grid. (b) shows the aerofoil nodes (i.e., Z coordinates) generated using the grid. In both figures, the red crosses represent the pivot point of the ribs.	73
Figure 39. Schematic of the fairing variables, coordinate systems and additional nodes for constraints and loading. Nodes 'AN-1' and 'AN-2' are co-located with the point 'RN-2' (shown slightly separated for clarity). XYZ-axes is the global coordinate system, and 123-axes is the hinge and the material coordinate system.	74
Figure 40. Deformed shape of the fairing full model at 80-degree rotation of the wingtip. (a) shows the 3-dimensional view, (b) the leading-edge view, and (c) the trailing-edge view of the fairing.	76
Figure 41. Various metrics used to quantify the objectives for cases with varying numbers of floating ribs (nfr). (a) shows the response of the metric for a half model. (b) shows snapshots of deformed shapes from the rear of the wing at various rotation angles.	78
Figure 42. Sensitivity of the objectives to changes in each variable. Torque and distortion are for the 20-degree rotation of the half model.....	81
Figure 43. Parametric study of core thickness (b) and facesheet thickness (tf). (a) shows the torque and distortion response for a 20-degree rotation of the pivoted rib. (b) shows the equivalent axial stiffness and bending rigidity in the morphing direction. (c) shows the geometry of the notable cases (13-plane view).	82
Figure 44. Loading diagram for analytical expressions.	83
Figure 45. Parametric study of core thickness (b) and chevron length (lc). (a) shows the torque and distortion response for a 20-degree rotation of the pivoted rib. (b) shows the	

equivalent in-plane stiffness and bending rigidity in the morphing direction. (c) shows the geometry of the notable cases.....	84
Figure 46. Parametric study of core thickness (<i>b</i>) and chevron angle (θ_c). (a) shows the torque and distortion response for a 20-degree rotation of the pivoted rib. (b) shows the equivalent in-plane stiffness and bending rigidity in the morphing direction. (c) shows the geometry of the notable cases.....	84
Figure 47. Parametric study of fairing span (<i>L</i>) and floating ribs (<i>nfr</i>). (a) shows the torque and distortion response for a 20-degree rotation of the pivoted rib. (b) and (c) show the corresponding deformed shape from the rear view of the fairing.....	86
Figure 48. Parametric study of pre-strain (εp). (a) shows the torque and distortion response for a 20-degree rotation of the pivoted rib. (b) shows the deviation of the fairing response at various rotation angles for different pre-strains. (c) to (e) show the deformed shapes from the rear view of the fairing.	87
Figure 49. Parametric study of pairs of fairing variables showing the torque and distortion response. (a) shows the effects of varying pre-strain (εp) and fairing span (<i>L</i>) for 10 and 20-degree rotation of pivoted rib. (b) shows the effects of varying pre-strain (εp) and the number of floating ribs (<i>nfr</i>) for 20-degree rotation of pivoted rib.	88
Figure 50. Performance of the randomly sampled design points from the reduced design space that outperformed the baseline solution. The results are extracted from the half model with a 20-degree rotation of the wingtip.	91
Figure 51. Pressure loading and boundary conditions of the unit cell.	93
Figure 52. Maximum vertical displacement (u_3) of the top facesheet under pressure loading for unit cells with various chevron wall lengths and facesheet thicknesses. (a) shows the displacement for the unit cell with no pre-strain, and (b) shows the displacement for the unit cells with 10% pre-strain.	93
Figure 53. Torque and distortion response for the baseline fairing with one floating for the case with and without pressure loading.....	94
Figure 54. Deformed shape of the baseline fairing with one floating rib at a 20-degree rotation for the case with and without pressure load. The legend shows the vertical (Z-axis) displacement. (a) shows the case with pressure load, and (b) shows the case without pressure load.	94
Figure 55. Lattice structure optimised for the three-point bending load case using principal stress directions (Reproduced from [155]). (a) shows the uniform lattice, and (b) shows the optimised lattice with spatially varying geometry.....	98
Figure 56. Examples of morphing wings with spatially varying lattice structures. (a) shows a wing with variable span, camber and twist (Reproduced from [185]), and (b) shows a modular wing with variable twist (Reproduced from [186]).	98

Figure 57. Wing global coordinate system (XYZ-axes) and the surface coordinate system ($\eta\zeta$ -axes) used for the flattened grid.....	103
Figure 58. Principal stress directions for a cantilever beam (Reproduced from [193]).....	104
Figure 59. Load paths for a cantilever beam under bending deformation (Reproduced from [159]). (a) shows the load case, (b) the horizontal load paths, (c) the vertical load paths, and (d) the force equilibrium within each load path sub-domain.....	105
Figure 60. Mohr's circle represents a stress or a strain state.	105
Figure 61. Material orientation with minimum strain energy for a given strain state. The strain state is represented as directionality. Snapshots of variation in strain energy with material orientation are shown at the top.	106
Figure 62. Fibre-reinforced elastomer panel properties for various fibre volume fractions. (a) shows the elastic moduli, and (b) shows the panel transverse strain at which each material field.....	109
Figure 63. The applied load case and the derived directions from the initial simulation of the cantilevered square plate.	110
Figure 64. Reaction forces for square plates with various orientations of the transverse direction (2-axis).....	111
Figure 65. Directionality parameter of the strain field with superimposed scaled principal strain vectors for the plate.....	112
Figure 66. Runge-Kutta method for tracing the vector field (Reproduced from [159]).....	114
Figure 67. Lattice generation process with seed points shown in green. (a) shows the traced lines, (b) shows the re-sampled lines at the intersection points, and (c) shows the core lattice with the added chevrons.	115
Figure 68. Unit cell geometry of the core.	115
Figure 69. FE models of the core. (a) shows a solid-based model. (b) shows a beam-based model with full lengths used for the walls. (c) shows a modified beam-based model with reduced length for the walls as the regions highlighted in red are modelled as rigid.	116
Figure 70. Comparison of homogenised properties of the unit cell from beam models to the solid model.....	117
Figure 71. Comparison of beam-based fairing model and shell-based fairing model with homogenised stiffness properties.	118
Figure 72. Flattened surface view of the fairing with a cosine-based variation of core orientation with an amplitude of 5 L_1 and a period of 30 L_2	119
Figure 73. Torque and distortion metric response for various curvilinear core geometry.	120
Figure 74. Lattice fairing generated by tracing the principal strain direction lines using the mid-span of the leading edge as the initial seed point.	121

Figure 75. Lattice fairing generated by tracing the principal strain direction lines using the mid-span mid-chord location on the top surface as the initial seed point.....	122
Figure 76. Torque and distortion metric response for the cores aligned with principal strain directions for lattice generated using different initial seed points.....	123
Figure 77. Improved spatially varying fairing design: (a) shows the lattice geometry of the improved fairing, (b) shows significantly improved torque and distortion responses, and (c) shows the deformed shape of the fairing at 40-degree rotation at the thickest region of the aerofoil (i.e., 30% chord).....	124
Figure 78. Transverse strain (2-axis) due to the unit cell being stretched in the 10% axial pre-strain (1-axis) for GATOR panels with (a) 6-millimetre and (b) 3-millimetre chevron separation (d) values.....	125

LIST OF ACRONYMS

AAW - Active Aeroelastic Wing

AFW - Active Flexible Wing

AR - Aspect Ratio

BWB - Blended Wing Body

CORSIA - Carbon Offsetting and Reduction Scheme for International Aviation

DARPA - Defence Advanced Research Projects Agency

DLR - German Aerospace Centre

EMC - Elastomeric Matric Composite

ETOPS - Extended-Range Twin-engine Operations Performance Standards

FDM - Fused Deposition Modelling

FEM - Finite Element Method

FFF - Fused Filament Fabrication

FishBAC - Fish Bone Active Camber

GATOR - Geometrically Anisotropic TermOplastic Rubber

IATA - International Air Transport Association

ICAO - International Civil Aviation Organization

MAS - Morphing Aircraft Structures

MORPHLET - Morphing Winglet

NASA - National Aeronautics and Space Administration

PACS - Pressure-Actuated Cellular Structure

PTERA - Prototype-Technology Evaluation and Research Aircraft

SAF - Sustainable Aviation Fuel

SAH - Semi-Aeroelastic Hinge

SAW - Spanwise Adaptive Wing

SMA - Shape Memory Alloy

TPU - Thermoplastic Polyurethane

LIST OF SYMBOLS

Fairing Geometry

ε_p – Pre-strain

L – Span

n_{fr} – Number of floating ribs

c – Fairing root chord

ϕ_m – Material orientation

ϕ – Sweep angle

T – Taper ratio

GATOR Panel Geometry

θ_c – Chevron angle

l_c – Chevron length

t_c – Chevron thickness

d – Chevron Separation

t_r – Rib thickness

b – Core thickness

t_f – Facesheet thickness

t_p – Panel thickness

1. PROBLEM STATEMENT

This thesis presents a numerical study of a morphing fairing design for folding wingtip joints. This chapter presents the motivation behind morphing concepts, a survey of various morphing concepts studied in the literature, and the proposed design for the fairing of folding wingtip joints. The literature survey highlights the features of the morphing concepts that are useful for the morphing fairing proposed in this thesis, along with the technical limitations identified in the previously studied concepts. This chapter further highlights the research gap in the methods used for analysing the proposed morphing fairing, along with the motivation for the analysis methods presented in the following chapters.

1.1. Motivation

The work carried out in this thesis is motivated by a desire to reduce the environmental impact of commercial aviation, with the realisation that making meaningful improvements will require substantial changes to the way we design and build airliners. Shape adaptive, or “morphing”, aircraft structures are one promising route to improving operating efficiency. This thesis will explore the use of a compliance-based morphing fairing to cover the joint on a hinged wingtip, but first, this chapter presents the wider context behind this work, including the impact that aviation has on our climate and the work that has been done to date on morphing aircraft concepts.

In the Paris Agreement, 195 state signatories committed to stabilising the global mean temperature 1.5°C above the pre-industrial levels [1]. Achieving this goal requires reducing CO₂ emissions to net zero by 2050-2060 and greenhouse gas emissions by 2070-2100 [2]. In support of the Paris Agreement, the International Civil Aviation Organization (ICAO) [3] and the International Air Transport Association (IATA) [4] adopted strategies for achieving net-zero carbon emissions in aviation by 2050. These include the Carbon Offsetting and Reduction Scheme for International Aviation (CORSIA) [5], which incurs the cost of emissions on the operators, thereby providing the economic incentive for reducing emissions.

The trends in aviation emissions are shown in Figure 1, along with the projections based on various scenarios [6].

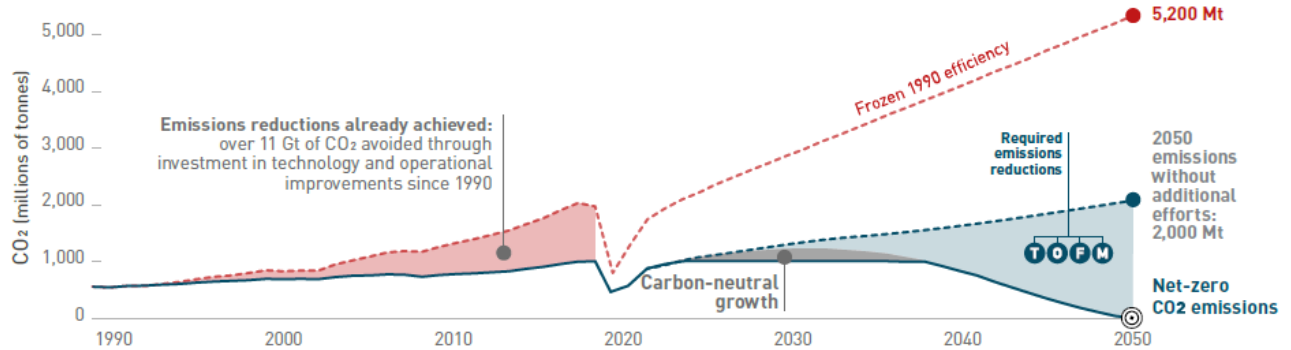


Figure 1. Trends in CO₂ emissions through aviation, along with estimates for reduced CO₂ emissions through technology development so far and potential reductions in the future [6].

It shows that the aviation industry has grown significantly in the past three decades, with demand for both passenger and freight increasing fourfold since 1990. The technology improvement has halved the energy used per mass per unit distance during the same period [7], leading to a cumulative 11 gigatonnes less CO₂ emission compared to meeting the aviation demand with the aircraft technology of 1990 [6]. However, as the reduced emissions are short of net zero and the aviation demand continues to grow, carbon emissions have continued to grow, as shown in the figure.

The predominant contribution to emissions in the aviation industry is from aircraft operations. The emissions from aircraft operations outweigh the combined emissions from aircraft production, fuel production, and infrastructure development [8]. Emissions from aircraft operations can be reduced by adopting sustainable fuel, improving aircraft efficiency, improving operational efficiency and reducing aviation demand [9]. Hence, various combinations of these strategies are presented in all pathways proposed for achieving net zero carbon emissions by 2050 [6]. In all pathways, the most significant reduction in emissions is projected from the adoption of sustainable aviation fuel (e.g., 53-71%), followed by improvements in aviation technology (e.g., 12-34%) and improvements in operational efficiency (e.g., 4-11%) [6, 9]. Sustainable aviation fuel strategies aim to adopt renewable energy sources for the aviation industry, such as fuels based on biomass products and waste. Operational improvement strategies include electric taxiing [10], improved turn-around operations [11], formation flying and increased Extended-Range Twin-engine Operations Performance Standards (ETOPS) rating for new aircraft.

Technological advancements are sought in various aircraft domains, including propulsion, aerodynamics, and structures, to reduce fuel consumption. These include propulsion efficiency gains in jet engines sought through the use of composite fans, power gearboxes, lean-burn combustors, and high bypass ratio designs [12]. Aerodynamic gains are sought through retention of laminar flow using passive and active techniques [13], reduction in skin friction drag [14], and improvements in the lift-to-drag ratio through trailing edge, leading edge, and wingtip devices [15]. Moreover, increased use of composite materials, integrated component designs, and tailored material orientations further aim to improve the aircraft's structural efficiency [16]. While incremental efficiency gains have been made in individual domains over the last three decades, in recent years, larger gains have been sought by integrating aerodynamic and structural design spaces using morphing structures [17-19].

1.2. Potential of Morphing Aircraft

Aircraft operate in various conditions, including different payloads, altitudes, speeds and temperatures. Each operating condition requires a different aircraft configuration for optimal efficiency. Additionally, within each flight mission, the aircraft performs various tasks such as take-off, landing, manoeuvres, and cruise, each requiring a different aircraft configuration for optimal efficiency. Hence, an aircraft optimised for a particular task will perform sub-optimally for the other tasks. For improved performance in multiple tasks during a flight mission and to enable extended capabilities with one aircraft configuration, the aircraft must adapt its wing shape during flight [19]. This change in aircraft wing shape to improve aircraft functionality is referred to as morphing. Morphing has been used since the dawn of flight in 1903, with the Wright brothers using wing warping [20] to control pitch and roll. Early camber morphing wings of biplanes, such as Parker's variable camber ribs, deformed compliantly to increase lift at low speeds [21].

In 1908, Henri Farman used articulated surfaces (i.e., flaps) hinged to the outboard trailing edge of both upper and lower wings to control flight [19]. The later monoplanes pursuing high speeds benefitted from such trailing-edge flaps, as they required rigid structures to avoid aeroelastic instabilities [17], hence needing flaps to change the wing camber. Today, aircraft use discrete rigid surfaces such as leading-edge (e.g., slats) and trailing-edge (e.g., flaps) devices to change the wing shape to enable low-speed tasks like landing while having a wing designed for efficient high-speed flight [19]. Some military aircraft undergo more significant planform changes, like variable sweep, to achieve supersonic speeds alongside high manoeuvrability and low landing speed [18]. In morphing aircraft, the wing geometry is typically changed using either rigid, segmented or deformable devices at various locations. Some examples of these devices for a wing's trailing edge are shown in Figure 2.

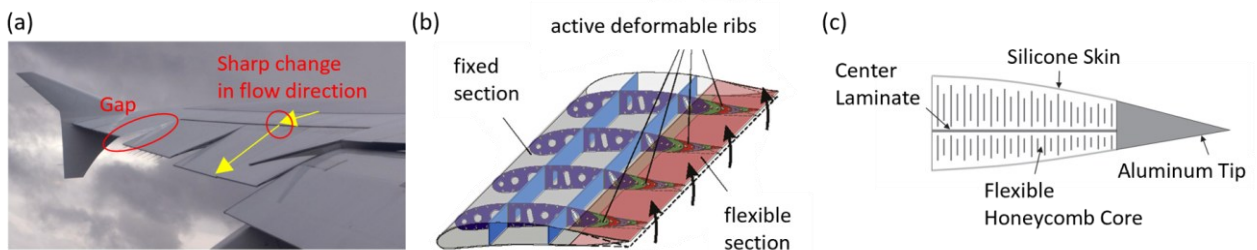


Figure 2. Wing trailing edge devices for morphing. (a) shows a plain flap (Adapted from [22]), (b) shows a segmented flap from DLR "finger" concept (Reproduced from [23]), and (c) shows a deformable flap from DARPA Smart Wing Program - Phase 2 (Reproduced from [24]).

Rigid devices, such as plain flaps shown in Figure 2a, are conventionally used in aircraft; hence, they are seldom referred to as morphing devices despite their deployment changing wing geometry. The rigid devices introduce a discontinuous curvature on the wing's surface, thereby requiring a sharp change in the flow direction. They also introduce gaps between the deployed device and the wing. These discontinuities on the wing surfaces introduce aerodynamic penalties that can be avoided with continuous and gapless devices [25, 26]. The segmented device in Figure 2b and the deformable device in Figure 2c achieve a continuous shape on the wing's trailing edge. The continuous shape and

the gap closure improve the aerodynamic efficiency by achieving higher lift-to-drag ratios [25, 26]. While these examples are for the wing's trailing edge, various morphing devices for different wing locations have been studied in the literature [17-19]. These devices are categorised into aerofoil, in-plane or out-of-plane wing morphing concepts, as shown in Figure 3.

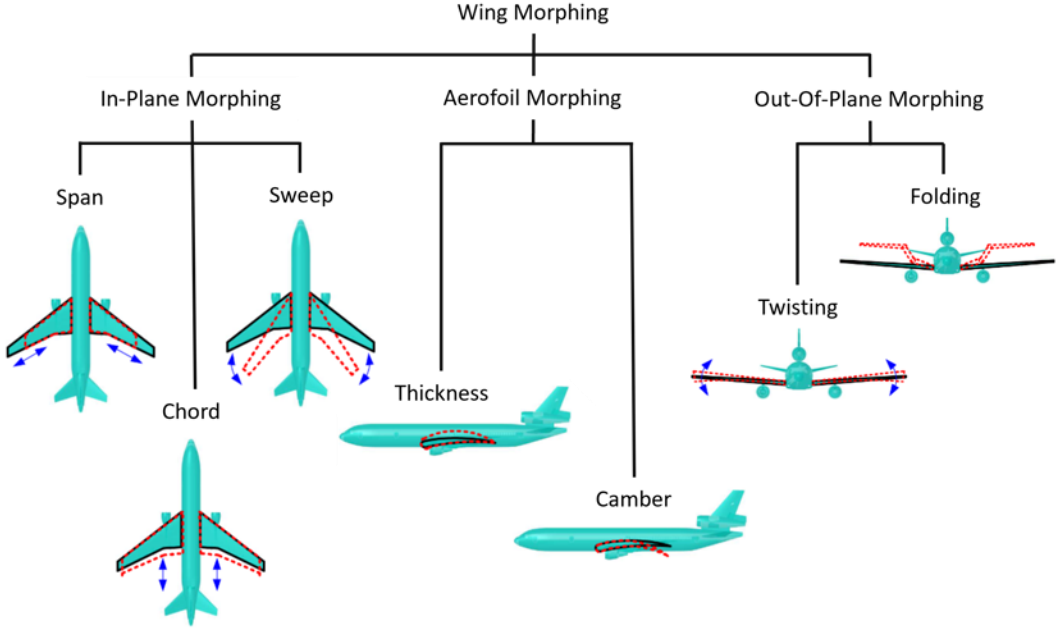


Figure 3. Various wing morphing concepts (Adapted from [27]).

Various morphing concepts have been studied extensively for different types of aircraft, although only a few concepts have been successfully implemented on flying aircraft. A historical survey of these concepts is presented by Weisshaar from the perspective of a former manager at the Defence Advanced Research Projects Agency (DARPA) [19]. Barbarino et al. presented a chronological survey of various morphing concepts along with their progress in numerical modelling, prototype testing, wind tunnel testing, and flight testing stages [17]. Li et al. presented a more recent review of various morphing concepts along with the methods used to analyse them [18]. Hence, the reader is directed to these works for a comprehensive survey of morphing concepts. The rest of this section discusses some examples of each morphing concept and their benefits and drawbacks. These morphing examples are shown in Figure 4.

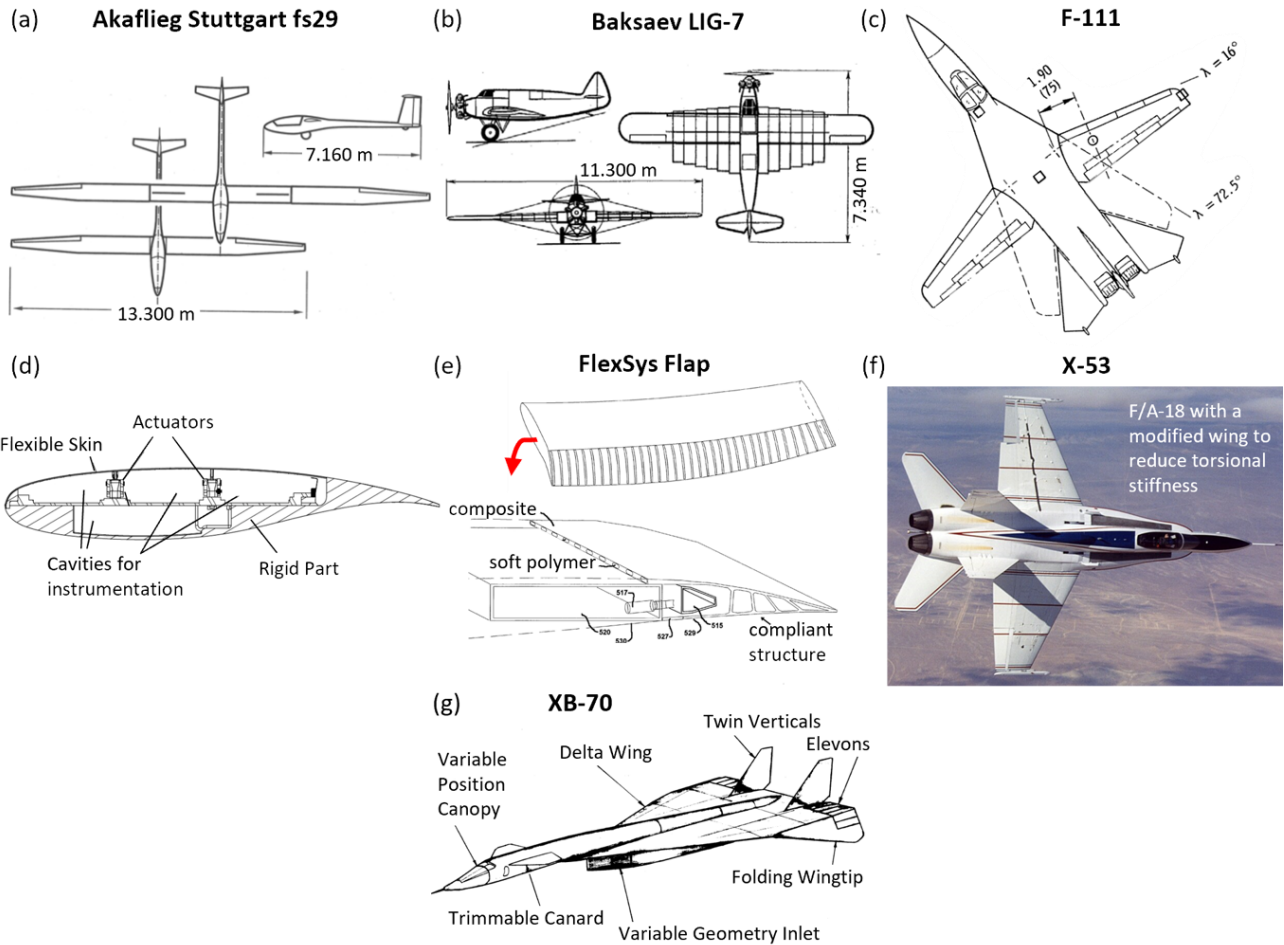


Figure 4. Examples of each morphing type. (a) shows Akaflieg Stuttgart fs29 glider with a variable span wing (Reproduced from [28]), (b) shows Baksaeve LIG-7 aircraft with a variable chord wing (Reproduced from [28]), (c) shows F-111 aircraft with a variable sweep wing (Reproduced from [29]), (d) shows a variable thickness wing cross-section (Reproduced from [30]), (e) shows FlexSys flap on a variable camber wing (Adapted from [31]), (f) shows X-53 aircraft with a twisting wing (Reproduced from [32]), and (g) shows XB-70 aircraft with a folding wing (Reproduced from [33]).

In-plane morphing concepts change the wing's planform through variable span, sweep angle or chord. Span morphing changes the wing's aspect ratio, affecting the aircraft's fuel efficiency and manoeuvrability [18]. High aspect ratio wings provide better fuel efficiency through reduced induced drag but at the cost of reduced manoeuvrability. Low aspect ratio wings are required for faster speeds and higher manoeuvrability, particularly in fighter aircraft for air combat manoeuvring. Hence, changing the aspect ratio of the wing based on the task (e.g., short wing for combat and long wing for cruise) improves the overall performance in both tasks instead of optimising aircraft for one task with a fixed design.

Figure 4a shows a German glider with a telescopic wing designed for performance soaring [28], which requires the glider to cover a given distance in the shortest time. Hence, it has a variable span to enable flight at different speeds depending on whether the glider is climbing or cruising. The fully extended wing enables climbing in weak thermal lift conditions and landing in short airfields. The fully retracted wing enables high-speed and aerobatic manoeuvres with high load factors. The telescopic

wing concept goes as far back as 1931, with the flight of MAK-10 [17], which changed its wingspan from 13 metres to 21 meters [28].

Figure 4b shows the Baksev LIG-7 aircraft, which had high aspect ratio wings designed for cruising flight [28]. For safe landing at slow speeds, the wing area was increased by 44% [17] by sliding six long-chord plywood sections from the fuselage to two-thirds of the wingspan. The long chord sections are fully enclosed within the fuselage and manually extended (and retracted) using tensioned cables. Chord morphing has also been studied for helicopter rotor applications. The Static Extended Trailing Edge (SETE) concept uses an X-truss mechanism to extend the chord by 30% by sliding a flat plate through a slot at the trailing edge [34]. The chord extension alleviates the retreating blade's stall, increasing the speeds, altitude and gross-weight capability at the flight envelop boundary.

Figure 4c shows the F-111 aircraft, which changes wing sweep from straight to sweptback (e.g., delta wing) position. Variable sweep is achieved mechanically by rotating the wing about a pivot point along with a forward translation of the wing to adjust the lateral stability [35]. Multiple production military aircraft use variable sweep angles, including General Dynamics F-111, Mikoyan-Gurevich MiG-23, and Panavia Tornado [19]. Variable sweep aircraft benefit from the high endurance in subsonic flights and low stall speeds (for operation from short runways) offered by straight wings, alongside increased manoeuvrability and reduced shockwave drag at transonic flight offered by sweptback wings [35]. Hence, an aircraft with variable sweep requires a smaller wing area and thrust-to-weight ratio relative to a fixed-wing counterpart with similar endurance, maximum speed, and stall speed [36].

Variable aerofoil thickness offers an effective aerodynamic flow control to reduce drag through small changes to the wing's cross-section geometry [37]. The thickness variation on the upper surface, as shown in Figure 4d, delays the transition of laminar flow to turbulent flow to reduce skin friction drag in subsonic flights [30]. Wind tunnel studies on this concept showed a 25% extension of the laminar flow region along the chord and a subsequent 18.5% reduction in drag [38]. Other studies have shown that in transonic flights with Mach numbers from 0.68 to 0.76, variation of only the upper surface by 1% of the chord can reduce the shockwave drag by 4 to 5.5% [39]. Moreover, for an A340-type wing, adjusting the local thickness around the shock location using an adaptive bump device showed a 4% reduction in drag, leading to a 2.1% fuel saving in transatlantic flights [40].

Variable camber offers the ability to adjust the wing's lift-to-drag ratio based on the aircraft's altitude, speed and weight [41]. Airbus reported a 10% increase in buffet boundary and 3-6% fuel savings achieved by reducing drag through active deployment of a traditional rigid trailing edge flap system over the course of a flight to modify local camber and spanwise lift distribution [42]. Variable camber also offers the ability to tailor the spanwise lift distribution on the wing to reduce lift at the wing tip, alleviating the wing root bending moment during manoeuvres and gust loading [43]. As variation of spanwise lift distribution can reduce the worst-case loads on the wing, the ultimate load case for which the wing structure is designed can be reduced, leading to an estimated weight saving of 10% [41].

Compliant variable camber concepts, such as the FlexFoil flap system shown in Figure 4e, deform the structure to provide continuous surface curvature while keeping the part count low to simplify the design. It uses flexible skin supported by a compliant frame to provide continuous curvature on the surface and extend the laminar flow region along the chord to up to 60% of the chord length in high lift conditions, as demonstrated in flight tests [44]. Another camber morphing concept at the trailing edge, Fishbone Active Camber (FishBAC) [25], uses a bending spine with stringers connecting to a pre-tensioned elastomeric matrix composite (EMC) skin. This design enables a continuous elastically lofted transition between the rigid wing and compliant trailing edge device by smoothly varying the stringer orientation from the chordwise direction on the rigid wing to the spanwise direction on the FishBAC device [26]. Aerodynamic studies show a 3% reduction in drag and a 7% improvement in lift-to-drag ratio through this gap closure at the wing's trailing edge [26].

Variable twist wings go as far back as the dawn of flight, with the Wright brothers using wing warping to control the pitch and roll in their first flight [20]. As flight speeds increased, flexible wings were prone to adverse aeroelastic twist, leading to deteriorating control effectiveness and roll reversal [45]. Hence, stiff wing structures were used for later high-performance aircraft but at the cost of increased structural weight and drag penalties [45]. The NASA/Rockwell Active Flexible Wing (AFW) program showed that a flexible wing with multiple leading and trailing edge devices can achieve a favourable wing twist that suppresses flutter, alleviates gust loads and controls manoeuvre loads while maintaining sufficient control authority [46]. The subsequent Active Aeroelastic Wing (AAW) program run by NASA, Air Force Research Laboratory and Boeing Company demonstrated reduced aerodynamic drag while increasing the control power in the flight test of X-53 aircraft shown in Figure 4f, enabling high aspect ratio, thin, and lighter wing designs [32].

Folding wings have been used in various production aircraft, including the Fairey Gannet, Grumman A-6 Intruder and Sukhoi Su-33, to reduce aircraft stowage space for hangers and naval carriers. Folding wings were also studied to improve aircraft performance in flight. The earliest known example is the Nikitin-Shevchenko IS aircraft, which used a biplane configuration for short runway operations and high climb rates and a monoplane configuration with a folded lower wing to achieve faster speeds [47]. The XB-70 aircraft, shown in Figure 4g, used in-flight folding wingtips to improve directional stability by increasing effective vertical surface area upon wingtip deflection [48]. It also reduced the longitudinal stability margin, thereby reducing drag through reduced trim requirement at supersonic speeds. It further increased compression lift by reflecting off the shockwaves from the inlet wedge, thus improving the lift-to-drag ratio in the folded wingtip configuration.

Morphing concepts improve aircraft performance, operational capability, and fuel efficiency at a likely cost to the design complexity, structural weight, and maintenance requirements [17]. Hence, morphing concepts require an identifiable need in aircraft mission requirements and supporting technologies that make morphing concepts cost-effective for them to be realised in production aircraft [19]. Several morphing concepts studied for military applications have made it to production aircraft in the last five decades, most notably sweep morphing wings. However, adopting new morphing concepts in commercial aviation has been slow due to the high development costs of new

aircraft and the high production volumes required for their economic success [43]. Instead, aircraft manufacturers deliver incremental design improvements through variants and derivatives of existing aircraft families.

The Carbon Offsetting and Reduction Scheme for International Aviation (CORSIA) [5], which places the cost of emissions on the airline operators, aims to accelerate the reduction in CO₂ emissions by incentivising the aircraft manufacturers to pursue fuel-efficient designs and the airlines to adopt them. To this end, aircraft manufacturers, including Boeing [49, 50] and Airbus [51], are studying various ultra-efficient high aspect ratio wing concepts, including truss-braced flexible wings [50] and folding wingtips [49, 51]. Given that the development of most previously discussed morphing concepts were stalled by design complexity, added weight, and integration issues, deformable structures with seamless design, such as deformable fairings, are explored for future aircraft.

1.3. Folding Wings

A typical short-range commercial jet aircraft (e.g., A320) spends more than three-quarters of its flight time in the cruise phase (e.g., 85% of flight time for a 2500 nautical mile flight [52]). In the cruise phase of the flight, the most significant contribution to drag comes from skin friction and induced drag [53], as shown in Figure 5a.

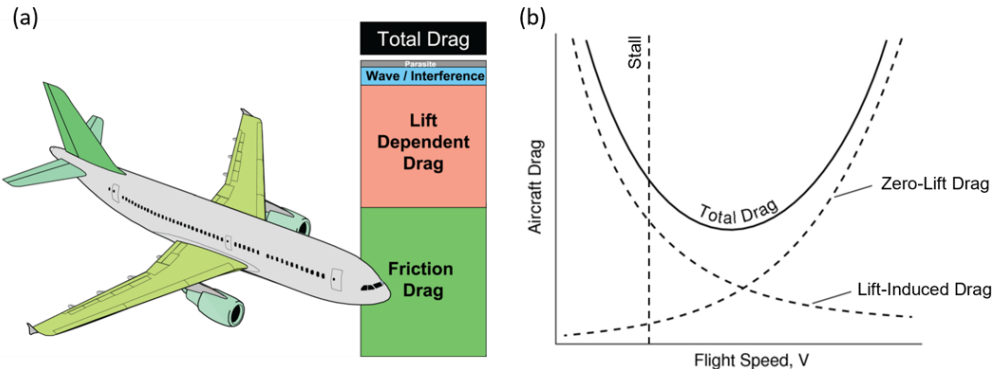


Figure 5. Drag breakdown for a typical medium-range jet aircraft. (a) shows the components of drag (Reproduced from [53]). (b) shows the variation of zero-lift drag and lift-induced drag with flight speed (Adapted from [54]).

These drag components are generally categorised as zero-lift drag (e.g., skin friction drag) and lift-induced drag, and their contributions to total drag vary with flight speed, as shown in Figure 5b. The relationship between the coefficient of total drag (C_D), zero-lift drag (C_{D0}) and lift-induced drag (C_{Di}) are shown in Equation 1, where parameter e is the Oswald efficiency, AR is the aspect ratio of the wing and C_L is the coefficient of lift.

$$C_D = C_{D0} + C_{Di} = C_{D0} + \frac{C_L^2}{e \pi AR} \quad \text{Equation 1}$$

The Oswald efficiency (e) represents the change in induced drag with lift relative to an ideal wing of the same aspect ratio with an elliptical lift distribution along the span. The aspect ratio (AR) represents the ratio of wing span to average chord length (defined as $AR = b^2/S$ where b is the

wing span and S is the wing area). The flight speed with the lowest total drag gives the longest flight time (i.e., endurance) with a given amount of fuel; however, it does not provide the longest attainable range for a jet aircraft. The maximum endurance (E) and range (R) are evaluated using the following expressions derived from the Breguet formula [55].

$$E = \frac{1}{g f} \left(\frac{C_L}{C_D} \right) \ln \left(1 + \frac{W_F}{W_P + W_E} \right) \quad \text{Equation 2}$$

$$R = \frac{a}{g f} \left(M \frac{C_L}{C_D} \right) \ln \left(1 + \frac{W_F}{W_P + W_E} \right) \quad \text{Equation 3}$$

The parameters W_F , W_P and W_E represent the weight of fuel, payload and the empty aircraft, respectively. The parameters g and f are gravitational acceleration and specific fuel consumption, and the parameters a and M are the speed of sound and Mach number. The equations indicate that reducing the aircraft's empty weight (W_E) or improving the engine efficiency (f) can improve both range (R) and endurance (E). From the aerodynamic design, the maximum endurance (E) is achieved by maximising the lift-to-drag ratio (C_L/C_D) whereas the maximum range (R) is achieved by maximising the product of Mach number and lift-to-drag ratio (MC_L/C_D).

For commercial airliners, maximising the range (R) for a given amount of fuel is essential to reduce the operating cost of the aircraft. The fuel efficiency of the aircraft can be increased by reducing the zero-lift drag or the lift-induced drag. The zero-lift drag predominantly consists of skin friction drag, and achieving a significant reduction in skin friction drag requires large reductions in the wetted surface area. A large reduction in the wetted surface area for a given payload capacity is achieved by the Blended Wing Body (BWB) aircraft concept [56, 57]. The BWB aircraft concept deviates from the conventional "tube and wing" aircraft configuration by blending in the fuselage with the wing to use the whole aircraft as a lift-generating surface. The BWB aircraft configuration with 800 passenger capacity is estimated to have 33% less wetted surface area relative to conventional aircraft configuration (e.g., Airbus A380) [56], thereby improving the lift-to-drag ratio [57]. However, the BWB aircraft concept presents multiple technical challenges in aircraft stability, control, handling qualities, engine acoustics and passenger cabin pressurisation [57]. Hence, recent reductions in skin friction drag are achieved only in small increments through reduced-friction skins (e.g., AeroShark riblet films) and laminar flow control techniques [13].

Significant reductions in the induced drag of the aircraft can be achieved by increasing the aspect ratio (AR) of the wing, as indicated by Equation 1. The wing's aspect ratio can be increased by increasing its span and reducing its mean chord while maintaining adequate wing area to perform tasks like take-off and landing at slow speeds. However, the airport gate code requirements limit the aircraft's wingspan according to gate categories in Table 1.

Table 1. Wingspan restrictions for airport gate compatibility [58, 59].

ICAO Code	FAA Group	Wingspan	Example Aircraft
A	I	<15 m	Cirrus SR22, Cessna 182T
B	II	15 m – 24 m	Bombardier CRJ700, de Havilland Canada DHC-6
C	III	24 m – 36 m	Boeing 737, Airbus A320
D	IV	36 m – 52 m	Boeing 767, Airbus A310
E	V	52 m – 65 m	Boeing 787, Airbus A350
F	VI	65 m – 80 m	Boeing 747-8, Airbus A380

Hence, each aircraft's operations are limited to airports with gate types compatible with the aircraft's wingspan. For instance, consider the Boeing 737 and Airbus A320 aircraft, which use the ICAO C gates. London Heathrow Airport has 86 gates compatible with ICAO C and 9 gates compatible with ICAO D [60]. Given that both aircraft have a wingspan of approximately 35.8 metres, any further increase in the wingspan of these aircraft types in a future variant will require them to use a larger gate. The next gate size, ICAO D, is significantly less common and likely to cost more at the London Heathrow Airport, thereby making it difficult for airlines to adopt a future aircraft variant with a longer wingspan. To circumvent such airport gate restrictions, aircraft manufacturers are developing folding wingtips for passenger aircraft to benefit from the reduced induced drag from high aspect ratio wings while using smaller airport gates [49]. For instance, the Boeing 777X aircraft, which is currently undergoing the certification process, has a wingspan of 71.75 metres in flight with extended wingtips and folds its wingtip after landing to decrease its wingspan to 64.85 metres, making it compatible with ICAO E gates [49].

The adoption of folding wingtips to circumvent the gate restriction in civil aircraft (e.g., Boeing 777X) is analogous to the use of folding wings in military aircraft to reduce their stowage space for naval carrier operations (e.g., Grumman F4F-4 [19] and Mikoyan MiG-29K [61]). While the adoption of folding wings led to increased weight from the joint components, the benefit of being able to fit more aircraft on a naval carrier deck outweighed the penalties [19]. As the wing folding is carried out only on the ground and not in flight, the wing joint is not covered with a dedicated fairing, thereby leaving the hinge components exposed when the wing is folded. The exposed hinge components on Mikoyan MiG-29K [61] and Boeing 777X aircraft [62] are shown in Figure 6.



Figure 6. Folding wing joints without fairing. (a) shows the Mikoyan MiG-29K (Reproduced from [61]). (b) shows the Boeing 777X aircraft (Reproduced from [62]).

From close inspection of these examples, it can be seen that the skin surface extends over the joint in a manner which fully encloses the hinge components when the wing is extended and locked in position for flight, creating a smooth outer surface around the joint, and removing the need for any additional fairing or covering. In contrast, in applications where the wingtip is capable of rotating in flight, the joint must be covered to provide a smooth aerodynamic surface to minimise potential drag penalties from an exposed hinge. For instance, the joint of the XB-70 folding wingtip, including the actuation motor and the hinges, was covered by a magnesium thorium fairing along the entire hinge line [48], as shown in Figure 7.

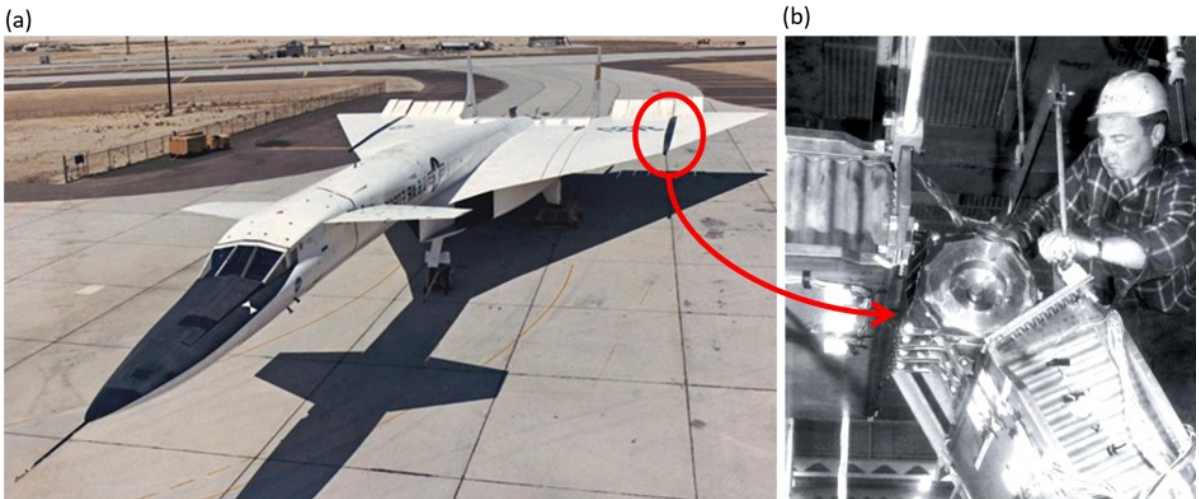


Figure 7. Folding wingtip joint of XB-70 aircraft. (a) shows the outer magnesium thorium fairing (Reproduced from [63]), and (b) shows the internal power hinge system on the wing spar (Reproduced from [48]).

It shows that the fairing creates a bulge around the joint as it encloses the internal components. The hinge is aligned with the aircraft's longitudinal axis, forming a cylindrical bullet-like shape along the flight's direction, thereby reducing its frontal area. The fairing further shields the hinge components from the heat of supersonic flights, where the leading edge temperatures can reach up to 265°C (510°F) at Mach 3 [64]. The magnesium-thorium alloy has a high resistance to creep between 260-315°C (500-600°F), making it suitable for high-temperature applications [65].

1.3.1. Semi-Aeroelastic Hinge Concept

While longer wingspans can help reduce induced drag, they also have the negative effect of increasing peak bending moments at the wing root during manoeuvre and gust loading due to the extended moment arm. As these loading scenarios are likely to be the limit design case for wing strength, an extended wingspan imposes a weight penalty on the wing due to the required structural reinforcement. Considering that a hinged wingtip is employed to reduce the wingspan to make the aircraft compatible with smaller airport gate sizes [49], it is desirable to use the hinged wingtip for gust load alleviation. To this end, Airbus, the University of Bristol, and others are developing the Semi-Aeroelastic Hinge (SAH) concept schematically shown in Figure 8.

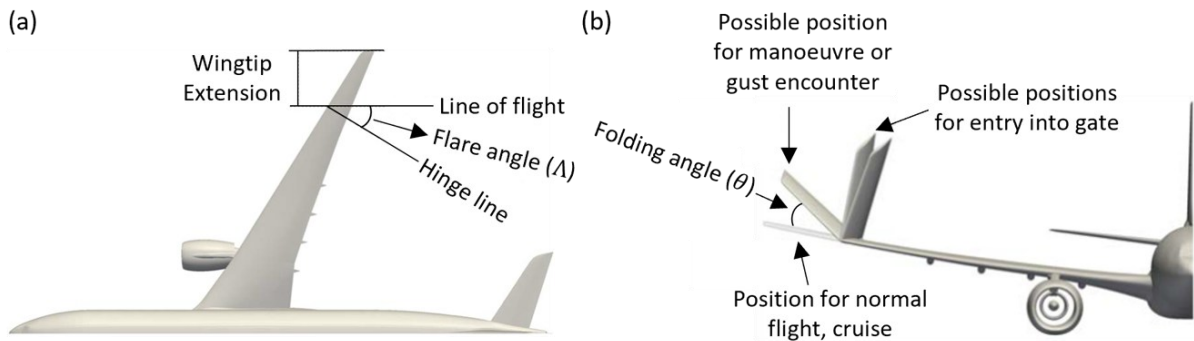


Figure 8. Semi-Aeroelastic Hinge (SAH) concept (Reproduced from [66]). (a) shows the top view, and (b) shows the front view of the aircraft's starboard side.

It uses a wingtip hinged to the inboard wing at an angle from the line of flight (Λ). The flare angle (Λ) creates a geometric coupling between the folding angle (θ) and the local angle of attack of the wingtip ($\Delta\alpha_{WT}$), as shown in Equation 4 [67].

$$\Delta\alpha_{WT} = -\tan^{-1}(\tan \theta \sin \Lambda) \quad \text{Equation 4}$$

It indicates that as the wingtip folds up (θ), it reduces the local angle of attack ($\Delta\alpha_{WT}$), thereby reducing the lift generated at the wingtip. As the lift generated at the wingtip reduces with the folding angle, there will be an equilibrium folding angle (also referred to as coasting angle) that balances the moment from the wingtip lift for a given flight condition (e.g., flight speed and altitude) against the moment from the wingtip weight and the torsional stiffness of the hinge. In the absence of aerodynamic loading (i.e., on the ground), the wingtip is envisioned to have a negative equilibrium folding angle (i.e., downward deflection). In this case, the moment from the wingtip weight is balanced by the moment from the torsional stiffness of the hinge. Hence, it is possible to adjust the torsional stiffness of the hinge in flight based on the flight conditions to achieve a planar equilibrium position of the wingtip (i.e., zero folding angle)[68].

The wingtip is envisioned at the planar (horizontal) position in cruise to maximise the wing's aspect ratio to reduce induced drag and freely flap in response to manoeuvre and gust loads to alleviate the peak bending moment at the wing root [69]. As a flexible hinge significantly reduces the transfer of bending moment across it, and the flare angle reduces the lift generated at the wingtip as the wingtip

folds, the SAH wingtip reduces the peak loads at the wing root during manoeuvres and gust encounters [51]. Hence, the SAH concept enables a typical jet airliner to increase its wingspan with a minimal increase in peak loads at the wing root during gust encounters (e.g., a 4.36% increase in peak loads for a 25% increase in wing span [67]). The numerical [67] and wind-tunnel [70, 71] studies on the SAH concept indicate that the lighter the wingtip, the lower the torsional stiffness of the hinge and the higher the flare angle, the greater the reduction in peak loads at the wing root. A light wingtip further benefits the aeroelastic stability by increasing the flutter speed. It reduces the inertial forces, enabling a rapid response of the wingtip to gust loading, thereby reducing the phase shift between the wing root bending moment and the folding angle. In contrast, low torsional stiffness and high flare angle worsen the aeroelastic stability by reducing the flutter speed of the wing [67, 69, 72]. Hence, the design of the SAH wingtip must trade off the load alleviation benefits against the mitigation of flutter, as the aircraft must avoid flutter within the design flight envelope (i.e., up to 115% of dive speed [69]).

In steady flight, reducing the wingtip motion due to turbulence is desirable to reduce structural vibrations while maintaining the ability to respond to severe manoeuvre and gust loads. An approach to achieving this behaviour uses a nonlinear torsional spring with high stiffness near zero folding angle and low stiffness beyond a threshold folding angle of the wingtip [73]. While the high stiffness near zero folding angle reduces the wingtip response to turbulence, it also delays the wingtip response to severe manoeuvre and gust loads, thereby reducing load alleviation. This delay in wingtip response is remedied by combining a nonlinear torsional spring with an active actuator to accelerate the initial response (i.e., up to the first peak). The combined system reduces the wingtip deflection due to turbulence while retaining the ability to rapidly respond to manoeuvre and gust loads exceeding a predefined threshold. A passive implementation of this approach is also proposed by using a combination of oblique springs connected to the torsional spring of the hinge to create a high static and low dynamic aeroelastic stiffness for the wingtip [68]. Another approach to reducing wingtip motion due to turbulence in steady flight is locking the wingtips in the planar position during cruise and releasing them only at the onset of gust or manoeuvre loads [74].

A fixed wingtip reduces the aircraft's roll rate relative to the baseline wing without the wingtip due to the increased aerodynamic roll damping from the longer wing. Hence, a longer wing with a fixed wingtip would likely require larger ailerons to increase the roll rate to meet the certification requirements of maximum time to complete a defined roll manoeuvre [75, 76]. In contrast, a freely hinged wingtip has similar roll acceleration as a wing without wingtips and a steady roll rate higher than that of a fixed wingtip, thereby indicating a passive alleviation of the roll damping [77-79]. Hence, a free hinge configuration is preferred for manoeuvres, especially when landing, to compensate for the reduced roll rate at low speeds due to diminished aileron authority. Further studies have also considered the possibility of the wingtip contacting the ground on impact landing and the presence of limit cycle oscillations in a freely hinged wingtip response [79] to determine the size of the wingtip and the stiffness of the wing required for the prototype aircraft for flight testing the SAH concept [51, 80].

The prototype aircraft, named AlbatrossOne, represents a 1:14 scale model of a typical short-range aircraft (e.g., Airbus A321) with a 2.6-metre wing without the wingtips [51]. Two different lengths of wingtips were tested, increasing the wingspan to 3.2 and 3.7 metres. The wingspan without the wingtip is equivalent to a 35-metre wing, and the wingspans with the two wingtip configurations are equivalent to 45-metre and 52-metre wings. Airbus first tested the wings in the wind tunnel to confirm the separation of wing bending mode frequency and wingtip flapping mode frequency to avoid flutter. The flight tests confirmed that the SAH wingtip is statically and dynamically stable throughout the flight and alleviates the wing bending moment relative to the fixed wingtip configuration.

The aircraft was modified for the second phase of flight tests by adding a yaw damper to improve the stability of the Dutch roll mode, a clutch to lock and release the wingtip, and an actuator to adjust the folding angle on command [80]. A tethered flight test [81] demonstrated the improved Dutch roll stability and confirmed the wingtip stall at high angles of attack [80]. An aerodynamic test (i.e., van-driven with a mounted wing on the side) demonstrated the wingtip release and adjustment mechanism. It also showed that the wingtip stall at high angles of attack (e.g., landing condition) could be mitigated by locking it at a 10-degree folding angle [80]. Furthermore, the flight tests demonstrated roll damping alleviation with the free wingtips by achieving 40% and 60% higher roll rates relative to the fixed configuration for short and long wingtips, respectively. It also demonstrated that the wingtips do not touch the ground on landing, as the folding angle decreases below zero only when the dynamic pressure decreases as the aircraft decelerates to a stop.

Further numerical and wind tunnel studies have identified various nonlinear responses of flared folding wingtips. A numerical study accounting for large folding angles of the wingtips identified the dependence of aerodynamic stiffness on the folding angle, indicating that the flutter speed changes with altitude [82]. Another study showed that large positive sideslip angles lead to flutter on the starboard wing, while large negative sideslip angles lead to flutter on the port wing [83]. The flutter boundary for a given sideslip angle further depends on the aircraft's angle of attack. Hence, a combination of the sideslip angle and angle of attack restricts the flight envelope for a given flare angle and flight speed to avoid flutter. Further studies on the aeroelastic stability of the wing identified stable limit cycle oscillations beyond the flutter boundary, which depend on the wingtip's flare angle [84]. It also indicates that a trailing edge tab on the wingtip can significantly change the stability boundary of the system. A study incorporating a fuel tank on the wingtip showed that changing the tank's location and filling levels enables the optimal wingtip folding angle across various angles of attack of the aircraft [85]. It further showed that favourable mass distribution along the wingtip enables dynamic load alleviation similar to that of a wingtip without a fuel tank, and the liquid sloshing in the tank reduces the incremental loads during turbulence by up to 10%. Moreover, recent studies have derived flight dynamic equations incorporating a flared folding wingtip [86] and the aeroelastic scaling factors to match the aeroelastic behaviour of small prototype aircraft to that of full-scale aircraft with flared wingtips [87].

Research on the aeroelastic behaviour of flared folding wingtips has advanced significantly in the last decade. The existing research demonstrates the benefits of free flared wingtip response in alleviating gust and manoeuvre loads and improving the roll rate by reducing the aerodynamic roll damping and the benefits of non-planar wingtip angles in avoiding tip stall at high angles of attack (i.e., landing conditions). Hence, it is evident that an aircraft with folding wingtips will spend a non-negligible portion of the flight time with its wingtips in a non-planar configuration, with most of this time in a free response state. Therefore, unlike the Boeing 777X aircraft that only folds its wings on the ground, an aircraft with the SAH wingtip requires a fairing around the wingtip joint to avoid a potential drag penalty due to the exposed hinge. The drag penalty from the exposed hinge will likely be worsened by the misalignment of the hinge axis with the aircraft's longitudinal axis. Moreover, an exposed hinge is further prone to degradation from debris and water, leading to increased inspection and maintenance requirements. Hence, a fairing around the SAH wingtip joint is essential for the real-world application of the concept in commercial aircraft.

1.3.2. Types of Folding Wing Fairing Structures

Various folding wing concepts designed for in-flight deployment have been studied in the literature over the last two decades. Some concepts use rigid fairings with sliding parts, while others use deformable structures as primary or secondary load-carrying components. This section explores the approaches that have been taken to date.

1.3.2.1. Rigid Fairing Structures

The folding wing concepts from the literature that use an inextensible fairing around the folding joint are shown in Figure 9.

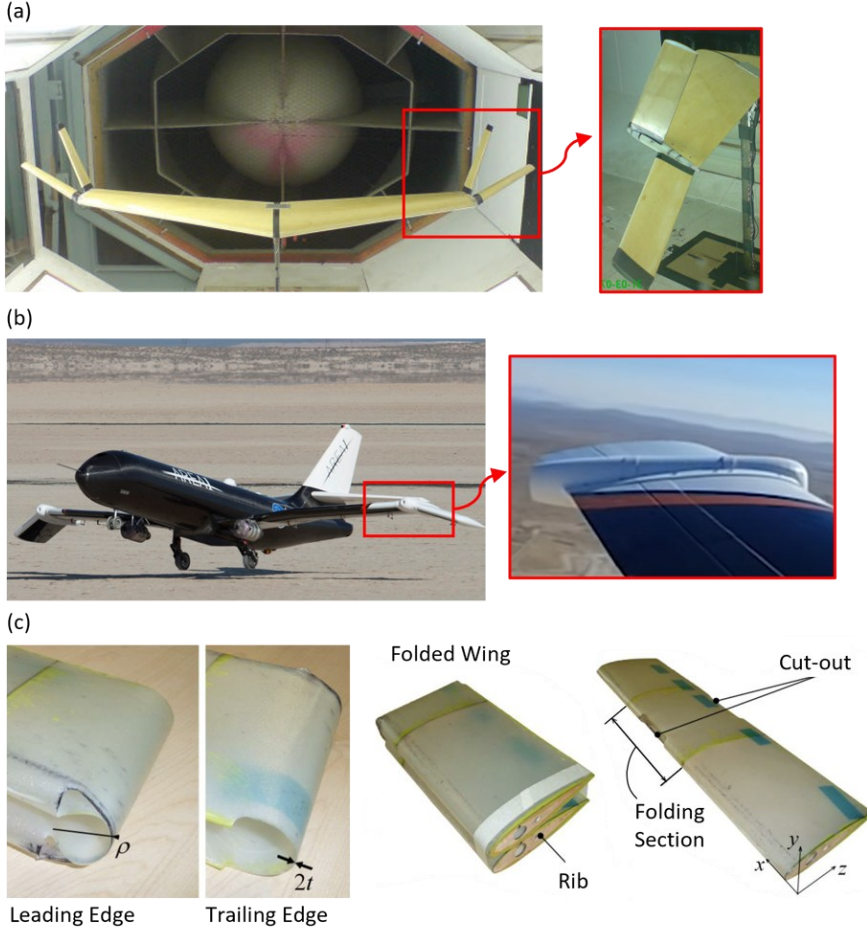


Figure 9. Folding wingtip concepts with rigid fairings. (a) shows the split wingtip concept (Adapted from [88]), (b) shows the Spanwise Adaptive Wing (SAW) concept (Adapted from [89]), and (c) shows the folding wing concept using the Brazier effect (Adapted from [90]).

Figure 9a shows a folding wing concept studied at the University of Bristol, designed to achieve flight control by using either a single or two split wingtips on each wing [91]. The numerical and wind tunnel studies showed that adequate pitching and rolling moments can be generated effectively using independently controlled single wingtips. However, this configuration achieved a stable banked flight turn only for specific bank angles. Hence, another control effector, either a pair of elevators or an extra pair of winglets (i.e., split winglets on each wing), was required to achieve a continuous range of bank angles. Numerical and wind tunnel studies on split winglets on each wing showed that this configuration provides effective control in all 3 rotational axes of the aircraft, particularly at moderate to high lift coefficients (e.g., low speed or high altitude flight) [88, 92]. The split winglets provide redundant control authority (i.e., the same control moments can be achieved by different combinations of the winglets deflections); hence, there would be scope for the winglets deflections to be further optimised to achieve a secondary function, such as reducing drag.

Figure 9b shows the Spanwise Adaptive Wing (SAW) concept studied by NASA on the Prototype-Technology Evaluation and Research Aircraft (PTERA) to provide yaw control, improve directional stability, and reduce wingspan on the ground [93]. The rigid bullet-shaped wingtip joint houses a torque-tube actuator with a nickel-titanium shape memory alloy (SMA) to fold the wingtip using a

temperature change stimulus [94]. The actuation system is driven by electrically induced temperature change, which makes the system lightweight, compact, and quiet [95]. The flight test of a subscale aircraft showed the -70 to +70 degree range of wingtip folding angle with a significant increase in yawing moment due to sideslip at high folding angles [96]. The flight test indicated an increase in directional stability with downward deflection of the wingtip. Furthermore, NASA and Boeing carried out full-scale mechanical testing on a F/A-18 wing retrofitted with a 565 newton-metre (5,000 pound-inch) SMA torque-tube actuator, demonstrating -90 to +90 degree folding of the 136-kilogram (300-pound) wingtip on the ground [93, 94].

Another interesting concept for folding wingtips took advantage of the fact that thin-walled cylindrical shapes undergo buckling above a threshold bending moment, where ovalisation of the cross-section shape due to bending loads leads to collapse of the top and bottom surfaces onto each other, thereby reducing the bending stiffness. This phenomenon is known as the Brazier effect, and the threshold moment at which the top and bottom surface collapses is the Brazier moment. A glass fibre wing with cutouts at leading and trailing edges, as shown in Figure 9c, using the Brazier effect to fold the wing, was studied at the University of Bristol [90]. The application of the Brazier effect to fold composite wind turbine blades for transport was further studied at the University of Limerick [97, 98]. This study indicated that similar to a cylinder with a circular cross-section, the Brazier moment of a wing with an aerofoil cross-section is proportional to the square root of the product of axial extensional and circumferential bending stiffness of the composite (i.e., $\sqrt{A_{11}D_{22}}$ where 1-axis is in longitudinal direction, and 2-axis is in circumferential direction). Hence, the layup of the composite material can be optimised locally to minimise the Brazier moment required to fold the wingtip [99].

1.3.2.2. Primary Load-Carrying Deformable Structures

The folding wing concepts that use a deformable joint section to carry the primary loads, such as bending and shear load from the wingtip to the inboard wing, are shown in Figure 10.

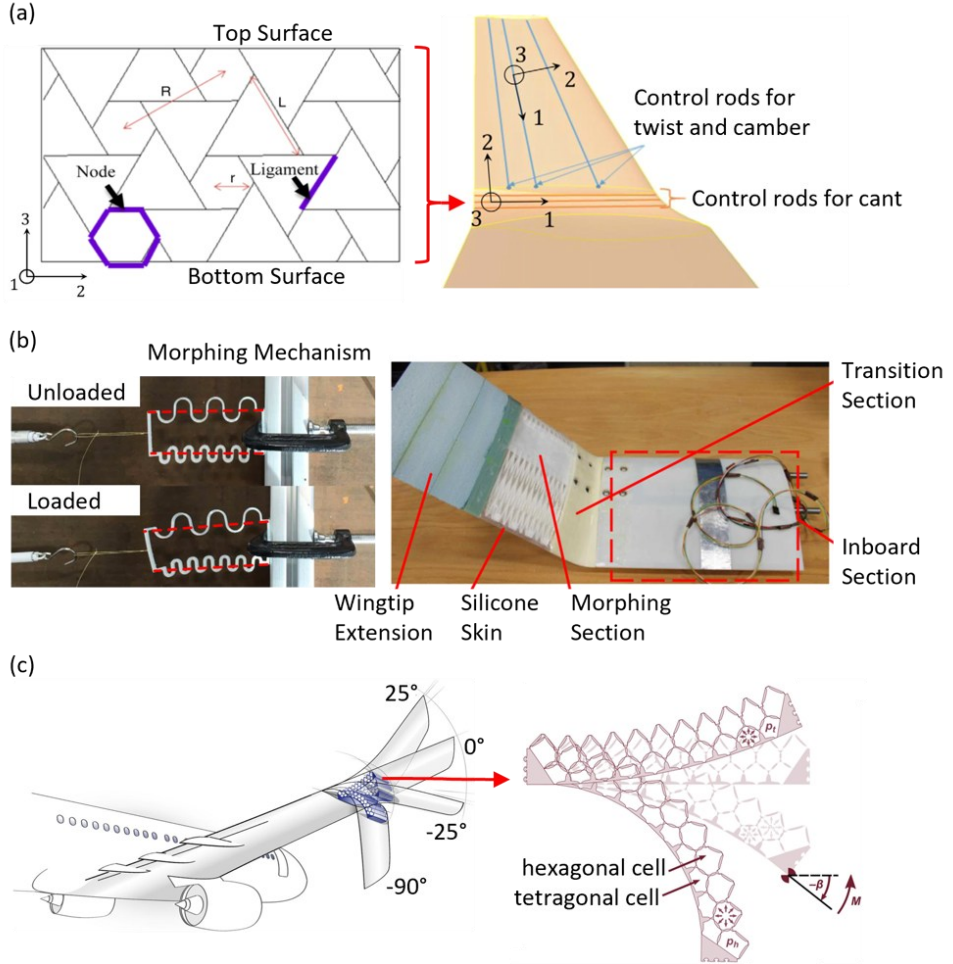


Figure 10. Folding wingtip concepts with primary load-carrying adaptive structures. (a) shows a chiral structure joint with actuation rods (Adapted from [100]), (b) shows the asymmetric stiffness twin corrugated panel joint (Adapted from [101, 102]), and (c) shows a pressure-actuated cellular structure (PACS) joint (Adapted from [103]).

Figure 10a shows a variable folding angle wingtip with a chiral cellular structure connecting the wingtip to the inboard wing [100]. The chiral structure is deformed compliantly either by twisting a node or changing the length of a ligament. The control rods along the chord change the folding angle by twisting three nodes in the joint section. The wingtip uses a different orientation of the same chiral structure with rods to change its twist and camber. The numerical study on this concept used an aluminium alloy for the chiral structure, with a softer aluminium alloy used for the outer surfaces. However, previous experimental studies on a camber morphing chiral structure indicated that a flexible material is required on the outer surface for the chiral structure to deform compliantly [104]. The numerical studies on this concept showed a 2% fuel saving in a typical flight mission by varying the wingtip's cant, twist and camber [105]. Moreover, it indicated at least a 5% reduction in the wing root bending moment by having the flexural axis of the wingtip forward of its aerodynamic centre in such a way that upward vertical gusts lead to a washout (i.e., nose-down) twist of the wingtip [100].

Figure 10b shows the folding winglet concept that uses a spar with two corrugated panels with asymmetric stiffness at the top and bottom sides [101, 102]. The wing spar bends when a linear

displacement is applied along the span, enabling the use of a linear actuator to fold the wingtip. The flexible honeycomb section provides the aerofoil shape at the leading and the trailing edge, while the silicone skin provides the outer surface. The mechanical tests on the prototype showed the ability to create as much as 45 degrees of rotation of the morphing section [102]. Wind tunnel tests demonstrated that the winglet deflection significantly changes the wing's lift and pitching moment coefficients. Further analytical studies considered the coupling between the axial and bending deformation for both trapezoidal and round corrugated panels [106], followed by optimisation of the morphing section geometry for regional jet aircraft, which reduced actuation forces and weight of the retrofitted winglet [107].

Folding wingtip designs that combine an auxetic honeycomb structure with internal inflatable tubes for actuation and flexible skin for the outer surface have been studied in the literature [108]. The auxetic core contracts in the transverse direction when it is compressed, thereby reducing the bump on the top surface as the wingtip folds. The pressure in the inflatable tube is reduced to release the wingtip and increased to return the wingtip to the locking position. Later adaptation proposed the use of shape memory polymer composite skin that is compliant when heated and stiff to resist aerodynamic load when cooled [109]. The wingtip is released by heating the skin, and it is returned to the horizontal position by increasing the pressure in the tubes.

Figure 10c shows another pressure-actuated cellular structure (PACS) that connects the wingtip with the inboard wing [103]. The cellular structure comprises rows of polygonal cells with rigid edges and flexible vertices. The pressure difference across rows of cells changes the wingtip's folding angle, while the overall pressure changes the stiffness of the morphing section [110]. This design approach enables wingtip actuation for flight control and wingtip release to respond freely to gusts by reducing stiffness. The walls of the cellular structure were fabricated using glass fibre-reinforced plastic to achieve the high load-bearing capacity required for the folding wingtip application [111]. Double layers of plain-woven fabric were used to make the walls of the cellular core to reduce the pressure leakage due to porosity. The numerical aeroelastic study of a Cessna Citation X aircraft with PACS joint designed to keep the wingtips straight during cruise showed a 4.2% reduction in wing root bending moment during a 2.5 g manoeuvre load case [103]. This reduction in wing root bending moment was increased to 7.8% by actively de-pressuring the cellular structure to reduce stiffness based on the manoeuvre load factor experienced by the aircraft. However, the de-pressurisation rate of the cellular core remains a challenge in achieving gust load alleviation using the PACS joints for the wingtip.

1.3.2.3. Secondary Load-Carrying Deformable Structures

The folding wing concepts that use deformable structures to carry only the secondary loads, such as aerodynamic pressure loads, while conventional mechanisms are used to carry the primary loads, are shown in Figure 11.

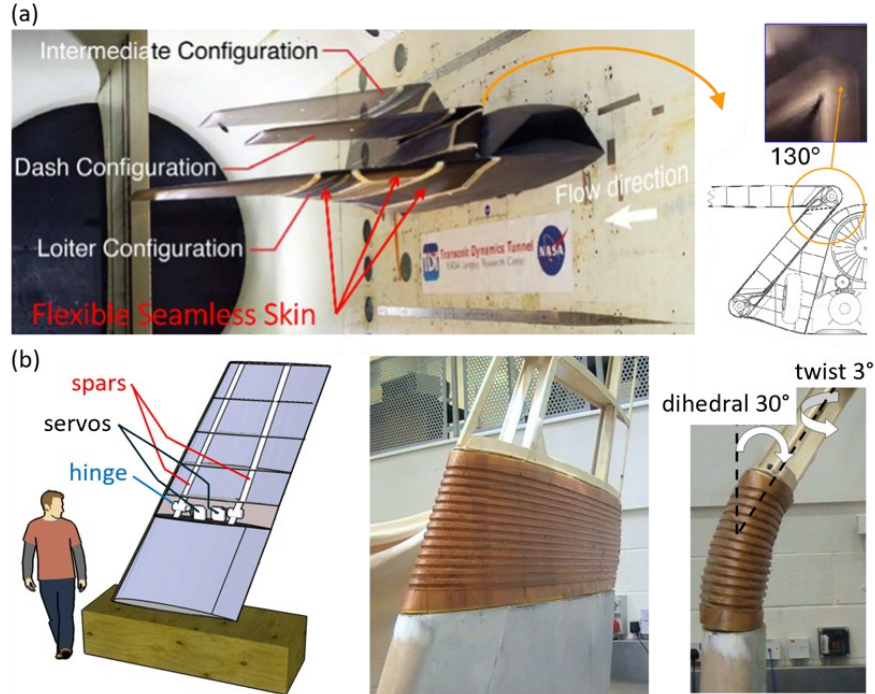


Figure 11. Folding wingtip concepts with secondary load-carrying adaptive structures. (a) shows the “Z-wing” concept studied by Lockheed Martin (Adapted from [112, 113]), and (b) shows the corrugated panel wingtip fairing studied in the MORPHLET project (Adapted from [114]).

Figure 11a shows the “Z-wing” concept developed by Lockheed Martin for the Morphing Aircraft Structures (MAS) program led by the Defense Advanced Research Projects Agency (DARPA) [113]. It shows a wing with two joints, one near the root and the other mid-span, which fold in a coordinated manner by roughly 130 degrees to shorten the wingspan by bringing the inboard wing flush with the fuselage [112]. The wing is designed to increase the loiter time using the long wingspan configuration and increase dash speed using the short wingspan configuration. A shape memory polymer with thermal activation was initially proposed for the outer skin around the joints to use its low stiffness (heated) state during wing folding and high stiffness (cooled) state in the rest of the flight to carry the aerodynamic pressure loads. While the shape memory polymer performed adequately in cyclic testing, the wires that heat the material degraded over time, leading to inadequate reliability in the system. Hence, the wing joints were instead covered by a flexible silicone-based elastomer skin with embedded fabric reinforcements to improve damage tolerance. The flexible skin is stretched on the outside of the fold while it is conformed to the cavity inside the fold [115]. The internal structure is a bullet-shaped casing around the hinge with inboard and outboard parts forming an interlocking interface with comb-like parts (referred to as fingers). The skin was held against the internal structure using a vacuum system to provide the out-of-plane stiffness to carry aerodynamic pressure loads [113]. Wind tunnel studies at transonic speeds showed that in the absence of an adequate vacuum to hold the skin against the underlying structure, the skin flapped about in travelling waves. Hence, the required vacuum pressure for each wing configuration was also determined. The vacuum-held flexible skin showed high stiction to the underlying joint structure, leading to large hysteresis as the skin deformation differs depending on the direction of motion.

Figure 11b shows the corrugated Kevlar panel fairing for folding wingtip joints studied in the morphing winglet (MORPHLET) project at the University of Bristol [114]. The wingtip was designed for narrow-body aircraft (e.g., Airbus A320 and Boeing 737) and was envisioned to reduce wingspan on the ground for airport gate compatibility [116]. The wing joint has two hinges which rotate at the same angle to fold the wingtip and at different angles to twist the wingtip. The corrugated panel was flexible in the in-plane direction along the corrugation (i.e., spanwise) but stiff in the in-plane and out-of-plane across the corrugation (i.e., chordwise). Finite element studies on the concept showed that the corrugated skin buckles on the compressive side as the wingtip folded. However, this buckling was mitigated by adding chordwise reinforcement to support the cross-section shape [117]. This design was fabricated with the Kevlar panel for the demonstrator. Further numerical optimisation studies have shown that retrofitting this folding wingtip system in narrow-body aircraft can provide a 4-5% improvement in the specific air range performance relative to fixed wingtips through all flight phases [118].

1.4. Morphing Skins

Morphing skins have been extensively studied for aircraft, automobile and wind turbine applications. Morphing skins undergo large deformations to enable large changes in the surface area and the shape of the structure. A comprehensive review of general morphing skin concepts studied in the literature is presented by Thill et al. [119], while a focused review on variable stiffness skin concepts is presented by Kuder et al. [120].

To focus the discussion in this section on morphing concepts relevant to folding wing applications, the features of a morphing skin essential for one-directional morphing are identified from a related study presented for camber morphing aerofoils by Gandhi et al. [121]. The study identified that a one-directional morphing skin is required to be highly anisotropic with low in-plane stiffness in the morphing direction and high out-of-plane stiffness in all directions. The low in-plane stiffness reduces the actuation energy required to deform the skin, while the high out-of-plane stiffness reduces the deformation of the skin under aerodynamic pressure loads and prevents the buckling of the skin under compressive load. The stiff and flexible direction for span, chord and camber morphing wings are shown in Figure 12.

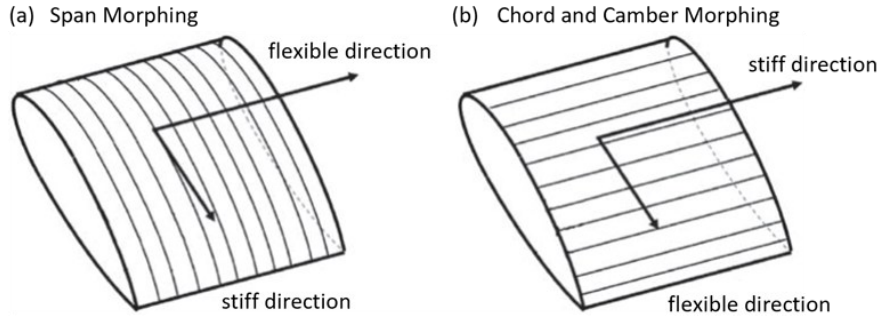


Figure 12. Stiff and flexible direction for (a) span morphing, (b) chord and camber morphing wing (Adapted from [122]).

Further studies have identified the desire to have skins with zero or near zero Poisson's ratio in order to avoid undesirable shrinking in the non-morphing direction and/or the increase in actuation energy required to constrain this Poisson's contraction [123]. Moreover, the studies on the SAH wingtip concept have indicated that the gust load alleviation of a flared hinge wingtip is improved by low wingtip mass and low torsional stiffness of the joint [67], making it essential for the fairing to be light and flexible in the direction across the hinge. Hence, the discussion of morphing skins presented in this section will focus on the morphing skin concepts that comprise these key features beneficial for folding wingtip fairing.

1.4.1. Elastomers

Elastomers are polymers capable of undergoing large elastic deformations due to low-density cross-links between the polymer chains [124]. They exhibit viscoelastic properties and have a low tensile modulus (i.e., 0.5 to 50 MPa) varying with strain, strain rate and temperature [119]. Elastomers are brittle below their glass transition temperatures (T_g), which tend to be low, and highly flexible above it enabling large elongation before breaking (i.e., up to 1,000%). While the flexibility of elastomers makes them suitable for large deformations in a specific morphing direction, it also limits their ability to carry aerodynamic pressure loads without excessive deformations. Moreover, elastomers have a high Poisson's ratio (e.g., 0.48 for thermoplastic polyurethanes [125]), exacerbating the necking effect of the Poisson's contraction in the non-morphing direction as the material is stretched in the morphing direction. Various remedies have been proposed to simultaneously increase load-carrying capability and reduce the Poisson's ratio of elastomer skins, including embedding fibre reinforcements in an elastomer matrix [122, 126], as shown in Figure 13 and using the elastomer as a facesheet of a sandwich panel by bonding the elastomer facesheet onto a zero Poisson's ratio core [127, 128]. Other studies have achieved negative Poisson's ratio in elastomeric matrix composites using unbalanced symmetric laminates with the layup orientation in the form of $[\alpha/\beta]_s$ where α and β have the same sign [129, 130].

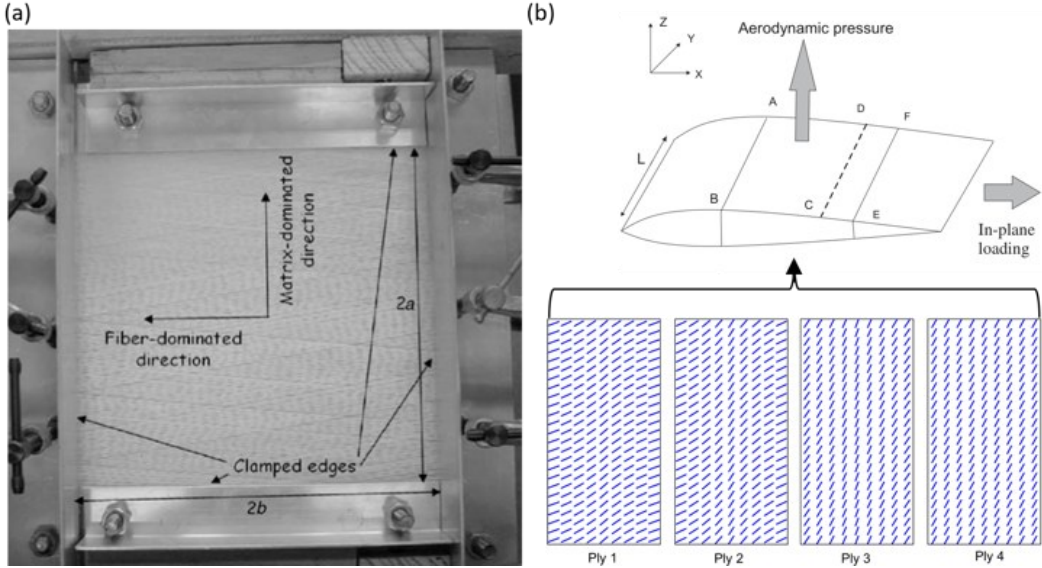


Figure 13. Fibre-reinforced elastomer skins. (a) shows straight fibre-reinforced elastomer skin (Reproduced from [122]), and (b) shows curvilinear fibre-reinforced elastomer skin (Adapted from [126]).

The properties of fibre-reinforced elastomer-matrix morphing skins were studied for one-directional morphing applications such as span morphing and chord morphing wings [122]. Straight fibres, as shown in Figure 13a, were oriented perpendicular to the morphing direction, enabling large skin deformation with low actuation force due to the flexibility of the elastomer matrix. The fibre reinforcement stiffened the non-morphing direction, enabling the application of pre-tension in this direction without skin rupture to increase the out-of-plane stiffness of the skin. High out-of-plane stiffness was essential to maintain the cross-section shape under aerodynamic pressure loading. The elastic properties of fibres and matrix, fibre volume fraction, and fibre layup can be used to obtain the desired stiffness properties of the fibre-reinforced elastomer skin. Further studies have considered using curvilinear fibres, as shown in Figure 13b, to increase the out-of-plane stiffness of the fibre-reinforced elastomer while keeping the in-plane stiffness in the morphing direction low [126]. The numerical optimisation study found that the aspect ratio of the plate, the in-plane loading direction, and the stacking sequence strongly influence the optimised fibre path.

1.4.2. Cellular Cores

Cellular structures have been used in early morphing applications such as the Active Aeroelastic Wing (AAW) Flight Research Program [32], which developed the X-53 aircraft by modifying the F/A-18 wing. The F/A-18 wing was modified by replacing the aluminium, titanium and composite skin with aluminium and thinner composite skin with a honeycomb substructure. The modifications reduced the wing stiffness by 17% relative to the F/A-18 aircraft wing, enabling it to achieve a favourable wing twist using multiple leading and trailing edge tabs.

The morphing skins developed for span, chord and camber morphing applications require large deformation in the morphing direction, near zero-Poisson's ratio and high out-of-plane stiffness [121, 123]. A topology optimisation study of cellular core geometry identified the core geometries that best

provide these properties [131]. A genetic algorithm optimisation coupled with a local search algorithm was used to optimise cellular core geometry for multiple objectives of minimising density, out-of-plane displacement, morphing actuation energy, and maximum local strain. The geometry of a unit cell was defined in two dimensions using a voxel grid, with each voxel grid cell being either filled with material or empty. Various filtering procedures were used to remove voids, isolated features and hinges from the unit cell. The solutions at the Pareto front, as shown in Figure 14, were categorised into 3 groups: strand-like, honeycomb-like, and homogenous topologies.

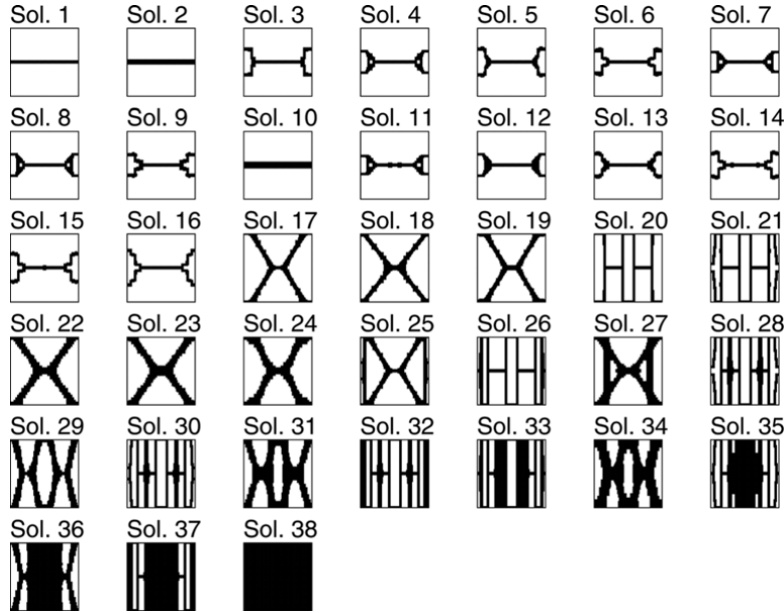


Figure 14. Unit cell shapes generated using topology optimisation for the one-directional morphing application (Reproduced from [131]). The morphing direction is horizontal.

Strand-like topologies in the morphing direction have the lowest density and the largest out-of-plane displacement due to a lack of stiffness in the non-morphing direction. Honeycomb-like topologies increased the stiffness in the non-morphing direction at a cost to density, but it decreased the out-of-plane displacement with little effect on morphing stiffness. Among the honeycomb-like topologies are accordion-type cores with parallel ribs in a non-morphing direction connected by a chevron or strand-like structure between them. These topologies additionally provide near zero-Poisson's ratio due to the continuous ribs in the non-morphing direction.

Cellular cores with a zero-Poisson's ratio have been extensively studied in the literature in the last two decades. Many of the one-dimensional morphing skins based on cellular cores use accordion-type topologies. Some of these concepts are shown in Figure 15.

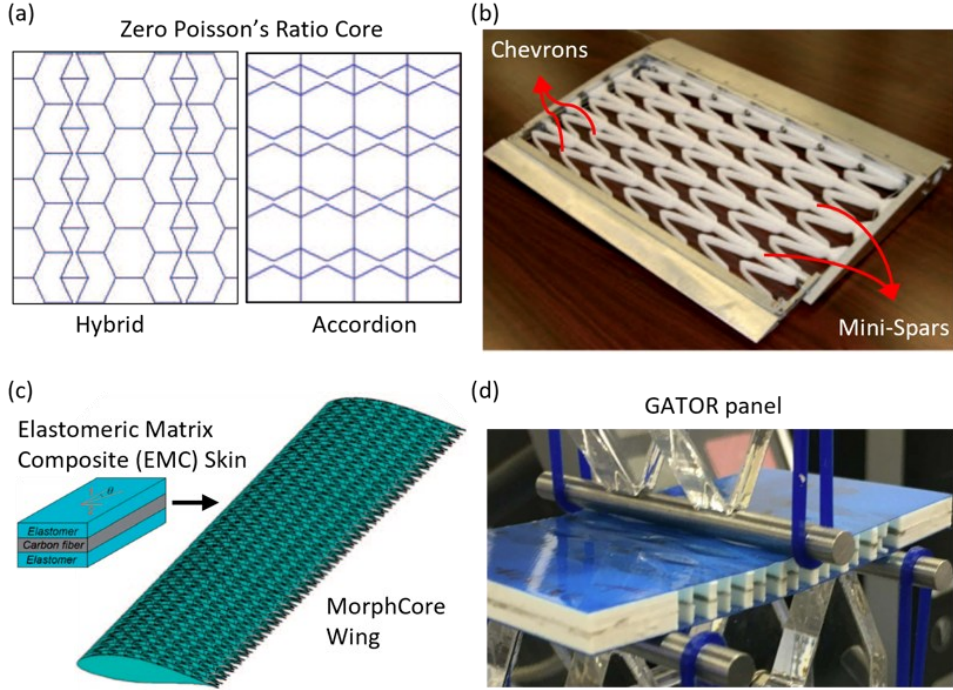


Figure 15. One-directional morphing sandwich panels. (a) shows the zero-Poisson's ratio cores (Adapted from [123]), (b) the accordion core used for chord morphing (Reproduced from [128]), (c) shows the fibre-reinforced elastomer skin with an accordion-type core used for span morphing (Adapted from [127, 132]), and (d) shows the 3D-printed GATOR skin panel (Reproduced from [133]).

Figure 15a shows two different core types proposed for one-directional morphing applications. It shows a hybrid core combining cells of conventional honeycomb cores with positive and negative inclined wall angles and an accordion core (also known as MorphCore [134]) with parallel ribs and chevrons between them. Analytical expressions derived for equivalent elastic properties for the cores enabled the comparison of their efficacy for one-dimensional morphing applications such as variable span, chord or camber devices [123]. It was shown that the restriction of deformation due to Poisson's ratio added significant stiffness in the morphing direction for non-zero Poisson's ratio cores (e.g., conventional honeycomb), whereas this stiffness was significantly lower for zero-Poisson's ratio cores. Additionally, it was shown that the accordion core provided high out-of-plane stiffness through their ribs, thereby making it advantageous for morphing skin applications.

The attachment of elastomer skin to a zero-Poisson's ratio accordion cellular core was studied for a chord morphing application of a helicopter rotor blade, as shown in Figure 15b [128]. The accordion core was made of parallel ribs (also referred to as mini-spars) with chevrons in between them. The core ribs provide high stiffness in the spanwise (non-morphing) direction, while the chevrons provide flexibility in the chordwise (morphing) direction due to their predominant deformation in bending rather than axial stretching. The angle of the chevron walls from the morphing direction determines the relative proportions of bending versus axial deformation in the chevron walls.

Two bonding configurations were studied for the skin where the elastomer sheet was bonded to only the ribs or both the ribs and chevrons [128]. The elastomer sheet was further pre-tensioned, and

flanges were added to the core to reduce the out-of-plane deformation of the elastomer sheet due to pressure load. The numerical study showed that a large pre-strain was required to reduce the local out-of-plane deformation to acceptable limits, and the flanges reduced the required pre-strain by reducing the local unsupported length of the elastomer sheet. The local out-of-plane deformation was reduced to acceptable limits without requiring excessive pre-strain by attaching the elastomer sheet to both ribs and chevrons; however, it increased the required actuation force for chord morphing.

The two approaches to achieving near zero-Poisson's ratio were combined to create a fibre-reinforced elastomer (also known as elastomeric matrix composite (EMC)) skin bonded to an accordion core (also known as MorphCore [134]) for a span morphing wing concept, as shown in Figure 15c [128, 132]. In this study, fibres in the elastomer skin and ribs of the core were oriented in the chordwise direction, keeping the spanwise direction flexible. The fibre-reinforced elastomer skin was attached to the ribs of a pre-compressed core, giving a nominal pre-tension to the EMC skin when the core was released. The pre-tensioned skin reduces the out-of-plane deformation of the outer surface under pressure load [121]. This combination of EMC skin and MorphCore substructure provided a span-morphing wing capable of 100% span extension in wind tunnel testing [132].

The combination of elastomer facesheets and zero-Poisson's ratio cellular core has been extensively studied for the Geometrically Anisotropic Thermoplastic Rubber (GATOR) skins concept shown in Figure 15d [135]. GATOR panels are fabricated using thermoplastic materials of different stiffnesses for a multi-material sandwich panel via 3D printing using the Fused Filament Fabrication (FFF) (also known as Fused Deposition Modelling (FDM)) technique [133]. The panels are 3D printed using NinjaFlex [136] for the facesheets and Armadillo [137] for the core. Both materials are thermoplastic polyurethane (TPU) and have different stiffness properties. NinjaFlex is the more flexible of the two, with a Young's modulus of 12 MPa and capable of 65% strain before yield [136], while Armadillo is stiffer, with a Young's modulus of 396 MPa and is capable of 18% strain before yield [137]. The panels are printed in halves (split in the thickness direction) and bonded afterwards to create the full panel [133, 135]. For each half panel, the facesheet was printed first on a flat plate, followed by the half-thickness of the core on top of it, providing good bond strength between the facesheet and the core due to the chemical similarity of the two materials. The two halves of the panel were finally bonded together using an epoxy-based glue, with the two half panels placed into an assembly jig to provide alignment and clamping force.

The geometry of the GATOR panels was optimised to improve the balance of in-plane flexibility in the morphing direction, in-plane stiffness in the non-morphing direction and out-of-plane stiffness throughout the panel [138]. The experimental tests of GATOR panels showed the panels are capable of up to 60% fully recoverable strain in the morphing direction with linear response for small deformation [133]. The facesheets were shown capable of withstanding some compression before buckling, providing linear panel stiffness up to the point of facesheet buckling, with the option of pre-tensioning the panels if larger compressive strains are to be applied. The panel deformation response did also show a dependency on the load history, leading to hysteresis, as expected for the hyperelastic

materials used [133]. However, a comparison of experimental results with the finite element simulation results showed that modelling the constituent materials of the panel as linear elastic has good agreement with up to panel deformation of 10% strain in the morphing direction [138].

An experimental study of a GATOR panel under transverse pressure loading (simulating aerodynamic pressure) showed only moderate bulging of the unsupported region of the facesheet even under large applied pressures [139]. This bulging was reduced by applying in-plane strain up to 10% in the morphing direction. At larger extensions, the increased distance between the continuous ribs, and the resulting increase in unsupported length for the skin sheet, led to an increase in local (i.e. within a unit cell) out-of-plane deformations, although these were considerably smaller than the global deformations. This indicates that reinforcing the continuous ribs (for example, with carbon fibre-reinforced polymer) could be an effective approach to reducing the global deformations under pressure loads without an excessive increase in actuation energy requirements. Detailed digital image correlation (DIC) measurements of the facesheets under extension and pressure loading showed non-uniform strain distributions due to the interaction between the chevrons and the facesheet. The non-uniform strain distribution due to stretching in the morphing direction is shown in Figure 16.

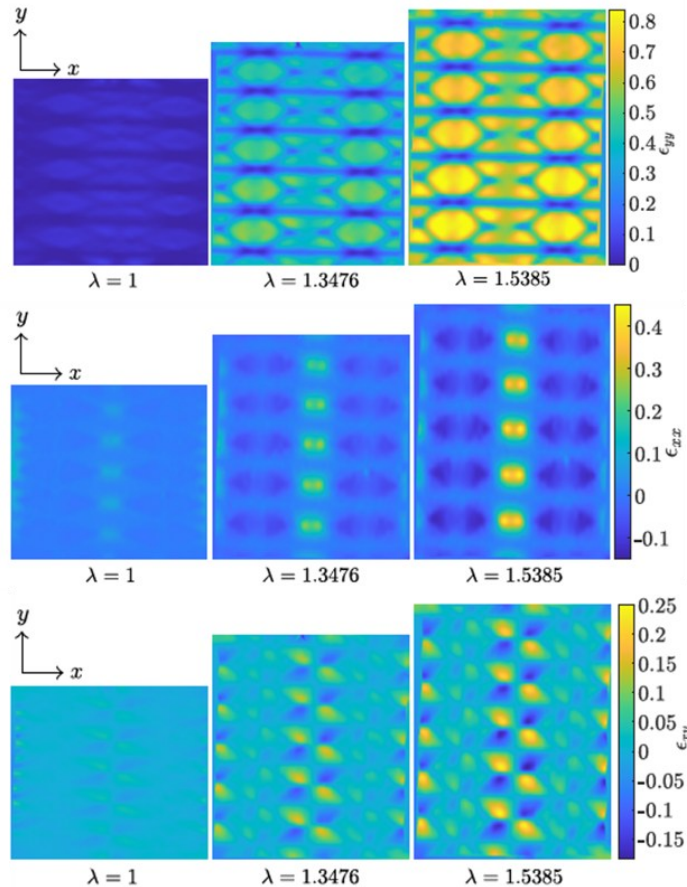


Figure 16. Non-uniform strain distribution on the facesheet of the GATOR panel (Reproduced from [139]). The parameter γ represents the ratio of deformed length to undeformed length of the panel in morphing direction.

For this particular geometry of the core, this interaction resulted in the yield strain of the facesheet material, NinjaFlex, being reached at 35 % strain of the GATOR panel in the morphing direction,

thereby limiting the elastic deformation range of the panel. Alternative core geometries in other studies, particularly ones with curved inclined walls, which eliminate the sharp corners at chevron tips and chevron-rib junctions, are shown to alleviate peak strains on the facesheet [140], along with reductions in peak stress on the interior junctions of the core [141]

1.4.3. Corrugated Panels

Morphing skins based on corrugated structures have also been studied for application to folding wing fairings [114]. A separate study systematically studied four different configurations of corrugated skin panels using tensile and bending experimental tests along the longitudinal and transverse direction of the corrugation [142], as shown in Figure 17.

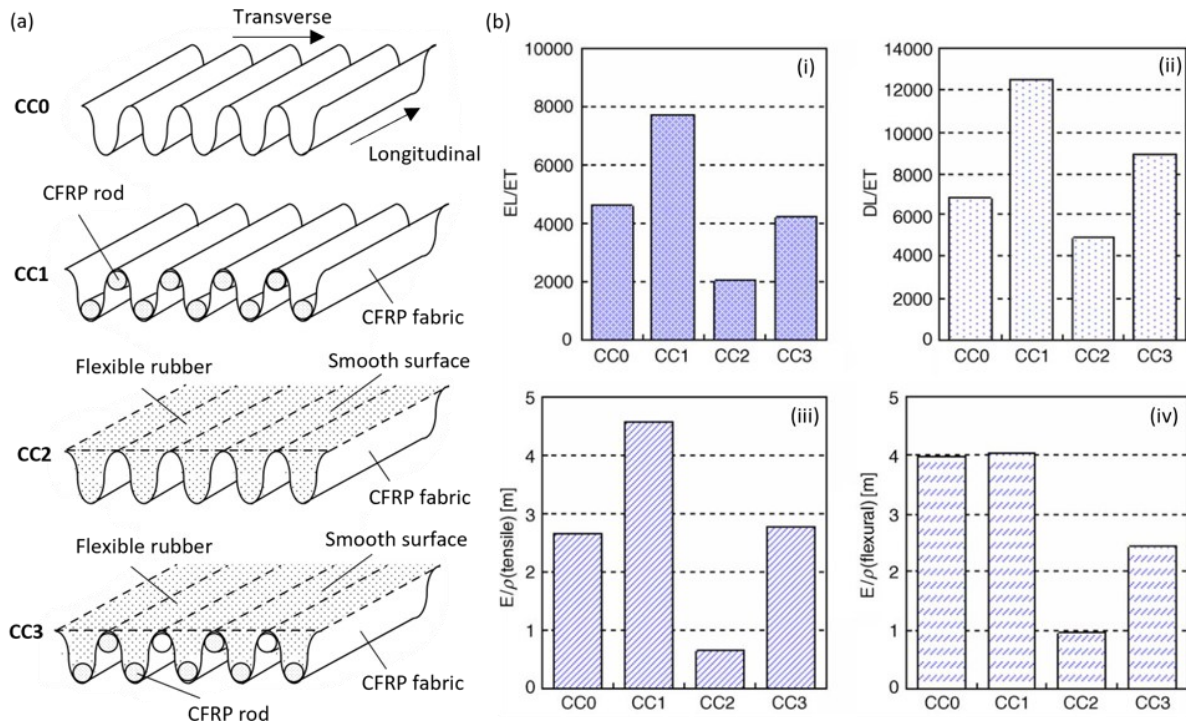


Figure 17. Stiffness properties of various configurations of corrugated panels (Reproduced from [142]). (a) shows the 4 configurations of the corrugated panel skin. (b) shows their stiffness properties where (i) and (ii) show the longitudinal tensile modulus and flexural rigidity as a ratio of transverse tensile modulus, and (iii) and (iv) show the specific tensile and flexural modulus in the longitudinal direction.

Corrugated panels are flexible in the direction transverse to the corrugation and stiff in the longitudinal direction, both in tensile and bending deformations. The stiffness in the longitudinal direction was further increased by adding stiff composite rods to the corrugation channel, as shown in Figure 14a for the CC1 and CC3 configurations. As another design option, the outer surface of the corrugated panel was made smooth by filling the corrugation channel with elastomer, as shown in the CC2 and CC3 configurations. The effects of these modifications on the corrugated stiffness properties are shown in Figure 17b. It shows improvement in anisotropy in b(i) and b(ii) for tensile moduli and flexural rigidity due to the addition of stiff rods to the corrugation channel. Consequently,

it increases the specific stiffness in the longitudinal direction, as shown in b(iii) and b(iv). In contrast, adding elastomer filling to the corrugation channels on its own in the outer surface reduces the anisotropy and specific stiffness. The configuration CC3 shows the best result where a smooth outer surface is achieved with an improved ratio of longitudinal flexural rigidity to transverse tensile modulus. However, it comes at the cost of increased mass and, therefore, reduced specific flexural stiffness. Other studies have considered filling the corrugation channel with shape memory polymer (SMP) materials to enable variable stiffness that responds to a temperature stimulus [143].

Another approach to creating a corrugated panel morphing skin with a smooth outer surface is attaching a separate surface skin layer to the peaks of corrugations. A design which uses segmented skin elements to form the surface has been studied for a combined camber and chord morphing application [144], as shown in Figure 18.

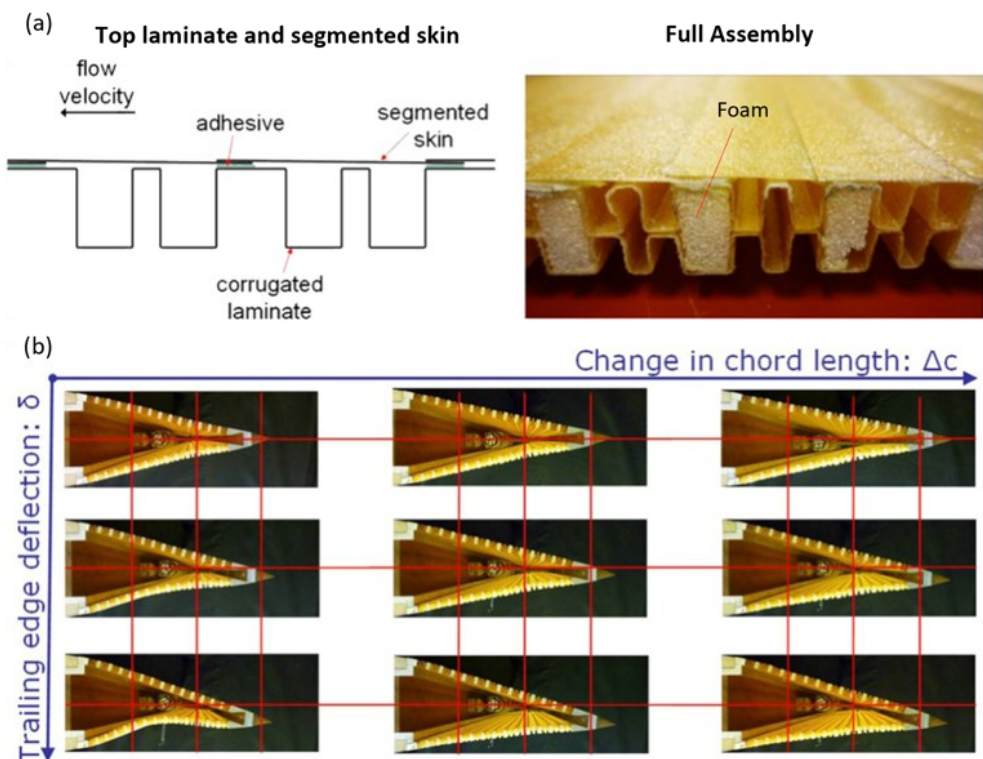


Figure 18. Corrugated panel skin for camber and chord morphing application (Reproduced from [144]). (a) shows the design of the morphing skin panel, and (b) shows the panel deformation due to camber and chord change.

Figure 18a shows two corrugated panels of glass fibre laminates bonded to foam rods. One side of each segmented skin strip is glued to the top laminate with a small overlap with the adjacent strip. The trailing edge section in Figure 18b demonstrated a 4% increase in chord and 12-degree deflection while maintaining a gapless outer surface in the wind tunnel tests. Stiff segmented skins help to keep the actuation force low while keeping the local out-of-plane deformation low due to pressure load. However, as segmented skins are not continuous, they do not seal the interior of the wing from the ingress of water and debris.

1.5. Proposed Folding Wingtip Fairing Concept

The research presented in this thesis focuses on the numerical analysis of a morphing fairing design for the folding wingtip joints – particularly relevant to the Semi-Aeroelastic Hinge (SAH) concept. To this end, this section discusses the requirements of the fairing for the SAH concept, the support structure proposed for study in this dissertation and the skin concept proposed for the fairing.

1.5.1. Fairing Requirements

The SAH concept has two distinct features that affect the design of the fairing, namely, the presence of a flare angle in the hinge and the requirement for low torsional stiffness of the joint [67]. The flare angle (Λ) creates a misalignment of the hinge axis and the aircraft's longitudinal axis (i.e., airflow direction), as shown in Figure 19.

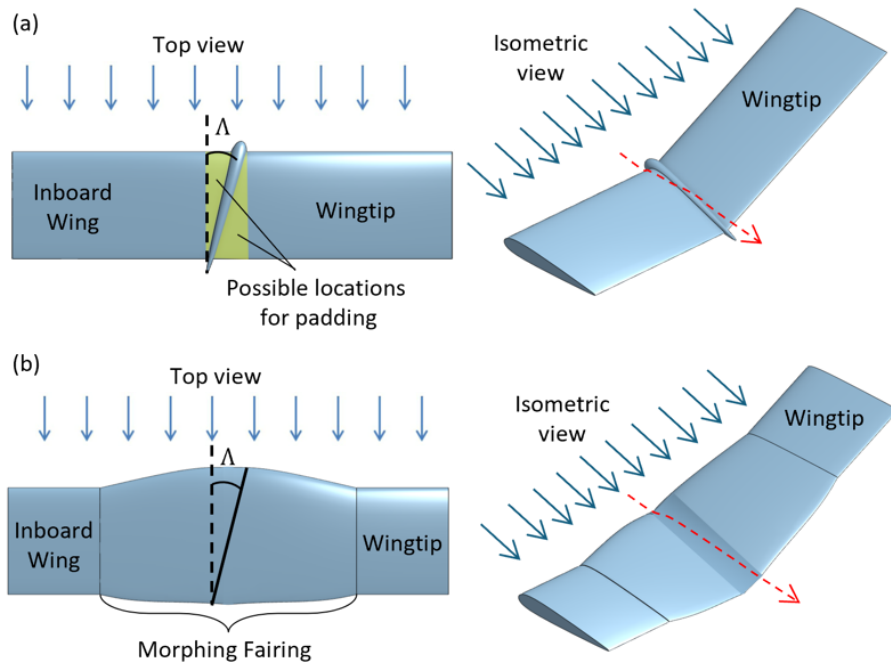


Figure 19. Types of fairings for Semi-Aeroelastic Hinge (SAH) wingtip concept. (a) shows a bullet-shaped rigid casing around the joint, and (b) shows a morphing fairing that encloses the joint section.

As a result, the oncoming airflow will reach the joint section of the wing at an angle to the hinge line. The joint will house internal components, such as the hinge, clutch and actuators [80], likely making the joint's diameter greater than the wing's thickness, similar to the XB-70 wingtip joint shown in Figure 7a and NASA's Spanwise Adaptive Wing (SAW) joint shown in Figure 9b. However, the XB-70 aircraft and SAW wing concept have their wingtip aligned with the direction of travel, making the bullet-shaped cylindrical casing around the hinge feasible for their design.

In the case of the SAH concept, a rigid bullet-shaped fairing will have the oncoming flow reach the fairing at an angle and change direction sharply around the fairing to traverse the surface curvature, as shown in Figure 19a. Sharp changes in flow direction will likely lead to flow separation, which will

incur a drag penalty at both the planar and rotated states of the wingtip. It is possible to minimise the magnitude of surface curvature around the joint by adding padding to the wing before and after the bullet-shaped casing, as shown in Figure 19a. While this approach would smoothen the surface curvature for the planar wing configuration, as the casing is not adaptive, it will still form sharp discontinuities in the surface when the wingtip is rotated upwards.

An alternative approach is shown in Figure 19b, where the entire joint region is covered by a compliant morphing fairing with a larger cross-section chord and thickness to enclose the joint within the aerofoil shape. This approach will likely provide a smooth, continuous surface around the joint, leading to lower drag in the planar and released configuration of the wingtip. Moreover, unlike the bullet-shaped casing, the morphing fairing would not have sliding surfaces, making it easier to seal internal components from water and debris ingress.

In addition to accommodating the flare angle, the fairing is required to minimise the added torsional stiffness, damping, and mass to the joint to improve the gust load alleviation of the wingtip [67]. The bullet-shaped fairing is likely to have a smaller added torsional stiffness since it does not have components that are being deformed as the wingtip fold. Instead, the bullet-shaped casing relies on the surfaces sliding across each other; hence, the only added stiffness will come from the friction within/between the components. In contrast, the morphing fairing will have skin that undergoes elastic deformation as the wingtip folds. Hence, this study aims to identify the skin configurations that minimise the amount of torsional stiffness added to the joint.

1.5.2. Support Structure

A morphing fairing requires a support structure underneath the fairing, and its configuration influences the stiffness and the deformed shape of the fairing. Hence, compliant support structures were used in various morphing applications to guide the deformation of the fairing, such as in the FlexSys leading and trailing edge devices [31, 44]. The SAH concept requires a hinged connection of the inboard wing and the wingtip to transfer the shear load while minimising the transfer of bending moment. Hence, to reduce the added torsional stiffness from the fairing components, it is desired that the support structure does not transfer bending moments across the joint. Additionally, the support structure should minimise the cross-section distortion and avoid the contact of the fairing with the joint as the wingtip folds.

The author proposed ribs pivoted to the wing spar in earlier research [145] to support the flexible fairing of a folding wing, as shown in Figure 20.

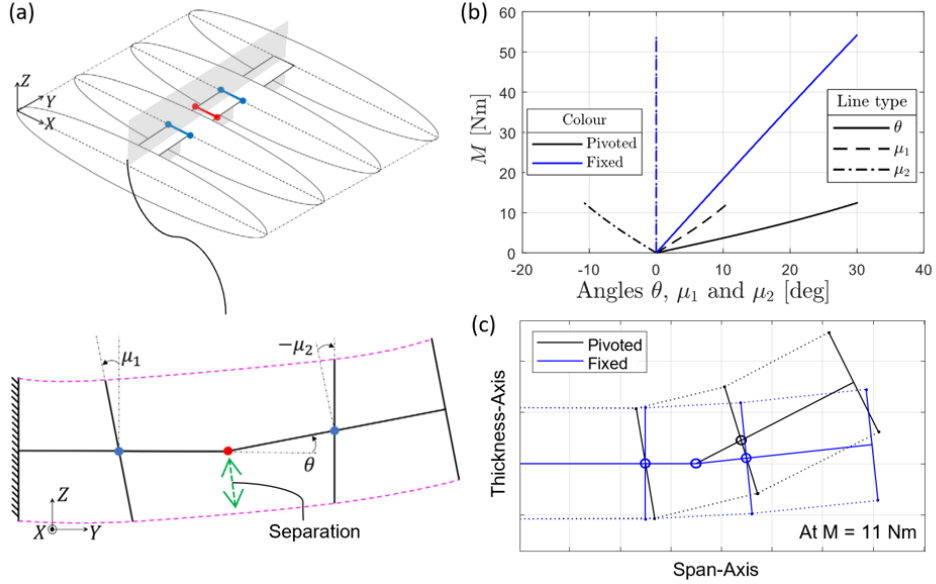


Figure 20. The morphing section has ribs that are free to pivot at their attachment to the spar, supporting flexible fairing (Adapted from [145]). (a) shows the morphing section geometry with the SAH hinge, which is shown in red, and pivoted rib hinges in blue. (b) shows the folding angle (θ) and rib pivoting angles (μ_1 and μ_2) for varying amounts of moment applied to the wingtip. (c) shows the deformed shape of the fairing with pivoted and fixed rib support structures.

Figure 20a shows the morphing fairing section with wingtip folding hinges in red and rib-pivoting hinges in blue. It also shows the wingtip folding angle (θ) and rib pivoting angles (μ_1 and μ_2) which changes independently with the moment applied to the wingtip. The flexible fairing connects the pivoted ribs; hence, the ribs pivot to balance the moment about their hinges, thereby spreading the fairing deformation between the bays. This process reduces the overall strain on the fairing and, therefore, the torsional stiffness of the joint, as indicated by the significantly lower moment values at a given value of θ in Figure 20b. The deformed shapes of both configurations for the same applied moment are shown in Figure 20c.

Figure 20c shows that the separation between the joint and the fairing decreases as the wingtip folds, making it likely that the fairing contacts the joint components at high folding angles for some support structure configurations. To avoid the fairing contacting the joint at large folding angles, the height of the ribs (i.e., half of the cross-section thickness) must be greater than the length between the wingtip folding hinge and rib pivoting hinge [145]. This requires the pivoting ribs to be close to the wingtip folding hinge, thereby adding support not based on the out-of-plane displacement of the fairing but rather on avoiding the fairing contacting the joint components. Hence, it is proposed that a single pivoting rib co-located with the wingtip folding hinge is used with freedom for the rib to pivot independently of the wingtip folding angle. This configuration is schematically shown in Figure 21.

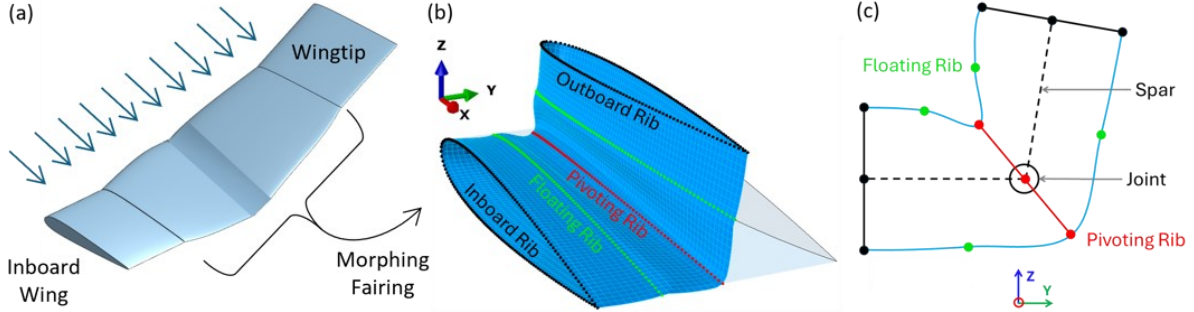


Figure 21. Proposed support structure for the fairing. (a) shows the location of the morphing fairing section, (b) shows the pivoting and floating ribs used to support the fairing, and (c) shows the cross-section view of these ribs from the rear.

A central pivoting rib ensures that the separation between the fairing and the joint is always maintained regardless of the folding angle. The independence of the rib pivoting angle (μ) and wingtip folding angle (θ) ensures that the deformation of the fairing is distributed across the rib bays by pivoting the rib to reduce the overall torsional stiffness for any folding angle. This present research further introduces floating ribs to support the skin, as shown in Figure 21b. Floating ribs are stiff structures that are only attached to the fairing that enforce the cross-section shape at their respective locations. They also reduce the unsupported length of the fairing panels in the span direction, which should reduce out-of-plane deformations caused by aerodynamic pressure. Hence, the number of floating ribs can be varied to improve the deformed shapes achieved under load, as will be explored in the chapters to come.

1.5.3. Skin Structure

The previously introduced Geometrically Anisotropic Thermoplastic Rubber (GATOR) skin is proposed for the fairing of folding wingtip joints, as it offers in-plane flexibility, near zero Poisson's ratio, and high out-of-plane stiffness. It also offers versatile design freedom to tailor its stiffness properties through manipulation of its geometry, fabrication using multiple materials, and spatial variation of its topology. The geometry for the GATOR panel and its default orientation on the wing section is shown in Figure 22.

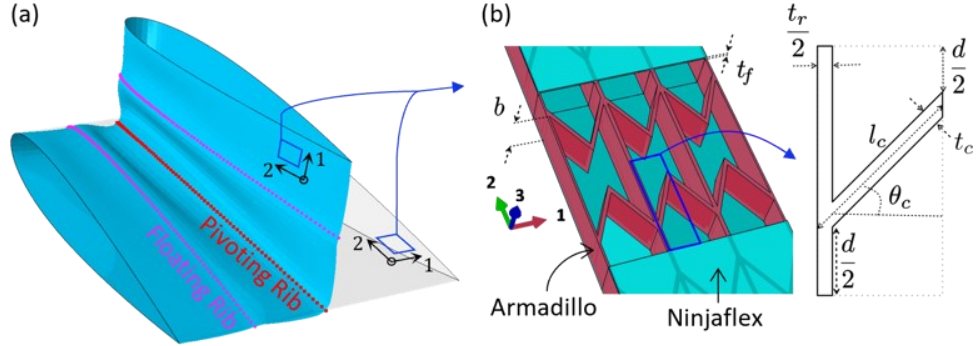


Figure 22. Geometry and orientation of the proposed GATOR fairing for folding wingtip joints.

In the GATOR panels, the facesheets are bonded to the chevrons and the ribs of the core, thereby reducing local out-of-plane deformation of the facesheet due to the pressure load. Figure 22b shows the geometric dimensions of the GATOR panel that can be varied to affect its stiffness properties. They are core thickness (b), facesheet thickness (t_f), rib thickness (t_r), chevron thickness (t_c), chevron length (l_c), chevron angle (θ_c), and chevron separation (d). Through the stiffness properties of the GATOR panel, these geometric variables will affect the torsional stiffness of the joint and the cross-section distortion of the fairing. This thesis undertakes a comprehensive study into the impact of these various geometry parameters on the performance of the morphing fairing, specifically with respect to the two primary design objectives of minimising torsional stiffness and distortion of the fairing cross-sections under wingtip rotation.

Further, it is possible for the local orientation of the MorphCore (also known as accordion core) to be spatially varied over the surface of the fairing to allow it to adapt to changes in required performance arising from the three-dimensional nature of this problem due to the aerofoil shape at the cross-section and the likely presence of taper and sweep in the underlying wing sections. This spatial variation of the core orientation will result in a non-uniform geometry of the cells that tessellate together to make up the core. A schematic representation of such fairing is shown in Figure 23.

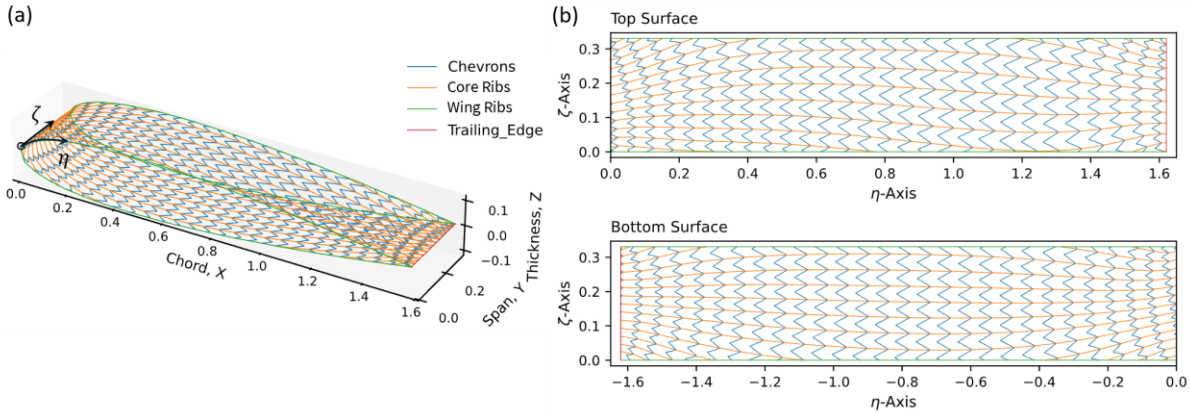


Figure 23. An example of the sort of continuous spatial variation of the local core orientation that is proposed for this fairing concept, as explored in Chapter 4. (a) shows the three-dimensional wing section, and (b) shows a flattened representation of the core within the fairing.

Figure 23a shows a half model of a fairing's core from the inboard rib (on the near side) to the central pivoting rib (on the far side). The fairing shown is without any floating ribs; hence, the fairing is continuous from the inboard rib to the pivoting rib. It is proposed that aligning the flexible direction of the core (i.e., the chevron direction) with the principal strain direction with the greatest deformation will improve the compliance of the fairing. Hence, this present research aims to vary the local orientation of the core to align it with either the principal strain lines, principal stress lines or another field-based variable that would improve the fairing performance. Aligning the local orientation of the core with the orientation of the field-based variable ensures continuity in the orientation and enables an intuitive understanding of the physics affecting the fairing performance.

1.6. Research Gaps

Extensive studies have been carried out on camber morphing and span-extending wings [17], and the knowledge gained from these studies on the behaviour of morphing skins [119] is useful for the study of morphing fairings for folding wings. While numerous studies on folding wings are available in the literature, to the author's knowledge, morphing fairing concepts that apply to hinge-based folding wings are limited. Two notable concepts studied are the elastomer skin held against the internal structure using a vacuum in Lockheed Martin's "Z-wing" project [112, 113, 115] and the corrugated skin with stiffened ribs studied for the MORPHLET project at the University of Bristol [114, 116, 118] described in Section 0. Both concepts were demonstrated with a prototype, and the "Z-wing" concept was tested in the wind tunnel. However, both studies presented limited design space exploration of the fairing. This research will, therefore, consider the gaps in existing knowledge that will be addressed as we explore the viability of the proposed fairing concept.

1.6.1. Stiffness Properties of Flexible Sandwich Panels

The GATOR panels, described in Section 1.4.2, have been studied using equivalent analytical models [135] and finite element models [138], fabricated through Fused Filament Fabrication (FFF) 3D printing [133], and tested in tension and bending [138, 139]. The equivalent elastic moduli of the

accordion core (also known as MorphCore) have been derived using analytical expressions for in-plane [123, 146] and out-of-plane [147] deformations. These analytical approaches model the walls of the cellular core as beams that are deformable in axial, bending, and transverse shear deformations [148]. Hence, the analytical models give accurate results for small deformations of cellular cores with slender walls. As the morphing cores undergo large deformation, the stiffness properties of the core deviate from the linear stiffness predicted by the analytical models [133].

A preliminary estimate for the stiffness properties of the sandwich panel has been found by modelling it as a laminated plate [135, 149]. The classical laminated plate theory (CLPT) requires that the strain distribution is uniform within each layer for any applied deformation. Numerical and experimental studies have shown that the strain distribution on the facesheet of the cellular core sandwich panels is not uniform due to the facesheet-core interaction [139, 150]. The non-uniform strain distribution on the facesheets increases the stiffness of the panel; hence, the analytical models based on the classical laminated plate theory (CLPT) underpredict the stiffness properties of these panels.

Accurately capturing the stiffness properties of the flexible sandwich panel fairing is essential to identify their effects on aircraft performance. Particularly, in the case of folding wingtips using the Semi-Aeroelastic Hinge (SAH) concept, the ability to alleviate gust loads is sensitive to the torsional stiffness of the joint. Hence, to design a fairing around the hinge, it is essential to model the fairing stiffness to minimise the added torsional stiffness to the joint. The finite element method offers an alternative to analytically derived equivalent stiffness properties of the morphing fairings as it can capture the interaction between the facesheet and the core [150] and the geometric nonlinearity in stiffness due to large deformations [149].

Cellular cores with small feature sizes, such as the accordion core, require a fine mesh for the finite element solution to converge to mesh-independent results [146, 147]. Using a fine mesh to model a sandwich panel with a cellular core is computationally feasible for small panels, such as samples for tensile and three-point bending tests, but at a high computation cost [150]. Consider a unit cell of the GATOR panel with approximately $12.5 \times 35.9 \times 12.6$ millimetres in 1, 2, and 3 directions shown in Figure 22b. It will require approximately 64 cells along the span and 90 cells around the circumference in the chordwise direction for a morphing section with a 1.6-metre chord (i.e., tip chord of A320 [151]) and 0.8-metre span. Using an average mesh size of 1 millimetre (assuming a 1-millimetre core wall thickness), each unit cell of the GATOR panel requires approximately 5,408 brick elements. For the assumed morphing wing section with 64×90 cells, the finite element model would require approximately 31,150,080 elements. The size of the model and the required simulation time make the full-scale analysis of the folding wing fairing impractical, particularly given that numerous simulations will be required for a parametric study or optimisation of the geometry.

An alternative approach to capture the stiffness properties of the flexible sandwich panel over the wing section geometry is to use a multi-scale finite element model, where the overall fairing is modelled using a shell surface, and the unit cell of the GATOR panel is modelled using brick elements. This multi-scale model could either have a unit cell coupled to each shell element, updating its stiffness properties based on its deformation (i.e., FE² method [152]) or use the homogenised stiffness

properties of the unit cell from the undeformed state of the GATOR panel as linear stiffness properties [153]. These methods are available in the literature but are rarely applied to study morphing structures due to the limited availability of user-friendly tools to apply these methods without having to code the procedure to create these models directly.

This work proposes to develop a finite element-based homogenisation tool coupled with a bespoke automated geometry generation tool to provide the ability to automatically generate and analyse models of various GATOR panel geometries, as this would create an effective tool for widely exploring the design space offered by GATOR panels. Additionally, a tool to generate wing section models of various geometries to simulate the fairing with homogenised properties of the GATOR panel is proposed as a computationally cost-effective way to study the effects of GATOR geometry on the wingtip fairing objectives. The combined tools would then enable the parametric study of the design space to identify the design features that improve the fairing and optimise its properties.

1.6.2. Spatial Variation of Cellular Core Orientation

Spatial variation of geometries and, therefore, the stiffness properties of rigid lattice structures have been studied as a means of reducing the deformation of structures while minimising the use of material [154]. The spatial variation of the geometry is achieved by changing the local diameter of lattice struts, the local size and shape of cells, or the type of cells altogether [155]. While an improved lattice structure can be found simply by running an optimisation, a computationally cheaper approach is to guide the direction of the lattice struts using a physics-based approach. To this end, various studies have considered aligning the lattice struts with the principal strain lines [156], principal stress lines [155] or load paths [157-160].

Spatial variation of fibre orientation in composites offers reduced out-of-plane displacement under pressure load [126] and increased critical buckling load of cylinders under a bending load [161]. Spatial variation of the orientation of lattice struts reduces compliance and is manufactured using 3D printing [154, 162]. While spatially varying topology of a structure can be used to optimise the structure for various objectives, to the author's knowledge, the application of this approach to improve compliance of one-directional morphing cellular structures is absent in the literature. Hence, this present study considers the utility of locally aligning the stiff and flexible direction of the GATOR panel's core with directions derived from the field variables, such as the principal stress and principal strain directions, to reduce the torsional stiffness of the fairing and distortion due to the folding of the wingtip.

1.6.3. Research Objectives and Thesis Outline

The research presented in the thesis focuses on the numerical analysis of a morphing fairing for folding wingtip joints, particularly aiming to meet the design requirements for the Semi-Aeroelastic Hinge (SAH) wingtip concept. To this end, the three main focus areas (organised into corresponding chapters) of the research are:

- **Chapter 2:** Identifying the appropriate level of fidelity to model the GATOR sandwich panel to capture its stiffness properties relevant to the folding wing,
- **Chapter 3:** Studying the effects of the GATOR panel geometry and fairing section geometry on the objectives of reducing the torsional stiffness and distortion of the fairing as the wingtip fold,
- **Chapter 4:** Studying the effects of spatially varying the orientation of the accordion-type core over the fairing section by aligning its features with directions derived from various field variables.

The overall goal is to improve the design of the morphing fairing as a potential approach to covering the Semi-Aeroelastic Hinge (SAH) wingtip joint on civil passenger aircraft.

Chapter 2 compares various homogenisation methods for the stiffness properties of the GATOR panels, including analytical and finite element methods. The study uses analytical expressions from Olympio and Gandhi [123] for the equivalent stiffness of accordion-type cores and improves their estimates by using effective lengths of chevrons and rib members rather than their full lengths. It further implements a procedure for solid-to-shell homogenisation of the GATOR panel by implementing the constraint equations and loading process described by Gigliotti and Pinho [153]. To implement this method for various geometries of the GATOR panel unit cell, an automated procedure for generating the geometry, creating the mesh, applying the periodic boundary conditions, running the load cases and extracting the shell stiffness matrix is scripted using the Python programming language. As the solid-to-shell homogenisation procedure used does not account for the transverse shear stiffness of the GATOR panel, the error introduced by this simplification is identified. Moreover, a shell model representing a fairing slice with homogenised stiffness properties of GATOR is compared to a full-scale model to identify the error introduced by assuming linear elastic stiffness properties for the shell model. The results presented in this chapter indicate the adequate level of fidelity required to model the GATOR panel fairing for the folding wing geometry.

Chapter 3 studies the effects of GATOR panel geometry and fairing section geometry on the torsional stiffness and distortion of the fairing as the wingtip folds. Similar to the homogenisation study, an automated fairing analysis procedure is developed to generate the geometry, create the mesh, apply the constraints for wingtip rotation, and extract the fairing simulation results, again using bespoke Python scripts. The study first identifies representative metrics for quantifying torsional stiffness and fairing distortions. It further identifies the design variables that strongly influence these objective metrics of the fairing. The parametric study is carried out in a reduced design space, considering only the design variables that have been shown to strongly affect the objective metrics of the fairing. This approach significantly reduces the computation cost while effectively exploring the most impactful region of the design space. The results presented in this chapter identify each design variable's trends with the objectives and their useful ranges for the fairing.

Chapter 4 studies the effects of spatially varying orientation of an accordion-type core over the wing sections. The orientation of the core is derived from the principal strain field lines of a shell fairing with isotropic properties under wingtip folding deformation. A procedure for tracing these field lines

from the finite element shell simulation [160] and creating a lattice over the wing section geometry is presented. The effects of using various field lines, such as the principal stress, principal strain and loadpath direction, are also explored in a benchmark study. The lattices created for the fairing by using principal field lines are compared to the original uniform orientation lattice in terms of the metrics for fairing performance. The results are presented and discussed to assess the applicability of this procedure for improving the compliance of morphing structures while reducing out-of-plane distortion.

Each chapter develops and applies a novel procedure for studying morphing structures for a folding wingtip joint fairing. The results identify the required level of fidelity for modelling, the geometric properties of the sandwich panel and the wing section for improving the fairing, and the effects of spatially varying core geometry on the fairing. The final chapter summarises the conclusions drawn from each technical chapter, highlighting their contribution to the overall development of the Semi-Aeroelastic Hinge (SAH) wingtip concept. It further presents recommendations for future work that could further improve the fairing's analysis and design, along with validation of the results through the fabrication and testing of prototypes.

2. EQUIVALENT ELASTIC PROPERTIES OF GATOR MORPHING SANDWICH PANELS

To explore the design and mechanical performance of the morphing fairing concept proposed in the previous chapter, it is necessary to first develop effective modelling tools for the GATOR sandwich panels, which form the heart of the concept. These panels combine flexible, highly strained elastomer facesheets with zero Poisson's ratio cellular cores in a manner that previous work has shown provides a good balance between high in-plane flexibility and high out-of-plane stiffness [133, 135, 138, 139], but the resulting geometric and material complexity of these structures requires careful consideration when deciding on an appropriate modelling approach, with a focus on the need to balance model fidelity and the depth of physics captured against computational cost. To this end, we will first consider in detail various aspects of their mechanics and how they impact the modelling approaches available before introducing the methods developed and implemented in this work.

2.1. Modelling Considerations for Compliant Sandwich Panels

A sandwich panel consists of a core stacked between two facesheets. Typically facesheets are thin, stiff layers that provide rigidity to the sandwich panel through their in-plane stiffness. The core is usually thick to distance the facesheets from the midplane in order to increase their second moment of area and, therefore, the sandwich panel's bending rigidity. The core is stiff against thickness-wise deformation to maintain the distance between facesheets and the midplane. It is also stiff in transverse shear deformation to reduce the rigid body motion of the facesheets due to core deformation, thereby engaging the facesheets in deformation as the panel deforms out-of-plane. The sandwich panel architecture provides high out-of-plane stiffness with relatively low density compared to panels that are homogenous through their thickness. Additionally, it partially decouples the in-plane and out-of-plane properties, which is desirable for various morphing applications, particularly in aircraft wings that adapt their shape to changing flight conditions [17, 119]. This partial decoupling of the stiffness properties is exploited by choosing a suitable core to achieve high in-plane flexibility while maintaining a high out-of-plane stiffness [133, 135].

Sandwich panels have been studied as wing skins for camber morphing [144], span extension [127, 132], wing twisting [100] and wingtip folding [114] applications. While the specific requirements of the skin panel may differ for each application, they all share the typical requirements of high out-of-plane stiffness with high in-plane flexibility in the morphing direction. High out-of-plane stiffness reduces the shape distortion of the wing due to aerodynamic loads and prevents the skin from buckling under compressive loads [121]. High flexibility in the morphing direction reduces the

actuation energy required to achieve the shape change on the wing [121]. A zero Poisson's ratio panel also reduces the actuation energy by avoiding the additional energy required to restrain the panel deformation in the direction perpendicular to the morphing direction [123]. In panels with non-zero Poisson's ratios, as the panel extends in the morphing direction, the perpendicular direction contracts if the Poisson's ratio is positive or expands if the Poisson's ratio is negative. Similarly, as the panel bends in the morphing direction, a double curvature is formed – anticlastic curvature for a positive Poisson's ratio and synclastic curvature for a negative Poisson's ratio [163]. In contrast, a zero Poisson's ratio core maintains a monoclastic curvature, which is desired for one-directional morphing applications undergoing out-of-plane deformation.

Cellular cores are preferred for morphing sandwich panels due to the relatively high in-plane flexibility achievable in the morphing direction while maintaining a relatively high out-of-plane stiffness. Additionally, cellular cores in flexible sandwich panels offer an extensive range of achievable equivalent elastic properties by varying their core geometries. In particular, MorphCore [134], also known as the accordion geometry [123, 127], provides high out-of-plane stiffness and near-zero Poisson's ratio through its parallel ribs and high in-plane flexibility in the direction perpendicular to the ribs through the bending deformation of the chevrons between the ribs [127, 132]. Flexible sandwich panels with MorphCore and elastomeric facesheets are fabricated through the fused fluid fabrication (FFF) 3D printing technique with thermoplastic polyurethane (TPU), as demonstrated by the Geometrically Anisotropic Thermoplastic Rubber (GATOR) sandwich panel concept [133, 135]. These GATOR panels are proposed as a compliant fairing for folding wingtip joints, as shown in Figure 24.

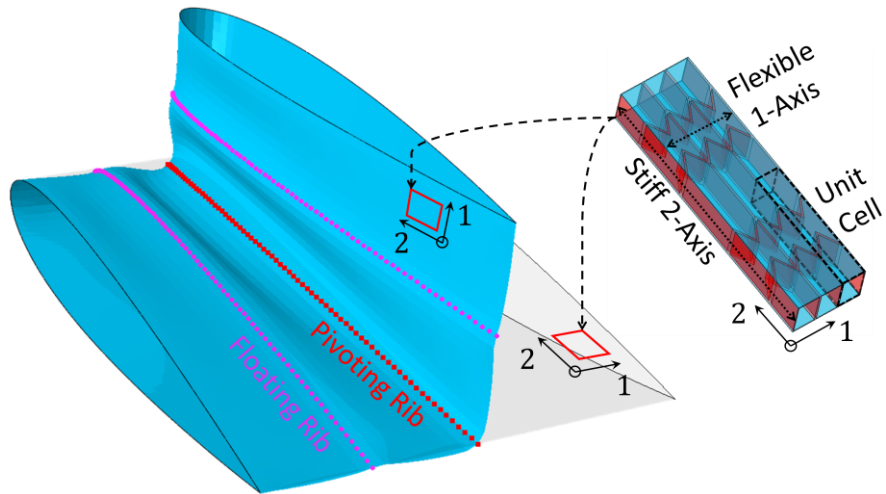


Figure 24. GATOR panel fairing on a folding wingtip joint.

GATOR panels cover the wingtip joint while carrying the aerodynamic loads and deforming in the direction across the hinge (i.e., 1-axis) to enable wingtip folding. The fairing provides a compliant aerodynamic surface that would improve the airflow around the joint and protect its components from water and other debris. The joint forms a hinge connection between the wingtip and the inboard wing, with the hinge axis oriented at an angle to the aircraft's longitudinal axis, as introduced by the Semi-Aeroelastic Hinge (SAH) concept [51, 80]. The hinge joint enables wingtip folding to shorten the

wingspan, enabling the aircraft to use a smaller airport gate than possible with its wingtip at planar position. The extended wingtip in flight provides a high aspect ratio wing that reduces induced drag and fuel consumption. Moreover, the outward orientation of the hinge axis, combined with the release of the wingtip to freely respond to gusts, alleviates the peak bending moment at the wing root [72], thereby reducing the structural weight penalty of the extended wingspan [67]. Hence, the SAH concept combined with GATOR fairings offers a practical approach to reducing fuel burn in the cruise phase of commercial airliners.

GATOR panels are made of numerous tessellated unit cells, each enclosing a pair of oppositely oriented chevrons, as shown in Figure 24. Due to the presence of such fine features, each unit cell requires a fine mesh to accurately capture its deformation and reaction forces in a finite element (FE) analysis. Hence, a full-scale, full-fidelity FE analysis of a GATOR panel fairing over the wing section geometry would be restrictively expensive for design exploration and optimisation, where many different configurations would need to be run. Alternatively, a multi-scale approach is proposed here where the elastic properties of the GATOR panel are homogenised to an equivalent shell stiffness, and a shell-based representation of the fairing on the wing section geometry with this equivalent stiffness properties is used to study the fairing response [164]. This approach significantly reduces the computation cost, enabling parametric studies of the design space offered by the GATOR panels as a fairing for folding wingtip joints.

Various homogenisation approaches are available in the literature, including analytical methods [123] and FE methods of different fidelities [152, 153]. This study explores the assumptions made in different homogenisation approaches, their effects on the equivalent properties of the GATOR panel, and their implications for the multi-scale modelling approach of the fairing.

The homogenisation approach suitable for the multi-scale modelling approach depends on various factors, including:

- (1) Equivalent stiffness properties required for the shell model of the fairing
- (2) Fidelity of the homogenisation method required to capture the GATOR panel's deformation mechanics,
- (3) Combined cost of the homogenisation method with the shell fairing model compared to a full-scale, full-fidelity analysis of the GATOR panel on the wing section.

Firstly, the equivalent stiffness properties required to define the constitutive properties of shell elements depend on the shell formulation used in the fairing model. A laminated plate modelled using Kirchoff-Love plate theory only requires the in-plane stiffness matrix (**A**), out-of-plane stiffness matrix (**D**) and the coupling matrix between the in-plane and the out-of-plane deformation (**B**) to define its constitutive properties. The formulation assumes that the plate's thickness remains unchanged and the cross-section remains straight and perpendicular to the mid-plane after deformation. These assumptions are valid only for thin plates with high transverse shear stiffness where thickness-wise deformation and transverse shear deformations can be ignored.

For plates with a high thickness-to-length ratio and low transverse shear stiffness, the transverse shear deformation of the plate becomes significant [165]. In this case, the Reissner–Mindlin plate theory can be used, extending the Kirchhoff–Love plate theory to include the transverse shear deformation as an additional rotation of the straight cross-section. This approach requires an additional transverse shear stiffness matrix (\mathbf{K}) along with the constitutive properties required for the Kirchhoff–Love plate. The true transverse shear deformation of the plate in static bending is nearly parabolic across its thickness [152, 166] due to the traction-free boundary at the top and bottom surface of the plate. Hence, modelling transverse shear deformation as an additional rotation of the straight cross-section overestimates the transverse shear stiffness in plates. Therefore, shear correction factors are required with the equivalent shear moduli in the transverse shear stiffness matrix to compensate for the additional artificial stiffness introduced to the shell model by the above-mentioned modelling assumption.

Analytical expressions for the shear correction factors are available for isotropic plates [167] and orthotropic laminates [165]. However, to the authors' knowledge, general expressions applicable to sandwich panels with cellular cores are not available in the literature. Alternatively, an equivalent transverse shear stiffness matrix can be evaluated using an FE-based homogenisation for the GATOR panel. This approach requires the application of pure transverse shear deformation to the unit cell. As the top and bottom faces of the unit cell must be traction-free, applying pure shear deformation requires constraining all the nodes of the unit cell to remove spurious bending modes that arise when shear deformation is applied using only the lateral faces [152]. These constraints connecting all the nodes of the unit cell are complex to implement in a model, and they make the homogenisation process computationally expensive. Hence, this study does not explicitly evaluate the transverse shear stiffness matrix. Instead, the effects of ignoring the transverse shear stiffness are studied by comparing it to a model that accounts for it, as described in the following sections.

Secondly, the accuracy of the homogenised properties calculated by each homogenisation method depends on the fidelity at which the GATOR panel's deformation is modelled. The analytical approaches follow a two-step process where the equivalent properties of the core are evaluated, followed by the calculation of the equivalent shell stiffness matrix using the classical laminated plate theory (CLPT). In the FE-based homogenisation methods, a unit cell of the GATOR panel is modelled using periodic boundary conditions. The unit cell is deformed in each plate deformation mode to evaluate the equivalent shell stiffness matrix.

In the analytical homogenisation, the equivalent in-plane properties of the core are evaluated by modelling the walls of the core as beams that deform in axial, bending, and transverse shear deformations [123, 146, 148]. The equivalent flexural moduli of the core significantly differ from the equivalent in-plane moduli due to the different loading conditions on the cell walls. The expressions evaluating the equivalent flexural moduli of the core require terms accounting for the torsional deformation of the walls [168]. A torsional coefficient is used in these expressions to account for thick cores, as the torsional deformation significantly differs between a beam-based model and a plate-based model of the core's walls. This torsional coefficient is based on the height-to-length ratio of the

wall and Poisson's ratio of core material, and it approaches one as the height-to-length ratio of the wall approaches zero [147, 169, 170].

The closed-form expressions available for the torsional coefficient [170] significantly deviate from the FE-derived values as the height-to-length ratio of the wall increases; hence, tabulated values from FE analysis are typically used for the torsional coefficient [147]. Other approaches model the core walls as thin plates and solve them using the generalised variational principle, providing better agreement with the FE-based bending deformation of the cellular core [168]. However, these analytical techniques do not provide closed-form expressions that can readily evaluate the flexural moduli of a cellular core [169]. Hence, this study does not evaluate the equivalent flexural moduli of the core using the analytical homogenisation method, as an FE-based torsional coefficient is required to evaluate it accurately. Instead, the equivalent in-plane moduli of the core are used with the classical laminated plate theory to evaluate the out-of-plane stiffness matrix of the GATOR panel. Considering that in a sandwich panel, the predominant contribution to the out-of-plane stiffness comes from the in-plane stiffness of the facesheets, this approach is not likely to introduce a significant error. However, the error introduced by this approach is identified by comparing its equivalent shell stiffness with that using FE-derived in-plane and out-of-plane moduli of the core to construct the equivalent shell stiffness using the classical laminated plate theory.

Classical sandwich structures are modelled as laminated plates with equivalent properties for each layer and perfect bonding between the layers without interlayer interaction. Hence, it assumes uniform strain in the in-plane at any thickness location and a continuous strain distribution through the thickness of the plate. The stiffness of a typical sandwich structure is determined using the in-plane stiffness of the facesheet and the transverse shear stiffness of the core. Higher fidelity approaches further account for the stiffness contribution of both the core and facesheets to all panel deformation modes. The modelling fidelity required for the sandwich panel is determined by classifying the panel in terms of its geometry and stiffness ratio between the core and the facesheets [171]. This classification is not pursued for the GATOR panel, as previous studies have suggested a strong interaction between the facesheet and the core, deviating from the assumptions of the classical sandwich panel theories. The experimental studies on the GATOR panel show a non-uniform strain distribution on the facesheets, where local strains can exceed the overall strain of the panel [139]. This non-uniform strain is attributed to the interaction between the chevrons in the core and the facesheet, resulting in the facesheet being pulled in the direction of the chevron displacement. The non-uniform strain on the facesheet increases the stiffness of the panel, thereby making the classical laminated plate theory's estimate of the panel stiffness an underprediction. Hence, the effect of chevron-facesheet interaction is further studied in the following sections.

Thirdly, the computation cost of running a multi-scale model depends on whether the constitutive properties of the shell elements are updated as the fairing deforms. As the GATOR panel deforms, the equivalent shell stiffness of the panel will also change. An FE-based homogenisation can find the new equivalent shell properties and the resultant loads at the different strain states for the GATOR panel unit cell. However, updating the new equivalent shell properties for each shell element requires a unit

cell to be repetitively homogenised at the strain state of that element. In cases where the shell element has more than one integration point, the unit cell homogenisation is repeated for the strain state from each integration point. This repetitive homogenisation process for each integration point of the element makes such multi-scale modelling approaches computationally expensive (e.g., FE² method [152, 172]).

Alternatively, a cheaper approach is to precompute the equivalent shell stiffness and resultant loads for various strain states of the unit cell and use interpolated values from the dataset to update the constitutive properties of the shell element as the analysis progresses. While using a precomputed dataset will reduce the cost compared to the concurrent multi-scale modelling, having to precompute the dataset for each GATOR panel design analysed limits the ability to explore the design space effectively. Hence, the multi-scale approach proposed in this study does not update the constitutive properties of the shell elements as the analysis progresses. Instead, the GATOR panel's equivalent stiffness properties attained from the undeformed state of the unit cell are used as linear elastic stiffness properties for the shell-based fairing. The effects of assuming linear elastic properties for shell elements are studied in the following section by comparing the results of the multi-scale and full-scale models.

In addition to the geometric nonlinearity of the GATOR panel deformation, the materials that make up the core and the facesheet also show nonlinear behaviour. GATOR panels are manufactured from elastomeric Thermoplastic Polyurethane (TPU) materials with a stiffer formulation, Armadillo [137], used for the core, and a softer formulation, Ninjaflex [136], used for the facesheets. Both materials share similar chemical formulations, providing strong bonding between the core and the facesheet in 3D printing. Due to their elastomeric nature, the GATOR panels show hysteresis behaviour under cyclic loading [138]; hence, a hyperelastic material definition should ideally be used to model the GATOR panel. However, comparison with FE simulation with linear elastic material properties shows good agreement with the experiment for the panel being stretched up to 10% in the morphing direction [138]. Hence, this study uses the linear elastic material properties of Armadillo and Ninjaflex for the facesheet and core, respectively.

This chapter studies the effects of different levels of homogenisation fidelity on the GATOR panel's equivalent stiffness properties. It also compares the results of the multi-scale and full-scale models for a simplified twin-panel geometry representative of a fairing slice along the span at the thickest chordwise location. The following section introduces the methods used for this study, including analytical and FE-based homogenisation. The subsequent section presents the results organised into 4 categories to assess the effects of different modelling assumptions, namely:

- (1) Timoshenko beam theory to model the core deformation,
- (2) Classical laminated plate theory to model the GATOR panel stiffness,
- (3) Kirchhoff-Love plate theory to model the GATOR panel deformation,
- (4) Linear elastic equivalent shell properties to model the GATOR panel fairing deformation.

The results indicate the level of fidelity required to model the GATOR panel as a fairing using the multi-scale modelling approach. It also highlights the method's limitations in terms of deformation ranges up to which the model is expected to be accurate. These findings indicate that the multi-scale modelling approach can be used for a parametric study of the GATOR panel as a fairing for folding wingtip joints. Hence, this enables a computationally affordable modelling approach to study morphing problems where the full-scale analysis is restrictively expensive.

2.2. Development of a Multi-scale Modelling Framework

The multi-scale modelling approach presented here focuses on the geometry of the fairing and the GATOR panel, shown in Figure 24. The pivoting rib, whose rotation axis is co-located with the wingtip joint, maintains a distance between the joint and the fairing [145]. Additional floating ribs, attached only to the fairing, enforce the cross-section shape at their locations. These rib locations provide the reference unsupported length of the panel used in this study for validating the modelling approach. In the default configuration, the wing section has a root chord of 1.6 metres, representing the tip chord of the typical single-aisle jet airliner (e.g., A320 aircraft [151]). For simplicity, the aerofoil is assumed to be NACA 0015, giving a maximum cross-section thickness of 240 millimetres. The span of the morphing section is 0.8 metres, giving an unsupported panel length of 200 millimetres between the inboard rib and the first floating rib. Note that in cases without floating ribs, the unsupported panel length is from the inboard rib to the pivoting rib, equalling 400 millimetres.

The geometry of the GATOR panel unit cell is shown in Figure 25.

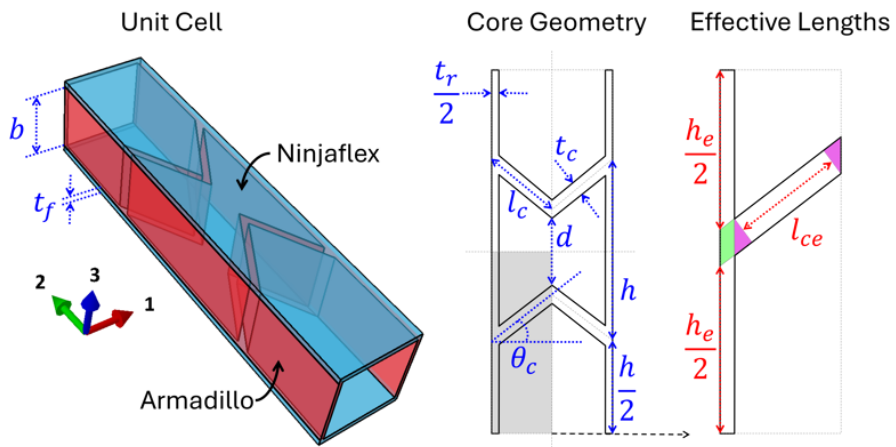


Figure 25. The geometry of the GATOR panel unit cell. Blue annotations show the variables defining the geometry. Red annotations show effective lengths used in the modified analytical homogenisation of the core.

It shows the separation between the chevrons (d) defined at the tips of the chevrons. The distance between the base (i.e., chevron-rib intersection) of the adjacent chevrons is shown as cell rib length (h) and is defined as a function of other variables by Equation 5.

$$h = 2l_c \sin \theta_c + t_c \sec \theta_c + d \quad \text{Equation 5}$$

This particular way of defining the core geometry ensures equal distance between the base of the chevrons. Olympio and Gandhi [123] used this geometry to derive the analytical expressions for the equivalent properties of the core used in this study. However, this geometry results in the minimum distance between the chevrons pointing at each other (i.e., negative Poisson's ratio hexagonal cell) being smaller than the minimum distance between the chevrons pointing away from each other (i.e., conventional hexagonal shape). The shorter distance between the chevron pointing at each other results in a larger strain on the facesheet of the GATOR panel in this region [139]. Hence, although this geometry definition is used in this chapter for consistency with analytical formulation, a different geometry definition with an equal spacing between the chevrons is used in the following chapters.

The values for GATOR panel variables are chosen arbitrarily following the guidance from studies of the GATOR panel in the literature [138]. Their default values and ranges used in the study are shown in Table 2.

Table 2. Dimensions of the unit cell geometry.

Variable		Default	Minimum	Maximum	Unit
Chevron angle	θ_c	60.0	40.0	70.0	deg
Chevron wall length	l_c	12.5	5.0	20.0	mm
Chevron wall thickness	t_c	1.0	0.5	1.5	mm
Chevron separation	d	6.0	2.0	10.0	mm
Rib thickness	t_r	1.0	0.5	1.5	mm
Core thickness	b	11.0	2.0	20.0	mm
Facesheet thickness	t_f	0.8	0.1	1.5	mm

In the default geometry configuration for this chapter, the unit cell measures $12.5 \times 59.3 \times 12.6$ millimetres in 1, 2 and 3 directions, respectively. The multi-scale modelling approach with first-order homogenisation typically requires the unit cell length scale to be at least an order of magnitude smaller than the panel length scale to keep the error below 1% [173]. With the default unit cell dimensions, 16 unit cells are required in the 1 direction to make up the 200-millimetre length between the ribs for the case with 1 floating rib. Hence, this model has a characteristic length ratio of 16 between the macro and meso scale, providing adequate scale separation for multi-scale modelling of the GATOR panel as a shell-based fairing.

Similarly, a length-to-thickness ratio above 15 is typically required for an isotropic panel to keep the transverse shear deformation negligibly small, enabling the use of Kirchhoff-Love plate formulation [174]. Although the GATOR panel has a length-to-thickness ratio of 15.9 for the unsupported length between the ribs, its behaviour will be significantly different from that of an isotropic panel. Hence, the length of the panel at which the transverse shear deformation can be ignored for the GATOR panel is studied further in the following section.

The analysis presented in this thesis uses the following linear elastic properties of the GATOR panel's materials, as shown in Table 3.

Table 3. Elastic properties of the materials used for the panel.

Property		Armadillo	Ninjaflex	Unit
Young's Modulus	E	396 [137]	22.9 [138]	MPa
Poisson's ratio	ν	0.48 [125]	0.48 [125]	

The Young's modulus of Armadillo is from the datasheet provided by the manufacturer, NinjaTek [137], and the Young's modulus of Ninjaflex is from experimental data from the literature [138]. The Poisson's ratio is not provided in the manufacturer's datasheet; hence, a typical value for thermoplastic polyurethane (TPU) from the literature is used [125].

2.2.1. Analytical Homogenisation

The analytical homogenisation of the GATOR panel's stiffness properties is carried out in two steps. First, the equivalent stiffness properties of the core are evaluated by considering the direct deformation of the unit cell walls. Second, the equivalent shell stiffness matrix for the sandwich panel is evaluated using the classical laminated plate theory.

The analytical expressions for equivalent elastic moduli for MorphCore [134], also known as the accordion geometry [123, 127], are derived by Olympio and Gandhi [123] for the geometry defined with blue annotations in Figure 25. These expressions are based on the direct deformation of the unit cell walls in bending, axial and transverse shear deformation. However, they tend to underpredict the core's equivalent moduli as the bending members' lengths (e.g., chevron and rib walls) that actively participate in deformation are shorter than their full lengths – due to the stiffening effect of the interaction area between the chevrons and the rib walls, and between the two halves of the chevron at their intersection. Hence, the expressions from Olympio and Gandhi [123] are modified by assuming the interaction areas are effectively rigid, leading to a reduction in the length of the wall undergoing deformation, as shown with red annotations in Figure 25. These effective lengths of the chevron wall and cell rib wall are given by Equation 6 and Equation 7, respectively.

$$l_{ce} = l_c - \frac{t_r}{2} \sec \theta_c - t_c \tan \theta_c \quad \text{Equation 6}$$

$$h_e = h - t_c \sec \theta_c \quad \text{Equation 7}$$

The modified expressions for the equivalent moduli of the core that use the effective lengths are shown in Equation 8 to Equation 10.

$$\frac{E_1}{E} = \frac{\beta_e^3}{\alpha \cos \theta_c (\beta_e^2 + \tan^2 \theta_c (1 + \kappa \beta_e^2))} \quad \text{Equation 8}$$

$$\frac{E_2}{E} = \frac{\alpha \eta \beta_e}{2 \alpha_e \cos \theta_c} \quad \text{Equation 9}$$

$$\frac{G_{12}}{E} = \frac{\beta_e^3 \cos \theta_c}{\frac{2}{\alpha} \left(\frac{\alpha_e}{\eta} \right)^3 \cos^2 \theta_c \left(1 + \kappa \left(\frac{\beta_e \eta}{\alpha_e} \right)^2 \right) + \alpha (4 \cos^2 \theta_c (1 + \kappa \beta_e^2) + \beta_e^2 \sin^2 \theta_c)} \quad \text{Equation 10}$$

where:

$$\eta = \frac{t_r}{t_c}, \quad \beta_e = \frac{t_c}{l_{ce}}, \quad \alpha_e = \frac{h_e}{l_{ce}}, \quad \alpha = \frac{h}{l_c}$$

The parameters E and ν are Young's modulus and Poisson's ratio of the core material, respectively. The parameter κ is a correction factor used with the transverse shear deformation, and it is evaluated as $\kappa = 2.4 + 1.5 \nu$. Note that these expressions are identical to that of Olympio and Gandhi [11] for the case where the effective lengths of the chevron and the cell rib equal their full lengths (i.e., $h_e = h$ and $l_{ce} = l_c$).

The Poisson's ratio (ν_{12}) of the core is assumed to be zero due to the ribs restricting deformation in the 2-axis. Hence, the modified expressions in Equation 8 to Equation 10 provide the in-plane properties of the core required for evaluating the shell stiffness matrix using the classical laminated plate theory. The shell stiffness matrix relates the strains and curvatures of the panel to the distributed forces and moments along the edges of the plate according to Equation 11.

$$\begin{bmatrix} \mathbf{N} \\ \mathbf{M} \end{bmatrix} = \begin{bmatrix} \mathbf{A} & \mathbf{B} \\ \mathbf{B} & \mathbf{D} \end{bmatrix} \begin{bmatrix} \boldsymbol{\varepsilon} \\ \boldsymbol{\kappa} \end{bmatrix} \quad \text{Equation 11}$$

where:

$$\begin{aligned} \mathbf{N} &= [N_{xx} \quad N_{yy} \quad N_{xy}]^T, & \mathbf{M} &= [M_{xx} \quad M_{yy} \quad M_{xy}]^T, \\ \boldsymbol{\varepsilon} &= [\varepsilon_{xx} \quad \varepsilon_{yy} \quad \gamma_{xy}]^T, & \boldsymbol{\kappa} &= [\kappa_{xx} \quad \kappa_{yy} \quad \kappa_{xy}]^T \end{aligned}$$

The vectors \mathbf{N} is the forces, \mathbf{M} is the moments, $\boldsymbol{\varepsilon}$ is the strains, and $\boldsymbol{\kappa}$ is the curvatures. For clarity, the vector of distributed forces and moments is hereafter referred to as distributed loads, and the vector of strains and curvatures is referred to as the strain state. The shear strain and torsional curvature are defined in the engineering convention, where $\gamma_{xy} = \partial u / \partial y + \partial v / \partial x$ and $\kappa_{xy} = 2 \partial^2 w / \partial y \partial x$, respectively. The sub-matrices of the shell stiffness matrix are evaluated as

$$(A_{ij}, B_{ij}, D_{ij}) = \int_{-t_p/2}^{t_p/2} Q_{ij}(1, z, z^2) dz, \quad (i, j = 1, 2, 3) \quad \text{Equation 12}$$

where:

$$\mathbf{Q} = \frac{1}{(1 - \nu_{12}\nu_{21})} \begin{bmatrix} E_1 & \nu_{21}E_1 & 0 \\ \nu_{12}E_2 & E_2 & 0 \\ 0 & 0 & G_1(1 - \nu_{12}\nu_{21}) \end{bmatrix}$$

The subscripts i and j are the matrix indices, and the variable t_p is the thickness of the whole panel. The matrix \mathbf{Q} represents the in-plane stiffness of each layer normalised by the thickness. The \mathbf{Q} matrix for the core is evaluated using the equivalent properties from Equation 8 to Equation 10. The \mathbf{Q} matrix for the facesheet is evaluated using the isotropic properties of Ninjaflex from Table 3. The equivalent shell stiffness matrix found using Equation 12 can be used to define the constitutive properties of the shell elements of the fairing in the multi-scale modelling approach.

The expressions used to evaluate the equivalent moduli of the core assume that the walls of the core can be modelled as Timoshenko beams. The classical laminated plate theory used to evaluate the equivalent shell stiffness of the GATOR panel assumes uniform strain in each in-plane layer as the unit

cell deforms. The errors introduced by these assumptions are studied by comparing the results from analytical and FE-based homogenisation methods.

2.2.2. Finite Element Homogenisation

The unit cell of the GATOR panel (referred to as the representative volume element (RVE) or microstructure) is modelled using solid elements, and its constitutive response is evaluated as a solution to a classical boundary value problem [175]. This approach captures the effects of material heterogeneity and non-uniform strains within the RVE. If the fairing (referred to as the macrostructure) is also modelled using solid elements, then a first-order homogenisation method that uses the first-order gradients of the displacement field can be used to evaluate equivalent stiffness for the macrostructure. However, this solid-to-solid homogenisation approach cannot capture higher-order deformation modes, such as bending curvature, that are expressed in the second-order gradients of the displacement field [175]. As the fairing is modelled as a shell surface in this study, a solid-to-shell homogenisation method is required to evaluate the equivalent shell stiffness for the macrostructure. The solid-to-shell homogenisation technique accounts for the second-order gradients of the displacement field [175] to capture the bending deformation modes. This section describes the implementation of the second-order solid-to-shell homogenisation approach for this study.

The RVE represents a repeating unit of the panel that tessellates to form an infinite panel. Hence, the deformation of each RVE face must be compatible with the deformation of the opposite face at the adjacent RVE. Periodic boundary conditions (PBC) are applied to the RVE face nodes to satisfy this deformation compatibility condition. The PBCs couple the identical nodes on opposite faces of the RVE through a set of constraint equations [153]. These constraint equations also include additional terms corresponding to external nodes, which are used to apply deformations to the RVE. The constraint equations used to apply the PBCs to the RVE are shown in their general form in Equation 13 to Equation 15.

$$-u_1^1 + u_1^2 + Au_1^\varepsilon + Bu_1^\kappa + \frac{1}{2}Cu_3^\varepsilon + \frac{1}{2}Du_3^\kappa = 0 \quad \text{Equation 13}$$

$$-u_2^1 + u_2^2 + \frac{1}{2}Au_3^\varepsilon + \frac{1}{2}Bu_3^\kappa + Cu_1^\varepsilon + Du_1^\kappa = 0 \quad \text{Equation 14}$$

$$-u_3^1 + u_3^2 + Eu_1^\kappa + Fu_2^\kappa + \frac{1}{2}Gu_3^\kappa = 0 \quad \text{Equation 15}$$

where:

$$\begin{aligned} A &= X_1^1 - X_1^2, & B &= zA, & C &= X_2^1 - X_2^2, & D &= zC \\ E &= -\frac{1}{2}((X_1^1)^2 - (X_1^2)^2), & F &= -\frac{1}{2}((X_2^1)^2 - (X_2^2)^2), \\ G &= -(X_1^1 X_2^1 - X_1^2 X_2^2) \end{aligned}$$

The displacements and the coordinates of each node are annotated as u_D^f and X_D^f , respectively, where the subscript D refers to the degree of freedom, and the superscript f is the face identifier, with 1 and 2 referring to the positive and negative face of each axis. The constraint equations define the

relative displacement of the node pair in each degree of freedom. The constraint equations couple the strains ε_{xx} , ε_{yy} and γ_{xy} of the RVE to the 1, 2, and 3 direction displacements of the external node u_D^ε , respectively. Similarly, the constraint equations also couple the curvatures κ_{xx} , κ_{yy} and κ_{xy} of the RVE to the 1, 2, and 3 direction displacements of the external node u_D^κ . The locations of the external nodes are arbitrary since only their applied displacements affect the RVE deformation. A factor 1/2 is used with the coefficient of shear and torsion terms in the constraint equations as the shear strain and torsional curvature are defined in the engineering convention.

The equations can be intuitively explained for an individual node pair. For instance, consider a node pair on the 1-axis. As the unit cell is centred about the origin, the 2-axis and 3-axis coordinates of the pair will be identical. However, the 1-axis coordinates of the pair will have the same magnitude with opposite signs (i.e., $X_1^1 = L_1/2$ and $X_1^2 = -L_1/2$). For this case, the constraint equations can be simplified as Equation 16 to Equation 18.

$$-u_1^1 + u_1^2 + L_1 u_1^\varepsilon + z L_1 u_1^\kappa = 0 \quad \text{Equation 16}$$

$$-u_2^1 + u_2^2 + \frac{1}{2} L_1 u_3^\varepsilon + \frac{1}{2} z L_1 u_3^\kappa = 0 \quad \text{Equation 17}$$

$$-u_3^1 + u_3^2 - \frac{1}{2} y L_1 u_3^\kappa = 0 \quad \text{Equation 18}$$

where:

$$z = X_3^1 = X_3^2, \quad y = X_2^1 = X_2^2$$

These expressions indicate that for a node pair on the 1-axis:

- The relative displacement in 1-direction is only due to strain and curvature in the 1-direction,
- The relative displacement in 2-direction is only due to shear and torsion,
- The relative displacement in 3-direction is only due to torsion.

As the PBCs define the difference in the node pair displacement in each degree of freedom, a case with zero relative displacements can still have non-zero individual displacements as long as they are identical on both nodes. For instance, in pure bending of the RVE in the 1-direction, both nodes are individually displaced in the 3-direction with identical displacement, so the difference between them is zero.

The homogenisation is carried out by loading the RVE in each shell deformation mode and evaluating the reaction forces on the external nodes used to apply the deformations. The deformed shapes of the GATOR panel unit cell in the shell deformation modes are shown in Figure 26.

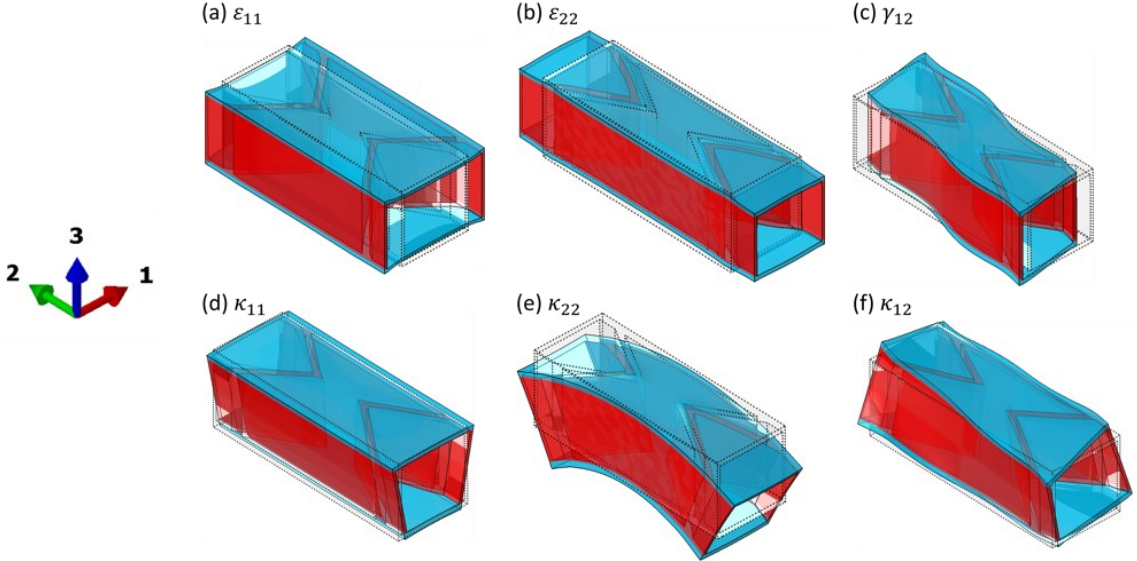


Figure 26. GATOR panel unit cell deformed to each shell deformation mode. Note that curvatures are stated in the form $\kappa_{\alpha\beta}$ where $\alpha, \beta \in [1, 2]$. It represents a midplane curvature evaluated by the gradient $\frac{\delta}{\delta\beta} \left(\frac{\delta}{\delta\alpha} (U) \right)$ where U is the displacement vector. A positive curvature is a hogging deformation while a negative curvature is a sagging deformation. For instance, κ_{11} represent a hogging curvature (about 2-axis) resulting from the nodes in the face normal to 1-axis being displaced in the 13-plane.

For instance, consider applying a pure strain of $\varepsilon_{xx} = 1$, where the applied displacement on reference nodes are $u_1^\varepsilon = 1$ and $u_2^\varepsilon = u_3^\varepsilon = u_1^\kappa = u_2^\kappa = u_3^\kappa = 0$. The column of the shell stiffness matrix corresponding to each applied deformation is given by Equation 19, where the index i refers to the row of the applied shell deformation mode and the column of the stiffness matrix corresponding to that applied deformation.

$$\mathbf{K}_{plate}(:, i) = \frac{1}{u_i A_{RVE}} \mathbf{F} \quad \text{Equation 19}$$

where:

$$\mathbf{K}_{plate} = \begin{bmatrix} \mathbf{A} & \mathbf{B} \\ \mathbf{B} & \mathbf{D} \end{bmatrix},$$

$$\mathbf{F} = [F_1^\varepsilon, F_2^\varepsilon, F_3^\varepsilon, F_1^\kappa, F_2^\kappa, F_3^\kappa]^T, \quad \mathbf{u} = [u_1^\varepsilon, u_2^\varepsilon, u_3^\varepsilon, u_1^\kappa, u_2^\kappa, u_3^\kappa]^T$$

Hence, in the case of $\varepsilon_{xx} = 1$, the index $i = 1$, giving the first column of the stiffness matrix. This procedure requires six load cases, each corresponding to a shell deformation mode, to fully populate the shell stiffness matrix. Each load case is analysed using a linear perturbation step in Abaqus; hence, the equivalent stiffness is evaluated from the tangential stiffness of the RVE about its initial strain state. The RVE is homogenised in its undeformed state, as linear elastic properties are assumed for the shell elements in the multi-scale model.

The results from the FE-based homogenisation procedure are compared with those from the analytical approach to identify the effects of assuming the Timoshenko beam model for the deformation of the core walls and classical laminated plate theory for evaluating the equivalent shell

stiffness. The FE-based homogenisation procedure used does not evaluate the equivalent transverse shear stiffness of the RVE. Hence, the effect of transverse shear deformation on the flexural stiffness of the panel is studied next by comparing the equivalent flexural stiffness from FE-based homogenisation with the equivalent flexural stiffness evaluated from an FE model of a cantilevered GATOR panel deformed with a tip displacement.

2.2.3. Full-Scale Panel Analysis

Evaluation of the equivalent transverse shear stiffness matrix through the homogenisation process is expensive due to the additional constraints involving all the nodes, which are required to apply pure transverse shear deformation to the RVE through its lateral faces [152]. Alternatively, the effects of transverse shear stiffness are studied using the deformation results from the following FE analysis. The displacement and reaction loads from FE simulation are input to two different analytical expressions for equivalent flexural moduli, one accounting for transverse shear deformation and the other ignoring it.

In the FE analysis, GATOR panels of various lengths are modelled with a cantilever fixture on one end and a vertical displacement applied at the other, as shown in Figure 27.

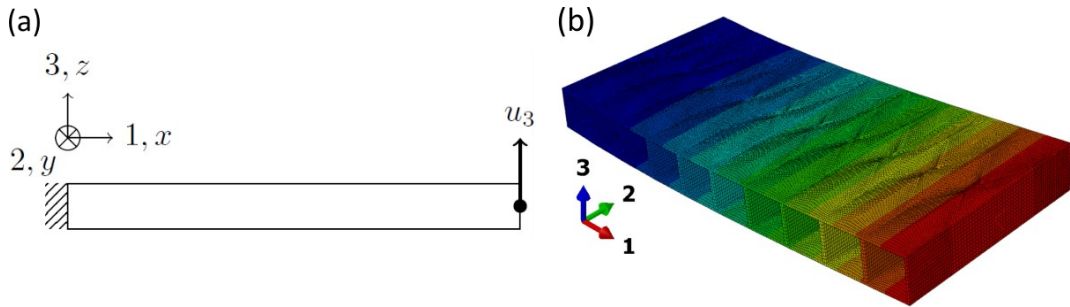


Figure 27. Tip displacement of the GATOR panel to evaluate equivalent flexural modulus and study the effects of transverse shear. (a) shows the loading diagram, and (b) shows an example of the full-scale model with 10 cells along the length.

The front and the back faces of the panel are free. The nodes on the left face are fixed, and the nodes on the right face are rigidly connected to the mid-point on the face where vertical displacement is applied. Hence, the panel's right and left faces are rigid due to the applied boundary conditions.

Various panel lengths along the 1-axis, from 1 cell to 20 cells, are used to study the significance of transverse shear deformation through their effect on the equivalent flexural moduli estimated using the displacement and reaction load data from FE simulation. The panels with short lengths are expected to undergo significant transverse shear deformation. Hence, for short lengths of the panel, the analytical expressions for equivalent flexural modulus that do not account for transverse shear stiffness are expected to underpredict the equivalent flexural modulus relative to the values from the FE-based homogenisation. In contrast, the transverse shear deformation decreases as the panel length increases, reducing the difference between the equivalent flexural modulus estimated here and the value evaluated from the FE-based homogenisation. In the analytical model that accounts for

the transverse shear deformation, the equivalent moduli is expected to be close to the values from FE-based homogenisation for all lengths of the panel.

The GATOR panel is designed to have a near-zero Poisson's ratio; hence, the equivalent Poisson's ratio terms ν_{12} approaches zero while $1 - \nu_{12}\nu_{21}$ approaches one, as shown in Table 4.

Table 4. Poisson's ratio terms of the GATOR panels from FE-based homogenisation.

	ν_{12}	$1 - \nu_{12}\nu_{21}$
In-plane	0.065	0.966
Out-of-plane	0.165	0.915

The near-zero Poisson's ratio makes the bending behaviour of the panel similar to that of a beam. Hence, the Euler beam equation can be used to model the bending behaviour instead of the Kirchhoff plate equation by assuming $\nu_{12} \approx 0$ and $1 - \nu_{12}\nu_{21} \approx 1$, as shown in Equation 20 and Equation 21.

$$\text{Kirchhoff Plate: } M_x = \frac{Et^3}{12(1 - \nu_{12}\nu_{21})} \left(\frac{d^2w}{dx^2} + \nu_{12} \frac{d^2w}{dy^2} \right) \quad \text{Equation 20}$$

$$\text{Euler Beam: } M_x = \frac{Et^3}{12} \frac{d^2w}{dx^2} \quad \text{Equation 21}$$

The variable M_x is the distributed internal moment about the y-axis at the cross-section facing the x-axis, and the variable w is the vertical displacement. Simplifying the plate problem to a beam problem reduces the 2-dimensional solution process to a 1-dimensional analysis. However, the effects of the small Poisson's ratio exist in the results; hence, the study is repeated with three different widths of the panel, from 1 cell to 3 cells on the 2-axis, to study these effects on equivalent flexural moduli of the panel.

The FE analysis of the cantilevered plate evaluates the vertical reaction force (F_3) and the tip rotation angle (θ_2) about the 2-axis for an applied tip displacement (u_3) using a linear analysis step. These values are used to evaluate the equivalent flexural moduli (E_1^D) by considering the Euler and Timoshenko beam models shown in Equation 18 and Equation 19, respectively.

$$\text{Euler: } E_1^D = 4 \frac{F_3}{u_3} \frac{1}{L_2} \left(\frac{L_1}{L_3} \right)^3 \quad \text{Equation 22}$$

$$\text{Timoshenko: } E_1^D = 6 \frac{F_3}{\theta_2} \frac{1}{L_2} L_1^2 \left(\frac{1}{L_3} \right)^3 \quad \text{Equation 23}$$

The Euler beam model does not capture the effects of transverse shear; hence, the flexural modulus evaluated from this model for short panels is expected to have large errors compared to the flexural modulus from FE-based homogenisation. The error in flexural modulus will decrease for longer panels as the transverse shear deformation becomes negligible for panels with a high length-to-thickness ratio (typically ≥ 15 for isotropic panels [174]). If this length of the panel where the transverse shear effects become negligible is less than the unsupported length of the panel on the fairing (i.e., length of 16 cells), it indicates that the shell model based using the Kirchhoff-Love plate formulation is

adequate to model the fairing in the multi-scale model. Alternatively, if large errors exist in the equivalent flexural moduli from the Euler model for a panel length beyond 16 cells, then a shell formulation that accounts for transverse shear deformation is required for the multi-scale modelling approach.

The equivalent flexural modulus from the Timoshenko beam model is expected to be close to the equivalent flexural modulus from the FE-based homogenisation. The Timoshenko beam model accounts for the transverse shear deformation as an additional rotation of the straight cross-section. However, neither the Euler nor the Timoshenko beam models include the effects of thickness-wise deformation. The effects of thickness-wise deformation are expected to decrease with increasing panel length. Hence, a close agreement between the equivalent flexural modulus values from the Timoshenko beam model for short panels with the FE homogenised flexural modulus would suggest a negligible effect of the thickness-wise deformation on the flexural moduli of the panel.

2.2.4. Simplified Fairing Analysis

The multi-scale modelling approach assumes a linear elastic constitutive model for the shell elements by defining the homogenised properties of the GATOR panel as constants that do not change with deformation. Previous studies using FE modelling and experimental testing have shown that the GATOR panel shows nonlinear behaviour due to geometric nonlinearity in their deformation [138]. The full-scale model captures the geometric nonlinearity in the fairing stiffness due to GATOR panel deformation, while the multi-scale model with equivalent linear elastic properties for the shell elements ignores these changes in fairing stiffness. The effect of this simplification is studied by comparing a full-scale and multi-scale model for a representative fairing section.

A twin-plate, half model is modelled to represent a fairing slice along the span from the inboard rib to the pivoting rib at the thickest chordwise location for a typical jet airliner wing section, resulting in an upper GATOR panel and a lower GATOR panel with the wingtip hinge between them, as shown in Figure 28.

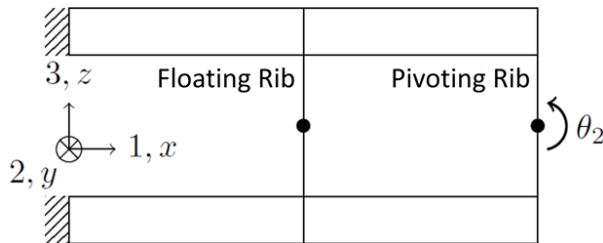


Figure 28. Representative fairing model for analysis of the effects of geometric nonlinearity in the GATOR panel deformation.

Only the inboard half of the fairing is modelled (hence the presence of the wingtip hinge, pivoting rib, and applied rotation θ_2 at the rightmost end of the model) due to the symmetry of the fairing in this initial simplified representation. The torque-rotation response of the multi-scale model and the full-scale model of the twin-plate are compared to evaluate the accuracy of the modelling approach.

Variations in two design variables, the number of floating ribs and the pre-strain on the fairing, are used to study the robustness of the agreement between the multi-scale and full-scale models.

The spacing between the ribs is the same as the original wing section, and the thickness (i.e., height in 3-axis) of this representative fairing section is the maximum thickness of the wing section. For NACA 0015 aerofoil section with a 1.6-metre chord, the maximum thickness is 240 millimetres. Hence, given that the GATOR panel thickness is 12.6 millimetres, the multi-scale mode has two shell surfaces with 227.4 millimetres between them. For both the full-scale and multi-scale models, the left end is fixed, and the nodes of the ribs are rigidly connected to their mid-point (shown as a dot on each rib in Figure 28). The mid-point of the pivoting rib is constrained in translation in 2 and 3 axes and in rotation in 1 and 3 axes. As the wing section fairing is envisioned to have span-wise pre-tension, a pre-strain is applied to this representative model by displacing the pivoting rib's mid-point in the 1-axis direction. In the case without pre-strain, the mid-point of the pivoting rib is also constrained in translation in the 1-axis. A rotation is applied to the mid-point of the pivoting rib about the 2-axis, and the reaction torque on this node is measured to study the change in torsional stiffness due to deformation.

It is expected that the full-scale model will show a softening of torsional stiffness as the pivoting rib rotates due to the buckling of the facesheets of the GATOR panel that is being compressed. The local buckling of the facesheets is not captured in the multi-scale model; hence, its torque result is expected to deviate from the full-scale model's torque values following the onset of facesheet buckling. While pre-strain is expected to delay the onset of facesheet buckling, it is also expected to cause changes in the equivalent stiffness of the GATOR panel. The comparison of torque results from the full-scale and multi-scale analysis is used to identify the maximum folding angle of the pivoting rib and ranges of pre-strain, beyond which the multi-scale model significantly deviates from the full-scale model. It provides the design space of the GATOR panel fairing of the wing section that can be explored with the multi-scale modelling approach in parametric studies.

2.3. Results and Discussion

The material properties of the core and facesheet in the GATOR panel are shown in Table 3. The dimensions of the GATOR panel geometric variables are presented in Table 2. The GATOR panel defined by these properties and dimensions are studied using the methods described above. The meshes for the FE analysis are generated using GMSH [176], an open-source design and meshing program. The FE analysis is carried out using Abaqus [174], a commercial FEM solver. The model generation, meshing, analysis and results extraction process are automated using bespoke Python scripts, as both GMSH and Abaqus allow access to them through an application programming interface (API).

The FE models for homogenisation and full-scale analysis use first-order brick elements with reduced integration (C3D8R). The GATOR panel models are meshed with 1-millimetre elements to give equivalent moduli values converged to within $\pm 1\%$ error compared to models with half the element size. Similarly, models of the core are meshed with 0.25-millimetre elements, giving equivalent

moduli values converged to within $\pm 1\%$ error compared to models with half the element size. The finer mesh required for the core models is due to the sensitivity of the equivalent E_1 value to the mesh size. However, as the contribution of the facesheets to the equivalent moduli is more significant in the GATOR panels, a coarse mesh was adequate to get converged results for the GATOR panels. Moreover, the shell-based fairing model uses the first-order quadrilateral elements with reduced integration (S4R). A mesh size of approximately 8-millimetre gives converged results in torque values compared to models with half its element size.

2.3.1. Timoshenko Beam Assumption

This study compares the error introduced by modelling the core walls as Timoshenko beams to evaluate the equivalent core stiffness. The original formulation from Olympio and Gandhi [123] and its modified formulation presented in this chapter are compared to the FE-based homogenisation of the core. Olympio and Gandhi [123] use the definition of the core dimensions shown in blue in Figure 25. The modified formulation uses the shortened effective length for the chevron and the rib height to evaluate their deformation. These reduced lengths are schematically shown in red in Figure 25, and their analytical expressions are shown in Equation 6 and Equation 7. The equivalent stiffness properties evaluated for the core using the methods described above are shown in Table 5, along with the error calculated relative to the FE-homogenised values.

Table 5 Comparison of analytical and FE-based homogenisation for default configuration.

	FEM	Olympio and Gandhi (2009)	Modified Formulation
ν_{12}	-0.001	0	0
E_1 [Pa]	108,946	55,751	115,247
E_2 [Pa]	32,586,859	31,680,000	33,971,448
G_{12} [Pa]	27,390	19,295	29,226
E_1 error		-49%	6%
E_2 error		-3%	4%
G_{12} error		-30%	7%

Both the analytical formulations assume Poisson's ratio to be zero, and the FE-based homogenisation evaluates a negligible value for it, thereby giving a close agreement between the methods. Similarly, the equivalent E_2 evaluated from all the methods are similar, giving a maximum error of $\pm 4\%$. Significant errors are evaluated for the equivalent E_1 and G_{12} values from the original formulation. Axial deformation of the core in the 1-axis direction requires the bending deformation of chevrons, while shear deformation in the in-plane requires the bending deformation of both chevrons and ribs. As the effective bending lengths of these walls are less than the length used in the geometry definition, the original formulation significantly underpredicts the core's equivalent E_1 and G_{12} values. The modified formulation uses shortened effective lengths for the chevron wall and rib height, thereby reducing the error between its equivalent moduli values and FE-homogenised values.

The effects of changing the chevron length, thickness and width on the error in the core's equivalent E_1 and G_{12} values evaluated by the modified analytical formulation are presented in Figure 29.

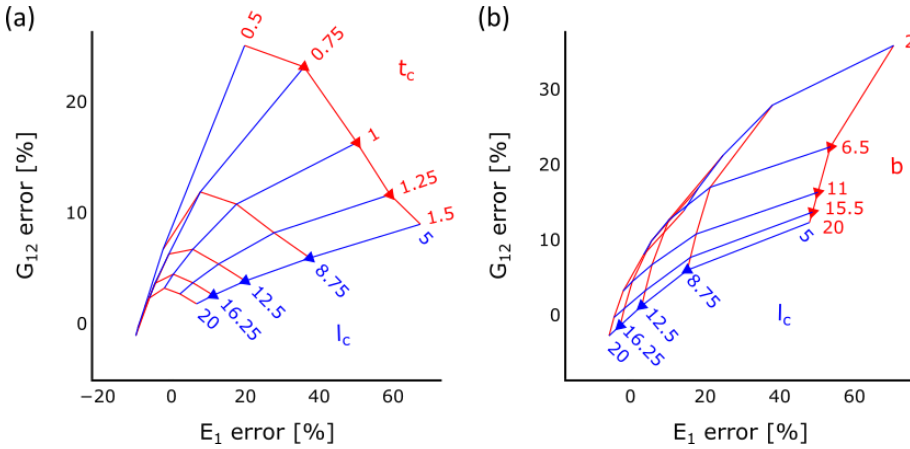


Figure 29. Effects of changing the chevron dimensions on the error between the equivalent moduli values from modified analytical formulation and FE-based homogenisation. Note that each carpet plot varies the length of the chevron wall and one of the cross-section dimensions, thereby, changing the slenderness ratio of the chevron wall.

The blue lines represent the effects of changing the chevron length (l_c) for constant values of chevron thickness (t_c) in Figure 29a and for constant values of chevron height (b) in Figure 29b. It shows that for any chevron thickness (t_c) or height (b), increasing chevron length (l_c) reduce the error in the core's equivalent E_1 and G_{12} values. This reduction in error is attributed to the increasing length-to-thickness ratio of the chevron walls. The increasing length-to-thickness ratio of the chevron walls reduces the significance of chevron deformation modes that are not accounted for in the analytical formulation, such as thickness-wise and height-wise deformation due to Poisson's ratio. Hence, the equivalent moduli values from the modified analytical formulation get closer to the FE-homogenised values.

The red lines show the effects of changing chevron thickness (t_c) in Figure 29a and the effect of changing chevron height (b) in Figure 29b for constant values of the chevron length (l_c). These red lines in Figure 29a, indicates that error in equivalent E_1 decreases with decreasing chevron thickness (t_c). Similar to increasing chevron length (l_c), this trend is attributed to the increasing length-to-thickness ratio of the walls which reduces the significance of the deformation modes not accounted for in the analytical model. In contrast to the trend in equivalent E_1 , the error in equivalent G_{12} initially increases with decreasing chevron thickness (t_c) before reversing the trend for further decrease in chevrons thickness (t_c) for the cases with long chevrons (l_c). While the latter decrease in the error is attributed to the increasing length-to-thickness ratio of the beams, the initial increase in the error with decreasing chevron thickness (t_c) is unintuitive. Hence, it should be explored in further analytical studies.

Another unintuitive trend is shown by the red lines in Figure 29b, where the error in equivalent E_1 and G_{12} values increase with decreasing chevron height (b). The decreasing chevron height (b) increases the length-to-height ratio of the chevron walls, thereby making the wall shape closer to a typical beam rather than a plate despite the increasing error. The increasing error between the analytical and the FE-based approach comes solely from the changes in equivalent moduli values in the FE-based homogenisation while the analytical values remain the same. This change in FE-

homogenised values is attributed to the change in height-wise (3-axis) strain distribution as the chevron wall deforms in bending, as shown in Figure 30.

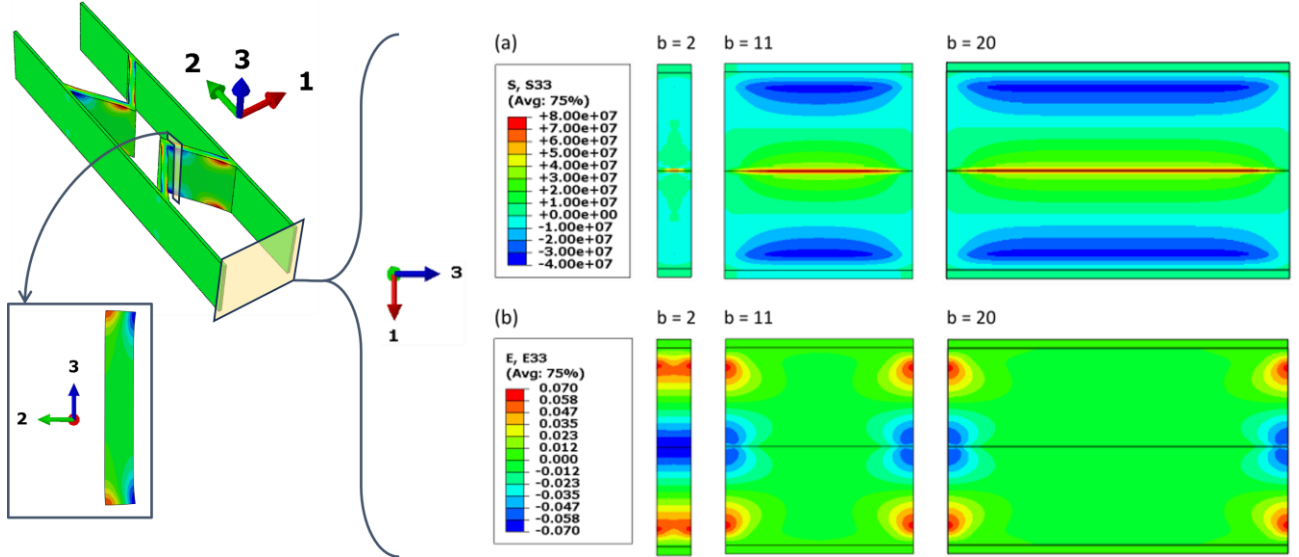


Figure 30. The direct stress and strain distribution in the height-wise (3-axis) direction for various core heights for the load case of $\varepsilon_{xx} = 1$ in the FEM homogenisation. (a) shows the stress distribution, and (b) shows the strain distribution.

As the chevron walls bend, they develop significant length-wise strains on the free lateral faces, with tensile strain on one side and compressive strain on the other. These length-wise strains on the faces further cause height-wise strains due to the high Poisson's ratio of the core material (i.e., 0.48, as shown in Table 3), resulting in an anticlastic curvature. These height-wise strains become significant as the core height decreases, as shown in Figure 30b. These height-wise strains introduce an additional deformation mode not accounted for in the analytical models, thereby increasing the error as this deformation mode becomes more significant with decreasing core height (b).

The results of comparing the equivalent moduli from the modified analytical formulation and FE-based homogenisation show the limitations of the analytical approach in accurately calculating the equivalent moduli for the variety of core geometries. The analytical approach shows good agreement with FE-based homogenisation for the cases with high length-to-thickness ratio walls and adequate height to reduce the effects of height-wise strains. However, the analytical approach is not suitable for a parametric study of the core dimensions since it may introduce significant errors for some geometries.

2.3.2. Laminated Plate Assumption

The equivalent shell stiffness of the GATOR panels is evaluated using an analytical and FE-based homogenisation approach, as described in sections 2.2.1 and 2.2.2, respectively. A combined approach where FE-homogenised core properties are used with the classical laminated plate theory (CLPT) to evaluate the equivalent shell stiffness of the GATOR panel is used for two cases. In the first case, only the in-plane properties of the cores are used to evaluate both \mathbf{A} and \mathbf{D} matrix. In the second case, both in-plane and out-of-plane equivalent properties are used to evaluate the \mathbf{A} and \mathbf{D} matrix,

respectively. A comparison of equivalent stiffness properties from these methods is presented in Figure 31.

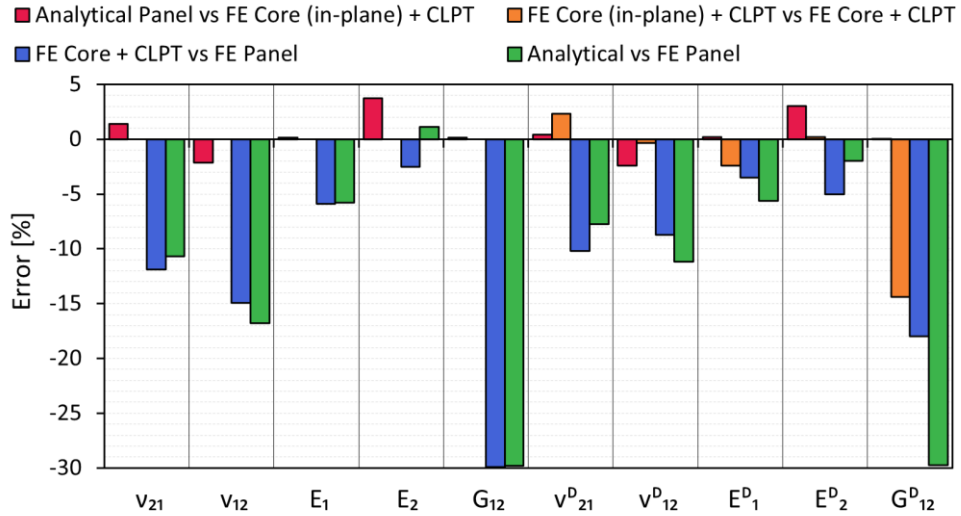


Figure 31. Comparison of various methods of homogenising the GATOR panel stiffness properties.

The red bars compare the stiffness values from the modified analytical method with those from the combined method using the in-plane properties of the core. It shows close agreement with an error of less than $\pm 4\%$ due to similar core properties from both methods, as presented in Table 5. The figure further shows that the error in the GATOR panel's equivalent E_1 and G_{12} becomes negligible with an error of less than $\pm 0.2\%$. The facesheet properties are identical in the two methods, while the core properties differ by up to 7%, as shown in Table 5. Hence, the negligible error in the GATOR panel's equivalent E_1 and G_{12} indicate that the predominant stiffness contribution to these two deformation modes comes from the facesheets rather than the core.

Cellular cores typically have vastly different equivalent moduli from in-plane and out-plane deformation modes. Hence, the GATOR panel's equivalent properties evaluated by the combined method using the in-plane moduli of the core are different from the combined method that uses both in-plane and out-of-plane moduli of the core. The comparison of these two approaches is shown by the orange bars in Figure 31. While these orange error bars show that the in-plane properties are identical, the out-of-plane properties are significantly different, particularly for equivalent E_1^D and G_{12}^D . The negative error bars for equivalent E_1^D and G_{12}^D indicate that these out-of-plane moduli of the core are greater than the corresponding in-plane moduli. Especially the error of -14% for the equivalent G_{12}^D indicates that the torsional stiffness of the core is significantly higher than its in-plane shear stiffness; hence, their out-of-plane moduli should be explicitly evaluated.

The blue bars in the figure show the error introduced by ignoring the core-facesheet interaction in the GATOR panel. The blue bars compare stiffness properties from the combined method using FE-homogenised core properties against the FE-homogenised GATOR panel properties. Hence, the only difference between the two methods is due to the negligence of the non-uniform facesheet deformation in the combined method. The figure shows large errors for equivalent Poisson's ratios and moduli, indicating that the effect of core-facesheet interaction on the equivalent stiffness is

significant. This error is particularly substantial for equivalent G_{12} and G_{12}^D with values of -30% and -18%, respectively. Hence, the negligence of core-facesheet interaction significantly underpredicts the equivalent stiffness of the GATOR panel.

The green bars in the figure compare the equivalent stiffness from analytical homogenisation to that from FE-based homogenisation. The analytical homogenisation ignores the core-facesheet interaction and uses the core's in-plane stiffness to evaluate the GATOR panel's in-plane and out-of-plane properties. Hence, the green bars show significant errors due to the simplifications in the analytical model, giving errors as large as -30% for equivalent G_{12} and G_{12}^D . Hence, the effects of the out-of-plane stiffness of the core and the core-facesheet interaction must be captured in the homogenized stiffness properties of the GATOR panel.

The effects of core-facesheet interaction are further studied by varying the chevron thickness (t_c) and facesheet thickness (t_f) using the combined method with FE-homogenised core properties and FE-based homogenisation of the GATOR unit cell. The errors in the equivalent GATOR panel properties are shown in Figure 32, and the non-uniform strain distributions on the facesheet are shown in Figure 33.

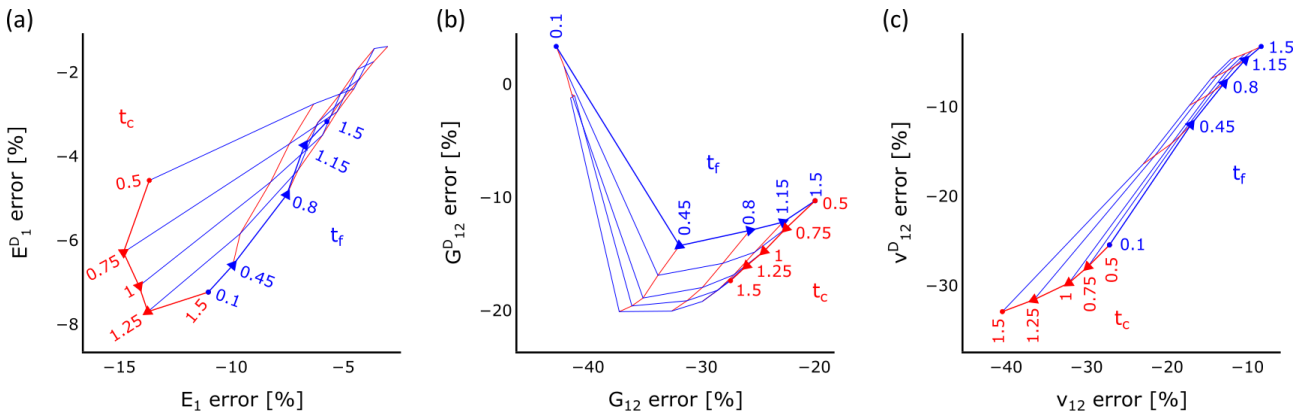


Figure 32. The error in equivalent properties from the combined approach using FE-homogenised core properties relative to FE-based homogenisation of the GATOR panel. It shows the error due to facesheet-core interaction for various values of facesheet and chevron thickness.

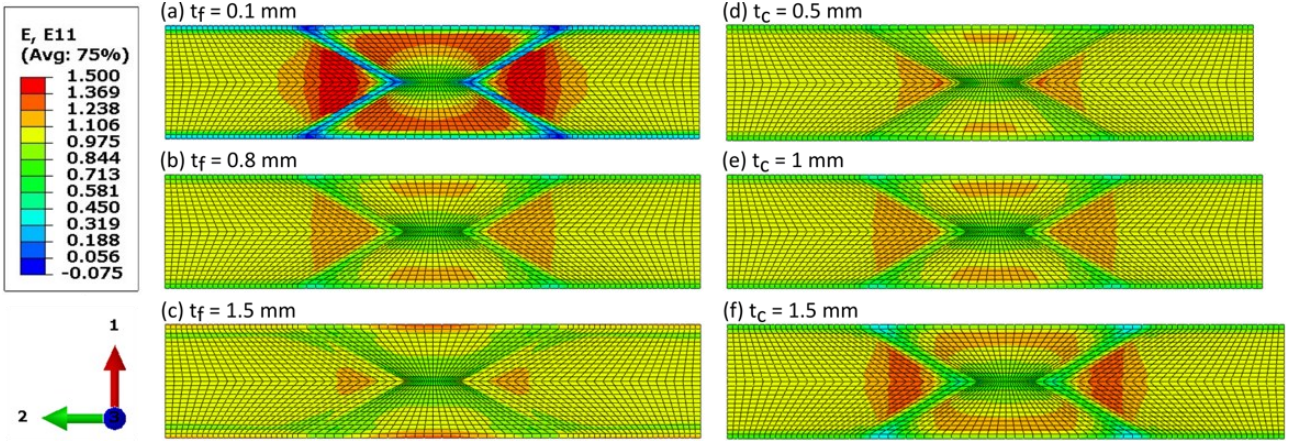


Figure 33. Direct strain distribution in the morphing direction (1-axis) on the facesheet from the top view for an applied strain of $\varepsilon_{11} = 1$ for various values of facesheet and chevron thickness.

The blue lines in Figure 32 show decreasing errors for increasing facesheet thickness (t_f), except for the anomaly in the very thin facesheets (i.e., $t_f = 0.1$) for out-of-plane shear modulus G_{12}^D . The anomaly indicates that the effect of facesheet-core interaction in torsional deformation is negligibly small for very thin facesheets compared to facesheet thickness (t_f) above 0.45 millimetres. Hence, a similar equivalent G_{12}^D is evaluated from the combined method and the FE-based homogenisation. The reduction in error with increasing facesheet thickness (t_f) indicates that the non-uniformity of the facesheet deformation due to facesheet-core interaction decreases with increasing facesheet thickness (t_f). This decrease in non-uniformity of the facesheet deformation is shown in Figure 33a to Figure 33c for axial deformation of the unit cell (i.e., $\varepsilon_{11} = 1$). It shows that increasing facesheet thickness (t_f) reduces the ability of the chevrons to pull the facesheet in the direction of their displacement, thereby reducing non-uniformity in the facesheet deformation.

Similarly, the red lines in Figure 32 show decreasing errors for decreasing chevron thickness (t_c), except for the anomaly in the very thin facesheets (i.e., $t_f = 0.1$). Decreasing chevron thickness (t_c) reduces the stiffness of the chevron walls. This reduction in chevron stiffness reduces their ability to pull the facesheets in the direction of their displacement. Hence, decreasing chevron thickness (t_c) leads to reducing non-uniformity in facesheet deformation, as shown in Figure 33d to Figure 33f. The decreasing non-uniformity in the facesheet deformation reduces the effects of core-facesheet interactions, making the equivalent stiffness from the classical laminated plate theory (CLPT) closer to that from the FE-based homogenisation of the GATOR unit cell.

These results comparing the equivalent stiffness from classical laminated plate theory (CLPT) and FE-based homogenisation shows that the negligence of core-facesheet interaction introduces significant error to the equivalent stiffness properties of the GATOR panel. The classical laminated plate theory (CLPT) results with the core's in-plane properties alone compared against those with the core's in-plane and out-of-plane properties show that the negligence of the core's out-of-plane properties also introduces significant error, particularly in torsional stiffness of the GATOR panel. Hence, the analytical approach to homogenising the equivalent stiffness of the GATOR panel is inadequate for the multi-scale modelling approach.

2.3.3. Kirchhoff-Love Plate Assumption

The FE-based homogenisation method proposed for the multi-scale modelling approach does not evaluate the equivalent transverse shear stiffness. While transverse shear deformation can be significant for panels with a low length-to-thickness ratio, their effect decreases as the panel length increases. Hence, this section studies the effect of the transverse shear deformation for various lengths of the GATOR panel using a cantilevered panel with tip displacement loading, as described in section 2.2.3. The panel is simplified to a beam model considering the near-zero Poisson's ratio of the GATOR panel. However, the study is repeated with multiple widths (i.e., in 2-axis) of the panel to study the effects of the Poisson's ratio. The displacements and the reaction loads are used to evaluate an equivalent flexural modulus (E_1^D) along the 1-axis. The equivalent E_1^D values from the study are shown in Figure 34, along with their error relative to FE-based homogenisation values and their incremental change as panel length increases.

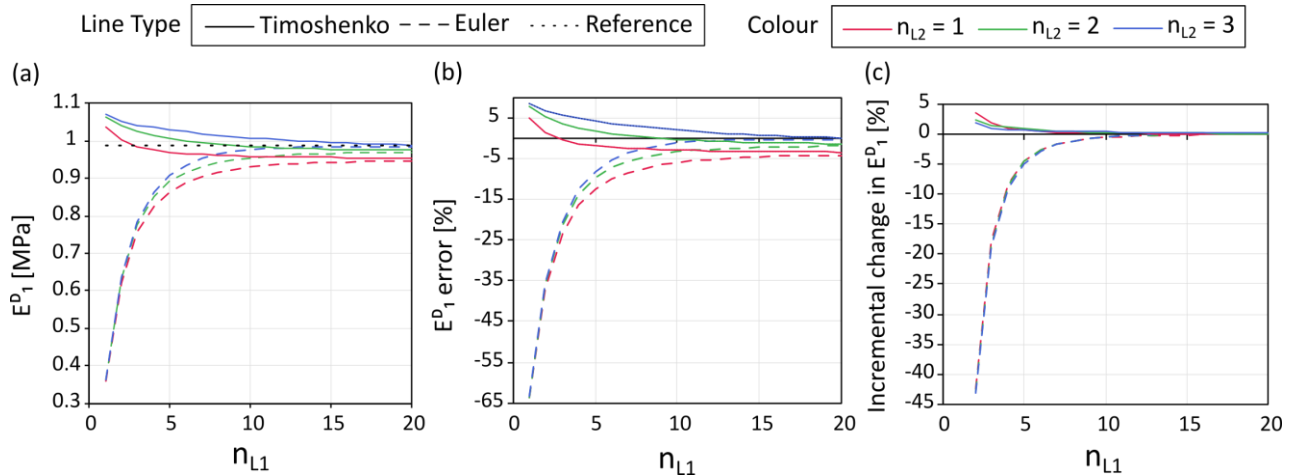


Figure 34. Equivalent flexural modulus (E_1^D) along 1-axis evaluated by fitting full-scale FE analysis data to Euler and Timoshenko beam equations. The reference value is from the FE-based homogenisation of the GATOR panel unit cell. (a) shows the equivalent E_1^D values, (b) shows their error relative to the reference value, and (c) shows the incremental change in the equivalent E_1^D values as panel length increases.

Figure 34a shows that the equivalent E_1^D from the Euler beam model is significantly lower relative to the reference value from the FE-based homogenisation for short lengths of the panel, thereby giving significant error in Figure 34b. This underprediction in equivalent E_1^D is due to the transverse shear deformation mode that is neglected in the Euler beam model. It further shows that as the number of cells along the length (i.e., 1-axis) of the panel increases, the equivalent E_1^D from the Euler model gets closer to the reference value. This reduction in the error is attributed to the increasing length-to-thickness ratio of the panel, which reduces the significance of the transverse shear deformation. In contrast, the Timoshenko beam model accounts for the transverse shear deformation. Hence, the equivalent E_1^D from the Timoshenko beam model shows close agreement with the reference value. The negligible change in equivalent E_1^D for long panels indicate negligible effects of the transverse shear deformation at these length-to-thickness ratios of the panel.

Figure 34a shows the shift in the equivalent E_1^D lines with an increasing number of cells along the width, indicating that although the Poisson's ratio is small, it is not entirely negligible. Hence, the error in the equivalent E_1^D , shown in Figure 34b, is not entirely due to negligence of the transverse shear deformation. It also includes the error due to the Poisson's ratio, which is ignored when simplifying the plate deformation to a beam model. However, the flattening of the equivalent E_1^D line in Figure 34a for increasing number of cells along the length indicates the reducing effects of transverse shear deformation. The incremental percentage change in the equivalent E_1^D is shown in Figure 34c for each additional cell added along the length of the panel. It shows that the incremental change reduces to less than $\pm 1\%$ for panels at least 9 cells long for the Euler model and 4 cells long for the Timoshenko model.

The unsupported length of the GATOR panel between the ribs in the wing section, shown in Figure 24, is 16 cells long. At this panel length, the maximum incremental change in equivalent E_1^D is $\pm 0.1\%$, indicating that the effects of the transverse shear deformation are negligibly small. Hence, the shell formulation based on Kirchhoff plate theory can be used to model the GATOR panel fairing on the wing section without introducing significant errors due to the negligence of transverse shear deformation.

2.3.4. Linear Elasticity Assumption

This section studies the effect of geometric nonlinearity in the GATOR panel deformation, which changes stiffness properties as the panel deforms. In the multi-scale modelling approach, the GATOR panel stiffness properties are homogenised at the undeformed state, and these homogenised properties define the linear elastic constitutive properties for the shell model. Hence, the effects of geometric nonlinearity in the GATOR panel deformation are not captured by the multi-scale model due to the stiffness properties in the shell element not being updated based on their strain state. This section evaluates the error introduced by the multi-scale model by comparing it to the full-scale model for a simplified fairing slice geometry described in section 2.2.4. The torque response from the two models for various values of applied pre-tension and number of floating ribs are shown in Figure 35.

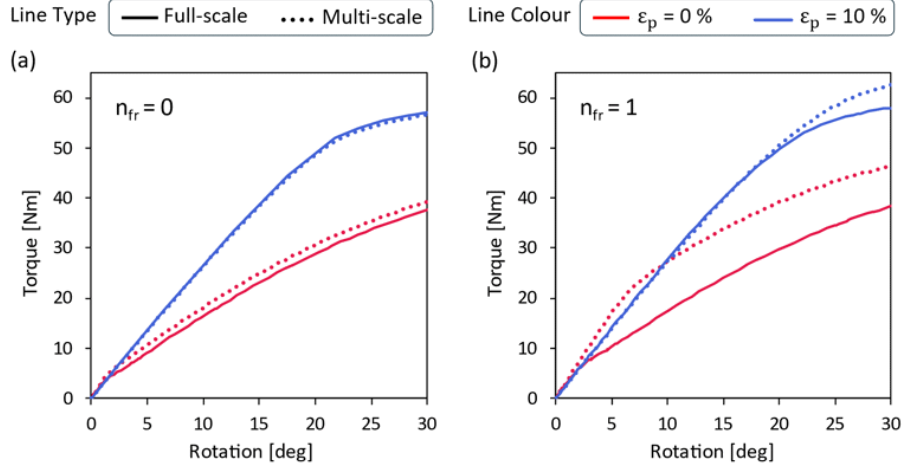


Figure 35. Comparison of torque response between multi-scale and full-scale for the twin-plate models.

It shows in Figure 35a, close agreement between the multi-scale and the full-scale model response for the fairing slice without floating rib for the full 30-degree rotation range. The error in the multi-scale model's torque response at 30-degree rotation is 3.9% and -0.9% for the case with 0% and 10% pre-strain, respectively. The case without pre-strain has a slightly higher error than the case with pre-strain due to more prominent local buckling of the facesheet on the top panel. The error due to the local buckling of the facesheet is more significant in cases with a floating rib, as shown in Figure 35b. It shows that the torque response of the multi-scale model deviates significantly from that of the full-scale model in both cases but at different rotation angles. For the case without pre-strain, the multi-scale model's torque response deviates (with an error exceeding 10%) from the full-scale model after about 2 degrees of rotation. The case with 10% pre-strain shows close agreement between the multi-scale and full-scale models up to a rotation of 20 degrees, after which the multi-scale model response deviates from the full-scale model response.

The trends in the torque response are explained through various features in the deformed shapes of the full-scale fairing slices shown in Figure 36 for all the configurations at an approximately 20-degree rotation angle.

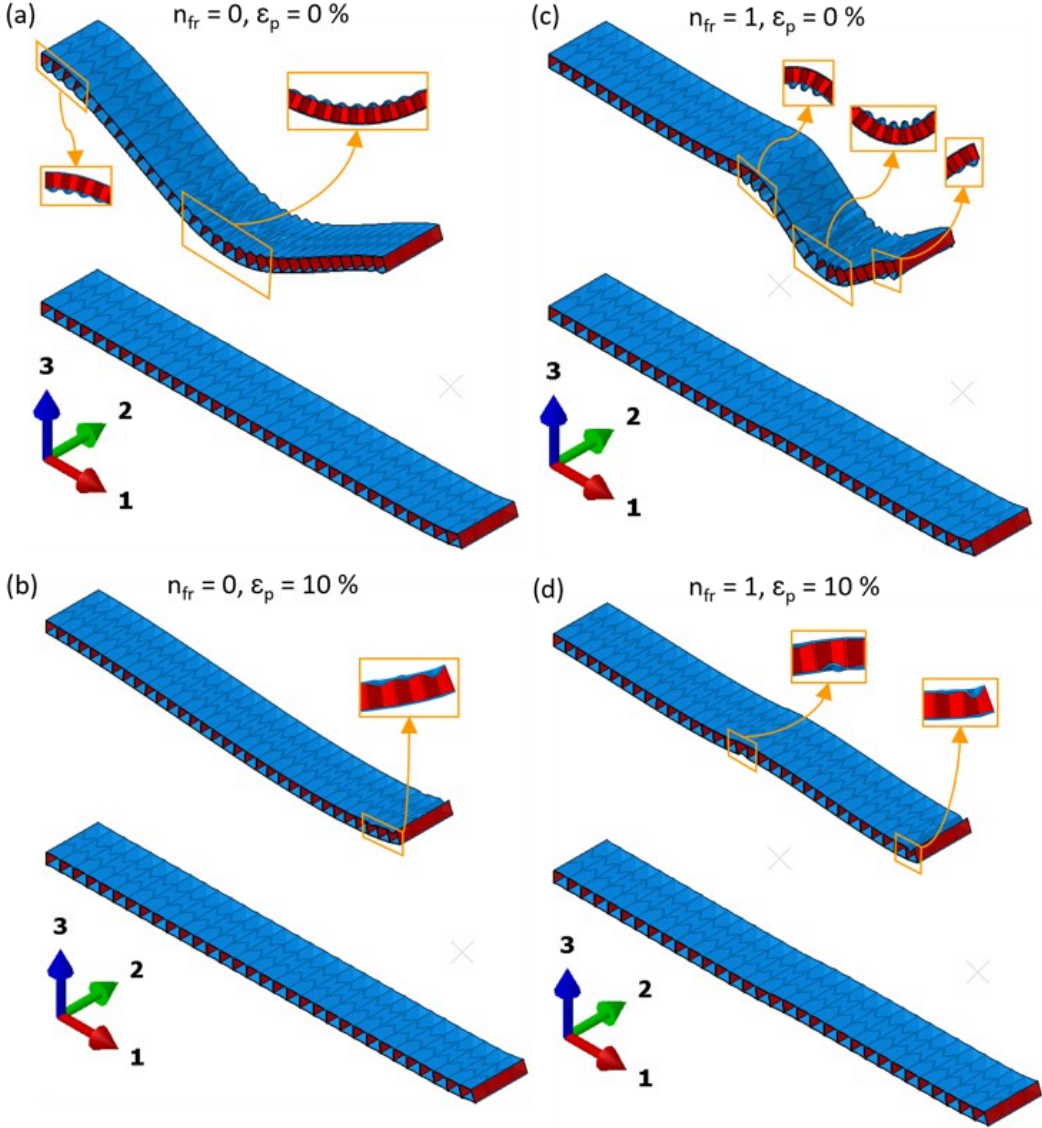


Figure 36. Deformed shapes of the full-scale model of the fairing slice at 20-degree rotation (a) and (b) shows the 0% and 10% pre-strain case for the fairing slice without floating rib. (c) and (d) shows the 0% and 10% pre-strain case for the fairing slice with a floating rib.

It shows that the cases without pre-strain in both configurations have more prominent buckling of the facesheet than those with 10% pre-strain. Comparing the two cases without pre-strain in Figure 36a and Figure 36c indicates that the case with a floating rib has localised regions with steep panel curvatures that have the cells with buckled facesheets, whereas in the case without floating ribs, these regions are more spread out and have shallower panel curvature. Moreover, the amplitudes of buckled facesheets are larger in the case with a floating rib compared to the case without it. These comparisons indicate that the case with a floating rib creates more prominent changes in the cell geometry of the GATOR panel as the pivoting rib is rotated. As the stiffness changes due to geometric nonlinearity in deformation are not captured by the multi-scale model, these changes lead to greater error in the multi-scale model for the fairing slice case with a floating rib.

This study indicates that the multi-scale and full-scale models show good agreement in their torque response up until the rotation angle at which the facesheets in the full-scale model undergo significant local buckling. It further shows that the applied pre-tension on the panel delays the rotation angle at which the facesheets undergo local buckling, thereby extending the rotation angles up to which both models give similar results. Hence, the multi-scale model offers a cheaper alternative to the full-scale model in studying the wingtip fairings with pre-tensioned GATOR panels up to a threshold rotation angle of the wingtip.

2.4. Conclusions

This chapter proposed a multi-scale modelling approach as an alternative to the full-scale, full-fidelity model of the GATOR panel fairing for folding wingtip joints. The multi-scale modelling approach comprises two steps: (1) homogenisation of the GATOR panel stiffness properties to an equivalent shell stiffness matrix, and (2) shell model of the fairing with homogenised GATOR panel properties. The study showed that analytical models underpredict the core's stiffness, and this can be corrected by using a shortened effective length for the bending members rather than their full length. It also showed that the core-facesheet interaction in the GATOR panel is significant. Hence, evaluating the equivalent stiffness of the GATOR panel as a laminated plate underpredicts the panel's stiffness. Alternatively, an FE-based homogenisation approach is used in the multi-scale model, which evaluates the required stiffness properties for the shell model based on the Kirchhoff plate theory. The study further showed that the effect of transverse shear decreases with the length of the panel and that its effect becomes negligible for the unsupported panel length present in the wing section geometry. Finally, the comparison of the multi-scale and full-scale models showed good agreement in the torque response. However, the effects of geometric nonlinearity in the GATOR panel deformation became significant at large rotations of the fairing slice, particularly in cases with floating ribs, leading to deviation of the multi-scale model's torque response from the full-scale model. The multi-scale model accurately evaluates the torque response of the GATOR fairing up to the deformation at which the facesheets buckle under compression. Hence, within this deformation limit, the multi-scale model offers a computationally cheaper alternative to the full-scale model to explore the design space offered by GATOR panels when used as fairings for folding wingtip joints.

3. DESIGN STUDIES OF GATOR MORPHING FAIRINGS FOR FOLDING WINGTIP JOINTS

This chapter applies the multi-scale modelling approach introduced in Chapter 2 to folding wingtip fairing made of GATOR panels. A parametric study of design space provided by the GATOR panel geometry and the fairing geometry is presented. As the focus is on developing a fairing with minimal torsional stiffness and distortion of the cross-section as the wingtip fold, the fairing section is assumed to be symmetric to simplify this study. To this end, a symmetric aerofoil profile is used without taper, sweep or flare angle. The chapter presents the method used to generate the shell geometry representing the fairing, as well as the constraints and load cases applied to achieve pre-strain and the fairing deformation due to folding wingtip. As the fairing is modelled as a symmetric wing section, a half-model of the fairing, from the inboard rib to the pivoting rib, is modelled to reduce the computational cost.

The chapter first defines the metrics that can be used to represent torsional stiffness and the distortion of the fairing. Reaction torque is an intuitive choice for the torsional stiffness; however, no such intuitive metrics are available for the fairing distortion. Hence, various metrics based on strain energy, curvature and displacement of the fairing are studied. Secondly, a sensitivity study of the chosen metrics to changes in the design variables is studied to reduce the design space by eliminating those variables that do not have a notable impact on the objective metrics. Thirdly, the variables that strongly influence the objectives are explored further in a parametric study, identifying their trends with the objectives and the range of their values that improve the objectives relative to the baseline design. Finally, the conclusions highlight the insights from the study and their significance for further analysis of the concept.

3.1. Modelling of GATOR panel Fairing

The results presented in Chapter 2 indicated that the multi-scale modelling approach provides adequate fidelity to study the effects of the design variables on the fairing objectives in low folding angles. The fairing designs with high torsional stiffness or large distortions at low folding angles are not viable for large folding angles of the wingtip, and the proposed modelling approach can identify these designs, thereby reducing the design space to feasible solutions. Hence, the multi-scale modelling approach is useful for understanding the basic design trade-offs and highlighting promising configurations for future analysis with more expensive methods better suited to capturing material and geometric nonlinearity.

The fairing section modelled in the chapter is sized to represent a wingtip added to the tip of a typical single-aisle commercial jet airliner along with this proposed fairing. Hence, the fairing section is modelled with a root chord (c) of 1.6 metres, representing the tip chord of an airliner (e.g., A320 aircraft [151]). A symmetric aerofoil profile is used to simplify the analysis process to focus on fairing objectives of reducing torsional stiffness and distortion using the available design variables without the complexity introduced by the asymmetry. To this end, NACA 0015 aerofoil is used to avoid folding deformation of the wingtip due to applied pre-tension on the skin panels. In an unsymmetric aerofoil profile, the unbalanced moment contribution from the top and bottom skins due to pre-tension will result in a non-zero initial folding angle. While this is not expected to cause any real issue during the implementation of the device (it would just cause small offsets in the torque response curves), for this parametric study, it is helpful to have the partial simplification of a symmetric initial condition. Additionally, the wing section used for the analysis has no taper, sweep or flare angle, further simplifying the fairing geometry. The default configuration and the range of values for the fairing variables are shown in Table 6.

Table 6. Variables of the fairing section.

Variable		Default	Minimum	Maximum	Unit
Pre-tension	ε_p	0.1	0	0.2	
Span	L	0.8	0.6	1.0	m
Floating ribs	n_{fr}	0	0	2	

The range of values used for each fairing variable is adapted from the previous parametric study of the fairing for folding wing joints [145]. The default configuration represents the mid values of the ranges, except for the floating ribs whose default value is zero, as they are newly introduced in this study.

The GATOR panels manufactured in previous works [133, 139] were fabricated via multi-material 3D printing using two different formulations of Thermoplastic Polyurethane (TPU) manufactured by Ninjatek. A soft material, ‘Ninjaflex’, capable of 65% strain before yield [136], is used for the facesheets, while a stiffer material, ‘Armadillo’, capable of 18% strain before yield [137], is used for the core. The multi-scale model uses the GATOR panel’s initial stiffness response as linear elastic stiffness properties for the shell-based fairing. Hence, like in Chapter 2, the GATOR panel unit cell used in the FE-based homogenisation uses the linear elastic material properties shown in Table 7.

Table 7. Elastic properties of the materials used for the panel [133].

Property		Armadillo	Ninjaflex
Young’s Modulus	[MPa]	396	22.9
Poisson’s ratio		0.48	0.48

The geometry definition of the GATOR unit cell is similar to the geometry presented in Chapter 2. The only difference between them is that in this chapter, the minimum distance between the chevrons in the 2-axis direction is the same regardless of whether the chevrons are pointing at each other (i.e.,

negative Poisson's ratio hexagonal shape) or away from each other (i.e., conventional hexagonal shape). This uniform distance between chevrons is shown in Figure 37 as chevron separation (d).

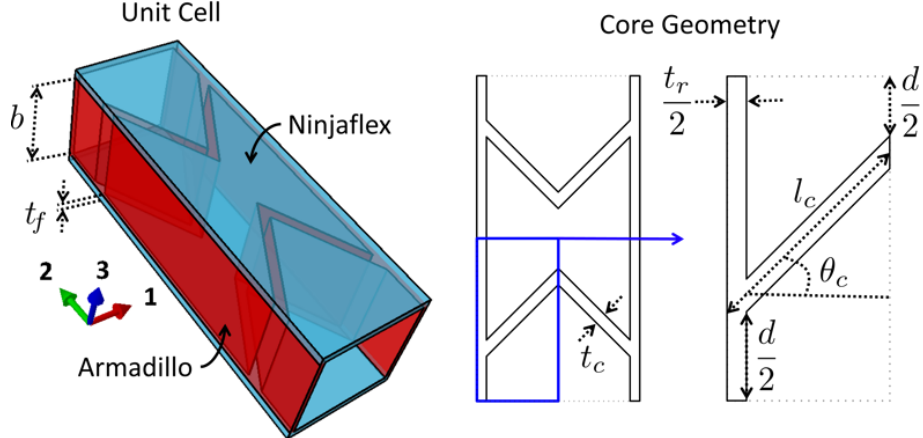


Figure 37. The geometry of the GATOR panel unit cell.

The unit cell's geometry significantly affects the panel's equivalent stiffness properties. The desired properties of the shell stiffness to achieve low torsional stiffness and distortion of the fairing include high in-plane flexibility in the morphing direction (i.e., 1-axis), near-zero Poisson's ratio in the non-morphing direction (i.e., 2-axis), and high out-of-plane stiffness. The effects of unit cell geometry on these properties are studied using the range of values and default configuration shown in Table 8.

Table 8. Variables of the sandwich panel.

Variable		Default	Minimum	Maximum	Unit
Chevron angle	θ_c	60.0	40.0	70.0	deg
Chevron wall length	l_c	12.5	5.0	20.0	mm
Chevron wall thickness	t_c	1.0	0.5	1.5	mm
Chevron separation	d	6.0	2.0	10.0	mm
Rib thickness	t_r	1.0	0.5	1.5	mm
Core thickness	b	11.0	2.0	20.0	mm
Facesheet thickness	t_f	0.8	0.1	1.5	mm

The range of values used for each panel variable is adapted from the previous parametric study of the GATOR panel [138] to capture the geometry with the desired properties for the fairing. The default configuration is arbitrary and approximately represents the mid values of the ranges. In the default configuration, this unit cell has the dimensions $12.5 \times 35.9 \times 12.6$ millimetres in 1, 2, and 3 directions, respectively. For simplicity, these dimensions are referred to as the length, width and thickness, respectively.

3.1.1. Definition of Wing Fairing Geometry

The FE-based homogenisation process described in Chapter 2 and the analysis of the shell fairing described in this chapter are repeated for various geometries of wing sections and equivalent shell properties. The process of mesh generation, finite element analysis, and results extraction are therefore automated using a Python script, enabling simultaneous analysis of multiple cases. This

section describes the process of generating the fairing model for finite element analysis and extracting the simulation results for the parametric study.

The geometry of the wing section is defined in three steps. First, the nodes of the flared ribs are defined using analytical expressions that account for the wing's sweep angle and taper ratio. Next, the surface nodes of the ribs are offset inward in the direction normal to the surface by half the thickness of the panel. The offset nodes represent the midplane of the GATOR panel fairing, where the homogenised equivalent stiffness properties are defined. Finally, the surface geometry of the wing section is defined in GMSH using the offset nodes of the flared ribs.

Initially, a grid of normalised chord locations $x \in [0,1]$ and spanwise rib locations $Y \in [0,L]$ is defined at the midplane (i.e., $Z = 0$) for a wing section of a given span (L). A pivot point is defined for each rib using a uniform normalised chordwise location (x_Λ) but a different spanwise location (Y_Λ). The grid points representing each rib are scaled, translated and rotated around their pivot point to account for their local chord, sweep angle, and flare angle. This transformation is carried out using the expressions in Equation 24 to Equation 26.

$$X = Y \sin \phi + x c \left(1 - \frac{Y}{L} (1 - T) \right) \quad \text{Equation 24}$$

$$X = X_\Lambda - (Y - Y_\Lambda) \cot \Lambda \quad \text{Equation 25}$$

$$Y = \frac{c \left(x_\Lambda \left(1 - \frac{Y_\Lambda}{L} (1 - T) \right) - x \right) + Y_\Lambda (\cot \Lambda + \sin \Lambda)}{\cot \Lambda + \sin \Lambda - x c \frac{1}{L} (1 - T)} \quad \text{Equation 26}$$

The parameters c , ϕ and T represent the wing section's root chord, sweep angle and taper ratio, respectively. Equation 24 represents a line along the span at a given normalised chord location (x) and is used to evaluate the X coordinates of the scaled grid points. Equation 25 represents a line along the rib rotated by flare angle (Λ) about the pivot point of the rib. Combining Equation 24 and Equation 25 gives Equation 26, which evaluates the Y coordinates of the transformed grid. This transformed grid is shown in Figure 38a along with the pivot point of each rib.

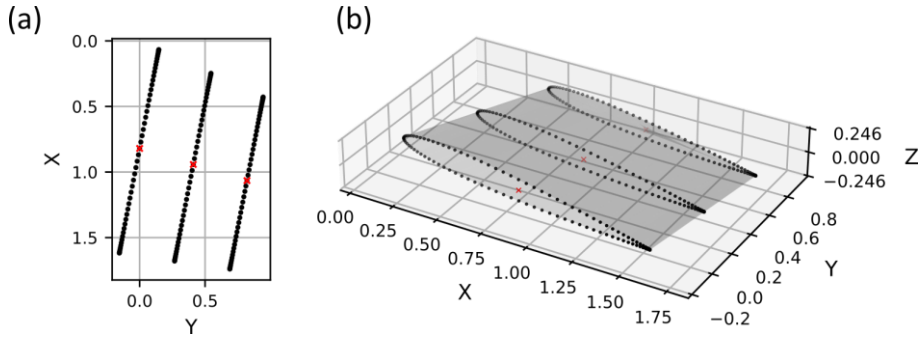


Figure 38. Fairing geometry. (a) shows the X and Y coordinates of the scaled grid and rotated grid. (b) shows the aerofoil nodes (i.e., Z coordinates) generated using the grid. In both figures, the red crosses represent the pivot point of the ribs.

The transformed grid is used with the NACA 4-digit series [177] aerofoil equations to define the nodes representing the outer surface of the ribs. These nodes of the ribs are shown in Figure 38b, along with the pivot points, which will be used to define the constraints for the FE simulation.

The rib nodes defined above are at the outer surface of the wing section. However, the homogenised shell stiffness is defined at the midplane of the GATOR panel. Hence, the rib nodes are offset by half the panel thickness in the direction of the inward pointing unit normal vector, as shown in Equation 27.

$$P_{ij}^{midplane} = P_{ij}^{surface} + \frac{t_p}{2} \hat{n}_{ij} \quad \text{where } P_{ij} = [X \quad Y \quad Z]^T \quad \text{Equation 27}$$

The variable t_p represents the thickness of the panel, \hat{n}_{ij} represents the unit normal vector, and the indices i and j refer to the grid location of the node in spanwise and chordwise directions. The normal direction is derived by rotating the tangential direction of the aerofoil equation by 90 degrees, while the derivative of the aerofoil equation gives the tangential direction. The offset nodes are used to create the surface representing the midplane of the fairing panel in GMSH. The fairing surface is discretised using a structured mesh with first-order quadrilateral elements (i.e., ‘S4R’ elements) with an average mesh size of 20 millimetres.

The linear elastic constitutive properties of the shell surface are defined using the equivalent shell stiffness matrix from the homogenisation process. Abaqus further estimates a transverse shear stiffness matrix if it is not explicitly defined, as the shell element used (i.e., ‘S4R’) is formulated based on the Reissner-Mindlin plate. This formulation approaches the Kirchhoff-Love plate formulation as transverse shear stiffness increases. The transverse shear stiffness matrix is estimated using the in-plane stiffness matrix [36], as shown in Equation 28.

$$K_{11} = K_{22} = \frac{1}{6}(A_{11} + A_{22}) + \frac{1}{3}A_{66} \quad \text{and} \quad K_{12} = 0 \quad \text{Equation 28}$$

$$\text{where } \begin{bmatrix} V_{13} \\ V_{23} \end{bmatrix} = \begin{bmatrix} K_{11} & K_{12} \\ K_{21} & K_{22} \end{bmatrix} \begin{bmatrix} \gamma_{13} \\ \gamma_{23} \end{bmatrix}$$

The variables V_{i3} and γ_{i3} where $i \in [1, 2]$ represent distributed transverse shear force and transverse shear strain, where i is the normal direction of the RVE face. As the panel is stiff in the 2-axis, the

estimated transverse stiffness is also high, thereby reducing the transverse shear deformation and making the shell deformation closer to that of the Kirchhoff-Love plate formulation.

The fairing variables, coordinate systems and the additional nodes used to define the constraints are shown in Figure 39.

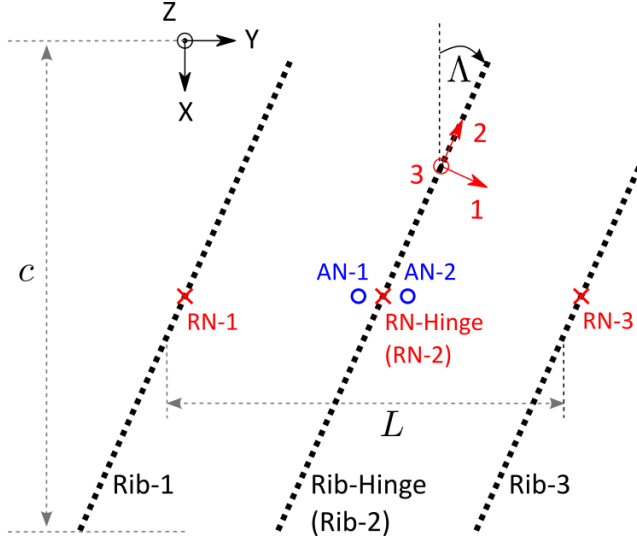


Figure 39. Schematic of the fairing variables, coordinate systems and additional nodes for constraints and loading. Nodes 'AN-1' and 'AN-2' are co-located with the point 'RN-2' (shown slightly separated for clarity). XYZ-axes is the global coordinate system, and 123-axes is the hinge and the material coordinate system.

It shows the 123-axes, which define both the hinge orientation and the orientation of the shell stiffness properties. A cylindrical coordinate system with the same directions shown in 123-axes (i.e., 1-axis being longitudinal and 2-axis being circumferential direction) is projected to the fairing surface to define material orientation on each element. The panel's stiff axis is aligned with the hinge axis, enabling the panel's flexible direction to undertake the greatest proportion of deformation due to folding. Hence, the projected 1-axis represents the morphing direction of the panel, and the 2-axis represents the stiff direction.

Additional nodes 'AN-1' and 'AN-2', shown in Figure 39, are introduced to define the constraints required to model the folding wingtip. These nodes are co-located with the hinge, which is represented by the pivot point of the central rib. This pivot point of the central rib is shown as 'RN-Hinge' in Figure 39. The fairing model can be reduced to a half model for wing sections symmetric across the central rib. The wing section is symmetric across the central rib for untapered and unswept wings with zero flare angle. The constraints applied to the ribs differ based on whether the model is a full model or a half model. Hence, these constraints are listed in Table 9.

Table 9. Constraints applied to fairing ribs.

Full Model

- The nodes of the inboard and outboard ribs are rigidly connected to ‘AN-1’ and ‘AN-2’, respectively.
 - The nodes of the central rib are rigidly connected to ‘RN-Hinge’.
 - The nodes of the floating ribs are rigidly connected to their respective pivot point.
-

Half Model

- The nodes of the inboard rib are rigidly connected to ‘AN-1’.
 - The nodes of the central rib are rigidly connected to ‘AN-2’.
 - The nodes of the floating ribs are rigidly connected to their respective pivot point.
-

The rest of the constraints are applied to pivot points and the additional nodes to restrict the motion of the ribs. Firstly, the fixture of the inboard rib is enforced by fixing the node ‘AN1’. Next, the co-location of ‘AN-2’ and ‘RN-Hinge’ with ‘AN-1’ is enforced by constraining the translation of ‘AN-2’ and ‘RN-Hinge’ to that of ‘AN-1’. Similarly, the hinge connection of the wingtip and the central rib is enforced by constraining the rotation of ‘AN-2’ and ‘RN-Hinge’ to the hinge axis, shown as the 2-axis in Figure 39. These two constraints are applied in Abaqus using the ‘Join, Revolute’ connector sections.

The fairing is loaded with an initial pre-tension step followed by a folding step. Pre-tension is applied to the fairing in the direction perpendicular to the hinge using artificial thermal loads. A pre-strain load vector \mathbf{F} , representing the distributed load generated on a constrained plate due to unit temperature change (ΔT), is defined with the constitutive properties of the shell section. The applied temperature change in this case is -1, and the resulting thermal load ($\mathbf{N}_{thermal}$) is applied to the shell elements, as shown in Equation 29.

$$\mathbf{N} = \mathbf{K}_{plate} \boldsymbol{\varepsilon} - \mathbf{N}_{thermal} \quad \text{Equation 29}$$

where

$$\begin{aligned} \mathbf{N}_{thermal} &= \Delta T \mathbf{F}, \\ \mathbf{F} &= \mathbf{K}_{plate} [\varepsilon_p \ 0 \ 0 \ 0 \ 0 \ 0]^T \end{aligned}$$

The wingtip folding deformation is applied as rotation to the node ‘AN-2’. Note that the nodes ‘RN-Hinge’ and ‘AN-2’ are constrained to rotate only about the hinge axis. As a result of this constraint, a rotation of the node ‘AN-2’ defined around the global X-axis will also result in a rotation around the global Y-axis to ensure the overall rotation of the node is always around the hinge axis. Hence, for simplicity, rotation is applied to the FE model as an X-axis rotation on ‘AN-2’, and the resulting reaction moment is also measured around the X-axis. This rotation and moment around the global X-axis are resolved to rotation and moment around the hinge axis using Equation 30 and Equation 31.

$$\theta = \frac{\theta_x}{\cos \Lambda} \quad \text{Equation 30}$$

$$M = \frac{M_x}{\cos \Lambda} \quad \text{Equation 31}$$

Note that the applied rotation angle is different for the full and half model of the fairing. In the full model, folding rotation (θ) is applied to the outboard rib through the node ‘AN-2’, effectively rotating

the entire section outboard of the hinge (i.e., the wingtip). In a symmetric wing section, the consequent rotation of the central rib is always half of the folding angle of the wingtip. Hence, in a half model, half the folding angle of the wingtip is applied to the central pivoting rib, again through the node 'AN2', to achieve equivalent fairing deformation. This rotation applied to the central rib of the half model is hereafter referred to as the rotation angle $\left(\frac{\theta}{2}\right)$.

For instance, consider a full model simulation of the baseline fairing at an 80-degree folding angle of the wingtip, shown in Figure 40.

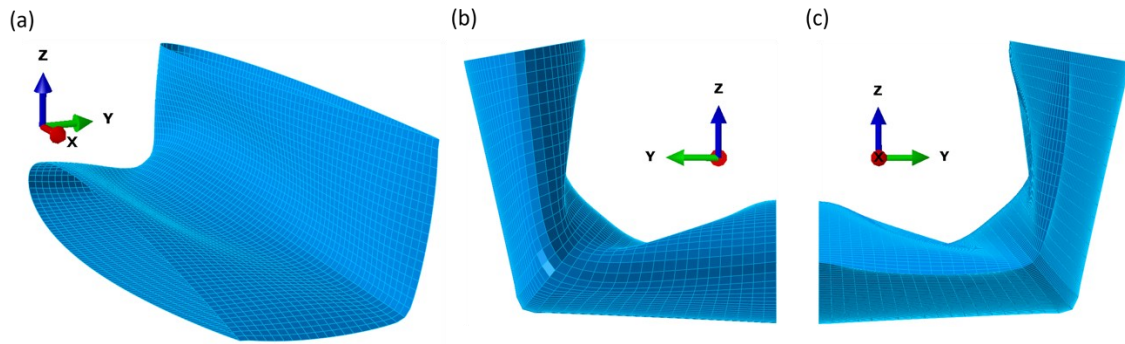


Figure 40. Deformed shape of the fairing full model at 80-degree rotation of the wingtip. (a) shows the 3-dimensional view, (b) the leading-edge view, and (c) the trailing-edge view of the fairing.

The deformation at the inboard region up to the central rib is identical to that of a half model with a 40-degree rotation angle applied to the central pivoting rib. However, the half model would produce half the reaction moment compared to the full model. Hence, the reaction moment from the half model should be doubled before comparing it to that of the full model. All the fairing configurations analysed in this study are symmetric about the central pivoting rib. Hence, they are analysed using the half model, thereby significantly reducing the FE simulation time.

3.1.2. Design Metrics for Quantifying Fairing Mechanical Performance

The study aims to identify the geometric features which improve the objectives of reducing the torsional stiffness of the joint and cross-section distortion of the fairing. Hence, these objectives must be quantified to compare the effect of various design variables on them. The reaction torque on the joint at a prescribed rotation angle is used to represent torsional stiffness, and it is evaluated from the FE results using the expression in Equation 31. In contrast, the distortion of the fairing is visually noticeable, as shown by the deformed baseline fairing in Figure 6. However, they are difficult to quantify as there is no a priori known desired shape to calculate the difference between a deformed shape and a desired shape in the simulation. Instead, three different metrics are studied to quantify the cross-section distortion. These metrics are based on three physically meaningful quantities integrated over the fairing surface, namely energy, curvature, and displacement, as defined in Equation 32 to Equation 34.

$$\text{Energy Metric} = \frac{\Delta J_{in-plane}}{\Delta J_{out-of-plane}} = \frac{\Delta \left(\frac{1}{2} \sum_e A (\mathbf{N} \cdot \boldsymbol{\varepsilon}) \right)}{\Delta \left(\frac{1}{2} \sum_e A (\mathbf{M} \cdot \boldsymbol{\kappa} + \mathbf{V} \cdot \boldsymbol{\gamma}) \right)}$$
Equation 32

$$\text{Curvature Metric} = \sqrt[2]{\frac{\sum_e A (\kappa_1^2 + \kappa_2^2)}{\sum_e A}} = \sqrt[2]{\frac{\sum_e A (\kappa_{11}^2 + \kappa_{22}^2 + \frac{1}{2} \kappa_{12}^2)}{\sum_e A}}$$
Equation 33

$$\text{Displacement Metric} = \frac{1}{n_b} \sum_i^{n_b} u_{3i} - \frac{1}{n_t} \sum_j^{n_t} u_{3j}$$
Equation 34

Equation 32 shows the energy metric, representing the ratio of incremental change in the strain energy due to in-plane and out-of-plane deformations. The summation is over all shell elements, and the variable A represent element area. The variables \mathbf{N} , \mathbf{M} and \mathbf{V} are the vectors of distributed in-plane forces, out-of-plane moments and transverse shear forces of shell elements, respectively. The variables $\boldsymbol{\varepsilon}$, $\boldsymbol{\kappa}$ and $\boldsymbol{\gamma}$ are the vectors of in-plane strains, out-of-plane curvatures and transverse shear strains of shell elements, respectively. The equation shows that the out-of-plane deformation energy includes bending and transverse shear deformation energies. However, the transverse shear deformation energy contributes less than 5% of the total out-of-plane deformation energy in all the cases considered in this section. Hence, the transverse shear deformation has a negligibly small effect on the energy metric.

Equation 33 shows the curvature metric, representing an area-weighted root mean square (RMS) of principal curvatures of the shell surface. The principle curvatures are annotated as κ_1 and κ_2 . However, for simplicity, the equivalent expression of engineering curvatures κ_{11} , κ_{22} and κ_{12} of the shell element are used to evaluate the metric.

Equation 34 shows the displacement metric, representing the difference in the average vertical displacement of the nodes on the bottom and top surfaces of the fairing. For the half model used in the analysis, this metric represents the average reduction in the thickness of the wing section. In this case, the summations are over the vertical displacement of the nodes in the bottom and top surface. The variable n_b and n_t represent the number of nodes in the bottom and top surface, respectively.

In order to have an initial understanding of the response of the fairing and the usefulness of the performance metrics, the effects of increasing the number of floating ribs on three different magnitudes of fairing rotation are studied, as shown in Figure 41.

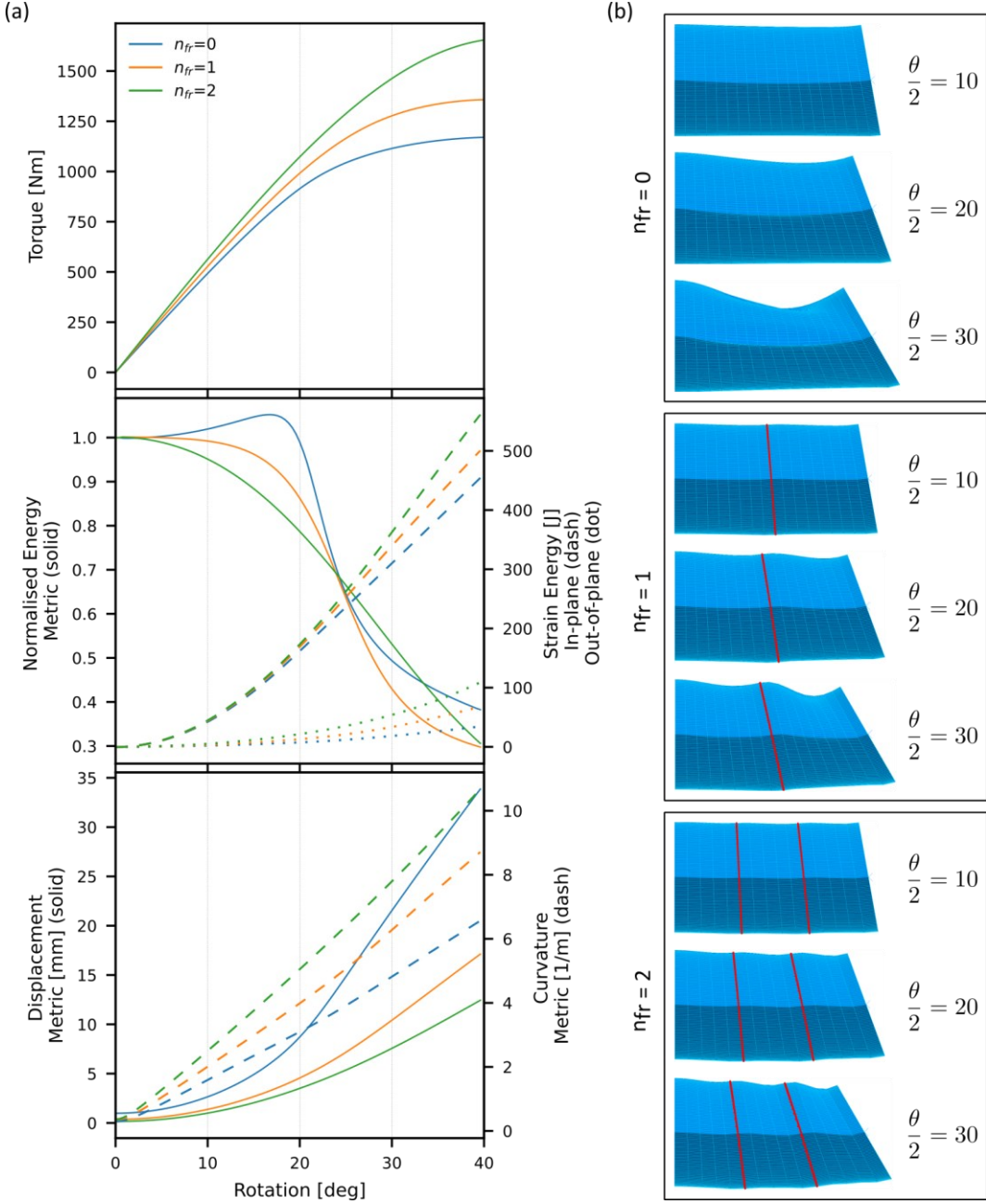


Figure 41. Various metrics used to quantify the objectives for cases with varying numbers of floating ribs (n_{fr}). (a) shows the response of the metric for a half model. (b) shows snapshots of deformed shapes from the rear of the wing at various rotation angles.

It shows the folding response of the fairing for different metrics alongside snapshots of the deformed shape at various rotation angles. Note that the results presented are for a half model; hence, the 40-degree rotation angle of the pivoted rib is equivalent to an 80-degree folding angle of the wingtip. The number of floating ribs (n_{fr}) is changed between the cases, leading to a different unsupported panel length between the ribs. Adding floating ribs (n_{fr}) reduces the cross-section distortion of the fairing but at the cost of increased torsional stiffness of the joint. The top graph in Figure 41a shows the increase in torque with the number of floating ribs (n_{fr}). The middle and bottom graphs show the effect of the number of floating ribs (n_{fr}) on the metrics considered to quantify the cross-section distortion of the fairing.

The middle graph in Figure 41a shows the energy metric normalised by its initial value for each case. It shows a steep drop in the metric as the fairing undergoes large out-of-plane deformation due to buckling of the top skin between 20 to 30 degrees of rotation. This sharp drop in the metric aligns with the softening of the torque gradient in the top graph of Figure 41a, indicating a drop in stiffness. It further aligns with the significant increase in cross-section distortion shown between the same rotation angles in Figure 41b. Hence, the normalised energy metric is useful in indicating the rotation angle beyond which the cross-section gets distorted significantly due to the buckling of the top skin.

The in-plane and out-of-plane components of strain energy increase with the number of floating ribs, as shown in the middle graph of Figure 41a. In contrast, Figure 41b shows reduced cross-section distortion with more floating ribs (n_{fr}). The increase in out-of-plane strain energy is due to the increase in the number of rib bays, each with a similar deformation mode shape to that of the fairing with no floating ribs (n_{fr}). Hence, the “wavelength” of the out-of-plane deformation decreases with the floating ribs (n_{fr}), leading to increased curvature, as shown by the curvature metric in the bottom graph in Figure 41a. The curvature increase on the fairing increases the out-of-plane strain energy for the fairing with more floating ribs (n_{fr}), despite it reducing the distortion of the fairing. The reduced out-of-plane displacement with more floating ribs (n_{fr}), as shown in Figure 41b, further results in greater in-plane displacement (e.g., more compression on top surface), thereby increasing the in-plane strain energy.

The curvature metric is useful for comparing the effects of design variables on the fairing objectives for cases with a constant number of floating ribs. Authors previously used a curvature-based metric to compare the effects of sandwich panels with positive, negative and zero Poisson’s ratio core on the fairing objectives [164]. The displacement metric shown in the bottom graph of Figure 41a further compares the effects of floating ribs on the fairing distortion. The figure shows that the displacement metric decreases with more floating ribs (n_{fr}), which is consistent with the deformed shapes shown in Figure 41b. Moreover, similar to the normalised energy metric, the displacement metric shows a change in the gradient where the out-of-plane displacement of the fairing rapidly increases due to the buckling of the top skin. This change gradient in the displacement metric aligns with the softening of the torque gradient, indicating a drop in stiffness.

Each metric provides some insights into the effects of the design variable on the fairing objectives. The normalised energy metric indicates the rotation angle at which the top skin buckles, and the curvature metric indicates the out-of-plane deformation as the wingtip folds. However, in the case of varying numbers of floating ribs, their trends are inconsistent with the visually observed distortion of the fairing shape. In contrast, the displacement metric indicates out-of-plane deformation as the wingtip folds and the rotation angle at which the top skin buckles. Its trends are consistent with the visually observed distortion of the deformed fairing shape. Hence, the displacement metric offers a robust measure that better represents the distortion of the cross-section shape for this parametric study.

In the rest of the study, the reaction torque is used to measure torsional stiffness and the displacement metric is used to measure fairing distortion as the wingtip folds. These metrics are used

in the following section to study the sensitivity of the objectives to each design variable and the trends of the objectives with the design variables that strongly affect them.

3.2. Results and Discussion

Two types of analyses are carried out using the models presented above. First, a sensitivity study of the fairing objectives is presented for each design variable. This study enables the variables that strongly affect the objectives to be selected for more detailed parametric studies, thereby reducing the design space. In the parametric study, a pair of variables strongly affecting at least one of the objectives are studied to identify the trends and the ranges of design variable values that reduce trade-offs between the objectives. The parametric study focuses on the panel layer thicknesses, chevron geometry and the fairing variables. Moreover, considering the buckling of the top skin between 20 to 30 degrees of rotation, as shown in Figure 41, the results presented for the parametric study use the torque and distortion metric values from 20-degree rotation.

3.2.1. Sensitivity Study

In the parametric study, each design variable is swept through a set of values uniformly distributed between the limits shown in Table 6 and Table 8 for fairing and panel variables. Ten sample points are used for each panel variable, while five are used for each fairing variable (except for the number of floating ribs, which has 3 discrete values). The sensitivity of each objective to the variation in each design variable is evaluated by calculating the range of variation in the objective value as a percentage of its value in the baseline configuration. The expression for sensitivity value is shown in Equation 35, where the objective value is shown as O_i with i referring to minimum, maximum or default value.

$$\text{Sensitivity} = \frac{O_{\max} - O_{\min}}{O_{\text{default}}} \quad \text{Equation 35}$$

The evaluated sensitivity of the metrics to changes in each design variable is shown in Figure 42.

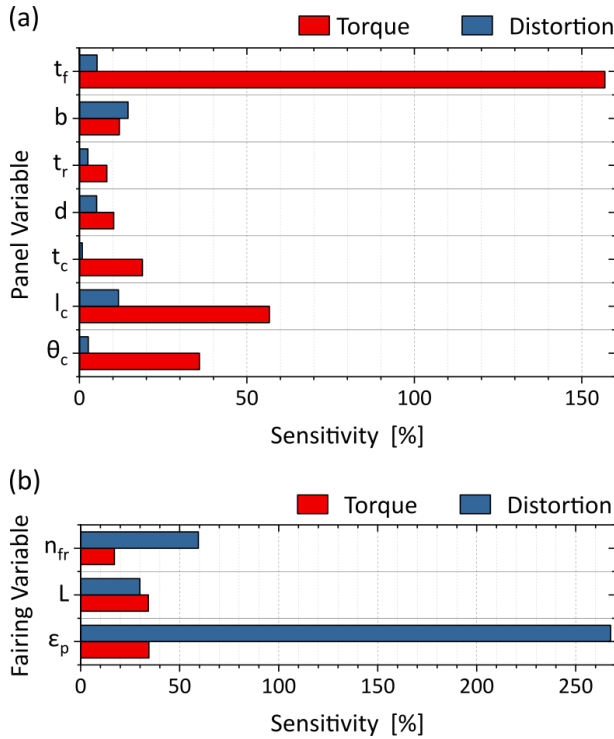


Figure 42. Sensitivity of the objectives to changes in each variable. Torque and distortion are for the 20-degree rotation of the half model.

Figure 42 shows that all the panel variables significantly influence torque (> 5%), with facesheet thickness (t_f) having the predominant effect, followed by the chevron dimensions. Chevron length (l_c) has the dominant influence from the chevron dimensions, followed by the chevron angle (θ_c) and thickness (t_c). For all the panel variables except the core thickness (b), their effect on the distortion metric is much smaller than their effect on torque. The core thickness (b) and the chevron length (l_c) significantly influences the distortion metric, with the influence of the other variables being relatively small ($\leq 5\%$). In contrast, all the fairing variables show a strong influence on both objectives, with the number of floating ribs (n_{fr}) and the pre-strain across the hinge (ϵ_p) having the dominant effect on the distortion metric, followed by the fairing span (L). The observations from the sensitivity study enable the reduction of the design space by eliminating the variables that do not significantly influence the objectives. The following parametric study of the influential variables shows the trends of the objectives and useful ranges of the variable values that improve the objectives.

3.2.2. Panel Layer Thicknesses

In the parametric study, a variable that strongly influences an objective is paired with another variable that strongly influences the other objectives to explore the feasibility of decoupling the objectives and reducing their trade-off. The core thickness (b) strongly influences the distortion metric, with a smaller effect on the torque. In contrast, the facesheet thickness (t_f) strongly influences torque with negligible effect on distortion. Hence, the core thickness (b) paired with the facesheet thickness (t_f) offers a relatively decoupled design space to improve both objectives.

The torque and distortion responses for various core thickness (b) and facesheet thickness (t_f) values are shown in Figure 43a.

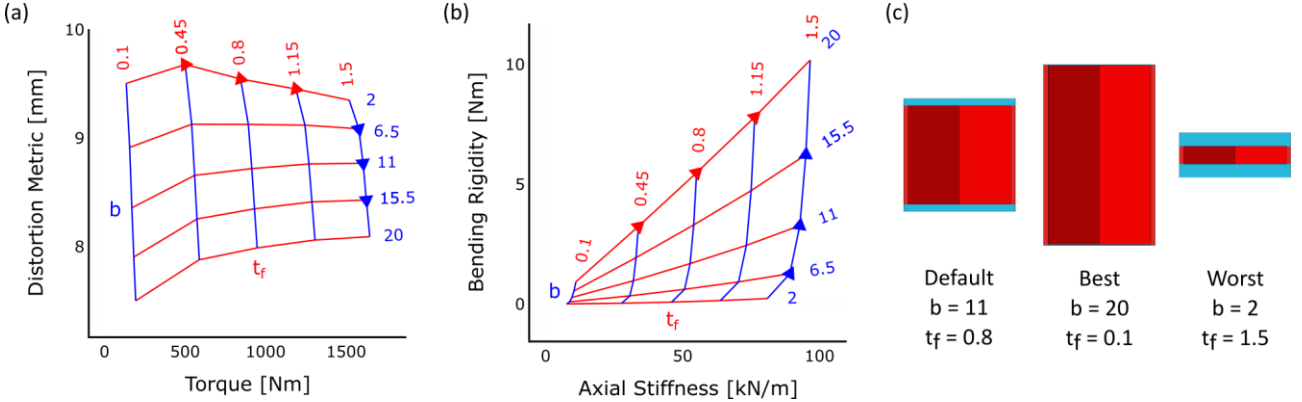


Figure 43. Parametric study of core thickness (b) and facesheet thickness (t_f). (a) shows the torque and distortion response for a 20-degree rotation of the pivoted rib. (b) shows the equivalent axial stiffness and bending rigidity in the morphing direction. (c) shows the geometry of the notable cases (13-plane view).

For comparisons between the cases, the torque and distortion values are shown for a rotation angle of 20 degrees before the onset of top skin buckling. The blue lines show steep reductions in distortion with relatively modest increases in torque for increasing core thickness (b). The red lines show large increases in torque with relatively small increases in distortion for increasing facesheet thickness (t_f). These effects on the fairing objectives are related to the changes in the panel's axial stiffness and bending rigidity in the morphing direction (i.e., 1-axis). The panel's axial stiffness and bending rigidity for a nominal 1×1 metre flat panel are shown in Equation 36 and Equation 37, respectively.

$$\text{Axial Stiffness} = t_p E_1 \quad \text{Equation 36}$$

$$\text{Bending Rigidity} = \frac{t_p^3 E_1^D}{12} \quad \text{Equation 37}$$

The variable t_p is the panel thickness, E_1 is the equivalent modulus from the in-plane stiffness matrix (i.e., \mathbf{A} -matrix), and E_1^D is the equivalent modulus from the out-of-plane stiffness matrix (i.e., \mathbf{D} -matrix).

Figure 43b shows the axial stiffness and bending rigidity in the morphing direction for various core (b) and facesheet thicknesses (t_f). The blue lines show large increases in bending rigidity with increasing core thickness (b), which consequently reduces the fairing distortion. The red lines show large increases in the axial stiffness with increasing facesheet thickness (t_f), which increases torque. The red lines further indicate that increasing facesheet thickness (t_f) only increases in-plane stiffness for panels with thin cores, while it increases both in-plane stiffness and bending rigidity for panels with thick cores. In panels with thick cores, the facesheets are further away from the midplane; hence, any increase in facesheet thickness (t_f) significantly increases bending rigidity. However, increasing facesheet thickness in panels with thick cores does not reduce distortion, as shown in Figure 43a, despite increasing bending rigidity. Instead, increasing facesheet thickness (t_f) shows a slight increase

in distortion for all core thicknesses (*b*) due to the simultaneous increase in the axial stiffness. Increasing axial stiffness favours bending deformation of the top skin over large compressive deformations, thereby increasing the distortion. Hence, the best solution for the fairing objectives is a GATOR panel with a thick core and thin facesheets, which improves bending rigidity and axial flexibility, respectively. In contrast, the worst combination is having a thin core and thick facesheets. Figure 43c shows the 13-plane view of these panel geometries.

3.2.3. Chevron Geometry

The deformation of the sandwich panel is complex due to the interaction of the facesheets and the chevrons. However, the trends in the stiffness properties due to the changes in the chevron geometry can be explained using the mechanics of the chevron deformation. Consider the axial and bending deformation of the core in the 1-axis shown in Figure 44.

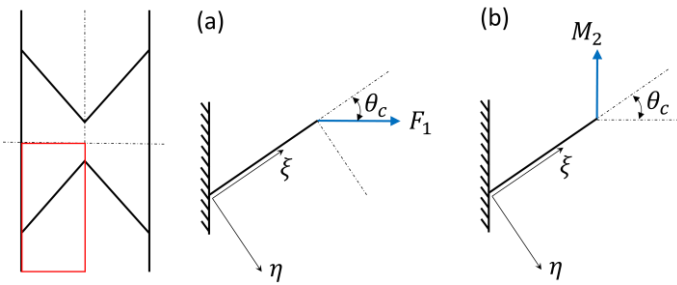


Figure 44. Loading diagram for analytical expressions.

The corresponding analytical expressions for axial [148] and bending [147] displacements of the chevron walls are shown in Equation 38 and Equation 39, where k and q are shear (typically $k = 2.4 + 1.5\nu$) [178] and torsional [169] coefficients respectively, and K and I are polar and area moments of inertia.

$$\delta_1 = \frac{F_1 l_c}{Ebt_c} \left[\left(\frac{l_c}{t_c} \right)^2 \sin^2 \theta_c + k \sin^2 \theta_c + \cos^2 \theta_c \right] \quad \text{Equation 38}$$

$$\theta_2 = M_2 l_c \left[\frac{q}{KG} \sin^2 \theta_c + \frac{1}{EI} \cos^2 \theta_c \right] \quad \text{Equation 39}$$

The terms in the square bracket in Equation 38 correspond to the chevron's bending, transverse shear and axial deformation, respectively. The $\sin^2 \theta_c$ values increase with increasing chevron angle (θ_c) while the $\cos^2 \theta_c$ values decrease. Hence, the chevron's bending and transverse shear displacements increase while its axial displacement decreases with larger chevron angles (θ_c). The expression further indicates that the bending displacement increases significantly with the slenderness (length-to-thickness ratio) of the chevrons. The increasing bending displacement reduces the relative contribution of the chevron's transverse shear deformation to panel displacement, hence reducing the chevron's transverse shear stiffness contribution to the equivalent axial stiffness of the panel. Furthermore, the terms in the square bracket in Equation 39 correspond to the chevron's torsional and transverse bending deformation, respectively. The expression indicates that the chevron's rotation due to torsion increases while its rotation due to transverse bending decreases with larger

chevron angles (θ_c). The torsional coefficient (q) decreases from unity with the increasing height-to-length ratio of the wall [147, 168, 170], thereby reducing the torsional stiffness for longer chevrons. These analytical trends are used in the following discussion to contextualise the effects of the chevron geometry on the FE-generated stiffness properties shown in Figure 45 and Figure 46.

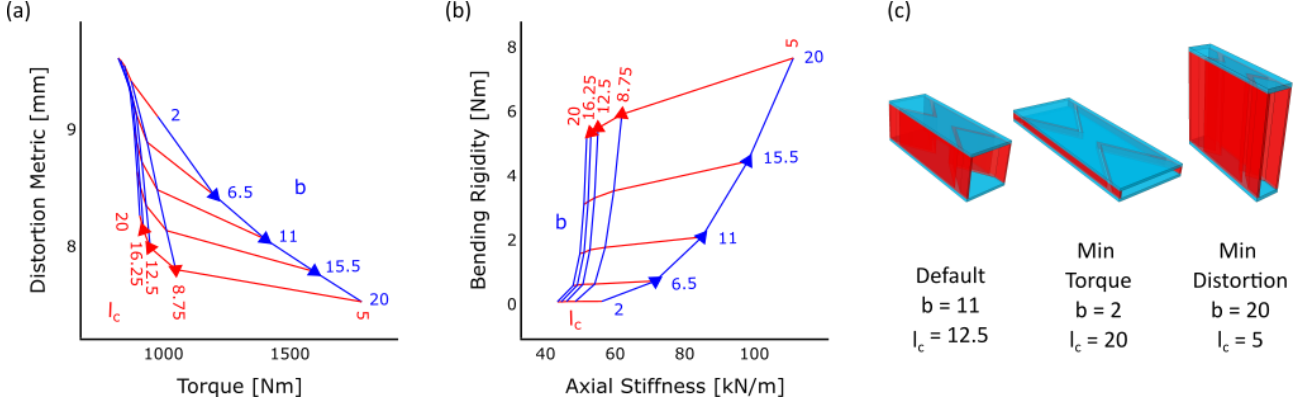


Figure 45. Parametric study of core thickness (b) and chevron length (l_c). (a) shows the torque and distortion response for a 20-degree rotation of the pivoted rib. (b) shows the equivalent in-plane stiffness and bending rigidity in the morphing direction. (c) shows the geometry of the notable cases.

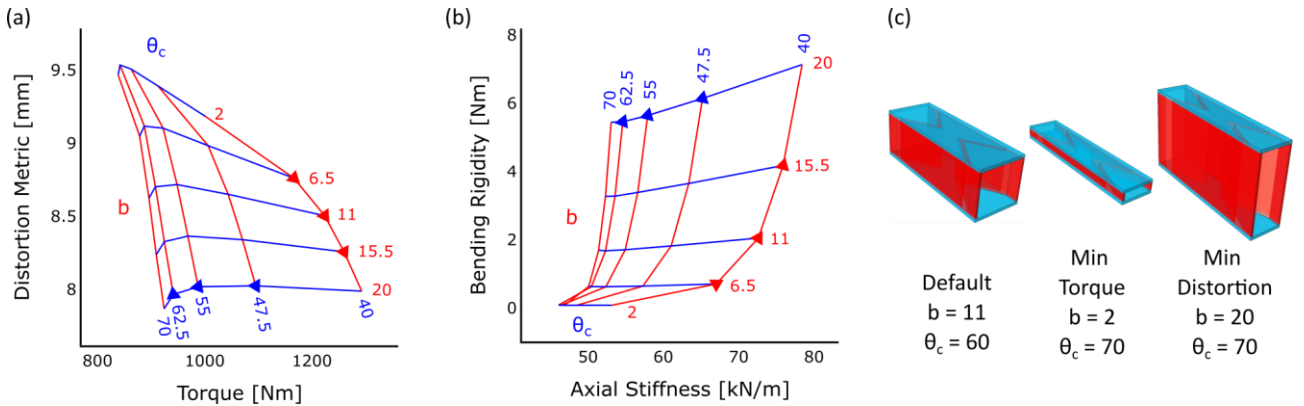


Figure 46. Parametric study of core thickness (b) and chevron angle (θ_c). (a) shows the torque and distortion response for a 20-degree rotation of the pivoted rib. (b) shows the equivalent in-plane stiffness and bending rigidity in the morphing direction. (c) shows the geometry of the notable cases.

The red lines in Figure 45a show a large decrease in torque for the initial increase in the chevron length (l_c), followed by smaller reductions for subsequent increases. The large initial decrease in torque is attributed to the large initial drop in the panel's axial stiffness, as shown in Figure 45b, due to the reduced stiffness contribution from the chevron's transverse shear stiffness. Once the chevron's transverse shear stiffness contribution is negligible, typically for a slenderness ratio greater than 15, the incremental reductions in the panel's axial stiffness with increasing chevron length (l_c) becomes very small. Consequently, a further increase in chevron length (l_c) provides only a smaller reduction in torque for panels with long chevrons. Moreover, the red lines in Figure 45a indicate that distortion of the fairing increases with longer chevrons (l_c). This increase in distortion is due decreasing bending rigidity of the panel, as shown by the red lines in Figure 45b, particularly for thicker cores. This trend is attributed to the reduction in the chevron's torsional stiffness due to the decreasing height-to-length ratio of the chevron wall.

The blue lines in Figure 45a further show that while the effect of increasing core thickness (b) is predominantly on distortion, for short chevrons, it also increases torque. This increase in torque is due to increasing axial stiffness from thicker cores when combined with short chevrons, as shown by the rightmost blue line in Figure 45b. Short chevrons undergo a larger proportion of transverse shear deformation relative to longer chevrons when the panel is deformed axially in the morphing direction. Hence, increasing core thickness (b) amplifies the panel's high axial stiffness due to the chevron's transverse shear stiffness by increasing the cross-section area of the chevrons.

The effects of the chevron angle (θ_c) on the stiffness properties of the panel and the fairing objectives are shown in Figure 46. The blue lines show a decreasing incremental reduction in torque and axial stiffness with a uniform increase in chevron angle (θ_c). This trend agrees with Equation 38, which indicates that the chevron's displacement contribution of bending and transverse shear deformation increases while the contribution of the chevron's axial deformation decreases with larger chevron angles (θ_c). Moreover, in Equation 38 the bending and transverse shear contribution is proportional to $\sin^2 \theta_c$ whose gradient decreases from 45 to 90 degrees. This decreasing gradient results in a decreasing step change in axial stiffness with a uniform increase in chevron angle (θ_c), as shown by the blue lines in Figure 46b. The decreasing axial stiffness of the panel with larger chevron angles (θ_c) results in the decreasing torque shown in Figure 46a. Hence, both trends share the pattern of decreasing incremental reductions for uniform increases in chevron angle (θ_c).

The blue lines in Figure 46b show decreasing bending rigidity with larger chevron angles (θ_c), particularly for thick cores. Note that the transverse bending stiffness of the chevron wall is proportional to the cube of the core thickness (b^3) due to the area moment of inertia. Hence, the chevron's transverse bending stiffness is significant for thick cores, and its contribution to the panel's bending rigidity decreases with increasing chevron angle (θ_c), as indicated by Equation 39, resulting in decreasing bending rigidity. While the reducing bending rigidity does not translate to consistent trends in distortion metric in Figure 46a, it shows a consistent drop in distortion metric for high values of chevron angles (θ_c) with no corresponding increase in bending rigidity in Figure 46b. Similar to the facesheet thickness (t_f) in Figure 43, this trend is attributed to the reducing axial stiffness of the panel, which enables greater in-plane compression of the top skin before increasing out-of-plane deformation, thereby resulting in a reduced distortion of the fairing. Hence, the distortion metric is affected not only by the panel's bending rigidity but also by its axial stiffness, as the skin deformation favours the lower energy deformation mode between the in-plane and out-of-plane deformation.

3.2.4. Fairing Geometry Variables

The variables defining the overall fairing geometry strongly affect both fairing objectives, as indicated by the sensitivity in Figure 42. The effects of floating ribs (n_{fr}) and the fairing span (L) are shown in Figure 47.

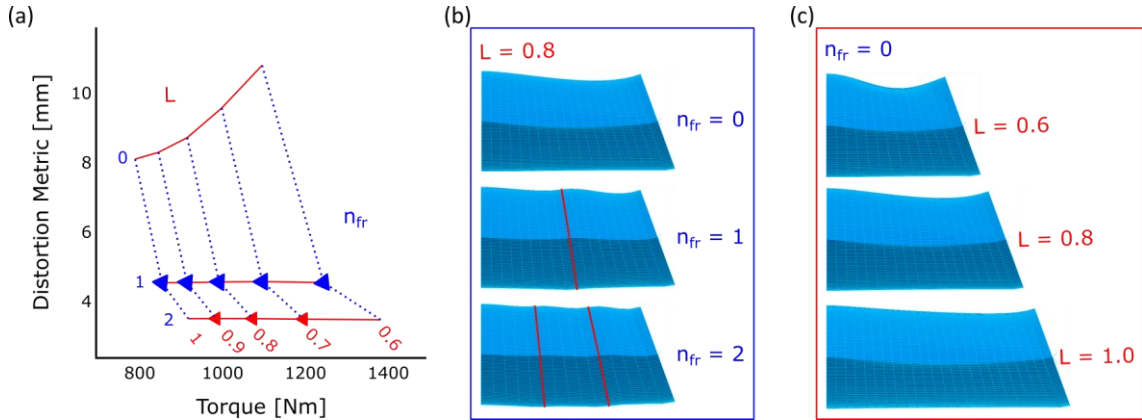


Figure 47. Parametric study of fairing span (L) and floating ribs (n_{fr}). (a) shows the torque and distortion response for a 20-degree rotation of the pivoted rib. (b) and (c) show the corresponding deformed shape from the rear view of the fairing.

The blue dotted lines show that adding the first floating rib reduces the distortion significantly, with a smaller subsequent reduction with additional floating ribs (n_{fr}). Floating ribs (n_{fr}) reduce the unsupported length of the skin between the ribs, as shown in Figure 47b, resulting in reduced out-of-plane deformation of the panel. Floating ribs further maintain the cross-section thickness at their locations, thereby constraining the fairing deformation. This constrained fairing deformation adds stiffness to the fairing, increasing the torque with increasing floating ribs (n_{fr}). The red lines indicate that the increase in torque due to the floating ribs (n_{fr}) can be offset by increasing the span (L) of the fairing. A longer fairing section reduces the overall axial strain (i.e., 1-axis strain) by distributing the displacement over a longer length, thereby reducing the axial stiffness of the skin and, therefore, the resulting torque. This reduction in axial strain delays out-of-plane deformation of the top skin, thereby significantly reducing distortion for the fairing without a floating rib, as shown in Figure 47c. However, in the fairings with floating ribs, the out-of-plane deformation of the fairing is already reduced by the floating ribs; hence, Figure 47a shows that further reduction in distortion due to the span (L) increase is negligibly small. Therefore, a long span (L) with few floating ribs (n_{fr}) is desired to achieve a balanced solution for both objectives.

Pre-strain (ε_p) on the fairing in the direction perpendicular to the hinge (i.e., 1-axis) delays the onset of compressive strains on the top skin as the wingtip folds. Large compressive stress on the top skin may trigger panel buckling, which distorts the cross-section shape due to large out-of-plane deformation. Figure 48 shows the effects of pre-strain (ε_p) on the torque and distortion response of the fairing.

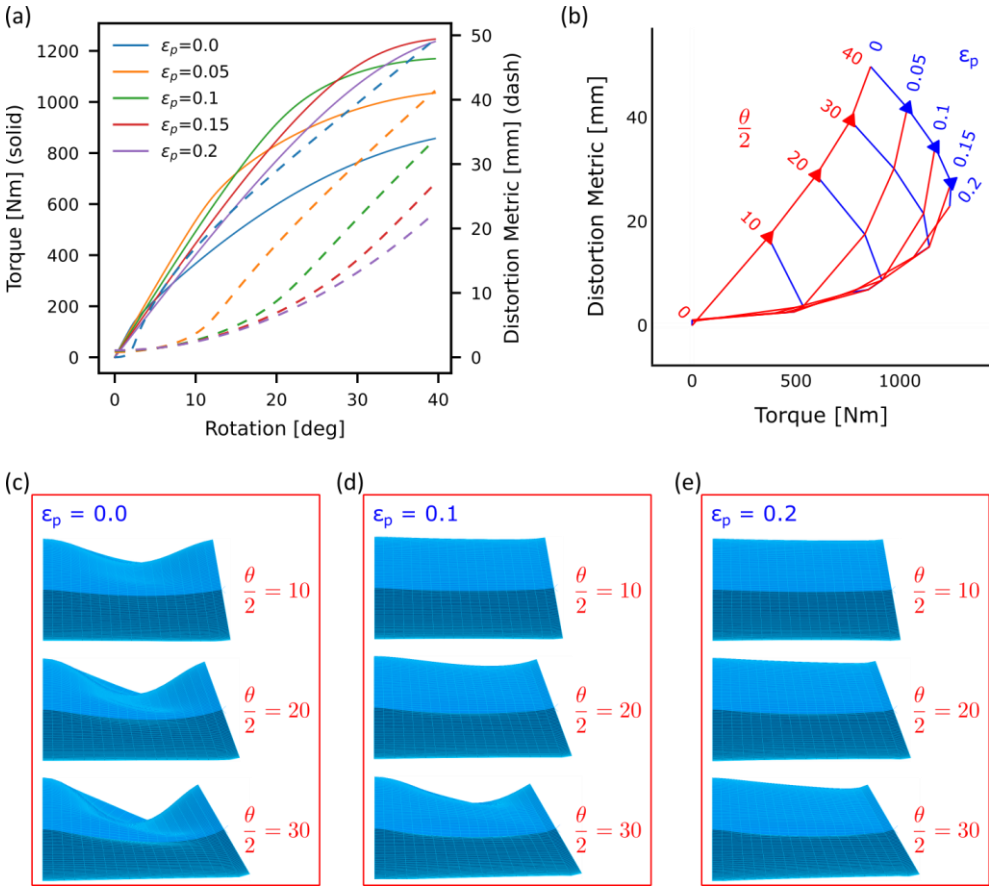


Figure 48. Parametric study of pre-strain (ϵ_p). (a) shows the torque and distortion response for a 20-degree rotation of the pivoted rib. (b) shows the deviation of the fairing response at various rotation angles for different pre-strains. (c) to (e) show the deformed shapes from the rear view of the fairing.

Figure 48a shows that in a fairing with no pre-strain, the top skin undergoes compression from the start of folding, leading to the early buckling of the top skin, indicated by the jump in the distortion metric. Buckling of the top skin reduces the torsional stiffness but at the cost of a severely distorted cross-section, as shown in Figure 48c. The applied pre-strain (ϵ_p) delays the onset of buckling as a pre-tensioned top skin can withstand greater compression before encountering compressive strain. This delay in buckling extends the linearity in the fairing deformation, as shown in Figure 48a. It also shows that pre-strain (ϵ_p) reduces the torsional stiffness in the linear response of the fairing. This trend agrees with the 2-dimensional analytical results presented by the authors in a previous study on the effects of pre-tensioned skin over a hinged wingtip with multiple pivoted rib supports [145]. Furthermore, buckling of the top skin qualitatively changes the torque and distortion metric response, as indicated by Figure 48b. It shows that the 0% pre-strain (ϵ_p) case deviates from the general trend at the beginning, followed by the 5% pre-strain (ϵ_p) case after 10 degrees of rotation and the 10% pre-strain (ϵ_p) case after 20 degrees. Hence, in the following parametric studies, which include changing the pre-strain, the trends in the objectives are studied considering the region before and after buckling of the top skin.

Figure 49 shows the effects of varying the fairing span (L) and the number of floating ribs (n_{fr}) with various pre-strain (ε_p) across the hinge.

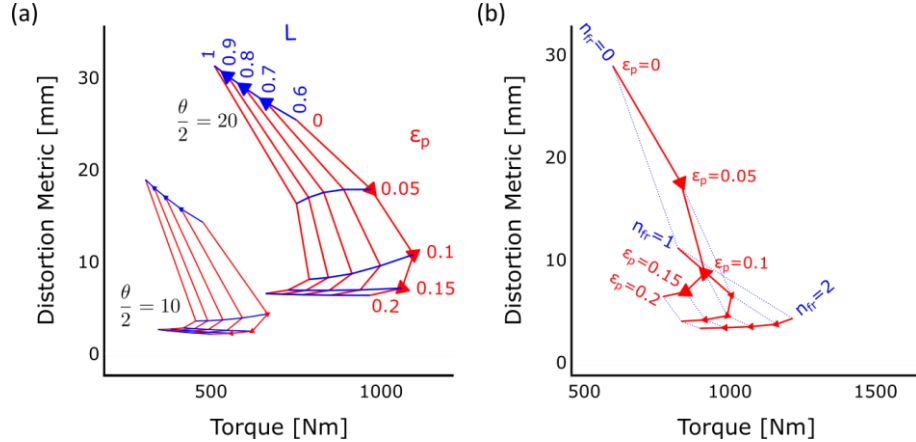


Figure 49. Parametric study of pairs of fairing variables showing the torque and distortion response. (a) shows the effects of varying pre-strain (ε_p) and fairing span (L) for 10 and 20-degree rotation of pivoted rib. (b) shows the effects of varying pre-strain (ε_p) and the number of floating ribs (n_{fr}) for 20-degree rotation of pivoted rib.

The effects of varying pre-strain (ε_p) and span (L) on torque and distortion are shown in Figure 49a. The red lines show decreasing torque and distortion for increasing pre-strain (ε_p) above 5% for the 10-degree rotation angle. In contrast, for the 20-degree rotation angle, this trend is observed for pre-strain (ε_p) above 10% due to the buckling of the top skin in the 5% pre-strain (ε_p) cases before the 20-degree rotation. In the post-buckling results shown for 20-degree rotation for pre-strains (ε_p) below 10%, increasing pre-strain (ε_p) increases the torque while reducing distortion. Moreover, the blue lines show decreasing torque with increasing span (L) for all cases. It also shows a subtle reduction in distortion with longer spans (L) for all pre-strained cases. In contrast, the distortion metric increases with the span (L) for cases without pre-strain. Hence, these results indicate the benefits of increasing pre-strain (ε_p) and span (L) to reduce both torque and distortion of the fairing.

The effects of pre-strain (ε_p) on fairings with various numbers of floating ribs (n_{fr}) are shown for a 20-degree rotation in Figure 49b. The blue dotted lines show reducing distortion and increasing torque with increasing floating ribs (n_{fr}). The red lines change direction for the cases with zero and one floating rib, indicating the onset of buckling before 20-degree rotation for cases with less than 10% and 5% pre-strain, respectively. The other red line (i.e., for two floating ribs case) shows that the buckling of the top skin can be avoided by constraining the fairing deformation with more floating ribs (n_{fr}), thereby giving a consistently low distortion for these cases. It also shows that increasing torque due to more floating ribs (n_{fr}) can be offset using pre-strain, similar to the effects of increasing the span (L) shown in Figure 47. Therefore, the combined effects of these fairing variables can improve both objectives while minimising their trade-offs.

3.2.5. Key Insights

The sensitivity study identified the design variables that significantly influence the fairing objectives of reducing torque and cross-section distortion. Hence, the subsequent parametric study focused on these design variables, thereby significantly reducing the design space. For instance, consider pairing each panel variable with every other panel variable to produce carpet plots similar to the one presented in the parametric study. This approach would produce 21 different pairs of panel variables, each with, realistically, a minimum of 5×5 sample points (i.e., 225 simulations). In contrast, by considering the design variables that strongly affect at least one fairing objective and pairing each of these variables with variables that strongly affect the other objective, the parametric study of the panel variable was reduced to 4 different pairs (i.e., 100 simulations). Additionally, the sensitivity study used 10 sample points of each of the 7 panel variables (i.e., 70 simulations). Hence, this approach reduced the number of simulations required for the study by 68% relative to studying every possible pair.

The parametric study of the panel layer thicknesses indicated that the GATOR sandwich panels with thick cores and thin facesheets increase bending rigidity without a notable penalty to the axial flexibility in the morphing direction, agreeing with the previous analytical [135], FEM [138] and experimental [133] studies. The novelty of this study is in determining the relationship between panel design variables and the behaviour of the folding wingtip fairing through their effects on the panel's axial stiffness and bending rigidity. A systematic study of the 3-dimensional fairing in a reduced design space was presented in pairs of design variables that predominantly affect different fairing objectives. It highlighted a relatively weak coupling between the fairing objectives for changing core and facesheets thicknesses. The core thickness predominantly affects distortion, while facesheet thickness predominantly affects torque, with a relatively small influence on the other objective. This context enables the core thickness to be increased to reduce distortion with only a small penalty on torque and the facesheet thickness to be reduced to reduce torque with only a small penalty on distortion. Hence, an improved configuration relative to the baseline will have a core thickness of 11 to 20 millimetres and a facesheet thickness of 0.1 to 0.8 millimetres.

The parametric study of the chevron geometry highlighted the relationship between the analytical expressions for the core's in-plane [148] and out-of-plane [147] displacements in the morphing direction with the observed trends in the FE studies. It highlighted that for the plate's in-plane deformation in the morphing direction, a large chevron angle reduced the contribution from the chevron's in-plane (i.e., axial stretching/compression) deformation while increasing the contribution from the chevron's out-of-plane (i.e., bending and transverse shear) deformation. As the out-of-plane stiffness of the chevron is much lower than its in-plane stiffness, a high chevron angle between 60 and 70 degrees is preferred to reduce the torque. Similarly, a high length-to-thickness ratio of chevrons increases the chevron's bending deformation contribution to the plate's in-plane deformation in the morphing direction. As the bending stiffness of the chevron is much lower than its axial and transverse shear stiffness, a long chevron of between 12.5 and 20 millimetres is preferred to reduce torque relative to the baseline configuration. Note that the increasing chevron length has

a small penalty on fairing distortion; however, the improvement in the torque response is disproportionately large, thereby making it a favourable trade-off.

The parametric study of the fairing variables indicated that adding floating ribs reduced the fairing distortion significantly with a small cost to the torque response. This small increase in torque due to floating ribs can be offset by a small increase in the fairing span. Hence, a design with at least 1 floating rib and a 0.9 to 1 metre fairing span improves both objectives relative to the baseline. Moreover, the study indicated that pre-strain delays the buckling of the top skin, thereby reducing the cross-section distortion. It further extends the linear torque response of the fairing and reduces its torsional stiffness. A pre-strain of at least 10% is required to achieve a 20-degree rotation angle of the pivoted rib (i.e., 40-degree rotation of the wingtip) before the top skin buckles. However, if a lower pre-strain is required to reduce fatigue on the materials, the study showed that 2 floating ribs could eliminate the sharp increase in distortion due to top skin buckling for any pre-strain. Note that the buckling considered here is the panel's global buckling, and the panel's facesheets are likely to buckle locally before the panel buckling, thereby reducing the panel's axial stiffness. Hence, a full-scale FE study is required to study the nonlinearity in the panel's response under large compression.

3.2.6. Proposed Solution

The reduced design space outlined in Section 3.2.5, which improves the fairing performance relative to the baseline, is summarised in Table 10.

Table 10. Reduced design space that improves the fairing relative to the baseline.

Variable		Default	Minimum	Maximum	Unit
Pre-tension	ε_p	0.1	0.1	0.2	
Span	L	0.8	0.8	1.0	m
Chevron angle	θ_c	60.0	60.0	70.0	deg
Chevron wall length	l_c	12.5	12.5	20.0	mm
Core thickness	b	11.0	11.0	20.0	mm
Facesheet thickness	t_f	0.8	0.1	0.8	mm

This design space is sampled with 100 points using the Latin Hypercube method to identify a preliminary solution to the fairing design. In this study, the number of floating ribs is set to 1, and all the other variables are set to their default values as stated in Table 6 and Table 8. The performance of these randomly sampled design points are shown in Figure 50.

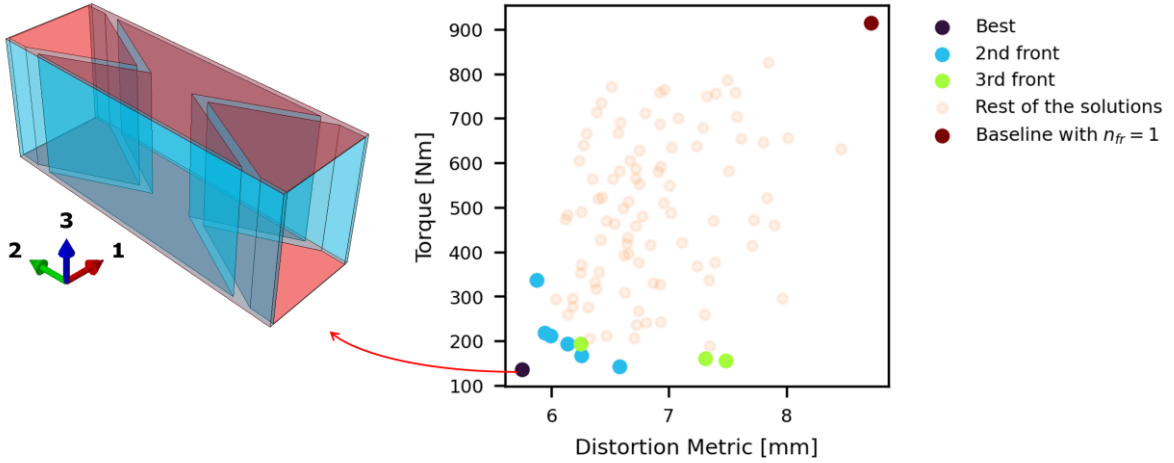


Figure 50. Performance of the randomly sampled design points from the reduced design space that outperformed the baseline solution. The results are extracted from the half model with a 20-degree rotation of the wingtip.

It shows that all the randomly sampled design points from the selected region outperform the baseline solution. It further shows that one solution outperforms all the other solutions in both objectives. The unit cell shape for this best-performing solution is illustrated in the figure. As this best-performing solution is identified from a randomly sampled design space rather than from a formal optimisation framework, it is not guaranteed to be the optimum. Hence, its values are presented only as indicative values for expected torque and distortion response from a preliminary design. The design variable values for the best-performing solution are shown in Table 11, along with their percentage change relative to the baseline.

Table 11. Proposed Design.

Variable	Values	Percentage change from baseline
Pre-tension	ε_p	0.19
Span	L	0.97 m
Chevron angle	θ_c	63.4 deg
Chevron wall length	l_c	14.5 mm
Core thickness	b	16.4 mm
Facesheet thickness	t_f	0.1 mm

It shows that the facesheet is thinner in the best-performing solution relative to the baseline, while all other selected variables are greater. In particular, the pre-tension, span, core thickness and chevron wall length are significantly higher than the baseline solution. The results in the sections 3.2.2 to 3.2.5 indicate that thinner facesheet, longer span, and longer chevron walls help to reduce torque, while the thicker core and higher pre-strain help to reduce distortion. Hence, the best-performing solution identified represents a trade-off between the two objectives. This trade-off between the objectives is evident in the 2nd and 3rd fronts of best solutions shown in Figure 50, where multiple solutions are spread out across the frontier between the two objectives. Given the strong trade-off

between the objectives, it is recommended to implement a multi-objective Pareto search optimisation framework in future work on this concept.

3.2.7. Pressure load considerations

The analysis so far has only considered the fairing deformation due to the rotation of the wingtip. However, deformation due to the pressure load can change the outer surface of the fairing, leading to aerodynamic penalties. This deformation of the fairing due to pressure load can occur locally on the facesheet and globally on the overall panel. This section presents a study of the effects of the pressure loads on the fairing deformation.

Firstly, the effects of a constant suction pressure load on the facesheet deformation are studied for various sizes of the unicell, facesheet thickness and applied pre-strain. To analyse the worst-case pressure loading scenario, the pressure load at the stagnation point for a cruising altitude of 11 kilometres (approximately 36,000 feet) and a cruising speed of 0.8 Mach number is evaluated. The stagnation pressure for compressible flow is evaluated using Equation 40, where P is the static pressure and γ is the ratio of specific heats for air [179].

$$P_0 = P \left(1 + \frac{\gamma - 1}{2} M^2 \right)^{\frac{\gamma}{\gamma - 1}} \quad \text{Equation 40}$$

The static pressure for the cruising altitude is evaluated using 0.2234 as the static pressure ratio and 101.3 kPa as the sea level pressure [180]. The ratio of specific heats is assumed to be constant at 1.4. These parameters from the cruising condition lead to a static pressure of 22.6 kPa and a stagnation pressure of 34.5 kPa. Note that the worst-case pressure loading on the facesheet will be the difference between the stagnation pressure and the static pressure, equalling to 11.9 kPa. However, as a conservative estimate representing a safety factor of 2.9, the stagnation pressure value is used as the pressure load to analyse the facesheet deformation.

The unit cell size changes the unsupported length of the facesheet between regions where it is bonded to the core. Hence, the unit cell size is varied by changing the length of the chevron wall. Additionally, the facesheet thickness is varied to study its effect on facesheet deformation. In some cases, a pre-strain is applied by stretching the unit cell in the morphing direction (1-axis). To model the unit cell as if it is embedded within the panel, symmetric boundary conditions are applied to the faces of the unit cell normal to the 2-axis. Moreover, the displacement of the mid-plane in the 3-axis is set to zero to avoid rigid body motion of the unit cell. Finally, the suction pressure load is applied to the top surface, and the maximum vertical displacement of the facesheet is measured. These loading conditions are annotated in the deformed model of the unit cell shown in Figure 51.

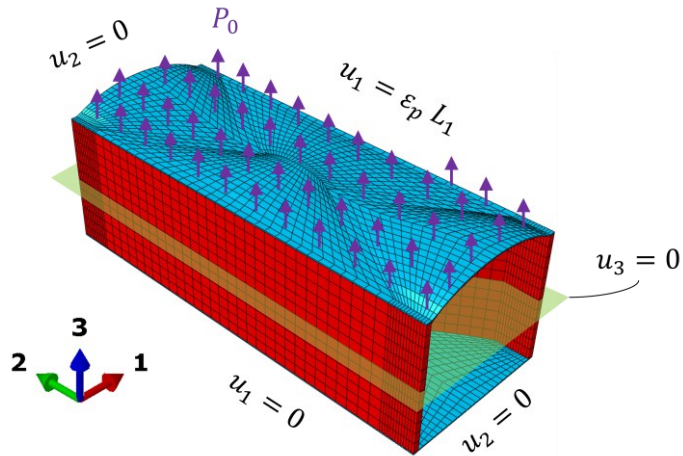


Figure 51. Pressure loading and boundary conditions of the unit cell.

The maximum vertical displacement of the top facesheet under pressure loading is shown in Figure 52 for various lengths of chevron wall and facesheet thicknesses.

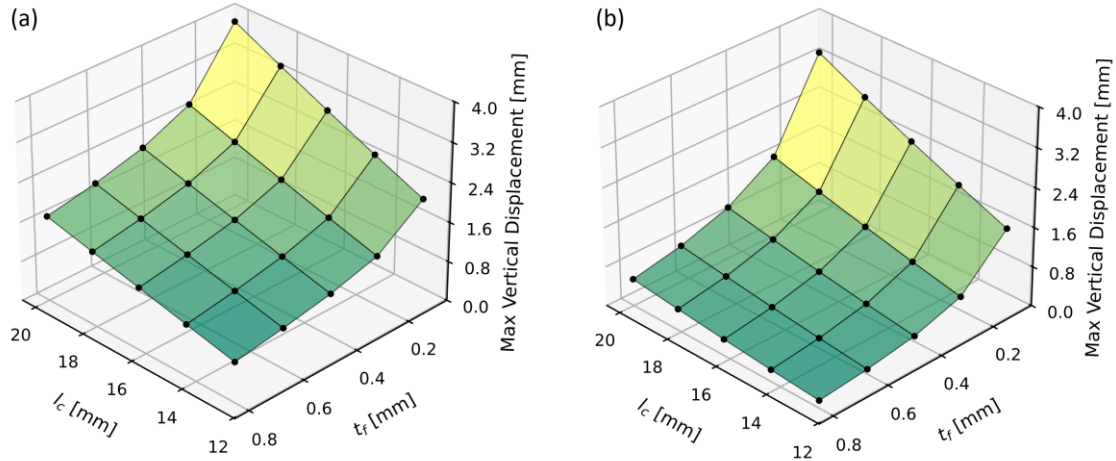


Figure 52. Maximum vertical displacement (u_3) of the top facesheet under pressure loading for unit cells with various chevron wall lengths and facesheet thicknesses. (a) shows the displacement for the unit cell with no pre-strain, and (b) shows the displacement for the unit cells with 10% pre-strain.

Figure 52a shows the results for the unit cells with no pre-strain, whereas Figure 52b shows the results for the unit cell with 10% pre-strain. Both figures show the results for a sweep of chevron wall lengths and facesheet thicknesses within the selected range from Section 3.2.5. From all the cases considered, the largest vertical displacement due to pressure load is for the unit cell with a 20 millimetre long chevron wall and 0.1 millimetre thick facesheet without any pre-tension. In this worst displacement case, the displacement is 3.8 millimetres, which is equivalent to 0.24% of the chord. Hence, the local displacement of the facesheet under pressure load is negligibly small for the unit cell sizes considered in this study.

Next, the effect of the pressure loading on the global deformation of the fairing is analysed for the baseline case with one floating rib. Note that the pressure distribution varies along the chord of the fairing, with the peak loading being at the stagnation point near the leading edge. The pressure

loading at the stagnation point is the difference between the stagnation pressure and the static pressure, equalling 11.9 kPa. Hence, as a conservative estimate, this peak pressure is applied uniformly to the fairing as a negative pressure load (suction) on the top surface and a positive pressure load on the bottom surface. The torque and distortion response of the fairing with and without this pressure loading is shown in Figure 53, and the deformed shape of the fairing at a 20-degree rotation is shown in Figure 54.

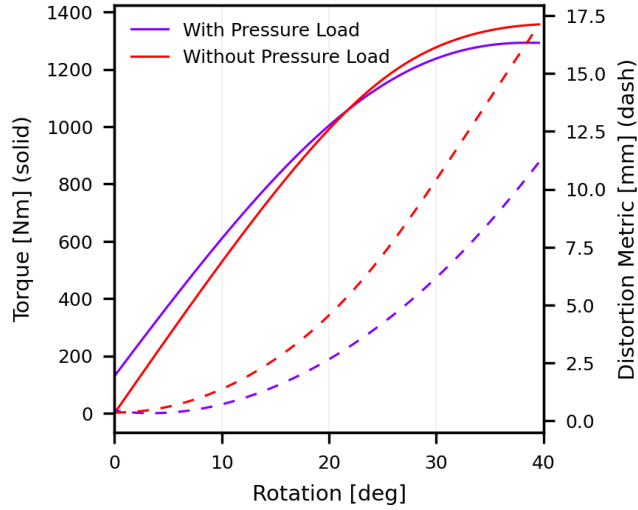


Figure 53. Torque and distortion response for the baseline fairing with one floating rib for the case with and without pressure loading.

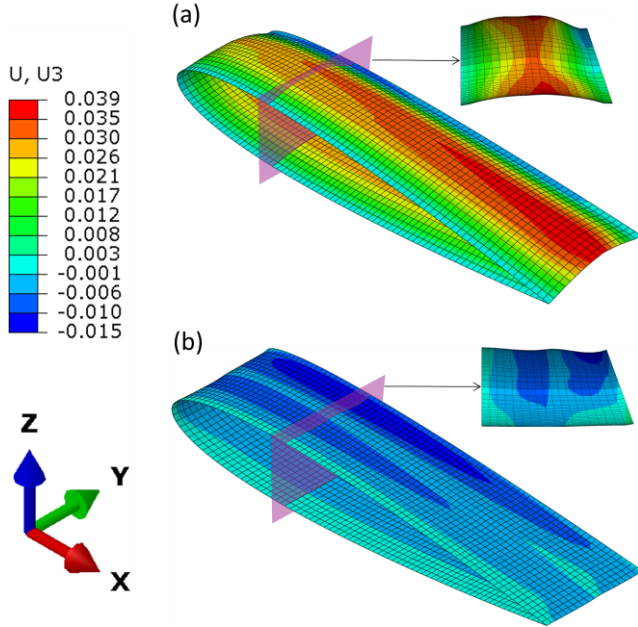


Figure 54. Deformed shape of the baseline fairing with one floating rib at a 20-degree rotation for the case with and without pressure load. The legend shows the vertical (Z-axis) displacement. (a) shows the case with pressure load, and (b) shows the case without pressure load.

Figure 53 shows a non-zero torque at zero-rotation angle for the case with pressure load, indicating the initial torque due to the unequal pressure loading on the top and bottom surface (i.e., negative pressure on the top surface and positive pressure on the bottom surface). Moreover, the figure shows

a slightly smaller gradient in the torque response for the case with pressure load, indicating a slightly reduced torsional stiffness relative to the case without pressure load. Additionally, the distortion response shows significantly lower distortion metric for the case with pressure load relative to the case without pressure load. Note that, as emphasised in the definition of the displacement metric in Section 3.1.2, the chosen distortion metric indicates the reduction in the average cross-section thickness of the fairing. Hence, Figure 53 indicates that the pressure loading alleviates the reduction in the average cross-section thickness of the fairing as the wingtip folds. However, the pressure loading increases the overall vertical displacement of the fairing by raising the entire cross-section in the middle of the rib bay, as shown in Figure 54. In the figure, the case with pressure loading shows a peak vertical displacement of 39 millimetres, whereas in the case without pressure loading, the greatest vertical displacement is -15 millimetres. The peak displacement value of 39 millimetres represents 2.5% of the chord length, hence, the effect of this displacement of the airflow around the fairing should be analysed in future studies. Additionally, a distortion metric that accounts for the vertical displacement of the entire cross-section is required for further studies on the global deformation due to pressure loading.

3.3. Conclusions

The work presents a modelling and analysis framework for analysing a morphing fairing for folding wingtip joints made of a flexible sandwich panel with a cellular core. The framework focuses on finding the right balance between fidelity and computational cost, firstly, by adopting a multi-scale modelling approach with homogenisation of the panel properties to equivalent shell properties and modelling of the fairing over the wing section as a shell surface, and secondly, by using a sensitivity study to determine the critical design variables whose effects on the fairing are then analysed in detail using a parametric study. In order to identify the driving features of the panel and the fairing which contribute to reducing the torsional stiffness of the joint and the cross-section distortion of the fairing, various metrics for quantifying these objectives are studied, and their robustness is evaluated using an initial study varying the number of floating ribs. Torque and displacement metrics were used in the subsequent studies to represent torsional stiffness and cross-section distortion, respectively. A sensitivity study reduced the design space for the parametric study by selecting only the variables that strongly influence the objectives. The parametric studies for the panel variables show that increasing core thickness contributes significantly to reducing distortion while reducing facesheet thickness and increasing chevron length and chevron angle contributes strongly to reducing torque. In contrast, all fairing variables contribute significantly to both objectives. In particular, increasing pre-strain and span improves both objectives, whereas more floating ribs reduce distortion at the cost of increased torque. Hence, a combined effect of these variables offers an opportunity to reduce the trade-off between the objectives. The study showed the variables that strongly influence the objectives, their trends with the objectives, and their range of values that improve the fairing performance relative to the baseline configuration. The study further highlighted the need to perform a 3-dimensional full-scale re-analysis of the optimal solution, particularly to study the effects of facesheet buckling on the sandwich panel fairing.

4. PRELIMINARY STUDIES OF SPATIALLY VARYING CORE GEOMETRY

Previous research has shown that spatially varying the orientation of anisotropic and orthotropic materials can provide a range of benefits in stiffening the structure [155, 161, 181-183]. Various methods have been employed to identify the optimal spatially varying material orientations to improve structural performance. It is proposed applying these methods to design morphing skin panels could improve their performance, particularly in cases with non-uniform loads and/or three-dimensional geometric complexity, where a spatially varying material orientation could enable spatially tailored compliance. However, to the authors' knowledge, a study identifying and implementing methods that help optimise structural compliance (as opposed to stiffness) is not available in the literature. This chapter undertakes an initial exploration of the use of spatial variation in the context of a morphing fairing.

4.1. Motivation for the Method

Orthotropic materials are commonly used in engineering applications for their directional stiffness properties. These materials include laminated composite panels of unidirectional plies used in wind turbine blades and sandwich panels with orthotropic cellular cores used in morphing skin panels [132]. In recent years, advanced manufacturing processes such as continuous tow shearing (CTS) tape layup [184] and polymer 3D printing techniques have enabled manufacturing panels with spatially varying stiffness properties. Spatially varying properties could be achieved by locally changing the geometry or the type of material used in the panel. Spatially varying stiffness properties offer improved structural performance in various applications. For instance, it increases critical buckling load and reduces imperfection sensitivity in cylinders with spatially varying fibre orientation [161, 181, 183]. It also improves the performance of stall-controlled wind turbine blades that use variable stiffness composite to tailor the extension-twist and bend-twist coupling [182]. In lattice structures, reduced structural compliance is achieved by aligning lattice members with the principal stress directions [155], as shown in Figure 55.

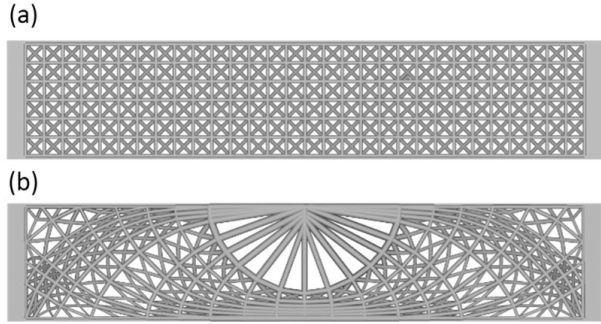


Figure 55. Lattice structure optimised for the three-point bending load case using principal stress directions (Reproduced from [155]). (a) shows the uniform lattice, and (b) shows the optimised lattice with spatially varying geometry.

Various examples of improved compliance in morphing wing designs achieved using spatially varying geometry are found in the literature. Two notable examples are shown in Figure 56.

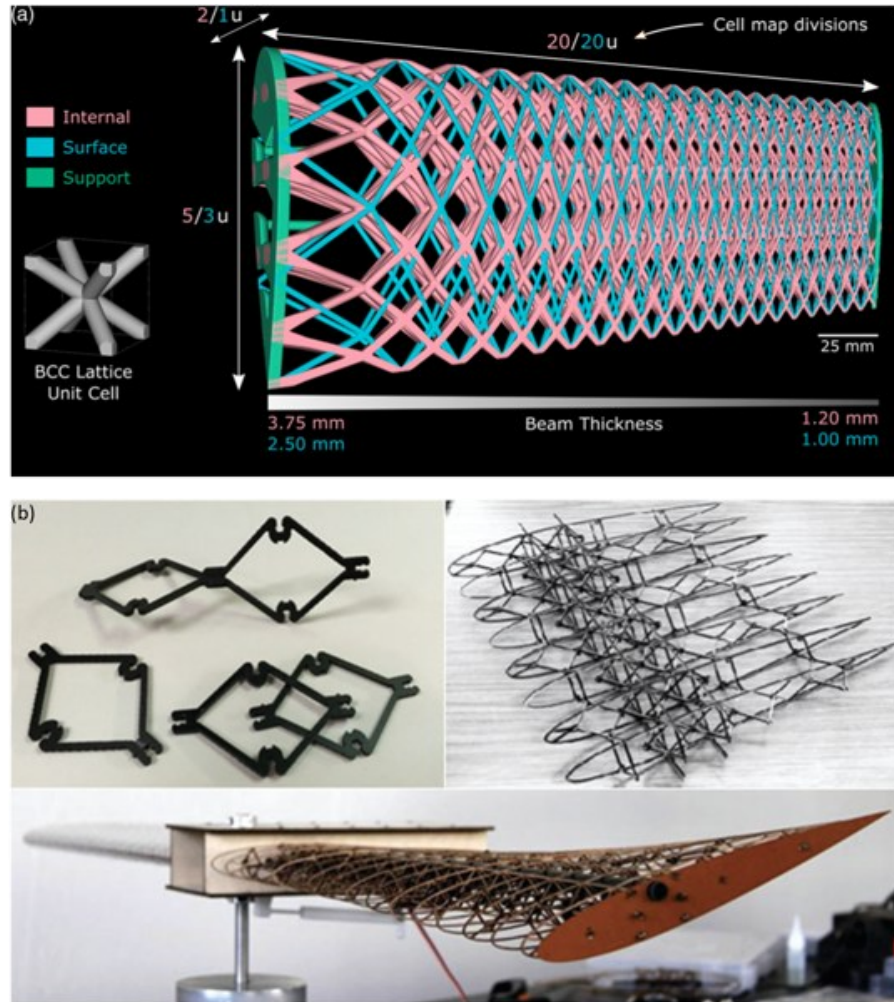


Figure 56. Examples of morphing wings with spatially varying lattice structures. (a) shows a wing with variable span, camber and twist (Reproduced from [185]), and (b) shows a modular wing with variable twist (Reproduced from [186]).

Figure 56a shows a multi-modal morphing wing that used a functionally graded lattice geometry to achieve variable span, camber and twist [185]. The design used spatially tailored thickness of lattice

members and geometry of the unit cells to provide the mechanical compliance required to achieve the desired morphing shape. The lattice was 3D printed with elastomeric polyurethane, and a low elastic modulus silicone skin was wrapped around it to create the wing surface. Figure 56b shows a variable twist wing that used a modular ‘building block’ approach to assemble a lattice structure with spatially tailored stiffness [186]. The modular approach reduces the manufacturing complexity while retaining the ability to spatially tailor the stiffness properties of the wing.

Methods of synthesising the spatially varying topology of morphing structures to achieve a desired deformed shape from a given initial shape using a minimum number of actuation locations are also found in the literature [187]. Morphing leading edge and trailing edge effectors have been developed using such topology optimisation approaches by FlexSys Inc [188]. While multiple examples of compliant internal structures with spatially varying geometry/stiffness are available in the literature, examples of spatially varying geometry in compliant skin panels are limited. A flexible matrix composite with curvilinear fibres was optimised to increase out-of-plane stiffness and in-plane flexibility in the morphing direction [126]. The study identified spatially varying fibre orientations for the layers of the laminates for a Pareto front of optimal solutions for the two objectives.

The optimal direction of alignment for the material depends on various factors, including the structure’s shape, load case, material properties and design objectives. These orientations can be found using an optimisation framework that trials various orientations to find the optimal solution. However, given the large design space, using a guide to align the material to improve compliance is desirable to reduce the computational cost. To this end, various methods of identifying suitable directions to align the material using the results of finite element (FE) analysis have been studied in the literature. Some of these methods are applied at the post-processing stage, and others require iterative FE simulations. Methods used at the post-processing stage either identify the principal direction of a particular field variable [155, 156] or the load path of a load variable [159, 160]. Methods which require iterative FE simulations include the transferred force [189] and the U* index [190] method. The transferred force approach evaluates the direction of the transferred force in each element using the change in reaction forces when the element is removed. The U* index approach depicts relative rigidity at a point using the change in total strain energy due to the fixing of an individual node. In this case, the load path is determined by the direction of the slowest descent in U* values. The study presented here focuses on the methods applied at the post-processing stage as they are computationally cheaper compared to the iterative methods.

Various studies have shown that the stiffness of a cellular lattice core can be increased by locally aligning the lattice members with the principal strain directions [154, 155]. It is proposed that this method can also improve the compliance of morphing fairing by aligning flexible members of the core (e.g., chevrons) with the principal strain direction with the greatest magnitude. This study focuses on understanding the feasibility and the limitations of using such spatially varying geometry to improve the compliance of morphing fairing. Initially, a simple benchmark study is presented to demonstrate the effect of aligning the material with the directions derived from the strain and stress fields. Thereafter, the effects of a spatially varying core as a fairing for folding wingtip joints are studied with

the 3D complexity of the wing section profile. Further arguments are drawn regarding the applicability and limitations of these methods for designing morphing fairings.

4.2. Approach and Methodology

The first study trials various spatially varying directions derived from the strain and stress fields to align the material axis of the structure. A theoretically optimal orientation is also evaluated by considering the material orientation, which reduces the strain energy for different strain states. An expression is then developed to replicate these theoretically optimal orientations using the principal strain directions. The developed expressions are used alongside other methods found in the literature to evaluate the effectiveness of this approach in improving the stiffness and compliance of a cantilevered square plate deformed with a vertical tip displacement. After this, in the second study, a beam-based modelling approach is introduced to represent the core of the fairing panels, which allows for physically meaningful spatial variation of their geometry and properties. The effects of aligning the ribs and chevrons of this core with the principal strain directions are then studied to identify their benefits on the fairing torque and distortion metrics.

Each study is carried out in two stages. In the first stage, the structure is modelled with isotropic properties and deformed to a given load case. The directions derived from the strain and stress fields of the deformed structure in the first stage are used to orient the anisotropic material in the second stage. The structure with spatially varying stiffness is generated and deformed in the second stage. The reaction loads from these structures are compared to structures with uniform stiffness to identify the effects of spatially varying stiffness on the structures' compliance (or stiffness).

As the structures considered in this study are skin panels, shell-based FE models are used in the first stage. These models reduce the field variables to a 2D space, simplifying the process of deriving the directions for orienting the material. The type of model used in the second stage depends on the scale separation between the material scale and their orientation scale. Consider the first study where the panel is made of fibre-reinforced elastomeric matrix composite. The diameter of the fibres (i.e., material scale) is multiple orders of magnitude smaller than the radius of curvature of a curved fibre path (i.e., orientation scale). Hence, a shell-based model can be used in the second stage, with the equivalent properties of the composite and different material orientations assigned to each element [173]. This approach has been used in various studies with spatially varying fibre orientations in the literature [161, 183, 191, 192].

In contrast, if the characteristic length in the material scale is similar to that of the orientation scale, then the material scale must be modelled explicitly. Consider the fairing model with only the core used in the second study. The dimensions of the unit cells of the core can be in the same order of magnitude as the radius of curvature of the orientation path. In this case, the equivalent stiffness properties of the unit cell from the uniform core will be significantly different from that of the core with spatially varying geometry. Hence, the homogenised properties of the uniform core cannot be used with varying material orientations in a shell-based model to represent the spatially varying geometry of the core. Instead, in the second study, the spatially varying core geometry is modelled

explicitly using beam elements to represent the walls of the core. This beam-based model only defines the core; hence, this study does not include the facesheets of the GATOR panel.

The FE simulation in the first study and the first stage of the second study is carried out using first-order quadrilateral shell elements with reduced integration (i.e., S4R elements) in Abaqus. The material properties are defined using a general shell section (i.e., ABD matrix). The results provide section force and strain tensors at the integration point of each element. The stress tensor can then be evaluated by dividing the section force tensor by the panel thickness. However, as the panel thickness is constant throughout the panel, the section force tensor can also be used directly to evaluate the principal stress and the load path directions. Similarly, the strain tensor is also used to evaluate the principal strain direction.

The procedure used for the analysis can be summarised with the following steps:

1. Initial shell analysis is carried out using isotropic material properties for the panel.
2. The panel is flattened by integrating along the surface (applicable only to curved panels, e.g., fairing).
3. Section force and strain tensor are rotated from the element's local material axes to the flattened panel's global axes.
4. Unit vectors are evaluated at the element's centroid using either principal stress, principal strain or load path directions (as described in more detail below).
 - 4.1. The unit vector's orientation defines the shell element's material orientation in the next iteration. Hence, the process is terminated here for shell-based models (i.e., the first study).
 - 4.2. The following additional steps are required only for beam-based models that explicitly define a lattice structure for the next iteration (i.e., the second study).
5. A linear interpolation function for the vector field is defined using Radial Basis Functions (RBF). It uses the vector data from the closest 4 points to interpolate the vector field for any given location.
6. Trajectory lines are traced using the Runge-Kutta method with iteratively positioned seed points to enforce unit cell dimensions.
7. Intersection points of the line traces are identified to define a lattice, and chevrons are added to the lattice to create an accordion-type core.
8. The accordion-type core defined in the flattened surface is mapped back to the original surface.

Steps 1 to 4 are used in the first study, where the fibre orientation of a cantilevered square plate made of elastomeric matrix composite is updated with the objective of either increasing stiffness or compliance under a tip displacement load case. The elastomeric matrix composite comprises stiff Armadillo TPU fibres embedded in a soft Ninjaflex TPU matrix. In the first stage of this study, only the isotropic properties of Ninjaflex TPU are used to design the plate's constitutive properties, while in the second stage, the equivalent stiffness properties of the elastomeric matrix composite are used.

In contrast, all 8 steps are used in the second study, where the geometry of the accordion-type core is varied using the principal strain direction with the objective of reducing reaction torque and distortion in the fairing. The first stage uses the isotropic properties of Armadillo TPU to define the constitutive properties of the shell-based fairing. In the second stage, the walls of the core are explicitly defined using beam elements with material properties of the Armadillo TPU and cross-section dimensions (e.g., beam width and height) representing the core geometry.

4.2.1. Derivation of the Material Orientation

The material properties in the initial simulation affect the directions derived from the stress or the strain field. Hence, an isotropic panel is defined with the corresponding panel thickness for each structure in step 1. For the case of the cantilevered square plate, a NinjaFlex panel of 0.6-millimetre thickness is used in the initial simulation, while for the fairing case, an Armadillo plate of 11-millimetre thickness is used. The stress and strain field is extracted from these initial simulations, and these fields are used to guide the orientation of the orthotropic material. Note that as the material in the initial simulation is isotropic, their principal stress and strain directions are identical. Hence, to avoid repetition in the analysis, only one of these directions is considered.

In step 2, the fairing panel over the wing section is transformed into a flat surface by integrating along the surface in two perpendicular directions. The orientation of these perpendicular axes is arbitrary; however, the process can be simplified if the axes are aligned with the element edges (e.g., tangential direction along the chord and wing span direction). Hence, in a structured mesh without skew, the cumulative sum of the distance between the nodes in each direction, as shown in Equation 41, is used to construct the flattened grid.

$$(x, \quad y)_{n,m} = \left(\sum_{i=2}^n \| \mathbf{R}_{i,m} - \mathbf{R}_{i-1,m} \|, \quad \sum_{j=2}^m \| \mathbf{R}_{n,j} - \mathbf{R}_{n,j-1} \| \right) \quad \text{Equation 41}$$

The variable $\mathbf{R}_{i,j}$ refers to the nodal coordinates of the flattened grid, and the subscript i and j refer to the indices of the grid. The origin of the flattened grid, denoted by indices $n = 1$ and $m = 1$, is at the leading edge of the inboard rib on the wing section, as shown in Figure 57.

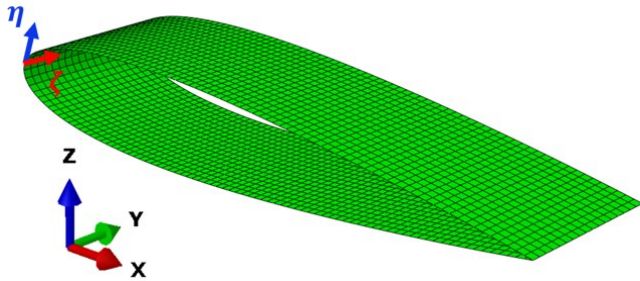


Figure 57. Wing global coordinate system (XYZ-axes) and the surface coordinate system ($\eta\zeta$ -axes) used for the flattened grid.

It shows the global coordinate system (XYZ-axes) and the panel coordinate system ($\eta\zeta$ -axes) used for the flattened grid. The ζ -axis runs along the span while the η -axis runs along the circumference of the aerofoil cross-section along the chord.

The field variables (i.e., stress and strain) are defined in the element's material coordinate system (123-axes) at the element centroid. Hence, all the field variables are rotated to the panel coordinate system in step 3 before the field vectors are evaluated in step 4. Since this analysis uses isotropic material properties at the start with a uniform material orientation, this step can be ignored for both the square plate and the fairing case. However, when the field variables from a panel with non-uniform material orientation are used, these field variables must be rotated to a consistent coordinate system.

4.2.1.1. Principal directions

Once the field variables are defined in a consistent coordinate system in the flattened grid, the stress and strain tensor for the in-plane deformation of a shell element are defined as shown in Equation 42

$$\boldsymbol{\sigma} = \begin{bmatrix} \sigma_{xx} & \sigma_{xy} \\ \sigma_{yx} & \sigma_{yy} \end{bmatrix}, \quad \boldsymbol{\varepsilon} = \begin{bmatrix} \varepsilon_{xx} & \varepsilon_{xy} \\ \varepsilon_{yx} & \varepsilon_{yy} \end{bmatrix} \quad \text{Equation 42}$$

where the first subscript is the normal direction of the face and the second subscript is the direction of the force or displacement. The principal stresses are the eigenvalues of the stress tensor ($\boldsymbol{\sigma}$), and the principal directions are their corresponding eigenvectors. Similarly, the principal strain values and their principal directions are given by the eigenvalues and eigenvectors of the strain tensor ($\boldsymbol{\varepsilon}$). These directions represent the coordinate axes where the same stress state can be represented with only the diagonal terms of the tensor (i.e., with zero shear components). Hence, aligning the material axis with the principal directions eliminates shear so that all the load is carried as axial loads, as shown in Figure 58.

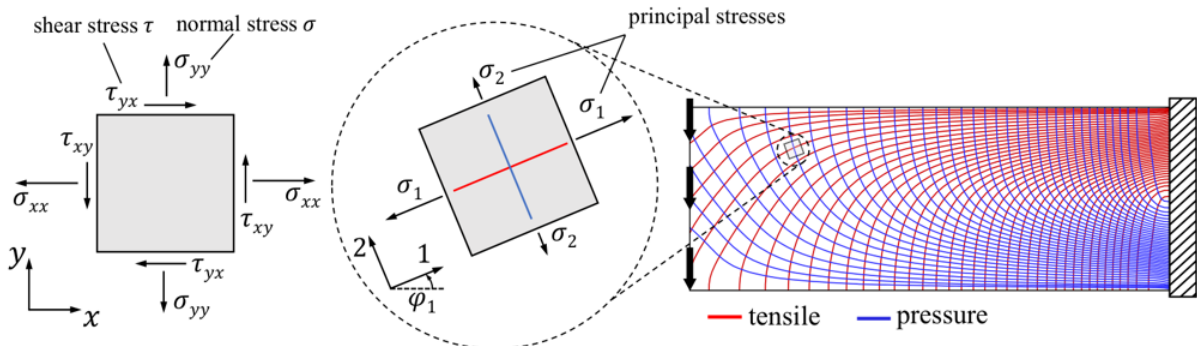


Figure 58. Principal stress directions for a cantilever beam (Reproduced from [193]).

The alignment of lattice walls in principal stress directions has been effectively used to stiffen lattice structures, as the axial stiffness of the walls is higher than their shear stiffness for isotropic materials [155].

One aspect of the numerical implementation that needs to be handled correctly, particularly for the second study, is ensuring the continuity of the derived directions across the adjacent elements. For instance, it is possible to get two opposite directions (i.e., $-\nu$ and $+\nu$ where ν is a 2D vector) across the adjacent elements, effectively representing the same stiffness properties but with different material orientation angles (e.g., 0-degree and 180-degree). Hence, these vectors should be flipped to point in the same direction to improve continuity in the vector field direction, which is essential for tracing the streamlines. Moreover, the vector directions derived from the field can change by 90 degrees across elements due to switching the maximum and minimum principal directions. As this study aims to achieve a continuous field, the vector directions are re-oriented to maximise the continuity of the vector field. To this end, the vector at the centroid of each element is rotated by 0, 90, 180 and 270 degrees, and their dot product with the vector of the adjacent element is evaluated. Then, the rotated vector that maximises the dot product with the vector of the adjacent element is retained for the element, and the other rotated vectors are discarded.

4.2.1.2. Load path directions

The load paths are evaluated separately for the x -axis and y -axis force components. Each load path represents the force component's trajectory across the structure between the external supports. The load paths can also form self-equilibrating circuits for a force component, especially if no external force is applied to the structure in the corresponding direction [159]. An example of the load path domains for a cantilever beam in bending deformation is shown in Figure 59.

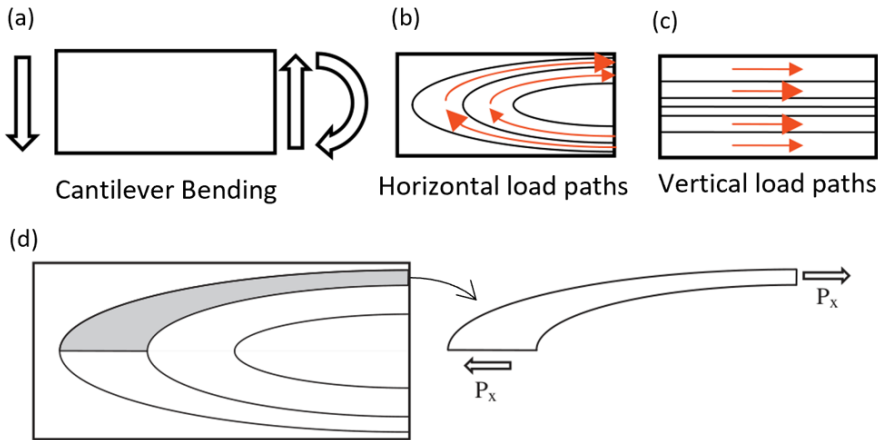


Figure 59. Load paths for a cantilever beam under bending deformation (Reproduced from [159]). (a) shows the load case, (b) the horizontal load paths, (c) the vertical load paths, and (d) the force equilibrium within each load path sub-domain.

It shows a cantilever beam where the only external force in the horizontal direction is applied through the fixture on the right side of the beam. Hence, the load path corresponding to the horizontal force loops back to the edge of the fixture, whereas the vertical forces are transferred across the beam. Figure 59d shows the sub-domain enclosed between two load path trajectory lines where forces are balanced at the ends. The horizontal force component is tangential to the trajectory lines; hence, the force component is not transferred across these lines. The load path vector for each load path component is the column of the stress tensor corresponding to the force direction. For instance, the x -axis load path's direction is the stress tensor's first column. A normalised vector defined by each column is used to trace the load path trajectories. A combined load path is also defined by the summation of the horizontal and the vertical load path [194], which is traced using its normalised vector.

4.2.1.3. Minimum strain energy direction

Consider the Mohr's circle representing either a stress or a strain tensor, as shown in Figure 60.

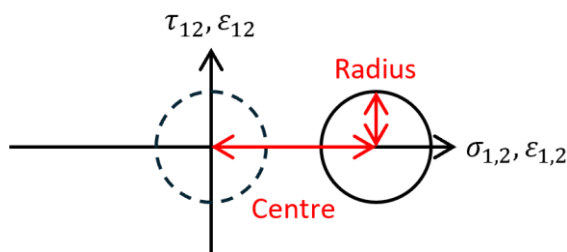


Figure 60. Mohr's circle represents a stress or a strain state.

The circle's centre represents the hydrostatic component of the tensor, while the radius represents the deviatoric component. The hydrostatic tensor changes the element's volume, while the deviatoric tensor changes the element's shape. If the centre of the Mohr's circle is at the origin, the hydrostatic tensor is zero, thereby making the magnitude of maximum and minimum principal values equal for

the tensor. However, the magnitude of the tensor's maximum and minimum principal values differs for a Mohr's circle away from the origin due to the hydrostatic component of the tensor.

A parameter which we will call 'directionality' is defined for this work based on the distance of the centre of Mohr's circle from the origin, as shown in Equation 43

$$\text{Directionality} = \frac{|\text{Centre}|}{\text{Radius}} = \frac{|\varepsilon_1 + \varepsilon_2|}{\varepsilon_1 - \varepsilon_2} = \frac{\left| \frac{(\varepsilon_{xx} + \varepsilon_{yy})}{2} \right|}{\sqrt{\left(\frac{\varepsilon_{xx} + \varepsilon_{yy}}{2} \right)^2 + \left(\frac{\gamma_{xy}}{2} \right)^2}} \quad \text{Equation 43}$$

When directionality is zero, Mohr's circle is at the origin; hence, the principal stress values have opposite signs but equal magnitude. As the directionality increases, Mohr's circle moves horizontally; hence, the magnitude of one principal stress exceeds that of the other.

Now consider a plate deformed by a strain state in the global xy-axes with a material orientation defined by the 12-axes, which can be rotated to reduce the strain energy for the strain applied, as shown in Figure 61.

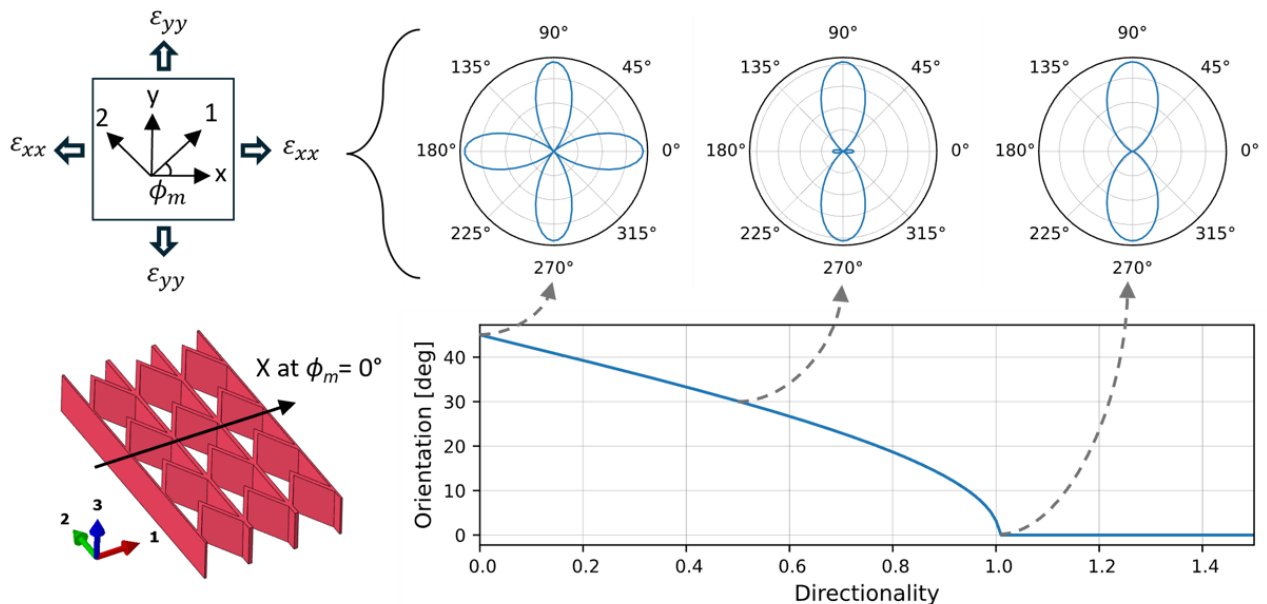


Figure 61. Material orientation with minimum strain energy for a given strain state. The strain state is represented as directionality. Snapshots of variation in strain energy with material orientation are shown at the top.

The strain energy of a shell element evaluated using the voigt strain vector ($\boldsymbol{\varepsilon}$) in the structure's coordinate system (xy-axes) is shown in Equation 44.

$$U = \frac{1}{2} \boldsymbol{\varepsilon}'^T \mathbf{A} \boldsymbol{\varepsilon}' \quad \text{where} \quad \boldsymbol{\varepsilon}' = \mathbf{R} \mathbf{T} \mathbf{R}^{-1} \boldsymbol{\varepsilon} \quad \text{Equation 44}$$

The matrices \mathbf{R} and \mathbf{T} are the Reuter's matrix and transformation matrix, respectively. The strain state is transformed into the material axes ($\boldsymbol{\varepsilon}'$) to calculate strain energy using the in-plane stiffness matrix

(A) defined in the material coordinate system. The material orientation with minimum strain energy is found by solving the derivative of the strain energy expression with respect to material orientation (i.e., $dU/d\phi_m = 0$) for the material orientation (ϕ_m). As the expression is nonlinear, the solution is found numerically using the Scipy library in Python.

For highly orthotropic materials, such as the accordion-type core shown in Figure 61, the material orientation required to minimise the strain energy depends on the directionality of the applied strain state. The polar plots on the top right of the figure show variations in strain energy for various material orientations for each strain state. The bottom right graph shows the variation of the material orientation that minimises strain energy against the directionality of the applied strain state. For a strain state where the Mohr's circle is at the origin, the minimum strain energy is achieved by deforming the core in shear by aligning the material axes (i.e., 1 and 2 axes) at a 45-degree angle to the xy-axes (as opposed to aligning the material axes with the principal directions). The high axial stiffness in the 2-axis of the core (i.e., along ribs) requires large actuation energy to deform it; hence, deforming the GATOR panel in shear is preferable to reduce strain energy in an entirely deviatoric strain state.

In contrast, as the hydrostatic strain component increases, the Mohr's circle moves horizontally away from the origin, increasing the directionality of the strain state. When the directionality approaches 1, the strain energy is reduced by aligning the core's flexible direction (1-axis) with the principal strain direction with the larger magnitude. This orientation enables the larger deformation to be in the flexible direction of the core and the smaller deformation to be in the stiff direction. Hence, it is desirable to calculate the minimum strain energy material orientation for each element for its strain state. However, due to the number of elements in the model and the numerical solution process required for the nonlinear equation (i.e., $dU/d\phi_m = 0$), evaluating the material orientations that minimise the strain energy is computationally expensive.

Alternatively, the minimum strain energy angle can be approximated directly from the maximum and minimum principal strain values and directions, as shown in Equation 45.

$$\phi_m = \phi_{P1} \pm \arctan2\left(\frac{P2}{P1}\right) \quad \text{Equation 45}$$

The angle ϕ_{P1} is the maximum principal direction, and the parameters $P1$ and $P2$ are the maximum and minimum strain values. The function *arctan2* is the inverse tangent function, which returns the angle between the range $[-\pi, \pi]$, thereby selecting the correct quadrant. As the ratio $P2/P1$ approaches 1, the inverse tangent function returns 45 degrees, similar to the directionality of the tensor approaching zero. Moreover, as the ratio $P2/P1$ approaches 0, the inverse tangent function returns 0 degrees, aligning the material orientation with the maximum principal direction, which has the greater magnitude in this case. Similarly, as the ratio $P2/P1$ approaches infinity, the inverse tangent function returns 90 degrees, aligning the material orientation with the minimum principal direction, which has the greater magnitude.

The orientation change based on the ratio of minimum to maximum principal strain values can either be added to or subtracted from the angle of the maximum principal strain direction. For clarity in the rest of the chapter, these expressions with addition and subtraction are referred to as minimum strain energy 1 and 2, respectively. The choice of operation changes the resulting orientation only at the shear-dominated regions, essentially changing the direction of the shear deformation on the material axes. However, for the regions with high directionality, the resulting orientation is always aligned with the principal direction with greater magnitude, regardless of the choice of operation.

4.3. Trial of Material Orientation Methods Using a Shell-Based Model

In this simplified study, various vector directions derived from principal stress, load path and minimum strain energy material orientation are used to define a spatially varying material orientation for a cantilevered square plate under vertical tip displacement.

4.3.1. Elastomeric Matrix Composites

The plate comprises an elastomeric matrix composite with Ninjaflex matrix and Armadillo fibres. As Armadillo and Ninjaflex are thermoplastic polyurethane (TPU) manufactured by Ninjatek, their similar chemical composition ensures good bonding between the fibres and the matrix. The Young's Modulus [136, 137] and the Poisson's ratio [125] of these materials are shown in Table 12.

Table 12. Elastic properties of the material [125, 136, 137]

Material	Young's Modulus [MPa]	Poisson's Ratio	Elongation at yield [%]
Ninjaflex	12	0.48	65
Armadillo	396	0.48	18

The material properties of the elastomeric matrix composite are evaluated using the rule of mixtures as shown in Equation 46 to Equation 49.

$$E_1 = E_f V_f + E_m (1 - V_f) \quad \text{Equation 46}$$

$$E_2 = \frac{E_f E_m}{E_f (1 - V_f) + E_m V_f} \quad \text{Equation 47}$$

$$G_{12} = \frac{G_f G_m}{G_f (1 - V_f) + G_m V_f} \quad \text{Equation 48}$$

$$\nu_{12} = \nu_f V_f + \nu_m (1 - V_f) \quad \text{Equation 49}$$

When the panel is deformed in the fibre direction (1-axis), both fibres and matrix have the same strain; hence, the panel cannot exceed the lowest of the two materials' elongation at yield, as shown in Table 12. However, when the panel is deformed in the direction transverse to the fibres (2-axis), the strain on the fibre and the matrix is inversely proportional to its contribution to the transverse

stiffness. Hence, the transverse strain at which each material will reach its yield strain is evaluated by Equation 50 and Equation 51.

$$\text{Fibre Yield: } \varepsilon_{22} = \varepsilon_{f\text{yield}} \frac{E_f}{E_2} \quad \text{Equation 50}$$

$$\text{Matrix Yield: } \varepsilon_{22} = \varepsilon_{m\text{yield}} \frac{E_m}{E_2} \quad \text{Equation 51}$$

As the elastic moduli in the transverse direction (E_2) vary with the fibre volume fraction, the transverse strain of the panel at which each material yields also changes with the fibre volume fraction. The variation in the elastic moduli of the panel and the transverse strain at which the material yields for various fibre volume fractions are shown in Figure 62.

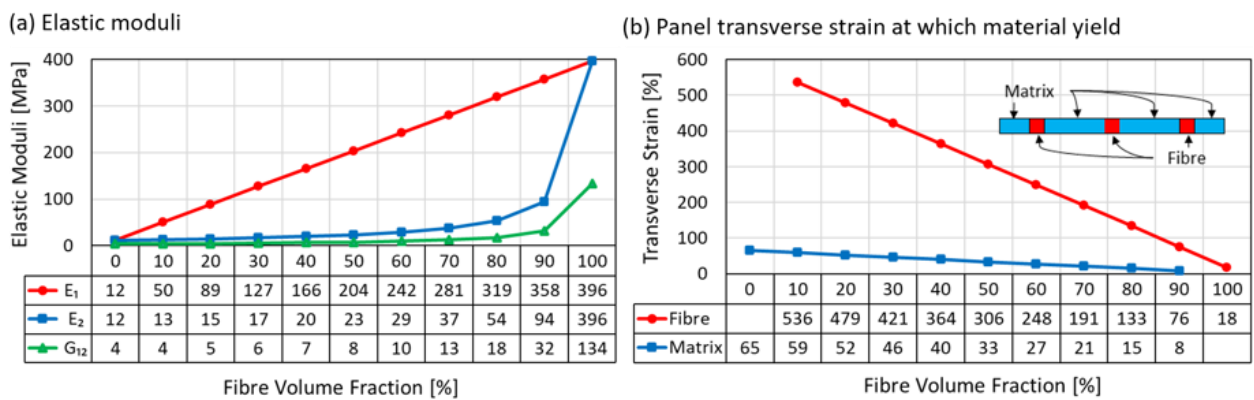


Figure 62. Fibre-reinforced elastomer panel properties for various fibre volume fractions. (a) shows the elastic moduli, and (b) shows the panel transverse strain at which each material field.

A fibre-reinforced elastomer panel with 20% fibre volume fraction shows strong anisotropy in the elastic moduli (i.e., $E_1/E_2 \approx 6$) while retaining large strain capability (i.e., $\varepsilon_{22} \leq 52\%$). Hence, this volume fraction is used in the rest of the analysis of the square plate. Note that as both materials have a Poisson's ratio of 0.48, the composite panel has the same Poisson's ratio regardless of the fibre volume fraction.

4.3.2. Analysis of the Cantilevered Square Plate

The square plate measures 200 millimetres along its edges. It is cantilevered on the left side, and a tip displacement of 2 millimetres is applied to the central node on the right side. The central node on the right side is rigidly connected to the rest of the nodes of the edge. In the initial simulation, the isotropic properties of the matrix, NinjaFlex, are used for the plate. The resulting vector directions derived from the stress and strain field are shown in Figure 63.

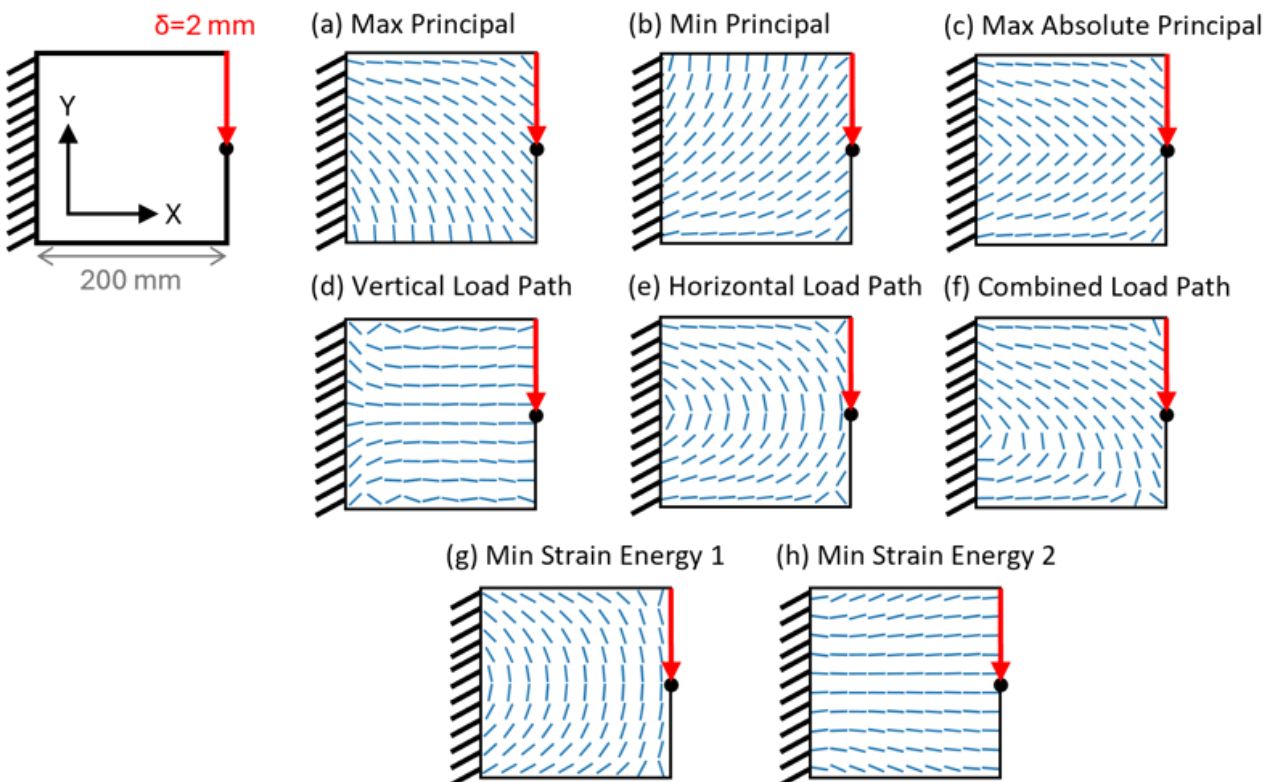


Figure 63. The applied load case and the derived directions from the initial simulation of the cantilevered square plate.

Note that as the material is isotropic, the principal directions derived from the stress and strain fields are identical. Hence, they are simply referred to as the principal directions. The load path directions are evaluated from the stress field (or equivalent section forces). The minimum strain energy material orientation is evaluated using the principal strain directions and values, as shown in Equation 45.

Various studies have aligned the fibres of composite materials (1-axis) in the principal directions and load path directions to reduce structural compliance for a given load case [193-195]. It is also plausible that aligning the transverse direction of composite materials (2-axis) with these vector directions can increase the compliance of morphing structures. Hence, the effects of aligning the fibre direction (1-axis) and the transverse direction (2-axis) with these vector directions are shown in Figure 64.

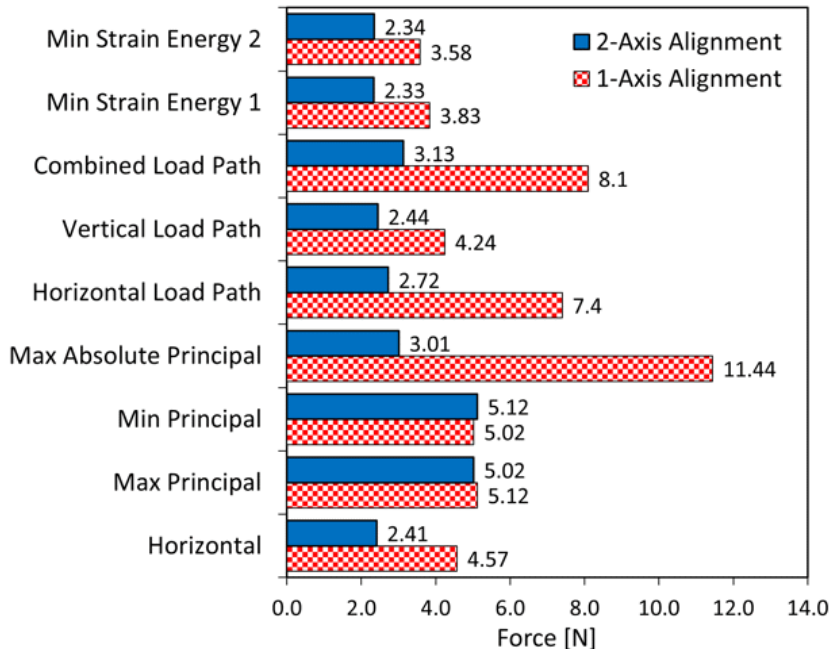


Figure 64. Reaction forces for square plates with various orientations of the transverse direction (2-axis).

Firstly, consider increasing the stiffness of the plate relative to the baseline case with uniformly aligned fibres in the horizontal direction. Figure 64 shows that aligning the fibres (1-axis) with either principal direction increases the reaction force relative to the baseline case. In contrast, with load path directions, improvements in stiffness are achieved by aligning the fibres with either the horizontal or the combined load path directions. The greatest increase in stiffness is achieved by aligning the fibres with the maximum absolute principal direction. This orientation ensures that the fibres are axially aligned with directions that undergo the largest deformation. Hence, in this orientation of the fibres, the fibres must undergo axial deformation for the panel to deform, thereby significantly increasing the stiffness. The second and third greatest improvement in stiffness relative to the baseline case is achieved by aligning the fibres with the combined load path and the horizontal load path directions, respectively. In both cases, the fibres at the top and bottom sides of the plate are aligned horizontally, thereby reducing the plate's compliance in bending.

Secondly, consider aligning the transverse direction of the composite (2-axis) with the vector directions shown in Figure 63 to increase the compliance of the plate relative to the baseline case of having the transverse direction horizontally (i.e., fibres aligned vertically). Figure 64 shows that only the two minimum strain energy material directions improve compliance relative to the baseline case. In both cases, the improvement in compliance relative to the baseline case is small, with only a 3.3% and 2.9% reduction in the reaction forces. The directions of these two minimum strain energy material orientations are explained using the variation of the directionality parameter for the strain field and the superimposed scaled principal strain vector for each element, as shown in Figure 65.

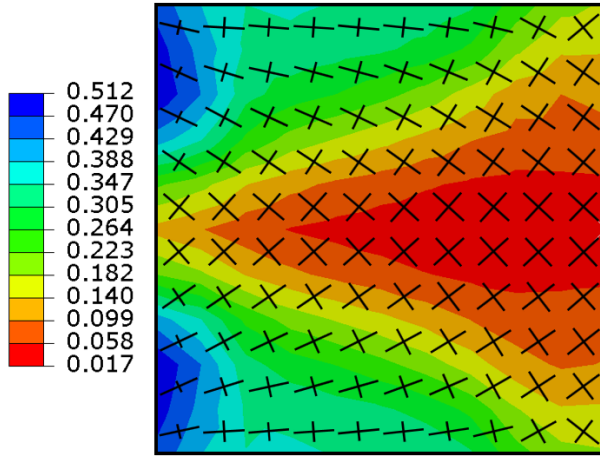


Figure 65. Directionality parameter of the strain field with superimposed scaled principal strain vectors for the plate.

It shows that at the root of the plate near the top and bottom edges, strain magnitude in one direction is greater than the other, leading to moderate directionality parameter values (i.e., approximately 0.5). Hence, in this region, the material's transverse axis (2-axis) is aligned closer to the direction of the greater strain magnitude. In contrast, the directionality parameter approaches zero at the region near the midplane, particularly towards the tip, indicating this region has predominantly deviatoric strain with little hydrostatic strain component. In this strain state, less energy is required to strain the material in shear; hence, the transverse axis (2-axis) is aligned 45 degrees to the greater strain magnitude.

The analysis in this section considered the effect of varying only the material orientation while keeping the stiffness properties of the material constant throughout the panel. With these constraints, only the minimum strain energy orientations improved the compliance of the cantilevered plate. Nonetheless, it showed that spatial variation of material orientation has a significant impact on stiffness in general, and with careful selection, it can be used to improve compliance. The next section studies the effects of spatially varying the geometry of an accordion-type core on the compliance of the fairing.

4.4. Fairing Core Analysis Using a Beam-Based Model

The stiffness properties of the core can be altered locally by changing the shape, size or orientation of the cells that tessellate to form the core. However, as the cells are stacked continuously, neither the shape, size, nor orientation can be spatially varied independently. Any changes in the unit cell's orientation must accompany compatible changes in the neighbouring cells' shapes, sizes, and orientations for the cells to tessellate together. These changes in the neighbouring cells will change their equivalent stiffness properties.

The beam-based approach proposed in this study is to model the core with spatially varying geometry using beam elements to represent its walls. While beam models were shown to underpredict the stiffness of the core in Chapter 2, the beam-based model offers the ability to model spatially varying core geometry over the fairing. The beam-based model of the fairing can capture the change of

torsional stiffness and distortion due to spatially varying core geometry relative to a uniform core. It further captures the effects of geometrically nonlinear deformation of the core as the beam-based model explicitly models the walls of the core.

An accordion-type core is modelled as the fairing with a beam element for each wall of the core. Quadratic (i.e., 3-noded) beam elements are used instead of linear (i.e., 2-noded) beam elements as they capture the typical “S” shaped deformation of the chevrons better than linear elements. The following section describes the additional steps (i.e., steps 5 to 8 in section 4.2) required to generate the accordion-type core with spatially varying geometry. The subsequent sections present three studies considering the beam-based model. Firstly, the homogenised stiffness properties of the unit cell modelled using beam elements are compared to those of the high-fidelity solid-based model presented in Chapter 2. Secondly, the beam-based modelling approach with the uniform core is compared to the shell-based modelling approach with homogenised stiffness properties of the uniform cores. Thirdly, the effects of spatially varying core geometry on the fairing’s reaction torque and distortion metric are presented.

4.4.1. Generation of Core Geometry for the Beam-Based Model

Once the vector directions at the element centroid are defined (i.e., in step 4 in section 4.2), the vector direction at any arbitrary location is determined by interpolating the vectors at nearby elements’ centroids. For a structured grid without skew, bi-linear interpolation can be used to evaluate the vector at arbitrary locations. However, this approach fails to extrapolate the vector at the edge of the domain between the centroid of the edge element and its edge. In contrast, the interpolation methods based on the radial basis functions are robust in these edge locations. Hence, in step 5, the radial basis function interpolation from the Scipy library in Python is used to evaluate the vector at any arbitrary location by linearly interpolating the vector from the nearest 4 element centroids.

In step 6, trajectory lines are traced using the fourth-order Runge-Kutta method [160], starting with a seed location. Each line is traced in positive and negative directions until the ends of the line are a pre-defined distance (d_t) outside of the structure’s domain (i.e., flattened grid). The tracing process is terminated for lines that form circulations within the domain after a pre-defined number of maximum tracing steps (n_{max}). The seed locations can be chosen arbitrarily to create traced lines. However, to create a lattice, the spacing between the traced lines can be controlled by using seed locations [196]. To this end, the seed point for each line can be placed at a pre-defined distance (e.g., width (L_1) or length (L_2) of the core’s unit cell) away from the previous line to create a grid-like set of trajectory lines. The Runge-Kutta method used for tracing the line is expressed in Equation 52 and illustrated in Figure 66.

$$\begin{aligned}
dp_1 &= \mathbf{v}(s_i) \times \Delta s \\
dp_2 &= \mathbf{v}\left(s_i + \frac{1}{2}k_1\right) \times \Delta s \\
dp_3 &= \mathbf{v}\left(s_i + \frac{1}{2}k_2\right) \times \Delta s \\
dp_4 &= \mathbf{v}\left(s_i + \frac{1}{2}k_3\right) \times \Delta s \\
p_{i+1} &= p_i + \frac{1}{6}(dp_1 + 2dp_2 + 2dp_3 + dp_4)
\end{aligned} \tag{Equation 52}$$

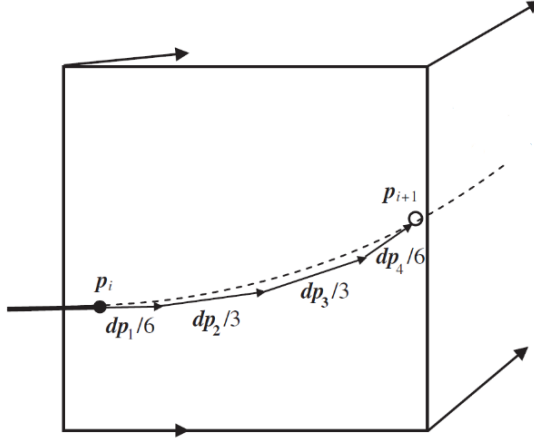


Figure 66. Runge-Kutta method for tracing the vector field (Reproduced from [159]).

The function $\mathbf{v}(s)$ represents the interpolated vector field, which returns a unit vector for a given location of the domain. Variable Δs is the overall step size and dp_i for $i \in [1,4]$ are the sub-steps which make up the full step in the Runge-Kutta method. These sub-steps help to reduce the cumulative error during the integration along the line relative to the Euler method with the same step size.

The lines traced for perpendicular vectors (e.g., maximum and minimum principle strain direction) do not necessarily have their data points at the intersection of both lines. Hence, the traced lines belonging to vector 1 and vector 2 need to be re-sampled at their intersections to create a lattice. Consider a segment of line 1 defined by points r_1 and r_2 , and a segment of line 2 that is defined by points r_3 and r_4 , where each point has x and y coordinates. To ensure that the intersection point evaluated is within the line segments defined by their points, the equation of the lines is formulated using first-degree Bezier parameters, as shown in Equation 53.

$$l_1 = r_1 + t_1(r_2 - r_1), \quad l_2 = r_3 + t_2(r_4 - r_3) \tag{Equation 53}$$

The Bezier parameters t_1 and t_2 has a range $[0, 1]$ within the line segment, and the Bezier parameter values at the intersection of the two lines are found by Equation 54.

$$t_1 = \frac{|r_1 - r_3 \quad r_3 - r_4|}{|r_1 - r_2 \quad r_3 - r_4|}, \quad t_2 = \frac{|r_1 - r_2 \quad r_1 - r_3|}{|r_1 - r_2 \quad r_3 - r_4|} \tag{Equation 54}$$

Hence, if both Bezier parameters t_1 and t_2 are within the range of $[0, 1]$, an intersection point lies within the segments of two lines. The coordinates of this intersection point are evaluated using the

equation of the line in Equation 53. Once a grid line lattice shape is generated with the re-sampled lines, the chevrons are added to the grid, replacing the line segments in this direction. This lattice generation process is schematically shown in Figure 67.

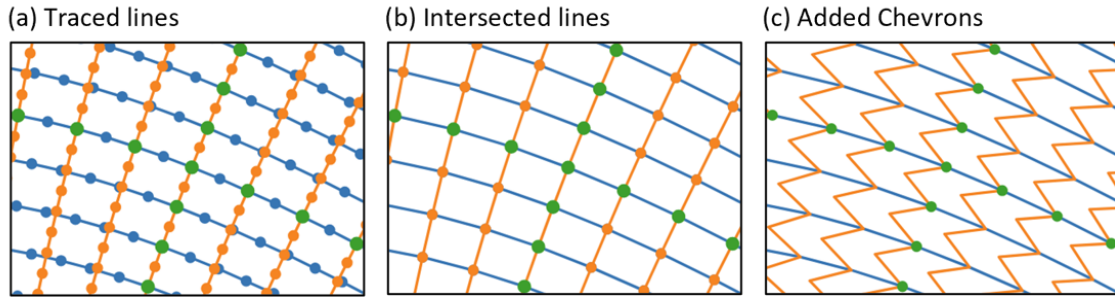


Figure 67. Lattice generation process with seed points shown in green. (a) shows the traced lines, (b) shows the re-sampled lines at the intersection points, and (c) shows the core lattice with the added chevrons.

Once the accordion-type core is defined on the flat surface, its nodes are mapped from the flat surface to the original surface of the 3D wing section. As the relationship between the nodal coordinate of the shell surface used in the first stage and the nodal coordinates of the flattened grid evaluated for the second stage in section 4.2.1 is known, the core's nodal coordinates are mapped to the 3D fairing surface in step 8 using the radial basis function interpolation.

4.4.2. Stiffness Properties of the Core

The core's geometry is the same as the baseline geometry used in the parametric design study in Chapter 3. In this study, the chevrons are oriented in the same direction to avoid adjacent chevrons contacting each other in a spatially varying core geometry. The unit cell geometry of the core is shown in Figure 68.

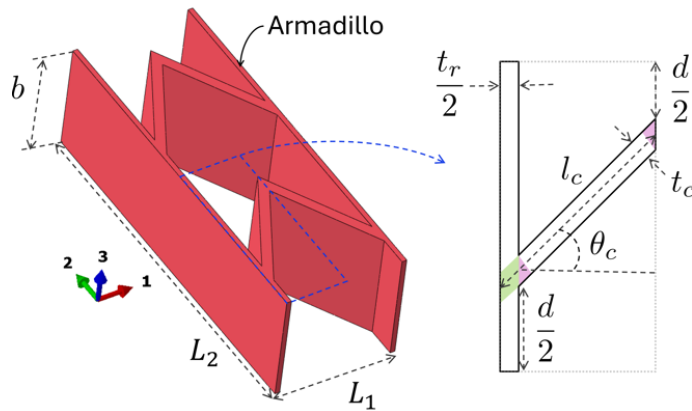


Figure 68. Unit cell geometry of the core.

The dimensions of the core are shown as L_1 for axial (1-axis) direction and L_2 for transverse (2-axis) direction. The geometric variable values in the baseline configuration are shown in Table 13.

Table 13. Baseline configuration of the core.

Variable		Value	Unit
Chevron angle	θ_c	60.0	deg
Chevron wall length	l_c	12.5	mm
Chevron wall thickness	t_c	1.0	mm
Chevron separation	d	6.0	mm
Rib thickness	t_r	1.0	mm
Core thickness	b	11.0	mm

An analytical formulation for the equivalent stiffness of the core was presented in Chapter 2. One of the significant sources of error in the analytical beam model was the fact that the intersections between adjacent walls lead to local stiffening, such that the effective lengths of the core's chevrons and ribs are shorter than their full lengths. It was shown that the modified analytical expressions based on the effective length of the core's chevron and ribs improved the accuracy of the beam-based analytical model. In the modified analytical model, the length of the chevron wall and the rib wall was reduced by removing the region highlighted in green and pink in Figure 68. Similar comparisons of equivalent stiffness properties are presented using a solid-based FE model and beam-based FE models, as shown in Figure 69.

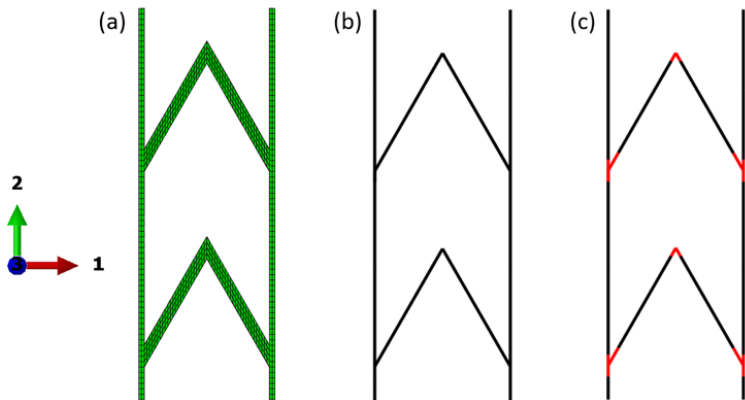


Figure 69. FE models of the core. (a) shows a solid-based model. (b) shows a beam-based model with full lengths used for the walls. (c) shows a modified beam-based model with reduced length for the walls as the regions highlighted in red are modelled as rigid.

The linear solid model has 0.5-millimetre brick elements, and beam models have one quadratic beam element per wall. The region highlighted in red in the modified beam model is modelled as rigid by assigning it material properties that are 10^3 times stiffer than Armadillo. The equivalent properties evaluated by these models are shown in Table 14.

Table 14. Equivalent stiffness properties of the core obtained from a solid, linear beam and quadratic beam model of the unit cell.

		Solid	Beam	Modified Beam
E_1	[Pa]	174,996	105,127	191,964
E_2	[Pa]	33,257,853	31,680,000	35,648,182
G_{12}	[Pa]	62,797	19,777	26,725
E^D_1	[Pa]	415,455	155,802	199,321
E^D_2	[Pa]	33,108,921	31,679,639	35,648,385
G^D_{12}	[Pa]	32,486	11,286	14,159

It shows the equivalent elastic moduli evaluated from the homogenised in-plane and out-of-plane stiffness matrix (i.e., A-matrix and D-matrix). The stiffness moduli from the beam model with full length for the walls have large errors relative to the high-fidelity solid model for in-plane shear (G_{12}), out-of-plane torsion (G^D_{12}) and both in-plane and out-of-plane moduli in the axial direction (i.e., E_1 and E^D_1), as shown in Figure 70.

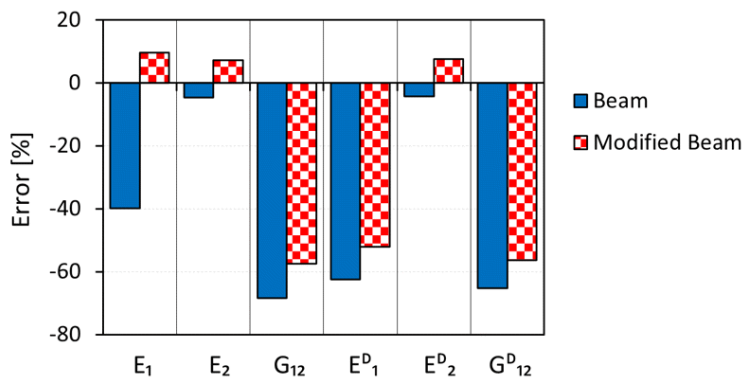


Figure 70. Comparison of homogenised properties of the unit cell from beam models to the solid model.

In the modified beam model with shortened wall lengths, the error in the axial modulus (E_1) relative to the solid model is 10%, as opposed to the -40% in the beam model with the full length of the walls. Moreover, the modified beam model has lower errors than the beam model with full wall lengths for shear, torsion, and 1-axis flexural moduli. Hence, the modified beam model with reduced wall lengths should ideally be used in the fairing model.

However, the modified beam model triples the number of beam elements in the model as three beam elements are defined for each wall as opposed to one as in the other beam model. The two beam elements at the ends are rigid, and the middle element is defined using Armadillo material properties. Moreover, the amount of shortening required on the ends of the walls is different for the chevrons, as shown in Figure 68. Hence, the procedure required for defining the rigid elements and shortening walls is complex for the fairing. Therefore, the beam modelling approach with full wall lengths is used for the fairing to simplify the analysis and study the effects of spatially varying core geometry with reduced computational cost.

4.4.3. Validation of the Beam-Based Fairing Model

The fairing has a NACA 0015 aerofoil profile with a 1.6-metre chord and a 0.4-metre span in the half model (i.e., the full span of the fairing is 0.8-metre). The fairing has zero flare angle, no floating ribs and 10% pre-strain along the span, identical to the baseline fairing configuration in Chapter 3. As pre-strain cannot be applied using a thermal load in the beam-based model, in this study, pre-strain is applied by defining a shorter span (i.e., 0.3635 metre) and stretching it to the actual span of the fairing half model (i.e., 0.4 metre). The beam-based fairing model with uniform core geometry and the comparison of its torque and distortion response to the shell-based model with homogenised stiffness properties are shown in Figure 71.

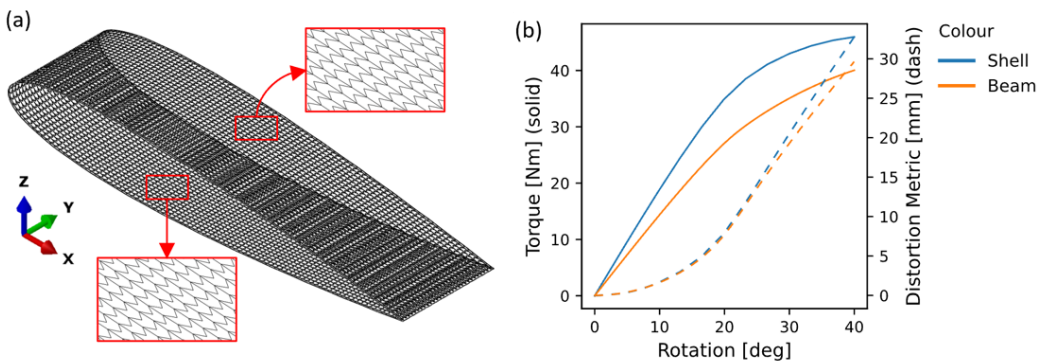


Figure 71. Comparison of beam-based fairing model and shell-based fairing model with homogenised stiffness properties.

As indicated by the homogenised stiffness of the beam-based unit cell in Figure 70, the beam-based model underpredicts the torque response of the fairing in Figure 71. The error in the torque response of the beam model relative to the shell model at 20-degree rotation is 23%. In contrast, the beam model accurately captures the deformation of the fairing, giving a closely matching distortion metric response. The distortion metric represents the average reduction in the thickness of the fairing as the wingtip folds, and it is evaluated using the expression in Equation 55.

$$\text{Distortion Metric} = \frac{1}{n_b} \sum_i^{n_b} u_{3i} - \frac{1}{n_t} \sum_j^{n_t} u_{3j} \quad \text{Equation 55}$$

The first term represents the average vertical displacement (u_3) of the bottom surface nodes (n_b) and the second term of the top surface nodes (n_t). This distortion metric was shown in Chapter 3 to provide a quantitative measure consistent with the shape distortion observed in the deformed shape of the fairing.

4.4.4. Analysis of Spatially Varying Core Geometry

The study considers the impact of spatially varying the size and orientation of the core on the torque and distortion response – initially through a nominal, prescribed shape function to drive the orientation before considering spatial variations determined from stress/strain fields.

4.4.4.1. Prescribed Cosine Variation

A nominal shape function, in this case, a cosine function, is first explored to see how the core geometry varies spatially when driven by a single prescribed shape function. The cosine function is defined in the chordwise direction, leading to the smoothly varying orientation of the core's ribs along the chord, as illustrated in Figure 72.

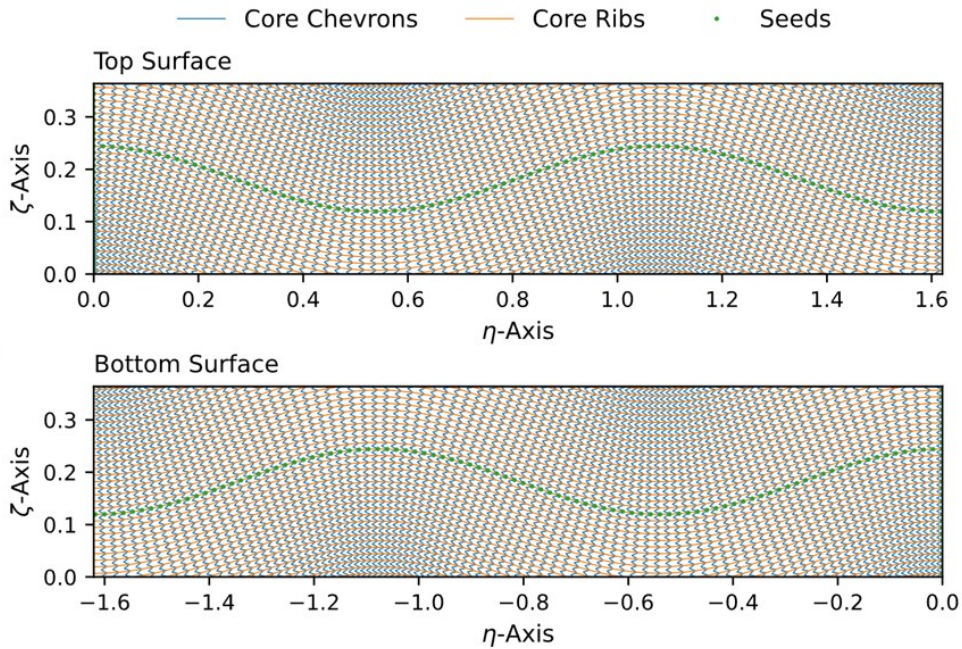


Figure 72. Flattened surface view of the fairing with a cosine-based variation of core orientation with an amplitude of $5 L_1$ and a period of $30 L_2$.

At any chordwise location, the orientation direction of the core is constant along the span dimension of the fairing. Various design cases with different amplitudes and periods of the cosine wave are analysed for the fairing. Both the amplitude and period are defined using the length (L_1) and width (L_2) of the unit cell of the core, shown in Figure 68. The spatially varying orientation of the core changes the shapes and sizes of the cells throughout the fairing depending on the waviness of the cosine function. The change in shape and size of the cells are small for cosine waves with small amplitudes and large periods. In contrast, cosine waves with large amplitudes and small periods produce sharply changing cell shapes and sizes, as shown in Figure 72.

The baseline unit cell size is enforced only by the placement of seed points, as described in section 4.4.1. Hence, the cell size can change drastically away from the seed line. The concave side of the cosine wave has a denser core as the chevron orientations converge. In contrast, the divergence of the chevrons on the convex side leads to a sparser core with larger cells. For this particular example shape function, the densification of the core, along with the curvilinear orientation, has the effect of increasing both the torque and distortion metrics relative to the baseline, as shown in Figure 73.

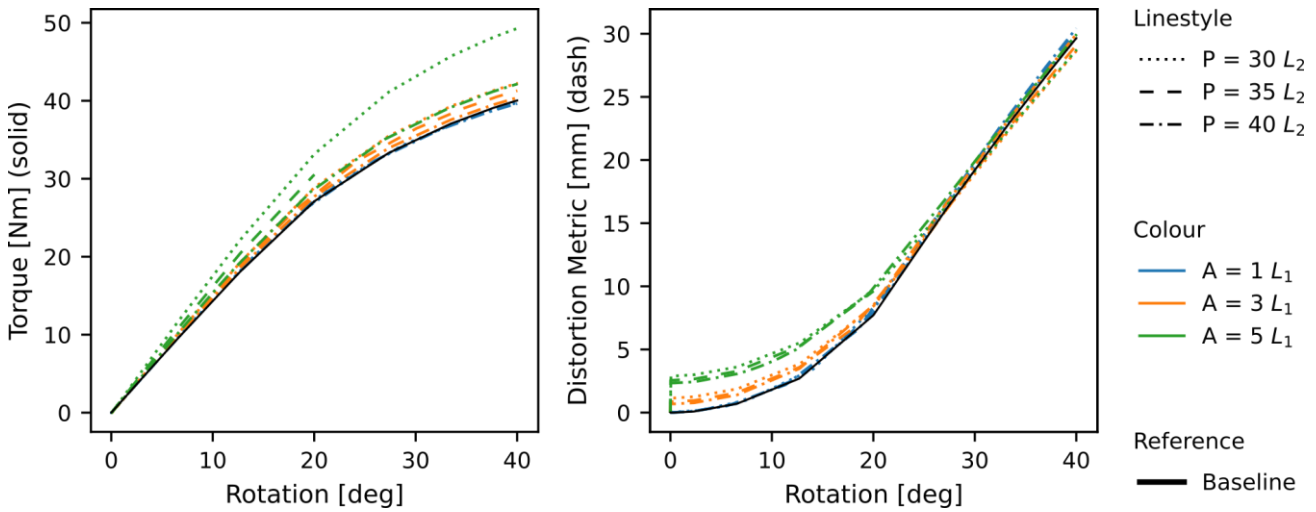


Figure 73. Torque and distortion metric response for various curvilinear core geometry.

The largest increase in torque is for the cosine wave with the shortest period and the largest amplitude. As the amplitude decreases and the period increases, the torque response tends towards the response of the baseline case with uniform core geometry. Curvilinear core orientation further distorts the fairing at the pre-strain stage before the folding rotation is applied. This distortion is shown in Figure 73 with the increase in distortion at 0-degree rotation for cosine waves with amplitudes $3 L_1$ and $5 L_1$. Hence, applying curvilinear orientation to the core deteriorates both the torque and distortion metric response of the fairing.

4.4.4.2. Structural Response-Driven Variation

To explore the effects of aligning the core walls with the directions derived from the stress/strain field similar to the approach considered in the cantilevered plate example above, it is necessary to first create an appropriate response field. As before, this is done by considering an isotropic material in order to understand the inherent deformation response before it is modified by anisotropy.

The shell-based fairing model with isotropic stiffness properties of Armadillo is used to produce the initial strain fields from the deformed fairing. The principal strain directions extracted at a 10-degree rotation of the fairing are used to generate a lattice fairing with spatially varying geometry, as shown in Figure 74.

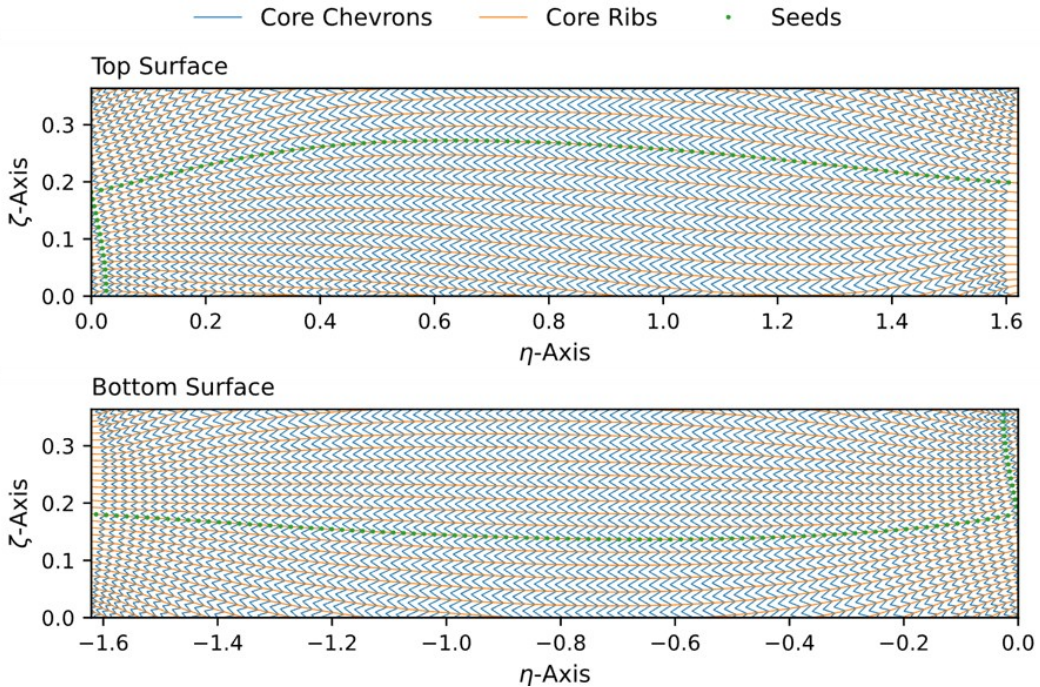


Figure 74. Lattice fairing generated by tracing the principal strain direction lines using the mid-span of the leading edge as the initial seed point.

The initial seed point for tracing the principal strain direction lines is located at the mid-span of the leading edge ($\eta = 0.0$). The two principal directions are traced from the initial seed point, enforcing the unit cell dimensions along each seed line. Cell size increases in the region away from the seed line, particularly on the top surface, relative to the baseline size near the initial seed. In contrast, placing the seed point in the mid-chord location of the top surface, as shown in Figure 75, reduces the size of the cells towards the leading and trailing edge of the fairing relative to the baseline size.

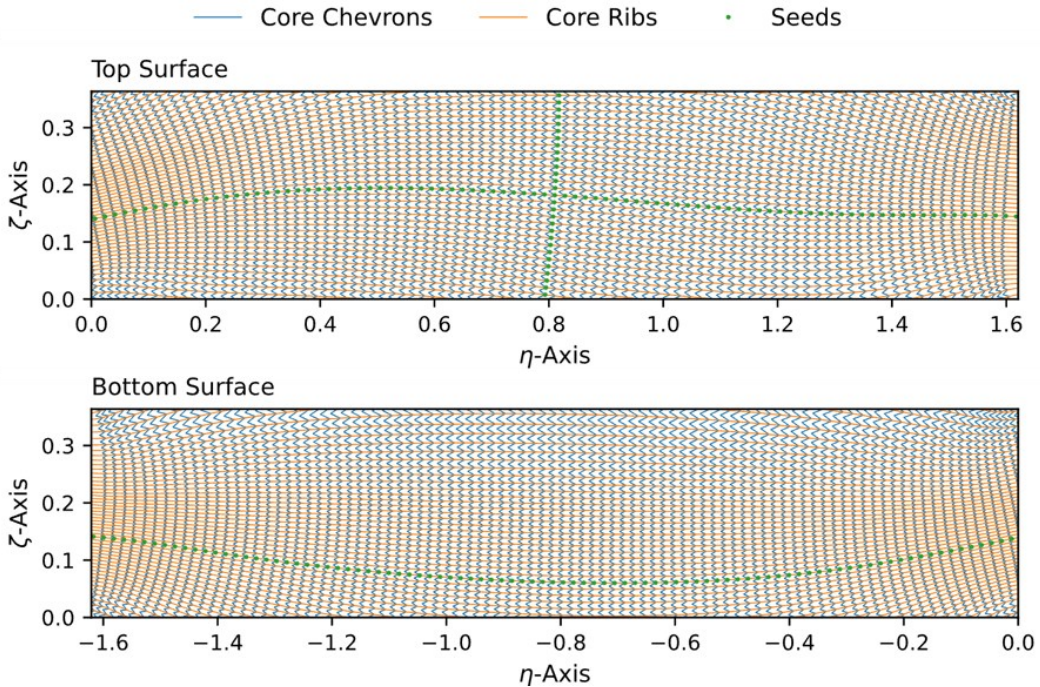


Figure 75. Lattice fairing generated by tracing the principal strain direction lines using the mid-span mid-chord location on the top surface as the initial seed point.

Figure 74 and Figure 75 indicate that the lattice geometry generated depends significantly on the initial seed point location where the baseline cell dimensions are enforced. The size of the cells in the rest of the fairing is determined relative to the cell size in the initial seed location, offering the ability to densify/sparsify the lattice by changing the initial seed location.

The 60-degree chevron angle (θ_c) is used to define the chevron geometry in all cells. Hence, the chevron length (l_c) is adjusted with the cell size to ensure the chevrons connect to the ribs on both sides. The larger the cell size, the longer the chevrons, thereby reducing the core's stiffness locally in regions with large cells. Hence, the fairing made of a sparse lattice is more compliant in torque response, as shown in Figure 76 for the case with a leading edge ($\eta = 0.0$) seed point.

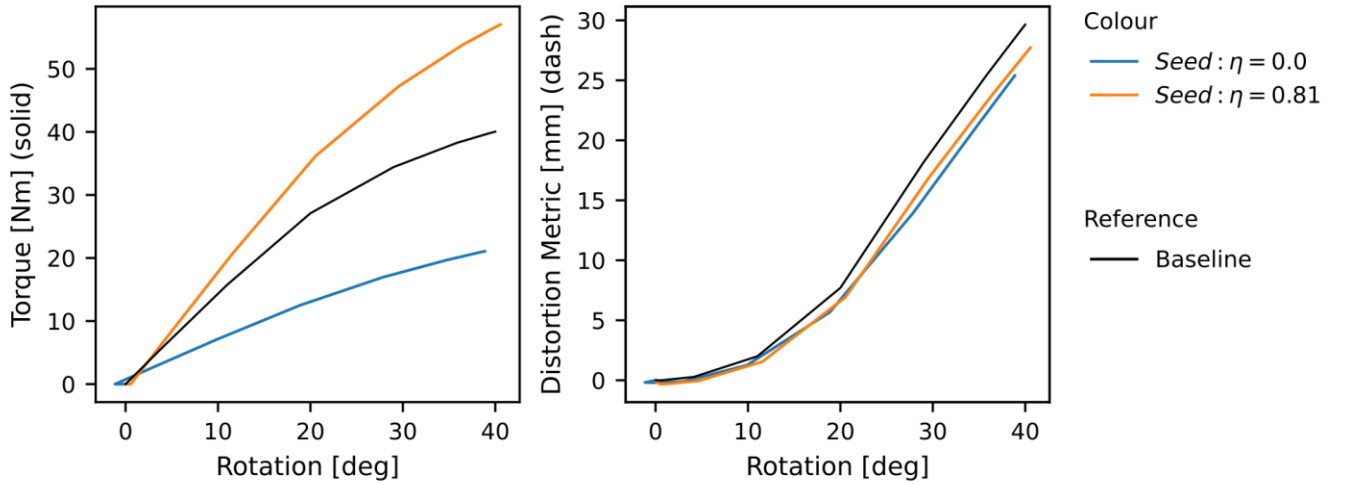


Figure 76. Torque and distortion metric response for the cores aligned with principal strain directions for lattice generated using different initial seed points.

Figure 76 shows the torque and distortion metric responses for the sparse lattice generated using the leading edge ($\eta = 0.0$) and the dense lattice generated using the top surface's mid-chord ($\eta = 0.81$) seed points. It shows that the sparse lattice reduces torque while the denser lattice increases it. For instance, at a 40-degree rotation, the sparse fairing has 47% less torque than the baseline fairing, while the dense lattice has 41% more than the baseline. In contrast, both fairings reduce the distortion metrics relative to the baseline fairing, with 11% and 8% less distortion in the sparse and dense fairing, respectively. Reduced distortion in both fairing indicates that aligning the core orientation with the principal strain direction delays the out-of-plane displacement of the fairing, regardless of the density of the lattice cells. In contrast, only the fairing with a sparse lattice reduces torque.

The rest of this section presents an improved fairing design, which combines a sparse lattice to reduce torque and chevrons aligned with the greatest strain direction to reduce distortion. It is noted that the reduced distortion stems from greater compliance in the in-plane compressive deformation of the core, such that its out-of-plane deformation is reduced. Hence, the strain field from a larger folding angle is expected to create greater anisotropy in the lattice fairing, thereby reducing fairing distortion through increased in-plane compliance. However, the current lattice generation procedure limits the maximum folding angle from which the strain field can be used to generate a lattice to the folding angle just before the onset of compressive strain on the top surface of the isotropic fairing model. These limitations are discussed in more detail in the following section.

The improved fairing design is generated using the strain field from a 15-degree rotation of the isotropic fairing. The torque and displacement responses of the fairing, along with the core geometry and deformed shape of the fairing at the thickest chord location, are shown in Figure 77.

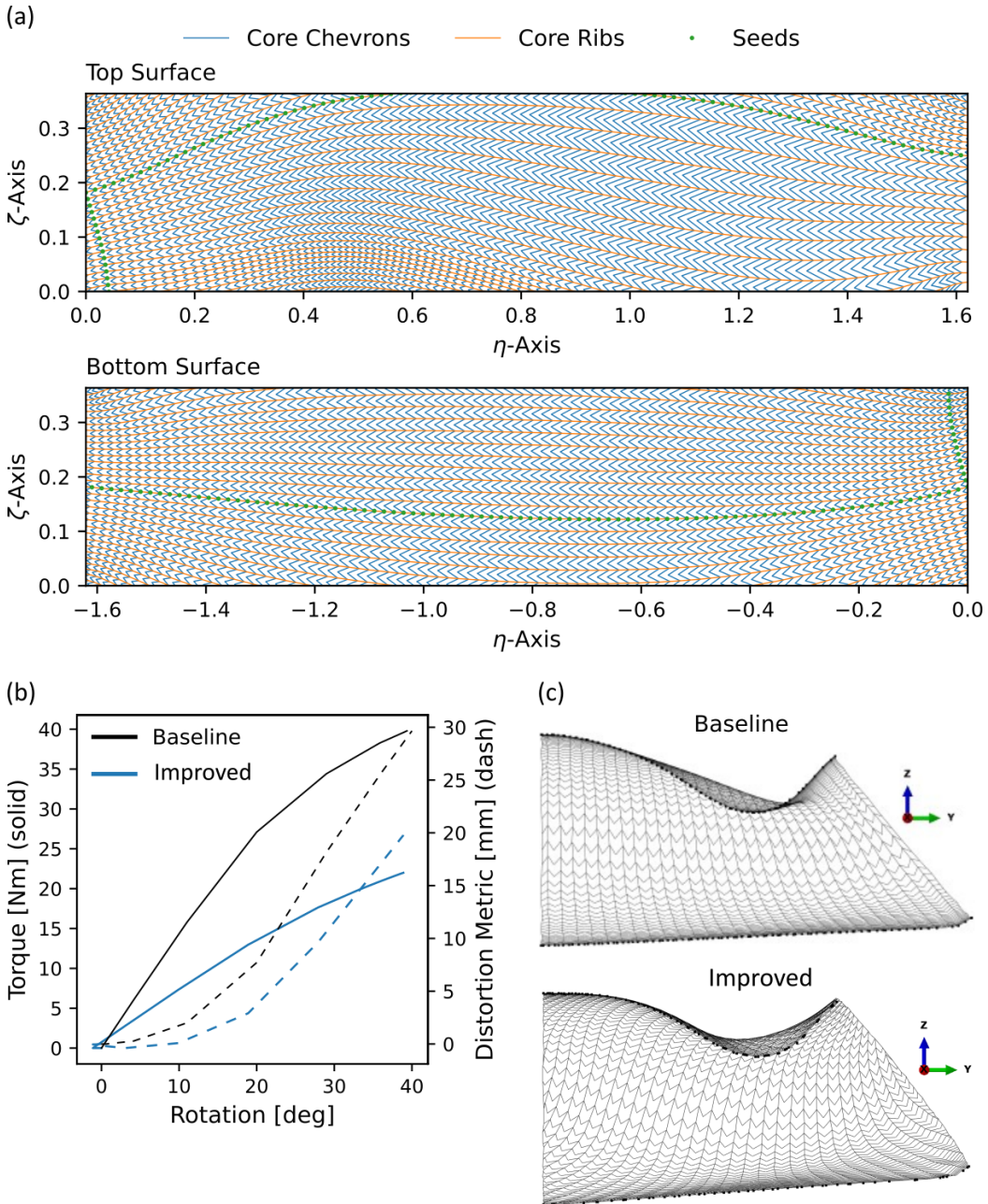


Figure 77. Improved spatially varying fairing design: (a) shows the lattice geometry of the improved fairing, (b) shows significantly improved torque and distortion responses, and (c) shows the deformed shape of the fairing at 40-degree rotation at the thickest region of the aerofoil (i.e., 30% chord).

Figure 77a shows the spatially varying geometry of the fairing with large variations in the cell sizes. Figure 77b shows that the improved fairing's torque and distortion metric response at 40-degree rotation are reduced by 44% and 30%, respectively, relative to the baseline fairing. The deformed shape of the fairing at this rotation at the thickest region of the aerofoil (i.e., 30%) chord is shown in Figure 77c. It shows greater retention of the aerofoil thickness relative to the uniform fairing in the folded wing configuration and, importantly, from an aerodynamic perspective, the elimination of the sharply folded or 'creased' region in the baseline configuration.

The magnitude of reductions in torque and distortion achieved are significant and show a very useful level of benefit from introducing spatial variation. Crucially, it also shows that introducing spatial variation allows for further decoupling of the design objectives in a manner which requires less design compromise.

4.4.5. Limitations of the Beam-Based Modelling Approach

The work above has shown that spatially varying lattice cores can be automatically generated and analysed, and several different design configurations were shown, with one, in particular, giving very significant performance improvements. However, it is important to keep in mind some limitations of this particular approach in creating and modelling the geometry, as discussed here.

A fairing designed for the folding wing requires a continuous and smooth outer surface. The facesheets bonded to the core, potentially with spatially varying geometry, provide this surface in the GATOR panel. The size of the cells in the core changes the unsupported lengths of the facesheet between the location where it is bonded to the core. Large unit cells will increase the unsupported length of the facesheet, leading to large out-of-plane displacement under a pressure load [128]. In contrast, a smaller unit cell will reduce the free undeformed length of the facesheet, thereby increasing the local strain on the facesheet for a given panel deformation, as shown in Figure 78.

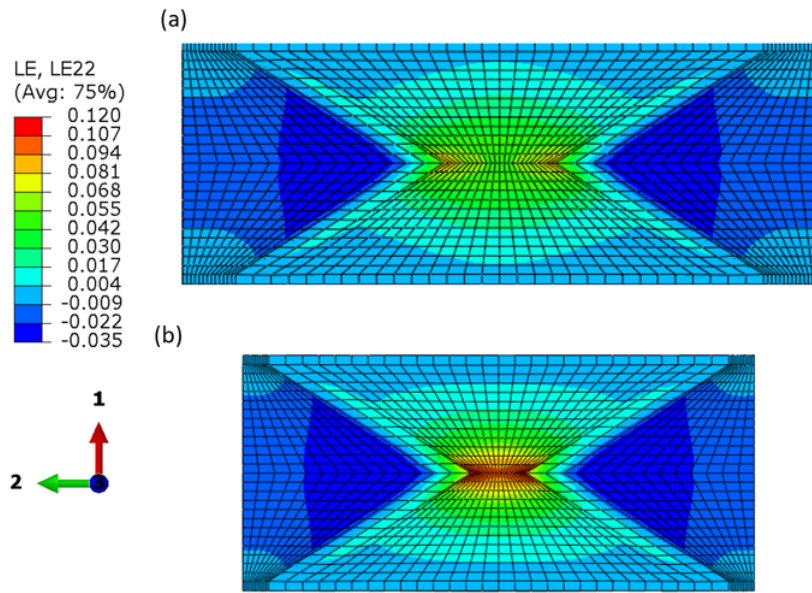


Figure 78. Transverse strain (2-axis) due to the unit cell being stretched in the 10% axial pre-strain (1-axis) for GATOR panels with (a) 6-millimetre and (b) 3-millimetre chevron separation (d) values.

It shows that a smaller distance between the chevrons increases the strain on the facesheet for the same deformation applied to both cells. Hence, in a spatially varying core geometry, it is desirable to constrain the cell sizes based on acceptable limits for maximum deflection under pressure load and maximum material yield strain in operating load cases.

Additional steps could be added to the line tracing process described in section 4.4.1 to add the capability to limit the cell sizes within a range of dimensions. These include a step to terminate the

line being traced based on its proximity to the already traced lines and a step to add additional seed points at the sparse regions of the traced lines. These additional steps will create traced lines which are discontinuous within the domain of the flattened fairing surface. The current procedure used in this study to re-sample the traced lines at the intersection points requires the traced lines to be continuous (i.e., each unit cell has another unit cell adjacent to all 4 of its faces). Hence, further improvement in the lattice generation process is required in future analysis.

As the lattice generation process requires traced lines to be continuous across the boundary (i.e., having an entry point and an exit point), the direction vector field must not have circulations. Hence, using the current procedure, a lattice cannot be generated for the load path vector fields with circulation regions. Moreover, the upper limits for the rotation angles from which the strain field can be used to generate a lattice using the current procedure are limited by the onset of compressive strain on the top skin. The compressive strain abruptly changes the principal strain directions, leading to traced lines forming asymptotes at regions where maximum and minimum principal directions swap. As the ribs or chevrons cannot converge to a line in a continuous lattice, the current lattice generation procedure cannot be used in these fields.

The current procedure uses the initial strain/stress field from a shell model with isotropic properties and generates a beam model lattice in the next iteration. As a similar field cannot be extracted from the beam model, the process cannot be iterated to optimise the spatially varying geometry of the lattice. In contrast, in shell-based studies similar to section 4.3.2, where material direction is assigned by changing the shell element's material axis, the procedure can be performed iteratively to optimise orientation [194]. Alternatively, an optimisation process can be applied to vary the lattice geometry using several control points for the beam-based model presented. The vector field from which the lines representing the core's ribs and chevrons are traced could then be varied using interpolated rotations and translations from these control points. These alternative approaches will be left to future work, as the main aim of this chapter has been to explore the basic viability of a spatially varying approach.

4.5. Conclusions

This chapter presented various methods of spatially varying the orientation of a material using the directions derived from the stress and strain field of the structure for a given load case. These methods are initially used in a shell-based model of a cantilevered plate made of elastomeric matrix composite. The stiffening effects of aligning the fibre direction with the direction derived from the deformed structure, such as the principal strain and load path direction, are studied. The largest increase in stiffness is achieved by aligning the fibres with the principal strain direction with the largest magnitude. Additionally, the material orientations that minimise the local strain energy for the local strain state were used to study their effects on the overall structural compliance. Only this material orientation improved the compliance of the plate relative to the reference uniform case. Further studies used a beam-based model of an accordion-type core geometry generated for a folding wing fairing. The core's ribs and chevron directions were aligned with the principal strain directions derived from a fairing with isotropic material properties deformed to various rotation angles. The

study showed that the overall density of the cells in the core determined whether the lattice reduced torque or increased it relative to the baseline. However, aligning the chevron with the principal strain direction with the greatest magnitude reduced the distortion of the fairing regardless of the cell density. An improved core design for the fairing was proposed using this insight. Further discussion highlighted the limitations of the methods used in this study, including the requirement for the lattice to be continuous. Further improvements in the lattice generation procedure and an optimisation procedure for improving the lattice design were also proposed for future work.

5. CONCLUSIONS

The thesis presented numerical studies of a morphing fairing design for folding wingtip joints, particularly focusing on the design requirements for the Semi-Aeroelastic Hinge (SAH) concept. The SAH concept has a free/flexible wingtip hinged to the inboard wing, with its rotation axis oriented at an outward angle to the aircraft's longitudinal axis. The low torsional stiffness of the hinge reduces the bending moment carried across the joint from the wingtip, and the outward orientation of the hinge axis reduces the local angle of attack at the wingtip as it folds up. These two features of the SAH concept enable it to alleviate gust loads, thereby enabling wingtip extension without a significant increase in the peak loads at the wing root. The free response of the wingtip further alleviates aircraft roll damping, improving its roll manoeuvrability to help meet aircraft certification requirements.

As the free response of the wingtip is required for gust load and roll damping alleviation in a non-negligible duration of the flight time, a fairing is required to cover the joint components both to seal it from debris and to provide an aerodynamic surface. The aeroelastic study of the SAH concept has identified low torsional stiffness, low wingtip mass and high flare angle as features that improve the load alleviation capability. Moreover, the SAH concept requires actuation to return the wingtip to a planform position when in steady flight and to an upright position after landing, as well as a clutch mechanism for instantaneous release of the wingtip on gust encounters. These requirements of the SAH concept limit the types of fairing that can be applied to the joint. To summarise, the fairing should minimise the added torsional stiffness and mass and must be able to accommodate non-zero flare angles and local bulges on the wing section around the joint created by the joint components.

The thesis proposed a fairing design based on a previously presented pivoting rib support structure and “Geometrically Anisotropic ThermOplastic Rubber” (GATOR) morphing sandwich panel skins. The pivoting rib is co-located with the SAH joint, sharing the same axis of rotation, but free to rotate independently of the folding angle, as its rotation angle is determined by the balance of moments on the rib due to the fairing panels on either side of it. The GATOR sandwich panel is made of an accordion-type core with parallel ribs and chevrons in between them and elastomeric facesheets bonded to the faces of the core. These panels are highly anisotropic with near-zero Poisson’s ratio due to high stiffness in the direction along the ribs of the core and high flexibility in the direction perpendicular to it. The thesis additionally proposed floating ribs that support the fairing at regular intervals between the outboard ribs of the fairing and the central pivoting rib. The floating ribs enforce the cross-section shape at their locations and reduce the distortion of the fairing as the wingtip folds. The thesis further proposed the use of spatial variation of the core geometry by

changing the orientation, size and shape of the cells to improve compliance and reduce distortion of the fairing.

5.1. Summary of the Results and Novel Contributions

The thesis presented a multi-scale modelling approach for studying the GATOR panel as a fairing with the wing section geometry. This modelling approach reduced the computational cost, enabling the parametric study of the effects of geometric features of the GATOR panel and the fairing geometry on the torsional stiffness and the distortion of the fairing. The multi-scale model comprises a unit cell of the GATOR panel whose elastic response is homogenised to an equivalent shell stiffness and a shell representation of the fairing over the wing section with equivalent properties of the GATOR panel. The homogenisation was carried out only at the undeformed state of the GATOR panel; hence, the equivalent stiffness of the shell fairing was defined as linear elastic properties. This modelling approach was validated in benchmark studies representing a fairing slice along the span at the thickest chordwise location of the wing section. The torque responses evaluated in the benchmark studies were comparable with the full-scale models, with an error below 2% for moderate folding angles of up to 40 degrees in configurations with applied pre-strain. Hence, this modelling approach offers a computationally affordable means of studying the mechanical performance of GATOR panel fairings over the wing section geometry.

The initial work presented a systemic study of the homogenised stiffness properties from analytical and finite element methods to identify the adequate level of fidelity required to represent the equivalent shell stiffness properties of the GATOR sandwich panel. The analytical expressions for the equivalent properties of an accordion-type core were used with the classical laminated plate theory to evaluate an equivalent shell stiffness for the GATOR panel. The finite element (FE) method used a unit cell of the GATOR panel with periodic boundary conditions on its vertical faces. The unit cell was deformed in each shell deformation mode, and its reaction forces were used to populate the columns of the shell stiffness matrix corresponding to each shell deformation mode. The following findings were identified by comparing various combinations of analytical, multi-scale and full-scale models:

- The analytical methods significantly underpredicted the stiffness properties of the accordion-type core with increasing error for thinner cores and stubbier chevron walls (i.e., low length-to-thickness ratio). The accuracy of the analytical methods was improved by using shortened lengths of the chevron and rib walls instead of their full lengths to account for the stiffening effect of the connections at the ends of these walls.
- The use of classical laminated plate theory underpredicted the stiffness of the GATOR panel due to the assumption of uniform strain on each layer of the laminate. The interaction between the facesheet and the core results in non-uniform deformation of the facesheet, significantly stiffening the GATOR panel. The FE-based homogenisation captures the non-uniform deformation of the facesheet, thereby providing representative equivalent stiffness properties for the GATOR panel.
- The equivalent flexural modulus in the morphing direction was evaluated by fitting the deformation response data from the FE-based full-scale models to the Timoshenko and Euler

beam equation to evaluate their discrepancy due to transverse shear deformation. The comparison of these equivalent flexural moduli with those evaluated by the FE-based homogenisation shows that the effects of transverse shear stiffness become negligibly small (i.e. error <1%) for panels longer than 9 cells in the morphing direction.

- Given that the fairing is at least 16 cells long between ribs in the case with 1 floating rib and 32 cells long in the case without floating ribs, the transverse shear stiffness is neglected in the multi-scale model. The comparison of the twin panels representing a slice of the fairing along the span at the thickest chordwise location showed good agreement between the multi-scale and full-scale models with moderately high folding angles (up to 40 degrees) in the configurations with pre-strain.

Secondly, the thesis presented a parametric study of the effects of the GATOR panel and fairing geometry on the torsional stiffness and the distortion of the fairing using the multi-scale modelling approach. The reaction torque of the hinge and the average reduction in the thickness of the fairing (referred to as the displacement metric) were identified as consistent metrics that represent torsional stiffness and cross-section distortion of the fairing. A sensitivity study identified the design variables that strongly influence each fairing metric, and the parametric study combined these design variables in pairs to identify their range of values that improve the objectives and reduce their trade-offs. The findings from both of these studies are summarised as follows:

- The sensitivity study showed that facesheet thickness, chevron length, and chevron angle significantly affected torque, while the core thickness and chevron length significantly affected distortion. In contrast, all fairing variables – fairing span, pre-strain and floating ribs, significantly affected both fairing objectives.
- The parametric study indicated weak coupling between the fairing objectives for changes in core and facesheet thicknesses. Thicker cores reduced distortion, while thinner facesheets reduced torque without a significant trade-off on the other objective. This weaker coupling indicates that these two variables, in particular, are effective in creating a better balance between in-plane and out-of-plane performance.
- The parametric study showed slender chevrons (i.e., high length-to-thickness ratio) undergo larger bending deformation, and large chevron angles increase the contribution of the chevron's bending deformation to panel deformation in the morphing direction. Hence, both slender chevrons and large chevron angles reduce fairing torque.
- The parametric study showed that floating ribs reduce distortion at some cost to torque, which can be offset by increasing the fairing span. Pre-strain further reduced the distortion by delaying the buckling of the top surface of the fairing.

Finally, the thesis presented a study of the effects of spatially varying the core geometry, without the facesheets, on the fairing objectives. Various methods of orienting the material to either increase stiffness or compliance were first trialled using a benchmark study. A method for approximating the material orientation that minimises strain energy was implemented using principle strain values and their directions. The field variables (i.e., stress and strain) were extracted from the deformed structure

with isotropic material properties. The directions derived from the fields (e.g., principal strain directions) defined the spatially varying orientation of the anisotropic material. A lattice with spatially varying cell size, shape, and orientation was created for the fairing geometry using the streamlines traced from the directions field. A beam-based lattice model was used to study the effects of the spatially varying geometry of the fairing objectives. The findings of the study are summarised as follows:

- The benchmark study used a cantilever plate made of fibre-reinforced elastomer composite with tip displacement loading. The stiffest plate design had fibres aligned with the principal strain direction with the highest magnitude, followed by the combined load path direction. The most compliant plate design had the material orientation optimised to minimise the local strain energy for the local strain state.
- The lattice generation process enforces the baseline unit cell dimensions between the traced lines at the initial seed location. Hence, the overall cell density of the lattice depends on the relative density of the traced lines in this initial seed location.
- The lattices generated using cosine waves to define the core's rib direction did not improve the torque nor distortion response of the fairing, indicating that regular curvilinear orientation does not improve the fairing objectives.
- The lattice generated using principal strain directions is denser for an initial seed point at the mid-chord of the top surface compared to having the initial seed point at the leading edge. The sparse lattice fairing showed a significantly lower torque than the baseline fairing with a uniform core, while the dense lattice showed a significantly higher torque than the baseline. Both spatially varied lattice fairings have lower distortion than the baseline fairing.

Overall, the thesis presented the development of numerical analysis methods to analyse highly deformable, compliance-based morphing fairings for complex geometry. A systematic exploration of the design space offered by the GATOR panel as a fairing for the folding wingtip joints was then undertaken. The presented studies focus on reducing torsional stiffness and fairing distortion – two features essential for a fairing for the SAH wingtip concept. The novel contributions of this thesis are summarised as follows:

- Developing solid-to-shell homogenisation and shell-based fairing model generation framework that automates the GATOR panel fairing analysis process
- Identifying the homogenisation fidelity required to represent GATOR panels as a shell surface to model the folding wingtip fairing,
- Identifying the design variables strongly influencing the fairing objectives and the pairs of those design variables that reduce the trade-offs between the objectives.
- Developing lattice generation framework using traced streamlines of various field-derived directions such as principal strain and load path.
- Identifying the benefits of core alignment with principal strain direction in reducing distortion and the effects of overall cell density on the torque response.

5.2. Recommendations for Future Work

The limitations of the current studies, along with their implications, technical challenges and recommended improvements in future studies, are summarised as follows:

- Negligence of transverse shear stiffness in the homogenisation of GATOR panel.
 - **Implication:** Error in shell-based fairing models with more than 1 floating rib due to transverse shear deformation.
 - **Technical Challenge:** In a plate model, the top and bottom surfaces must remain traction-free. Hence, to solve the boundary value problem for homogenisation as described in Section 2.2.2, transverse shear must be applied using the displacement of nodes on the vertical faces. However, such application of transverse shear only using the vertical faces leads to spurious bending modes [152]. These spurious bending modes are removed using volumetric constraints that couple all nodes of the model to apply a pure transverse shear deformation [152]. This approach makes the simulation expensive, particularly considering the fine mesh required to achieve convergence due to the small features of the cellular core.
 - **Recommendation:** The periodic boundary conditions used in the homogenisation method described in Section 2.2.2 consider a unit cell that can be tessellated by translating it to assemble the full panel. A reduced unit cell can be tessellated using a combination of translation and rotation to assemble the full panel. Hence, a reduced unit cell with appropriate boundary conditions [153] can reduce the RVE size required for the homogenisation process, thereby reducing the computational cost of evaluating the equivalent transverse shear properties.
- Assumption of linear elastic stiffness properties for the shell fairing.
 - **Implication:** Change in equivalent stiffness properties of the GATOR panel due to geometric nonlinearity in deformation is not reflected in the shell model.
 - **Technical Challenge:** Coupling a unit cell with each shell element is infeasible due to the computation cost.
 - **Recommendation:** Update the shell element's stiffness using the interpolated values from a pre-computed database of equivalent GATOR panel stiffness at various strain states.
- Beam-based lattice generated only for direction fields (e.g., principal strain) where the traced lines do not converge to an asymptote line or a point (e.g., vortex, source/sink).
 - **Implication:** Lattice fairing cannot be generated for some direction fields (e.g., load paths with circulations and principal strain directions with asymptotes) derived from a deformed structure.
 - **Technical Challenge:** The current lattice generation procedure requires the traced lines to be continuous; hence, traced lines cannot be discontinuous to prevent them from converging to asymptote lines and points.

- **Recommendation:** Combine the line tracing and lattice generation process to incorporate the ability to merge lines that converge to asymptotes and discontinue lines that converge to a point [196].

Other recommendations for future work include experimental testing of the twin-panel model representing a fairing slice along the span at the thickest chordwise location, before moving on to test more complex three-dimensional representations of the fairing. The experimental results can be used to validate and further develop the full-scale model and multi-scale model used in the numerical study presented in this thesis.

Further studies should consider the fatigue on the panel under repetitive loading, particularly focusing on possible debonding between the facesheet and the core. In addition to the shear load at the bonding area between the facesheet and the core due to the morphing deformation of the panel, the joint area is also subject to a peeling load due to suction aerodynamic pressure on the top surface of the wing. Hence, experimental studies should be carried out to characterise the bond strength between the facesheet and the core under a peeling load. Further analysis is also required to design flanges at the edges of the core walls that bond to the facesheet to increase the bond strength to carry pressure loading on the fairing.

REFERENCE

- [1] *The Paris Agreement*, December 2015. United Nations Framework Convention on Climate Change. URL <https://www.un.org/en/climatechange/paris-agreement>. Adopted by 196 Parties at the UN Climate Change Conference (COP21) in Paris, France.
- [2] Intergovernmental Panel on Climate Change. *Global Warming of 1.5°C: IPCC Special Report on Impacts of Global Warming of 1.5°C above Pre-industrial Levels in Context of Strengthening Response to Climate Change, Sustainable Development, and Efforts to Eradicate Poverty*. Cambridge University Press, May 2022. doi: [10.1017/9781009157940](https://doi.org/10.1017/9781009157940).
- [3] *Long term global aspirational goal (LTAG) for international aviation*, October 2022. International Civil Aviation Organization. URL <https://www.icao.int/environmental-protection/Pages/LTAG.aspx>. Adopted in 41st ICAO Assembly in ICAO Headquarters in Montreal, Canada.
- [4] *Net-Zero Carbon Emissions by 2050*, October 2021. International Air Transport Association. URL <https://www.iata.org/en/pressroom/2021-releases/2021-10-04-01/>. Adopted in the IATA 77th Annual General Meeting in Boston, USA.
- [5] International Civil Aviation Organization. Carbon Offsetting and Reduction Scheme for International Aviation (CORSIA), October 2016. URL <https://www.icao.int/environmental-protection/CORSIA>. Accessed: 2024-08-15.
- [6] Air Transport Action Group. Waypoint 2050 report. Research Report 2, Air Transport Action Group, September 2021. URL <https://aviationbenefits.org/environmental-efficiency/climate-action/waypoint-2050/>.
- [7] Candelaria Bergero, Greer Gosnell, Dolf Gielen, Seungwoo Kang, Morgan Bazilian, and Steven J. Davis. Pathways to net-zero emissions from aviation. *Nature Sustainability*, 6 (4): 404–414, January 2023. ISSN 2398-9629. doi: [10.1038/s41893-022-01046-9](https://doi.org/10.1038/s41893-022-01046-9).
- [8] Mikhail Chester and Arpad Horvath. High-speed rail with emerging automobiles and aircraft can reduce environmental impacts in California's future. *Environmental Research Letters*, 7 (3): 034012, July 2012. ISSN 1748-9326. doi: [10.1088/1748-9326/7/3/034012](https://doi.org/10.1088/1748-9326/7/3/034012).
- [9] International Civil Aviation Organization. ICAO Environmental Report 2022: Innovation for a Green Transition. Technical report, International Civil Aviation Organization, 2022. URL <https://www.icao.int/environmental-protection/Pages/envrep2022.aspx>.
- [10] Maximilian T. E. Heinrich, Fabian Kelch, Pierre Magne, and Ali Emadi. Regenerative Braking Capability Analysis of an Electric Taxiing System for a Single Aisle Midsize Aircraft. *IEEE Transactions on Transportation Electrification*, 1 (3): 298–307, October 2015. ISSN 2332-7782. doi: [10.1109/tte.2015.2464871](https://doi.org/10.1109/tte.2015.2464871).

- [11] Michael Schmidt. A review of aircraft turnaround operations and simulations. *Progress in Aerospace Sciences*, 92: 25–38, July 2017. ISSN 0376-0421. doi: [10.1016/j.paerosci.2017.05.002](https://doi.org/10.1016/j.paerosci.2017.05.002).
- [12] Rolls-Royce. UltraFan Demonstrator Aero Engine. URL <https://www.rolls-royce.com/products-and-services/civil-aerospace/ultrafan.aspx>. Accessed: 2024-08-15.
- [13] A. L. Braslow. History of Suction-Type Laminar-Flow Control with Emphasis on Flight Research. Tech Report PB99-166142, National Aeronautics and Space Administration, January 1999. URL <https://ntrs.nasa.gov/citations/19990078750>.
- [14] Jörg Zumkley. Aeroshark from lufthansa technik and basf now certified for boeing 777. Press Release, December 2022. URL <https://www.bASF.com/global/en/media/news-releases/2022/-12/p-22-433.html>.
- [15] James R. Hansen, D. Bryan Taylor, Jeremy Kinney, and J. Lawrence Lee. *The Wind and Beyond: A Documentary Journey into the History of Aerodynamics in America*. Number LC-2002-035774. National Aeronautics and Space Administration, 2003. URL <https://ntrs.nasa.gov/-citations/20040031410>.
- [16] Aerospace Technology Institute. INSIGHT: Composite Materials, September 2018. URL https://www.ati.org.uk/wp-content/uploads/2021/08/insight_9-composites_amended-2018-09-20.pdf. Accessed: 2024-08-15.
- [17] Silvestro Barbarino, Onur Bilgen, Rafic M. Ajaj, Michael I. Friswell, and Daniel J. Inman. A Review of Morphing Aircraft. *Journal of Intelligent Material Systems and Structures*, 22 (9): 823–877, June 2011. doi: [10.1177/1045389x11414084](https://doi.org/10.1177/1045389x11414084).
- [18] Daochun Li, Shiwei Zhao, Andrea Da Ronch, Jinwu Xiang, Jernej Droljnik, Yongchao Li, Lu Zhang, Yining Wu, Markus Kintscher, Hans Peter Monner, Anton Rudenko, Shijun Guo, Weilong Yin, Johannes Kirn, Stefan Storm, and Roeland De Breuker. A review of modelling and analysis of morphing wings. *Progress in Aerospace Sciences*, 100: 46–62, June 2018. ISSN 0376-0421. doi: [10.1016/j.paerosci.2018.06.002](https://doi.org/10.1016/j.paerosci.2018.06.002).
- [19] Terrence A. Weisshaar. Morphing Aircraft Systems: Historical Perspectives and Future Challenges. *Journal of Aircraft*, 50 (2): 337–353, March 2013. doi: [10.2514/1.c031456](https://doi.org/10.2514/1.c031456).
- [20] Orville Wright and Wilbur Wright. Flying-machine, March 1903. U.S. Patent No: US14922003A.
- [21] H F Parker. The Parker Variable Camber Wing. Tech Report NACA-TR-77, National Advisory Committee for Aeronautics, 1920. URL <https://ntrs.nasa.gov/citations/19930091138>.
- [22] Aviation Stack Exchange. Why do some aircraft have multiple ailerons per wing?, August 2015. URL <https://aviation.stackexchange.com/questions/921/why-do-some-aircraft-have-multiple-ailerons-per-wing>. Accessed: 2024-08-27.
- [23] Hans Peter Monner. Realization of an optimized wing camber by using formvariable flap structures. *Aerospace Science and Technology*, 5 (7): 445–455, October 2001. ISSN 1270-9638. doi: [10.1016/s1270-9638\(01\)01118-x](https://doi.org/10.1016/s1270-9638(01)01118-x).
- [24] Jonathan D. Bartley-Cho, Donny P. Wang, Christopher A. Martin, Jayanth N. Kudva, and Mark N. West. Development of high-rate, adaptive trailing edge control surface for the smart

- wing phase 2 wind tunnel model. *Journal of Intelligent Material Systems and Structures*, 15 (4): 279–291, April 2004. ISSN 1530-8138. doi: [10.1177/1045389x04042798](https://doi.org/10.1177/1045389x04042798).
- [25] Benjamin King Sutton Woods and Michael I. Friswell. Preliminary Investigation of a Fishbone Active Camber Concept. In *Volume 2: Mechanics and Behavior of Active Materials; Integrated System Design and Implementation; Bio-Inspired Materials and Systems; Energy Harvesting*. American Society of Mechanical Engineers, September 2012. doi: [10.1115/smasis2012-8058](https://doi.org/10.1115/smasis2012-8058).
- [26] Benjamin K. S. Woods, Laura Parsons, Alexander B. Coles, James H. S. Fincham, and Michael I. Friswell. Morphing elastically lofted transition for active camber control surfaces. *Aerospace Science and Technology*, 55: 439–448, August 2016. doi: [10.1016/j.ast.2016.06.017](https://doi.org/10.1016/j.ast.2016.06.017).
- [27] Hui Yang, Songcheng Jiang, Yan Wang, and Hong Xiao. Design, kinematic and fluid-structure interaction analysis of a morphing wing. *Aerospace Science and Technology*, 143: 108721, December 2023. ISSN 1270-9638. doi: [10.1016/j.ast.2023.108721](https://doi.org/10.1016/j.ast.2023.108721).
- [28] Terrence A. Weisshaar. Morphing Aircraft Technology - New Shapes for Aircraft Design. Tech Report RTO-MP-AVT-141, North Atlantic Treaty Organisation (NATO), Neuilly-sur-Seine, France., October 2006. URL <https://apps.dtic.mil/sti/citations/ADA479821>.
- [29] R. C. Monaghan. Flight-measured buffet characteristics of a supercritical wing and a conventional wing on a variable-sweep airplane. Tech Report NASA-TP-1244, National Aeronautics and Space Administration, May 1978. URL <https://ntrs.nasa.gov/citations/-19780015113>.
- [30] Andrei Vladimir Popov, Teodor Lucian Grigorie, Ruxandra Mihaela Botez, Youssef Mébarki, and Mahmood Mamou. Modeling and Testing of a Morphing Wing in Open-Loop Architecture. *Journal of Aircraft*, 47 (3): 917–923, May 2010. ISSN 1533-3868. doi: [10.2514/1.46480](https://doi.org/10.2514/1.46480).
- [31] Sridhar Kota and Joel A. Hetrick. Adaptive compliant wing and rotor system, 2003. U.S. Patent No: US 7,384,016 B2.
- [32] Ed Pendleton, Peter Flick, Donald Paul, Dave Voracek, Eric Reichenbach, and Ken Griffin. The x-53 a summary of the active aeroelastic wing flight research program. In *48th AIAA/ASME/ASCE/AHS/ASC Structures, Structural Dynamics, and Materials Conference*. American Institute of Aeronautics and Astronautics, April 2007. doi: [10.2514/6.2007-1855](https://doi.org/10.2514/6.2007-1855).
- [33] North American Rockwell Corp. B-70 Aircraft Study. Tech Report NASA-CR-115703, National Aeronautics and Space Administration (NASA), April 1972. URL <https://ntrs.nasa.gov/citations/19950002359>.
- [34] Olivier Léon, Eric Hayden, and Farhan Gandhi. Rotorcraft Operating Envelope Expansion Using Extendable Chord Sections. In *Proceedings of American Helicopter Society 65th Annual Forum*, Grapevine, TX, USA, May 2009.
- [35] Robert W. Kress. Variable sweep wing design. In *The evolution of aircraft wing design; Proceedings of the Symposium*. American Institute of Aeronautics and Astronautics, March 1980. doi: [10.2514/6.1980-3043](https://doi.org/10.2514/6.1980-3043).
- [36] R. Whitford. *Design for Air Combat*, chapter Variable Sweep Wings, page 72. Jane's Information Group, 1987. ISBN 9780710604262.

- [37] E Stanewsky. Adaptive wing and flow control technology. *Progress in Aerospace Sciences*, 37 (7): 583–667, October 2001. ISSN 0376-0421. doi: [10.1016/s0376-0421\(01\)00017-3](https://doi.org/10.1016/s0376-0421(01)00017-3).
- [38] Daniel Coutu, Vladimir Brailovski, Patrick Terriault, Mahmoud Mamou, and Youssef Mebarki. Aerostructural model for morphing laminar wing optimization in a wind tunnel. *Journal of Aircraft*, 48 (1): 66–76, January 2011. ISSN 1533-3868. doi: [10.2514/1.c000232](https://doi.org/10.2514/1.c000232).
- [39] David Zingg, Laslo Diosady, and Laura Billing. Adaptive airfoils for drag reduction at transonic speeds. In *24th AIAA Applied Aerodynamics Conference*. American Institute of Aeronautics and Astronautics, June 2006. doi: [10.2514/6.2006-3656](https://doi.org/10.2514/6.2006-3656).
- [40] G. Dargel and P. Thiede. *Assessment of Shock and Boundary Layer Control Concepts for Hybrid Laminar Flow Wing Design*, pages 383–414. Springer Berlin Heidelberg, 2002. ISBN 9783540458562. doi: [10.1007/978-3-540-45856-2_13](https://doi.org/10.1007/978-3-540-45856-2_13).
- [41] J. J. Spillman. The use of variable camber to reduce drag, weight and costs of transport aircraft. *The Aeronautical Journal* (1968), 96 (951): 1–9, 1992. doi: [10.1017/S0001924000024404](https://doi.org/10.1017/S0001924000024404).
- [42] E. Greff. The development and design integration of a variable camber wing for long/medium range aircraft. *The Aeronautical Journal*, 94 (939): 301–312, November 1990. ISSN 2059-6464. doi: [10.1017/s0001924000023186](https://doi.org/10.1017/s0001924000023186).
- [43] H. Hilbig and H. Wagner. Variable wing camber control for civil transport aircraft. In *International Council of the Aeronautical Sciences (ICAS) Proceedings*, number ICAS-84-5.2.1, pages 107–112, Toulouse, 1984.
- [44] Joel Hetrick, Russell Osborn, Sridhar Kota, Peter Flick, and Donald Paul. Flight testing of mission adaptive compliant wing. In *48th AIAA/ASME/ASCE/AHS/ASC Structures, Structural Dynamics, and Materials Conference*. American Institute of Aeronautics and Astronautics, April 2007. doi: [10.2514/6.2007-1709](https://doi.org/10.2514/6.2007-1709).
- [45] Edmund W. Pendleton, Denis Bessette, Peter B. Field, Gerald D. Miller, and Kenneth E. Griffin. Active aeroelastic wing flight research program: Technical program and model analytical development. *Journal of Aircraft*, 37 (4): 554–561, July 2000. ISSN 1533-3868. doi: [10.2514/2.2654](https://doi.org/10.2514/2.2654).
- [46] Boyd Perry, Stanley R. Cole, and Gerald D. Miller. Summary of an active flexible wing program. *Journal of Aircraft*, 32 (1): 10–15, January 1995. ISSN 1533-3868. doi: [10.2514/3.46677](https://doi.org/10.2514/3.46677).
- [47] Bill Gunston. *The Osprey Encyclopedia Of Russian Aircraft 1875-1995*. Osprey Aerospace, London, 1995. ISBN 1855324059.
- [48] J.W. Ross and D.B. Rogerson. XB-70 technology advancements. In *Aircraft Prototype and Technology Demonstrator Symposium*. American Institute of Aeronautics and Astronautics, March 1983. doi: [10.2514/6.1983-1048](https://doi.org/10.2514/6.1983-1048).
- [49] Boeing. Boeing 777X -Technical Specs. URL <https://www.boeing.com/commercial/777x/>. Accessed: 2022-05-27.
- [50] Neal A. Harrison, Krishna Hoffman, David S. Lazzara, Eric Y. Reichenbach, Anthony J. Sclafani, and Christopher K. Droney. Subsonic Ultra Green Aircraft Research (Phase IV Final Report - Volume I): Mach 0.80 Transonic Truss-Braced Wing High-Speed Design Report. Tech Report NASA/CR-20220016017, National Aeronautics and Space Administration (NASA), 2023.

- [51] Thomas Wilson, James Kirk, John Hobday, and Andrea Castrichini. Small scale flying demonstration of semi aeroelastic hinged wing tips. In *19th International Forum on Aeroelasticity and Structural Dynamics (IFASD 2019)*, Savannah, Georgia, USA, June 2019.
- [52] Flight Aware. Aircraft flight data from easyJet 3078 (A320): Hurghada, Egypt to Belfast, United Kingdom, September 2024. URL <https://www.flightradar24.com/live/flight/EZY3078>. Accessed: 2024-09-20.
- [53] Vladimir Kornilov. Combined blowing/suction flow control on low-speed airfoils. *Flow, Turbulence and Combustion*, 106 (1): 81–108, August 2020. ISSN 1573-1987. doi: [10.1007/s10494-020-00157-7](https://doi.org/10.1007/s10494-020-00157-7).
- [54] E. M. Greitzer and Z. S. Spakovszky and I. A. Waitz. MIT Lecture Notes: Thermodynamics and Propulsion, 2008. URL <https://web.mit.edu/16.unified/www/FALL/thermodynamics/>. Accessed: 2024-09-19.
- [55] Louis Bréguet. *Calcul du poids de combustible consommé par un avion en vol ascendant*. Gauthier-Villars, 1920.
- [56] R. Liebeck. Design of the Blended-Wing-Body subsonic transport. In *40th AIAA Aerospace Sciences Meeting & Exhibit*. American Institute of Aeronautics and Astronautics, January 2002. doi: [10.2514/6.2002-2](https://doi.org/10.2514/6.2002-2).
- [57] Paul Okonkwo and Howard Smith. Review of evolving trends in blended wing body aircraft design. *Progress in Aerospace Sciences*, 82: 1–23, April 2016. ISSN 0376-0421. doi: [10.1016/j.paerosci.2015.12.002](https://doi.org/10.1016/j.paerosci.2015.12.002).
- [58] Federal Aviation Administration. FAA Advisory Circular 18150/5300-13B - Airport Design, March 2022.
- [59] International Civil Aviation Organization. Annex 14 - Aerodromes - Volume I - Aerodromes Design and Operations, July 2004. URL <https://store.icao.int/en/annex-14-aerodromes>.
- [60] IFATC. Gates Information for Heathrow Airport (EGLL), 2024. URL <https://www.ifatc.org/-/gates?code=EGLL>. Accessed: 2024-09-24.
- [61] Alan Wilson. Naval variant of the second generation MiG-29, August 2017. URL <https://www.flickr.com/photos/ajw1970/36928677816/>. Accessed: 2024-09-24.
- [62] Dan Nevill. The folded wingtip of the Boeing 777X, seen at the rollout of the first 777-9 airframe in Everett, Washington., March 2019. URL <https://www.flickr.com/photos/dnevill/-40407369583/>. Accessed: 2024-09-24.
- [63] National Aeronautics and Space Administration. XB-70A Valkyrie on ramp at Dryden Flight Research Centre, 1967. URL <https://www.dvidshub.net/image/709611/xb-70a-parked-ramp>. Accessed: 2024-09-25.
- [64] W. H. Andrews. Summary of preliminary data derived from the XB-70 airplanes. Technical report, National Aeronautics and Space Administration, 1966. URL <https://ntrs.nasa.gov/citations/19660018723>.
- [65] T. E. Leontis. Properties of Magnesium-Thorium and Magnesium-Thorium-Cerium Alloys. *JOM*, 4 (3): 287–294, March 1952. ISSN 1543-1851. doi: [10.1007/bf03397693](https://doi.org/10.1007/bf03397693).

- [66] Thomas Wilson and Martin Herring. High Fidelity Simulation of the Folding Wing Tip. In *International Forum on Aeroelasticity and Structural Dynamics*, Saint Petersburg, Russia, June 2015.
- [67] A. Castrichini, V. Hodigere Siddaramaiah, D. E. Calderon, J. E. Cooper, T. Wilson, and Y. Lemmens. Preliminary investigation of use of flexible folding wing tips for static and dynamic load alleviation. *The Aeronautical Journal*, 121 (1235): 73–94, November 2016. doi: [10.1017/aer.2016.108](https://doi.org/10.1017/aer.2016.108).
- [68] Andrea Castrichini, Jonathan E. Cooper, Thomas Wilson, Alessandro Carrella, and Yves Lemmens. Nonlinear Negative Stiffness Wing-Tip Spring Device for Gust Loads Alleviation. In *15th Dynamics Specialists Conference*. American Institute of Aeronautics and Astronautics, January 2016. doi: [10.2514/6.2016-1574](https://doi.org/10.2514/6.2016-1574).
- [69] T. Wilson, A. Azabal, A. Castrichini, J. Cooper, R. Ajaj, and M. Herring. Aeroelastic behaviour of hinged wing tips. In *5th Aircraft Structural Design Conference*, Manchester, United Kingdom, October 2016. Royal Aeronautical Society.
- [70] Ronald C. Cheung, Andrea Castrichini, Djamel Rezgui, Jonathan E. Cooper, and Thomas Wilson. Testing of Wing-Tip Spring Device for Gust Loads Alleviation. In *58th AIAA/ASCE/AHS/ASC Structures, Structural Dynamics, and Materials Conference*. American Institute of Aeronautics and Astronautics, January 2017. doi: [10.2514/6.2017-0630](https://doi.org/10.2514/6.2017-0630).
- [71] Ronald Cheung, Andrea Castrichini, Djamel Rezgui, Jonathan Cooper, and Thomas Wilson. Wind Tunnel Testing of Folding Wing-Tip Devices for Gust Loads Alleviation. In *17th International Forum on Aeroelasticity and Structural Dynamics (IFASD 2017)*, pages 534–550, May 2018. ISBN 9781510861008.
- [72] V. Hodigere Siddaramaiah, D. E. Calderon, J. E. Cooper, and T. Wilson. Preliminary Studies in the use of Folding Wing-tips for Loads Alleviation. In *Royal Aeronautical Society Applied Aerodynamics Conference*, Bristol, UK, 2014.
- [73] A. Castrichini, V. Hodigere Siddaramaiah, D. E. Calderon, J. E. Cooper, T. Wilson, and Y. Lemmens. Nonlinear Folding Wing Tips for Gust Loads Alleviation. *Journal of Aircraft*, 53 (5): 1391–1399, September 2016. doi: [10.2514/1.c033474](https://doi.org/10.2514/1.c033474).
- [74] Andrea Castrichini, Thomas Wilson, and J. E. Cooper. On the Dynamic Release of the Semi Aeroelastic Wing-Tip Hinge Device. In *6th Aircraft Structural Design Conference*, October 2018.
- [75] European Union Aviation Safety Agency (EASA). Certification Specifications and Acceptable Means of Compliance for Large Aeroplanes (CS-25), December 2023. URL <https://www.easa.europa.eu/en/document-library/certification-specifications/group/cs-25-large-aeroplanes>. Accessed: 2024-10-04.
- [76] Federal Aviation Administration (FAA). 14 CFR Part 23 - Airworthiness Standards: Normal Category Airplanes, December 2016. URL <https://www.ecfr.gov/current/title-14/chapter-I/subchapter-C/part-23>. Accessed: 2024-10-04.
- [77] A. Castrichini, T. Wilson, F. Saltari, F. Mastroddi, N. Viceconti, and J. E. Cooper. Aeroelastics Flight Dynamics Coupling Effects of the Semi-Aeroelastic Hinge Device. *Journal of Aircraft*, 57 (2): 333–341, March 2020. doi: [10.2514/1.c035602](https://doi.org/10.2514/1.c035602).

- [78] Fintan Healy, Ronald Cheung, Theodor Neofet, Mark Lowenberg, Djamel Rezgui, Jonathan Cooper, Andrea Castrichini, and Tom Wilson. Folding wingtips for improved roll performance. *Journal of Aircraft*, 59 (1): 15–28, January 2022. ISSN 1533-3868. doi: [10.2514/1.c036372](https://doi.org/10.2514/1.c036372).
- [79] Thomas Wilson, Andrea Castrichini, John Paterson, and Raul Arribas Ardura. Non-linear aeroelastic behaviour of hinged wing tips. In *RAeS 6th Aerospace Structures Design Conference*, Bristol, United Kingdom, October 2018.
- [80] Thomas Wilson, James Kirk, John Hobday, and Andrea Castrichini. Update on AlbatrossONE Semi Aeroelastic Hinge Small Scale Flying Demonstrator Project. In *International Forum on Aeroelasticity and Structural Dynamics*, Madrid, Spain, June 2022.
- [81] Fintan Healy, Alessandro Pontillo, Djamel Rezgui, Jonathan E. Cooper, James Kirk, Thomas Wilson, and Andrea Castrichini. Experimental Analysis of the Dynamics of Flared Folding Wingtips via a Novel Tethered Flight Test. In *AIAA SCITECH 2022 Forum*. American Institute of Aeronautics and Astronautics, January 2022. doi: [10.2514/6.2022-1757](https://doi.org/10.2514/6.2022-1757).
- [82] Fintan Healy, Ronald Cheung, Djamel Rezgui, Jonathan Cooper, Thomas Wilson, and Andrea Castrichini. On the Effect of Geometric Nonlinearity on the Dynamics of Flared Folding Wingtips. *Journal of Aircraft*, 60 (2): 368–381, March 2023. ISSN 1533-3868. doi: [10.2514/1.c036877](https://doi.org/10.2514/1.c036877).
- [83] Fintan Healy, Djamel Rezgui, and Jonathan E. Cooper. Experimental Effect of Sideslip Angle on the Dynamic Behaviour of Flared Folding Wingtips. In *AIAA SCITECH 2023 Forum*. American Institute of Aeronautics and Astronautics, January 2023. doi: [10.2514/6.2023-0376](https://doi.org/10.2514/6.2023-0376).
- [84] Fintan Healy, Ronald Cheung, Djamel Rezgui, Jonathan Cooper, Thomas Wilson, and Andrea Castrichini. Experimental and Numerical Nonlinear Stability Analysis of Wings Incorporating Flared Folding Wingtips. *Journal of Aircraft*, 61 (1): 140–154, January 2024. ISSN 1533-3868. doi: [10.2514/1.c037167](https://doi.org/10.2514/1.c037167).
- [85] Fintan Healy, Joe De Courcy, Huaiyuan Gu, Djamel Rezgui, Jonathan Cooper, Thomas Wilson, and Andrea Castrichini. On the Dynamic Behavior of Wings Incorporating Floating Wingtip Fuel Tanks. *Journal of Aircraft*, 61 (3): 785–800, May 2024. ISSN 1533-3868. doi: [10.2514/1.c037519](https://doi.org/10.2514/1.c037519).
- [86] Huaiyuan Gu, Fintan Healy, Sanuja Jayatilake, Djamel Rezgui, Mark Lowenberg, Jonathan Cooper, Thomas Wilson, and Andrea Castrichini. Flight dynamics of aircraft incorporating the semi-aeroelastic hinge. *Aerospace Science and Technology*, 147: 109026, April 2024. ISSN 1270-9638. doi: [10.1016/j.ast.2024.109026](https://doi.org/10.1016/j.ast.2024.109026).
- [87] Huaiyuan Gu, Fintan Healy, Lucian Constantin, Djamel Rezgui, Mark Lowenberg, Jonathan E. Cooper, Thomas Wilson, and Andrea Castrichini. Aeroelastic Scaling of a High-Aspect-Ratio Wing Incorporating a Semi-Aeroelastic Hinge. *AIAA Journal*, pages 1–13, April 2024. ISSN 1533-385X. doi: [10.2514/1.j063646](https://doi.org/10.2514/1.j063646).
- [88] Patrick Bourdin, Alvin Gatto, and Michael Friswell. Potential of articulated split wingtips for morphing-based control of a flying wing. In *25th AIAA Applied Aerodynamics Conference*. American Institute of Aeronautics and Astronautics, June 2007. doi: [10.2514/6.2007-4443](https://doi.org/10.2514/6.2007-4443).

- [89] Matt Kamlet. NASA Tests New Alloy to Fold Wings in Flight. Online, January 2018. URL <https://www.nasa.gov/centers/armstrong/feature/nasa-tests-new-alloy-to-fold-wings-in-flight.html>. Accessed: 14 May 2022.
- [90] Xavier Lachenal, Paul M. Weaver, and Alberto Pirrera. Concept for a deployable wing. In *Volume 2: Mechanics and Behavior of Active Materials; Integrated System Design and Implementation; Bioinspired Smart Materials and Systems; Energy Harvesting*. American Society of Mechanical Engineers, September 2014. doi: [10.1115/smasis2014-7428](https://doi.org/10.1115/smasis2014-7428).
- [91] P. Bourdin, A. Gatto, and M. I. Friswell. Aircraft control via variable cant-angle winglets. *Journal of Aircraft*, 45 (2): 414–423, March 2008. ISSN 1533-3868. doi: [10.2514/1.27720](https://doi.org/10.2514/1.27720).
- [92] P. Bourdin, A. Gatto, and M. I. Friswell. Performing co-ordinated turns with articulated wing-tips as multi-axis control effectors. *The Aeronautical Journal*, 114 (1151): 35–47, January 2010. ISSN 2059-6464. doi: [10.1017/s0001924000003511](https://doi.org/10.1017/s0001924000003511).
- [93] Matt Kamlet. NASA to Test In-Flight Folding Spanwise Adaptive Wing to Enhance Aircraft Efficiency, October 2016. URL <https://www.nasa.gov/centers-and-facilities/armstrong/nasa-to-test-in-flight-folding-spanwise-adaptive-wing-to-enhance-aircraft-efficiency/>. Accessed: 2024-10-13.
- [94] Nikki Welch. Metal with Memory: F-18 Wing Fold, August 2018. URL <https://www.nasa.gov/aeronautics/metal-with-memory-f-18-wing-fold/>. Accessed: 2024-10-13.
- [95] Lillian Gipson. Metal with Memory: Shaping the Future of Aviation, October 2017. URL <https://www.nasa.gov/centers-and-facilities/armstrong/metal-with-memory-shaping-the-future-of-aviation/>. Accessed: 2024-10-13.
- [96] Patricia Ortiz and Nicholas Alley. Spanwise Adaptive Wing - PTERA Flight Test. Tech report, National Aeronautics and Space Administration, June 2018. URL <https://ntrs.nasa.gov/citations/20180004640>.
- [97] Aileen G. Bowen, Giovanni Zucco, and Paul Weaver. Folding of flexible hinges for aircraft wingtips and wind turbine blades. In *AIAA Scitech 2021 Forum*. American Institute of Aeronautics and Astronautics, January 2021. doi: [10.2514/6.2021-0204](https://doi.org/10.2514/6.2021-0204).
- [98] Aileen G. Bowen, Giovanni Zucco, and Paul M. Weaver. Folding aerofoil sections exploiting brazier phenomena. *Composite Structures*, 303: 116238, January 2023. ISSN 0263-8223. doi: [10.1016/j.compstruct.2022.116238](https://doi.org/10.1016/j.compstruct.2022.116238).
- [99] Aileen G. Bowen, Giovanni Zucco, and Paul M. Weaver. Morphing of symmetric cross-ply cylindrical shells by minimising the brazier moment: Optimised hinge folding. *Thin-Walled Structures*, 158: 107122, January 2021. doi: [10.1016/j.tws.2020.107122](https://doi.org/10.1016/j.tws.2020.107122).
- [100] J. E. Cooper, I. Chekkal, R. C. M. Cheung, C. Wales, N. J. Allen, S. Lawson, A. J. Peace, R. Cook, P. Standen, S. D. Hancock, and G. M. Carossa. Design of a Morphing Wingtip. *Journal of Aircraft*, 52 (5): 1394–1403, September 2015. doi: [10.2514/1.c032861](https://doi.org/10.2514/1.c032861).
- [101] Chen Wang, Hamed Haddad Khodaparast, and Michael I. Friswell. Conceptual study of a morphing winglet based on unsymmetrical stiffness. *Aerospace Science and Technology*, 58: 546–558, November 2016. ISSN 1270-9638. doi: [10.1016/j.ast.2016.09.015](https://doi.org/10.1016/j.ast.2016.09.015).

- [102] Chen Wang, Hamed Haddad Khodaparast, Michael I Friswell, Alexander D Shaw, Yuying Xia, and Peter Walters. Development of a morphing wingtip based on compliant structures. *Journal of Intelligent Material Systems and Structures*, 29 (16): 3293–3304, June 2018. doi: [10.1177/1045389x18783076](https://doi.org/10.1177/1045389x18783076).
- [103] Patrick Meyer, Christian Hühne, Kjell Bramsiepe, and Wolf Krueger. Aeroelastic analysis of actuated adaptive wingtips based on pressure-actuated cellular structures. In *AIAA SCITECH 2023 Forum*. American Institute of Aeronautics and Astronautics, January 2023. doi: [10.2514/6.2023-0825](https://doi.org/10.2514/6.2023-0825).
- [104] Alessandro Spadoni and Massimo Ruzzene. Numerical and experimental analysis of the static compliance of chiral truss-core airfoils. *Journal of Mechanics of Materials and Structures*, 2 (5): 965–981, July 2007. ISSN 1559-3959. doi: [10.2140/jomms.2007.2.965](https://doi.org/10.2140/jomms.2007.2.965).
- [105] Imen Chekkal, Ron Cheung, Christopher Wales, Jonathan E. Cooper, Naomi Allen, Simon Lawson, Andrew J. Peace, Simon Hancock, Robert Cook, Paul Standen, and Giovanni M. Carossa. Design of a Morphing Wing Tip. In *22nd AIAA/ASME/AHS Adaptive Structures Conference*. American Institute of Aeronautics and Astronautics, January 2014. doi: [10.2514/6.2014-1262](https://doi.org/10.2514/6.2014-1262).
- [106] Chen Wang, Hamed Haddad Khodaparast, Michael Ian Friswell, and Alexander David Shaw. An equivalent model of corrugated panels with axial and bending coupling. *Computers & Structures*, 183: 61–72, April 2017. ISSN 0045-7949. doi: [10.1016/j.compstruc.2017.01.008](https://doi.org/10.1016/j.compstruc.2017.01.008).
- [107] C. Wang, H. H. Khodaparast, M. I. Friswell, and A. D. Shaw. Compliant structures based on stiffness asymmetry. *The Aeronautical Journal*, 122 (1249): 442–461, January 2018. ISSN 2059-6464. doi: [10.1017/aer.2017.144](https://doi.org/10.1017/aer.2017.144).
- [108] Jian Sun, Hongliang Gao, Fabrizio Scarpa, Cristian Lira, Yanju Liu, and Jinsong Leng. Active inflatable auxetic honeycomb structural concept for morphing wingtips. *Smart Materials and Structures*, 23 (12): 125023, October 2014. doi: [10.1088/0964-1726/23/12/125023](https://doi.org/10.1088/0964-1726/23/12/125023).
- [109] Jian Sun, Linzhe Du, Fabrizio Scarpa, Yanju Liu, and Jinsong Leng. Morphing wingtip structure based on active inflatable honeycomb and shape memory polymer composite skin: A conceptual work. *Aerospace Science and Technology*, 111: 106541, April 2021. ISSN 1270-9638. doi: [10.1016/j.ast.2021.106541](https://doi.org/10.1016/j.ast.2021.106541).
- [110] Patrick Meyer, Hendrik Traub, and Christian Hühne. Actuated adaptive wingtips on transport aircraft: Requirements and preliminary design using pressure-actuated cellular structures. *Aerospace Science and Technology*, 128: 107735, September 2022. doi: [10.1016/j.ast.2022.107735](https://doi.org/10.1016/j.ast.2022.107735).
- [111] Patrick Meyer, Michael Vorhof, Josef Koord, Cornelia Sennewald, Chokri Cherif, and Christian Hühne. Anisotropic flexure hinges: Manufacturing and mechanical characterization for application in pressure-actuated morphing structures. *Composites Part B: Engineering*, 266: 110967, November 2023. ISSN 1359-8368. doi: [10.1016/j.compositesb.2023.110967](https://doi.org/10.1016/j.compositesb.2023.110967).
- [112] Derek Bye and Paul McClure. Design of a morphing vehicle. In *48th AIAA/ASME/ASCE/AHS/ASC Structures, Structural Dynamics, and Materials Conference*. American Institute of Aeronautics and Astronautics, April 2007. doi: [10.2514/6.2007-1728](https://doi.org/10.2514/6.2007-1728).

- [113] Thomas Ivanco, Robert Scott, Michael Love, Scott Zink, and Terrence Weisshaar. Validation of the lockheed martin morphing concept with wind tunnel testing. In *48th AIAA/ASME/ASCE/AHS/ASC Structures, Structural Dynamics, and Materials Conference*. American Institute of Aeronautics and Astronautics, April 2007. doi: [10.2514/6.2007-2235](https://doi.org/10.2514/6.2007-2235).
- [114] Narcis M. Ursache, Tomas Melin, Askin T. Isikveren, and Michael I. Friswell. Technology integration for active poly-morphing winglets development. In *Smart Materials, Adaptive Structures and Intelligent Systems, Volume 1*. ASME, January 2008. doi: [10.1115/smasis2008-496](https://doi.org/10.1115/smasis2008-496).
- [115] Michael Love, Paul Zink, Ron Stroud, Derek Bye, Steven Rizk, and David White. Demonstration of morphing technology through ground and wind tunnel tests. In *48th AIAA/ASME/ASCE/AHS/ASC Structures, Structural Dynamics, and Materials Conference*. American Institute of Aeronautics and Astronautics, April 2007. doi: [10.2514/6.2007-1729](https://doi.org/10.2514/6.2007-1729).
- [116] Narcis Ursache, Tomas Melin, Askin Isikveren, and Mike Friswell. Morphing winglets for aircraft multi-phase improvement. In *7th AIAA ATIO Conf, 2nd CEIAT Int'l Conf on Innov and Integr in Aero Sciences, 17th LTA Systems Tech Conf; followed by 2nd TEOS Forum*. American Institute of Aeronautics and Astronautics, September 2007. doi: [10.2514/6.2007-7813](https://doi.org/10.2514/6.2007-7813).
- [117] Michael I. Friswell. The prospects for morphing aircraft. In *IV ECCOMAS Thematic Conference on Smart Structures and Materials*, Porto, Portugal, July 2009.
- [118] D.D. Smith, A.T. Isikveren, R.M. Ajaj, and M.I. Friswell. Multi-disciplinary Design Optimisation of an Active Non-planar Poly-morphing Wing. In *27th Congress of the International Council of the Aeronautical Sciences, 2010*. URL https://www.icas.org/ICAS_ARCHIVE/ICAS2010/-ABSTRACTS/304.HTM.
- [119] C. Thill, J. Etches, I. Bond, K. Potter, and P. Weaver. Morphing skins. *The Aeronautical Journal*, 112 (1129): 117–139, March 2008. doi: [10.1017/s0001924000002062](https://doi.org/10.1017/s0001924000002062).
- [120] Izabela K. Kuder, Andres F. Arrieta, Wolfram E. Raither, and Paolo Ermanni. Variable stiffness material and structural concepts for morphing applications. *Progress in Aerospace Sciences*, 63: 33–55, November 2013. ISSN 0376-0421. doi: [10.1016/j.paerosci.2013.07.001](https://doi.org/10.1016/j.paerosci.2013.07.001).
- [121] Farhan Gandhi and Phuriwat Anusonti-Inthra. Skin design studies for variable camber morphing airfoils. *Smart Materials and Structures*, 17 (1): 015025, January 2008. ISSN 1361-665X. doi: [10.1088/0964-1726/17/01/015025](https://doi.org/10.1088/0964-1726/17/01/015025).
- [122] Gabriel Murray, Farhan Gandhi, and Charles Bakis. Flexible matrix composite skins for one-dimensional wing morphing. *Journal of Intelligent Material Systems and Structures*, 21 (17): 1771–1781, April 2010. doi: [10.1177/1045389x10369719](https://doi.org/10.1177/1045389x10369719).
- [123] Kingnidé Raymond Olympio and Farhan Gandhi. Zero Poisson's Ratio Cellular Honeycombs for Flex Skins Undergoing One-Dimensional Morphing. *Journal of Intelligent Material Systems and Structures*, 21 (17): 1737–1753, December 2009. doi: [10.1177/1045389x09355664](https://doi.org/10.1177/1045389x09355664).
- [124] Michelle M. Keihl, Robert S. Bortolin, Brian Sanders, Shiv Joshi, and Zeb Tidwell. Mechanical properties of shape memory polymers for morphing aircraft applications. In Edward V. White, editor, *Smart Structures and Materials 2005: Industrial and Commercial Applications of Smart Structures Technologies*, volume 5762, page 143. SPIE, May 2005. doi: [10.1117/12.600569](https://doi.org/10.1117/12.600569).

- [125] H.J. Qi and M.C. Boyce. Stress-strain behavior of thermoplastic polyurethanes. *Mechanics of Materials*, 37 (8): 817–839, August 2005. ISSN 0167-6636. doi: [10.1016/j.mechmat.2004.08.001](https://doi.org/10.1016/j.mechmat.2004.08.001).
- [126] Senthil Murugan and M.I. Friswell. Morphing wing flexible skins with curvilinear fiber composites. *Composite Structures*, 99: 69–75, May 2013. ISSN 0263-8223. doi: [10.1016/j.compstruct.2012.11.026](https://doi.org/10.1016/j.compstruct.2012.11.026).
- [127] Edward A. Bubert, Benjamin K. S. Woods, Keejoo Lee, Curt S. Kohera, and N. M. Wereley. Design and Fabrication of a Passive 1D Morphing Aircraft Skin. *Journal of Intelligent Material Systems and Structures*, 21 (17): 1699–1717, September 2010. doi: [10.1177/1045389x10378777](https://doi.org/10.1177/1045389x10378777).
- [128] Silvestro Barbarino, Farhan Gandhi, and Steven D. Webster. Design of extendable chord sections for morphing helicopter rotor blades. *Journal of Intelligent Material Systems and Structures*, 22 (9): 891–905, June 2011. ISSN 1530-8138. doi: [10.1177/1045389x11414077](https://doi.org/10.1177/1045389x11414077).
- [129] L. D. Peel. Exploration of high and negative poissonâ€™s ratio elastomerâ€¢matrix laminates. *physica status solidi (b)*, 244 (3): 988–1003, February 2007. ISSN 1521-3951. doi: [10.1002/pssb.200572717](https://doi.org/10.1002/pssb.200572717).
- [130] Y J Chen, F Scarpa, I R Farrow, Y J Liu, and J S Leng. Composite flexible skin with large negative poissonâ€™s ratio range: numerical and experimental analysis. *Smart Materials and Structures*, 22 (4): 045005, February 2013. ISSN 1361-665X. doi: [10.1088/0964-1726/22/4/045005](https://doi.org/10.1088/0964-1726/22/4/045005).
- [131] K. Raymond Olympio and Farhan Gandhi. Optimal cellular core topologies for one-dimensional morphing aircraft structures. *Journal of Mechanical Design*, 134 (8), July 2012. ISSN 1528-9001. doi: [10.1115/1.4007087](https://doi.org/10.1115/1.4007087).
- [132] Robert D. Vocke, Curt S. Kohera, Benjamin K.S. Woods, and Norman M. Wereley. Development and Testing of a Span-Extending Morphing Wing. *Journal of Intelligent Material Systems and Structures*, 22 (9): 879–890, June 2011. doi: [10.1177/1045389x11411121](https://doi.org/10.1177/1045389x11411121).
- [133] Rafael M Heeb, Michael Dicker, and Benjamin K S Woods. Manufacturing and characterisation of 3d printed thermoplastic morphing skins. *Smart Materials and Structures*, 31 (8): 085007, July 2022. doi: [10.1088/1361-665x/ac71ed](https://doi.org/10.1088/1361-665x/ac71ed).
- [134] Curt S Kohera, Benjamin KS Woods, Norman M Wereley, Peter C Chen, and Edward A Bubert. Cellular support structures used for controlled actuation of fluid contact surfaces, April 2011. U.S. Patent No. 7,931,240.
- [135] Benjamin K. S. Woods and Rafael M. Heeb. Design principles for geometrically anisotropic thermoplastic rubber morphing aircraft skins. *Journal of Intelligent Material Systems and Structures*, 34: 29–46, May 2023. ISSN 1045-389X. doi: [10.1177/1045389x221096155](https://doi.org/10.1177/1045389x221096155).
- [136] NinjaTek. NinjaFlex 3D Printing Filament. Technical report, Fenner Precision Polymers, 2016. URL <https://nijatek.com/wp-content/uploads/NinjaFlex-TDS.pdf>.
- [137] NinjaTek. Armadillo 3D Printing Filament. Technical report, Fenner Precision Polymers, 2016. URL <https://nijatek.com/wp-content/uploads/Armadillo-TDS.pdf>.

- [138] Rafael M. Heeb, Michael Dicker, and Benjamin K. S. Woods. Design Space Exploration and Modelling of GATOR 3D Printed Morphing Skins. In *ASME 2022 Conference on Smart Materials, Adaptive Structures and Intelligent Systems*, SMASIS2022. American Society of Mechanical Engineers, September 2022. doi: [10.1115/smasis2022-93488](https://doi.org/10.1115/smasis2022-93488).
- [139] Rafael Martin Heeb and Benjamin King Sutton Woods. Experimental characterisation of gator morphing aircraft skins under combined in-plane and out-of-plane loading. In *ASME 2024 Aerospace Structures, Structural Dynamics, and Materials Conference*, SSDM2024. American Society of Mechanical Engineers, April 2024. doi: [10.1115/ssdm2024-121418](https://doi.org/10.1115/ssdm2024-121418).
- [140] Kingnide Raymond Olympio, Farhan Gandhi, Laila Asheghian, and Jay Kudva. Design of a flexible skin for a shear morphing wing. *Journal of Intelligent Material Systems and Structures*, 21 (17): 1755–1770, September 2010. ISSN 1530-8138. doi: [10.1177/1045389x10382586](https://doi.org/10.1177/1045389x10382586).
- [141] Matthew DiPalma and Farhan Gandhi. A comparison of cellular lattices structures with curved and straight inclined walls. In *AIAA Scitech 2019 Forum*. American Institute of Aeronautics and Astronautics, January 2019. doi: [10.2514/6.2019-2050](https://doi.org/10.2514/6.2019-2050).
- [142] Tomohiro Yokozeki, Shin ichi Takeda, Toshio Ogasawara, and Takashi Ishikawa. Mechanical properties of corrugated composites for candidate materials of flexible wing structures. *Composites Part A: Applied Science and Manufacturing*, 37 (10): 1578–1586, October 2006. doi: [10.1016/j.compositesa.2005.10.015](https://doi.org/10.1016/j.compositesa.2005.10.015).
- [143] Xiaobo Gong, Liwu Liu, Fabrizio Scarpa, Jinsong Leng, and Yanju Liu. Variable stiffness corrugated composite structure with shape memory polymer for morphing skin applications. *Smart Materials and Structures*, 26 (3): 035052, February 2017. ISSN 1361-665X. doi: [10.1088/1361-665x/aa516d](https://doi.org/10.1088/1361-665x/aa516d).
- [144] C Thill, J A Etches, I P Bond, K D Potter, and P M Weaver. Composite corrugated structures for morphing wing skin applications. *Smart Materials and Structures*, 19 (12): 124009, November 2010. ISSN 1361-665X. doi: [10.1088/0964-1726/19/12/124009](https://doi.org/10.1088/0964-1726/19/12/124009).
- [145] Nuhaadh Mohamed Mahid and Benjamin King Sutton Woods. Initial exploration of a compliance-based morphing fairing concept for hinged aerodynamic surfaces. *Aerospace Science and Technology*, 136: 108244, March 2023. doi: [10.1016/j.ast.2023.108244](https://doi.org/10.1016/j.ast.2023.108244).
- [146] Jian Huang, Xiaobo Gong, Qiuhua Zhang, Fabrizio Scarpa, Yanju Liu, and Jinsong Leng. In-plane mechanics of a novel zero Poisson's ratio honeycomb core. *Composites Part B: Engineering*, 89: 67–76, March 2016. doi: [10.1016/j.compositesb.2015.11.032](https://doi.org/10.1016/j.compositesb.2015.11.032).
- [147] Jian Huang, Qiuhsua Zhang, Fabrizio Scarpa, Yanju Liu, and Jinsong Leng. Bending and benchmark of zero poisson's ratio cellular structures. *Composite Structures*, 152: 729–736, September 2016. doi: [10.1016/j.compstruct.2016.05.078](https://doi.org/10.1016/j.compstruct.2016.05.078).
- [148] Lorna J. Gibson and Michael F. Ashby. *Cellular Solids: Structure and Properties*. Cambridge University Press, May 1997. ISBN 9781139878326. doi: [10.1017/cbo9781139878326](https://doi.org/10.1017/cbo9781139878326).
- [149] Kingnidé R. Olympio and Farhan Gandhi. Flexible skins for morphing aircraft using cellular honeycomb cores. *Journal of Intelligent Material Systems and Structures*, 21 (17): 1719–1735, November 2009. doi: [10.1177/1045389x09350331](https://doi.org/10.1177/1045389x09350331).

- [150] Rafael M. Heeb. *Multi-material 3D Printed Thermoplastic Morphing Aircraft Skins: Manufacturing, Testing, Analysis, and Design Space Exploration*. Phd thesis, University of Bristol, October 2023.
- [151] AIRBUS. *A320 Aircraft Characteristics - Airport and Maintenance Planning*. AIRBUS S.A.S., Customer Services, Technical Data Support and Services, 31707 Blagnac Cedex, France, 39th edition, January 2020.
- [152] Aewis K.W. Hii and Bassam El Said. A kinematically consistent second-order computational homogenisation framework for thick shell models. *Computer Methods in Applied Mechanics and Engineering*, 398: 115136, August 2022. doi: [10.1016/j.cma.2022.115136](https://doi.org/10.1016/j.cma.2022.115136).
- [153] L. Gigliotti and S.T. Pinho. Exploiting symmetries in solid-to-shell homogenization, with application to periodic pin-reinforced sandwich structures. *Composite Structures*, 132: 995–1005, November 2015. doi: [10.1016/j.compstruct.2015.06.062](https://doi.org/10.1016/j.compstruct.2015.06.062).
- [154] S. Daynes, S. Feih, W. F. Lu, and J. Wei. Sandwich structures with 3D printed functionally graded lattice cores. volume 2017-August, 2017.
- [155] Stephen Daynes, Stefanie Feih, Wen Feng Lu, and Jun Wei. Optimisation of functionally graded lattice structures using isostatic lines. *Materials & Design*, 127: 215–223, August 2017. ISSN 0264-1275. doi: [10.1016/j.matdes.2017.04.082](https://doi.org/10.1016/j.matdes.2017.04.082).
- [156] Stephen Daynes, Stefanie Feih, Wen Feng Lu, and Jun Wei. Design concepts for generating optimised lattice structures aligned with strain trajectories. *Computer Methods in Applied Mechanics and Engineering*, 354: 689–705, September 2019. doi: [10.1016/j.cma.2019.05.053](https://doi.org/10.1016/j.cma.2019.05.053).
- [157] D.W. Kelly and M. Elsley. A procedure for determining load paths in elastic continua. *Engineering Computations*, 12 (5): 415–424, May 1995. doi: [10.1108/02644409510799721](https://doi.org/10.1108/02644409510799721).
- [158] D.W. Kelly and M.W. Tosh. Interpreting load paths and stress trajectories in elasticity. *Engineering Computations*, 17 (2): 117–135, March 2000. ISSN 0264-4401. doi: [10.1108/02644400010313084](https://doi.org/10.1108/02644400010313084).
- [159] D. Kelly, C. Reidsema, A. Bassandeh, G. Pearce, and M. Lee. On interpreting load paths and identifying a load bearing topology from finite element analysis. *Finite Elements in Analysis and Design*, 47 (8): 867–876, August 2011. doi: [10.1016/j.finel.2011.03.007](https://doi.org/10.1016/j.finel.2011.03.007).
- [160] Donald W. Kelly, Carl A. Reidsema, and Merrill C.W. Lee. An algorithm for defining load paths and a load bearing topology in finite element analysis. *Engineering Computations*, 28 (2): 196–214, March 2011. doi: [10.1108/02644401111109231](https://doi.org/10.1108/02644401111109231).
- [161] Mohammad Rouhi, Hossein Ghayoor, Jeffrey Fortin-Simpson, Tom T. Zacchia, Suong V. Hoa, and Mehdi Hojjati. Design, manufacturing, and testing of a variable stiffness composite cylinder. *Composite Structures*, 184: 146–152, January 2018. doi: [10.1016/j.compstruct.2017.09.090](https://doi.org/10.1016/j.compstruct.2017.09.090).
- [162] Stephen Daynes. Simultaneous optimisation of support structure regions and part topology for additive manufacturing. *Structural and Multidisciplinary Optimization*, 65 (11), November 2022. doi: [10.1007/s00158-022-03454-z](https://doi.org/10.1007/s00158-022-03454-z).
- [163] A. Alderson, K.L. Alderson, G. Chirima, N. Ravirala, and K.M. Zied. The in-plane linear elastic constants and out-of-plane bending of 3-coordinated ligament and cylinder-ligament

- honeycombs. *Composites Science and Technology*, 70 (7): 1034–1041, July 2010. ISSN 0266-3538. doi: [10.1016/j.compscitech.2009.07.010](https://doi.org/10.1016/j.compscitech.2009.07.010).
- [164] Nuhaadh Mohamed Mahid, Mark Schenk, Branislav Titurus, and Benjamin King Sutton Woods. Parametric studies of flexible sandwich panels as a compliant fairing for folding wingtip joints. In *ASME 2023 Conference on Smart Materials, Adaptive Structures and Intelligent Systems*, SMASIS2023. American Society of Mechanical Engineers, September 2023. doi: [10.1115/smasis2023-110481](https://doi.org/10.1115/smasis2023-110481).
 - [165] J. M. Whitney. Shear correction factors for orthotropic laminates under static load. *Journal of Applied Mechanics*, 40 (1): 302–304, March 1973. doi: [10.1115/1.3422950](https://doi.org/10.1115/1.3422950).
 - [166] N.J. Pagano. Exact solutions for rectangular bidirectional composites and sandwich plates. *Journal of Composite Materials*, 4 (1): 20–34, January 1970. doi: [10.1177/002199837000400102](https://doi.org/10.1177/002199837000400102).
 - [167] Eric Reissner. The effect of transverse shear deformation on the bending of elastic plates. *Journal of Applied Mechanics*, 12 (2): A69–A77, June 1945. doi: [10.1115/1.4009435](https://doi.org/10.1115/1.4009435).
 - [168] D.H. Chen. Bending deformation of honeycomb consisting of regular hexagonal cells. *Composite Structures*, 93 (2): 736–746, January 2011. ISSN 0263-8223. doi: [10.1016/j.compstruct.2010.08.006](https://doi.org/10.1016/j.compstruct.2010.08.006).
 - [169] D.H. Chen. Equivalent flexural and torsional rigidity of hexagonal honeycomb. *Composite Structures*, 93 (7): 1910–1917, June 2011. ISSN 0263-8223. doi: [10.1016/j.compstruct.2011.02.009](https://doi.org/10.1016/j.compstruct.2011.02.009).
 - [170] Eric Reissner and Manuel Stein. Torsion and transverse bending of cantilever plates. Tech Report NACA-TN-2369, NASA, June 1951. URL <https://ntrs.nasa.gov/citations/19930090894>.
 - [171] Rodrigo Jos  da Silva, J lio Cesar dos Santos, Rodrigo Teixeira Santos Freire, Fabiano Bianchini Batista, T lio Hallak Panzera, Andr  Luis Christoforo, and Fabrizio Scarpa. A core rigidity classifier method and a novel approach to account for geometric effects on the elastic properties of sandwich structures. *Composite Structures*, 282: 115075, February 2022. ISSN 0263-8223. doi: [10.1016/j.compstruct.2021.115075](https://doi.org/10.1016/j.compstruct.2021.115075).
 - [172] Vincent Beng Chye Tan, Karthikayen Raju, and Heow Pueh Lee. Direct fe2 for concurrent multilevel modelling of heterogeneous structures. *Computer Methods in Applied Mechanics and Engineering*, 360: 112694, March 2020. ISSN 0045-7825. doi: [10.1016/j.cma.2019.112694](https://doi.org/10.1016/j.cma.2019.112694).
 - [173] M.M. Ameen, R.H.J. Peerlings, and M.G.D. Geers. A quantitative assessment of the scale separation limits of classical and higher-order asymptotic homogenization. *European Journal of Mechanics - A/Solids*, 71: 89–100, September 2018. ISSN 0997-7538. doi: [10.1016/j.euromechsol.2018.02.011](https://doi.org/10.1016/j.euromechsol.2018.02.011).
 - [174] Dassault Systemes Simulia Corp. Abaqus documentation. In *SIMULIA User Assistance 2018*. Dassault Systemes Simulia Corp, 2018.
 - [175] M G D Geers, E W C Coenen, and V G Kouznetsova. Multi-scale computational homogenization of structured thin sheets. *Modelling and Simulation in Materials Science and Engineering*, 15 (4): S393–S404, May 2007. ISSN 1361-651X. doi: [10.1088/0965-0393/15/4/s06](https://doi.org/10.1088/0965-0393/15/4/s06).

- [176] Christophe Geuzaine and Jean-François Remacle. Gmsh: A 3-D finite element mesh generator with built-in pre- and post-processing facilities. *International Journal for Numerical Methods in Engineering*, 79 (11): 1309–1331, May 2009. doi: [10.1002/nme.2579](https://doi.org/10.1002/nme.2579).
- [177] C. L. Ladson and Jr. Brooks, Cuyler W. Development of a computer program to obtain ordinates for naca 4-digit, 4-digit modified, 5-digit, and 16 series airfoils. Tech report, NASA Langley Research Center, 1975.
- [178] Stephen Timoshenko and J. N. Goodier. *Theory of elasticity*. McGraw-Hill, New York, 3rd edition, 1970.
- [179] Pasquale M. Sforza. *Quasi-One-Dimensional Flow Equations*, pages 35–53. Elsevier, 2012. ISBN 9781856179126. doi: [10.1016/b978-1-85617-912-6.00002-5](https://doi.org/10.1016/b978-1-85617-912-6.00002-5).
- [180] D.J. Auld and K. Srinivas. Aerodynamics for students. Aerospace, Mechanical & Mechatronic Engineering, University of Sydney, 1995. URL http://www-mdp.eng.cam.ac.uk/web/library/-enginfo/aero/thermal_dvd_only/aero/contents.html.
- [181] Mohammad Rouhi, Hossein Ghayoor, Suong V. Hoa, and Mehdi Hojjati. Computational efficiency and accuracy of multi-step design optimization method for variable stiffness composite structures. *Thin-Walled Structures*, 113: 136–143, April 2017. doi: [10.1016/j.tws.2017.01.019](https://doi.org/10.1016/j.tws.2017.01.019).
- [182] Etana Ferede, Mostafa Abdalla, Farhan Gandhi, Gerard van Bussel, and Johannes Dillinger. Aeroelastic optimization of composite wind turbine blades using variable stiffness laminates. In *73rd American Helicopter Society International Annual Forum and Technology Display*, page 3023 – 3039, Fort Worth, Texas, USA, May 2017. American Helicopter Society.
- [183] R.L. Lincoln, P.M. Weaver, A. Pirrera, and R.M.J. Groh. Imperfection-insensitive continuous tow-sheared cylinders. *Composite Structures*, 260: 113445, March 2021. ISSN 0263-8223. doi: [10.1016/j.compstruct.2020.113445](https://doi.org/10.1016/j.compstruct.2020.113445).
- [184] Byung Chul Kim, Kevin Potter, and Paul M. Weaver. Continuous tow shearing for manufacturing variable angle tow composites. *Composites Part A: Applied Science and Manufacturing*, 43 (8): 1347–1356, August 2012. ISSN 1359-835X. doi: [10.1016/j.compositesa.2012.02.024](https://doi.org/10.1016/j.compositesa.2012.02.024).
- [185] Daniel Morton, Artemis Xu, Alberto Matute, and Robert F Shepherd. Autonomous material composite morphing wing. *Journal of Composite Materials*, 57 (4): 711–720, January 2023. ISSN 1530-793X. doi: [10.1177/00219983231151397](https://doi.org/10.1177/00219983231151397).
- [186] Benjamin Jenett, Sam Calisch, Daniel Cellucci, Nick Cramer, Neil Gershenfeld, Sean Swei, and Kenneth C. Cheung. Digital Morphing Wing: Active Wing Shaping Concept Using Composite Lattice-Based Cellular Structures. *Soft Robotics*, 4 (1): 33–48, March 2017. ISSN 2169-5180. doi: [10.1089/soro.2016.0032](https://doi.org/10.1089/soro.2016.0032).
- [187] Kerr-Jia Lu and Sridhar Kota. Design of compliant mechanisms for morphing structural shapes. *Journal of Intelligent Material Systems and Structures*, 14 (6): 379–391, June 2003. ISSN 1530-8138. doi: [10.1177/1045389x03035563](https://doi.org/10.1177/1045389x03035563).
- [188] Sridhar Kota. System for varying a surface contour, January 1998. US Patent No: US 5,971,328 A.

- [189] Hirofumi Harasaki and Jasbir S. Arora. New concepts of transferred and potential transferred forces in structures. *Computer Methods in Applied Mechanics and Engineering*, 191 (3-5): 385–406, November 2001. ISSN 0045-7825. doi: [10.1016/s0045-7825\(01\)00279-1](https://doi.org/10.1016/s0045-7825(01)00279-1).
- [190] Toshiaki Sakurai, Junichi Tanaka, Akinori Otani, Changjun Zhang, and Kunihiro Takahashi. Load Path Optimization and U* Structural Analysis for Passenger Car Compartments under Frontal Collision. In *SAE Technical Paper Series*, IBEC. SAE International, October 2003. doi: [10.4271/2003-01-2734](https://doi.org/10.4271/2003-01-2734).
- [191] Giovanni Zucco, Mohammad Rouhi, Vincenzo Oliveri, Enzo Cosentino, Ronan M. O'Higgins, and Paul M. Weaver. Continuous tow steering around an elliptical cutout in a composite panel. *AIAA Journal*, 59 (12): 5117–5129, December 2021. ISSN 1533-385X. doi: [10.2514/1.j060668](https://doi.org/10.2514/1.j060668).
- [192] Calum J. McInnes, Reece Lincoln, Alberto Pirrera, Byung Chul Kim, and Rainer M. Groh. On the Finite Element Discretization of Continuous Tow Sheared Structures. In *AIAA SCITECH 2022 Forum*. American Institute of Aeronautics and Astronautics, January 2022. doi: [10.2514/6.2022-2598](https://doi.org/10.2514/6.2022-2598).
- [193] Tim Heitkamp, Sebastian Kuschmitz, Simon Girnth, Justin-Dean Marx, GÃ¼nter Klawitter, Nils Waldt, and Thomas Vietor. Stress-adapted fiber orientation along the principal stress directions for continuous fiber-reinforced material extrusion. *Progress in Additive Manufacturing*, 8 (3): 541–559, September 2022. ISSN 2363-9520. doi: [10.1007/s40964-022-00347-x](https://doi.org/10.1007/s40964-022-00347-x).
- [194] Shengjie Zhao, Nan Wu, and Quan Wang. Load path-guided fiber trajectory in composite panels: A comparative study and a novel combined method. *Composite Structures*, 263: 113689, May 2021. doi: [10.1016/j.compstruct.2021.113689](https://doi.org/10.1016/j.compstruct.2021.113689).
- [195] Kun Marjadi and Satchi Venkataraman. Comparison of quantitative and qualitative information provided by different structural load path definitions. *International Journal for Simulation and Multidisciplinary Design Optimization*, 3 (3): 384–400, July 2009. ISSN 1779-6288. doi: [10.1051/ijsmdo/2009014](https://doi.org/10.1051/ijsmdo/2009014).
- [196] Junpeng Wang, Christoph Neuhauser, Jun Wu, Xifeng Gao, and RÃ¼diger Westermann. 3D-TSV: The 3D trajectory-based stress visualizer. *Advances in Engineering Software*, 170: 103144, August 2022. doi: [10.1016/j.advengsoft.2022.103144](https://doi.org/10.1016/j.advengsoft.2022.103144).

